computational atmospheric acoustics

computational atmospheric acoustics

by

ERIK M. SALOMONS

TNO Institute of Applied Physics,
Delft, The Netherlands

SPRINGER-SCIENCE+BUSINESS MEDIA,B.V.

A C.I.P. Catalogue record for this book is available from the Library of Congress.

ISBN 978-1-4020-0390-5 ISBN 978-94-010-0660-6 (eBook)
DOI 10.1007/978-94-010-0660-6

Printed on acid-free paper

Contents

preface

This book is intended for anyone who is interested in the computation of sound propagation in the atmosphere. In some simple cases the computation can be performed analytically. In most cases, however, the computation must be performed numerically, as the atmosphere is a complex medium for sound waves. The book describes current computational methods for sound propagation in the atmosphere.

The book is based on many excellent articles from the literature of atmospheric acoustics. Articles presented at the International Symposia on Long Range Sound Propagation have been particularly valuable.

The book was written 'on week-ends', but the inspiring atmosphere on week-days at the TNO Institute of Applied Physics has very much contributed to the book.

The author is grateful to Andrew Thean and Niels Salomons for many valuable comments on the text. Above all, the author is grateful to Marga Salomons, Michelle Salomons, and Lisa Salomons for help and support in writing the book.

Erik M. Salomons
TNO Institute of Applied Physics
May 2001

Chapter 1

Introduction

1.1 Atmospheric acoustics

Atmospheric acoustics is the science of sound propagation in the atmosphere. The basic geometry with a source and a receiver is illustrated in Fig. 1.1. Sound waves are generated by a source and travel through the atmosphere to a receiver. The source may be a whistling bird, as in Fig. 1.1. Other important examples of sources are cars, trains, and airplanes.

The atmosphere is a complex medium for sound propagation. Wind and temperature distributions in the atmosphere play an important role in the propagation. The influence of wind is illustrated by the fact that the sound from a source near the ground is often louder on the downwind side of the source than on the upwind side of the source. Sound propagation is affected not only by the distributions of the *mean* wind and temperature, but also by rapid *fluctuations* of wind and temperature, *i.e.* atmospheric turbulence.

The ground surface can be considered as the boundary of the propagation medium. Reflection of sound waves by the ground surface plays an important role in the propagation. One distinguishes *hard* grounds and *absorbing*

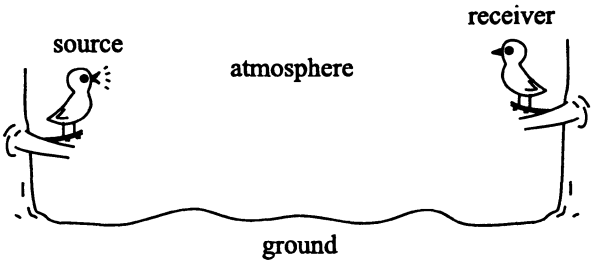

Figure 1.1. Basic geometry of sound propagation in the atmosphere.

grounds. A hard ground reflects a sound wave completely. An absorbing ground partly reflects and partly absorbs a sound wave. Many natural grounds, such as grassland, can be described as sandy soil covered with vegetation. These grounds are absorbing. Concrete is an example of a hard ground. A water surface can also be considered as a hard surface. Not only the ground material but also the terrain profile, *i.e.* the spatial variation of the ground level, has an effect on the propagation of sound waves.

General descriptions of the effects of the atmosphere and the ground on sound propagation can be found in Refs. [66, 124, 75, 108, 40, 51, 146]. Experimental results can be found in Refs. [157, 101, 102, 20, 115].

1.2 Scope of the book

During the past two decades, several accurate computational models have been developed for sound propagation in the atmosphere. These models take into account the complex effects of the atmosphere and the ground. The models are based on analogous models used in underwater acoustics, electromagnetics, and seismology.

The objective of this book is to present a self-contained description of computational models that are currently employed in atmospheric acoustics. The description includes a derivation of the models from basic acoustic principles. As meteorological effects play an important role in atmospheric acoustics, selected topics from boundary layer meteorology and wave propagation in turbulent media are also presented.

The models described in this book can be used for a wide variety of situations. The propagation distance may vary between a distance of the order of one meter and a distance of the order of ten kilometers. The source height and the receiver height may also vary. Emphasis will be on situations with source and receiver heights of the order of a few meters, but the models can also be used for high sources, *e.g.* a flying airplane.

The models described in this book take into account various effects of the atmosphere and the ground surface on sound propagation. Some models even take into account the complex effects of atmospheric turbulence and irregular terrain. In practice, detailed information about the state of the atmosphere and the state of the ground surface is always limited. Consequently, computational studies of atmospheric sound propagation are restricted to relatively idealized systems. A challenge in computational atmospheric acoustics is to find acceptable idealizations of real systems. The idealizations presented in this book are based on the author's experience. It should be noted that comparisons of model predictions with experimental results are not presented in this book.

With the models described in this book, both the amplitude and the phase of a sound wave can be computed. Emphasis will be on the amplitude, however, as the amplitude determines the loudness of a sound wave. The phase of a sound wave is relatively unimportant, in particular for propagation distances of

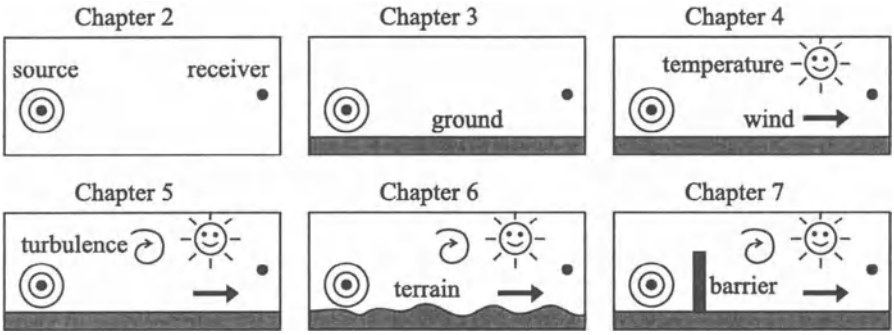

Figure 1.2. Illustration of the structure of the book. Chapters 2 to 7 describe sound propagation in systems of increasing complexity. In Chap. 2, an unbounded homogeneous atmosphere is considered. In Chaps. 3 to 7, the following elements are included successively: ground surface, wind and temperature distributions, turbulence, terrain, and a noise barrier.

the order of a kilometer or more.

The models are based on the theory of linear acoustics. This implies that the models are valid for most types of sound that occur in the atmosphere, but not for very loud sounds such as strong blast waves from explosions or sonic booms from supersonic airplanes. In all models, it is assumed that the source is a point source. A real source with finite dimensions can always be represented by a set of point sources.

1.3 Structure of the book

The main text of the book focuses on physical phenomena in atmospheric acoustics, and gives brief descriptions of the computational models; detailed mathematical descriptions of the models are presented in the appendices. In this way, the reader can first get a quick impression of a model from the main text, and next study the complete description of the model in an appendix.

The main text consists of the present introductory chapter followed by six chapters, which describe sound propagation in systems of increasing complexity (see Fig. 1.2).

Chapter 2 describes sound propagation in the simplest system: an unbounded homogeneous atmosphere, *i.e.* a homogeneous atmosphere without a ground surface. Chapter 3 describes sound propagation over a flat ground surface in a homogeneous atmosphere. Chapter 4 describes sound propagation over a flat ground surface in a refracting atmosphere, *i.e.* an atmosphere with inhomogeneous distributions of the temperature and the wind velocity. Chapters 5 to 7 describe the effects on sound propagation of atmospheric turbulence,

irregular terrain, and a noise barrier, respectively.

Chapter 2 is based on Appendices A and B. Appendix A presents the basic equations of linear acoustics. Appendix B introduces the sound pressure level and the sound power level, and describes spherical spreading and atmospheric absorption of sound waves.

Chapter 3 is based on Appendices C and D, which introduce the acoustic impedance of a ground surface and describe the reflection of spherical sound waves by a ground surface.

Chapter 4 is based on Appendices E, F, G, H, L, and N. Appendix E presents linear acoustic equations for moving inhomogeneous atmospheres. Appendices F, G, H, and L describe four computational models for atmospheric sound propagation (the FFP model, the CNPE model, the GFPE model, and the ray model). In Appendix N, wind and temperature profiles in the atmospheric surface layer are described.

Chapter 5 is based on Appendices I, J, and K. Appendix I presents an outline of the mathematical theory of atmospheric turbulence. Appendices J and K describe the incorporation of atmospheric turbulence in sound propagation models.

Chapter 6 is based on Appendix M, which describes computational methods for sound propagation over irregular terrain.

Chapter 7 is based on Appendix O, which describes computational methods for sound propagation over a noise barrier.

Chapter 2

Unbounded homogeneous atmosphere

2.1 Introduction

Sound in the atmosphere is produced by a sound source. The source may be a rapidly vibrating object, *e.g.* the membrane of a loudspeaker. A vibrating object generates a sequence of compressions and rarefactions in the air surrounding it. The corresponding local fluctuations in air pressure travel away from the source, in all directions. Such a traveling pressure fluctuation is called a sound wave. The difference between the fluctuating pressure and the average pressure, *i.e.* the variation of the pressure, is called the *acoustic pressure* or the *sound pressure*. A sound wave travels with a finite speed of about 340 m/s. This is experienced most clearly for sound pulses: it takes some time before a sound pulse generated by a source reaches a distant receiver.

A pure tone is a sound wave in which the sound pressure oscillates sinusoidally with time. The sound wave is called a *harmonic* sound wave in this case. The number of oscillations per unit time is called the frequency, which is expressed in units of hertz, abbreviated as Hz; 1 Hz equals 1 oscillation per second. The pitch of the tone is determined by the frequency. Most sound signals are mixtures of pure tones with different frequencies. The human ear is sensitive to frequencies in the range from roughly 20 Hz to 20 kHz.

The loudness of a pure tone is determined by the amplitude of the sinusoidal pressure oscillation. In acoustics, loudness is represented by the *sound pressure level*, which is directly related to the amplitude of the pressure oscillation, as will be explained in this chapter. The sound pressure level is expressed in decibels, abbreviated as dB. The decibel scale is defined in such a way that 0 dB corresponds roughly to the hearing threshold of a person with acute hearing, and 130 dB roughly to the threshold of pain.

In practice, sound pressures are often small in comparison with the total

E. M. Salomons, *Computational Atmospheric Acoustics*

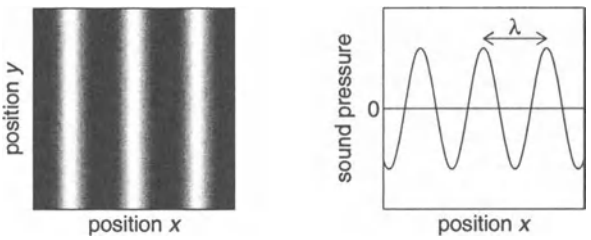

Figure 2.1. Left: cross-section of the sound pressure field of a plane harmonic sound wave, at fixed time t. A grey level scale is used, with the maximum positive and negative sound pressures indicated as white and black, respectively. Right: corresponding graph of the sound pressure as a function of propagation distance x. The wavelength λ is indicated in the graph.

pressure in the atmosphere, typically 0.1% or smaller. This fact is used in the mathematical description of sound that is called *linear acoustics*. In linear acoustics, only terms linear in the sound pressure are retained in the equations; quadratic and higher-order terms are neglected. The basic equations of linear acoustics, including the wave equation, are derived in Appendix A.

In the derivation of the equations of linear acoustics, the atmosphere is modeled as a compressible fluid, *i.e.* a gaseous medium in which local pressure fluctuations cause local density fluctuations. When a sound wave travels through this medium, alternating local compressions and rarefactions occur. The corresponding movement of air is represented by a (fluctuating) *fluid velocity*. The time average of the fluid velocity is equal to zero, as there is no net transport of air in a sound wave (here we ignore the effect of wind in the atmosphere).

2.2 Plane waves

The sound pressure at a point in the atmosphere is defined as the instantaneous pressure minus the time-averaged pressure at the point. The sound pressure is a function of position $\mathbf{r}$ and time t, and is denoted as $p(\mathbf{r}, t)$. We use boldfaced symbols for vectors in this book, so $\mathbf{r}$ represents a three-dimensional vector, *e.g.* $\mathbf{r} = (x, y, z)$ if a rectangular xyz coordinate system is used.

As an example, we consider a harmonic sound wave traveling in the x direction, with sound pressure

$$p(\mathbf{r}, t) = A\cos(kx - \omega t), \tag{2.1}$$

where A is the amplitude and $kx - \omega t$ is the phase, which depends on the angular frequency ω and the wave number k. The corresponding fluid velocity has an x component only, which is equal to $A'\cos(kx - \omega t)$, with amplitude A'. A sound wave with sound pressure given by Eq. (2.1) is called a plane wave, as

the sound pressure is constant within each plane perpendicular to the x axis. This is illustrated in Fig. 2.1.

Plane waves do not occur frequently in the open air, but are useful for illustrating wave propagation. Equation (2.1) shows that the sound pressure of a harmonic wave is a periodic function of time, with period $T = 2\pi/\omega$, at each point in the atmosphere. The number of oscillations per unit time is the frequency $f = 1/T$, so we have $\omega = 2\pi f$. Equation (2.1) also shows that the sound pressure at fixed time t is a periodic function of x, with spatial period $\lambda = 2\pi/k$, which is called the wavelength. Further, the sound pressure appears constant to an observer moving in the x direction with speed $c = \omega/k$, as the argument $(kx - \omega t) = k(x - ct)$ of the cosine function in Eq. (2.1) is constant for the receiver. In other words, acoustic pressure fluctuations travel with speed $c = \omega/k$, or $c = \lambda f$, which is called the sound speed. The sound speed is sometimes called the adiabatic sound speed, as sound propagation in air can be considered as an adiabatic process, *i.e.* a process without heat flow. The (adiabatic) sound speed in air is evaluated in Sec. A.2.

The sound speed in air is a function of the temperature of the air. At a temperature of 15°C we have $c = 340$ m/s. The sound speed increases with increasing temperature. A variation of the temperature by 1°C corresponds to a variation of the sound speed by about 0.6 m/s, within the temperature range between −20°C and +40°C. The temperature usually varies with position in the atmosphere, in particular with height above the ground. In the daytime, the temperature usually decreases with increasing height above the ground; at night, the temperature usually increases with increasing height.

A spatial variation of the sound speed causes an effect that is called *atmospheric refraction*: a sound wave is bent (refracted) toward regions where the sound speed is low. This is illustrated in Fig. 2.2, which shows two examples of a moving wave front. A wave front is defined as a surface on which the phase of a sound wave is constant. With increasing time, a wave front moves in the direction of sound propagation. The propagation direction at a point is defined as the direction of the vector normal to the wave front through the point. In the example of a plane wave with sound pressure given by Eq. (2.1), the wave fronts are plane surfaces perpendicular to the x axis, and the propagation direction is everywhere in the positive x direction. In the examples shown in Fig. 2.2, however, the upper part of the wave front travels slower or faster than the lower part, corresponding to upward and downward refraction, respectively. Consequently, the propagation direction follows the curves indicated in the figure.

The influence of wind on sound propagation makes the description of atmospheric refraction more complex. Wind can be taken into account approximately by treating wind speed as a contribution to the sound speed: sound waves travel faster in downwind directions and slower in upwind directions. Therefore, spatial variations of both the temperature and the wind speed contribute to atmospheric refraction. Atmospheric refraction is an important effect in atmospheric acoustics. A consequence of refraction is that a sound source often generates higher levels in downwind directions than in upwind directions (see Chap. 4).

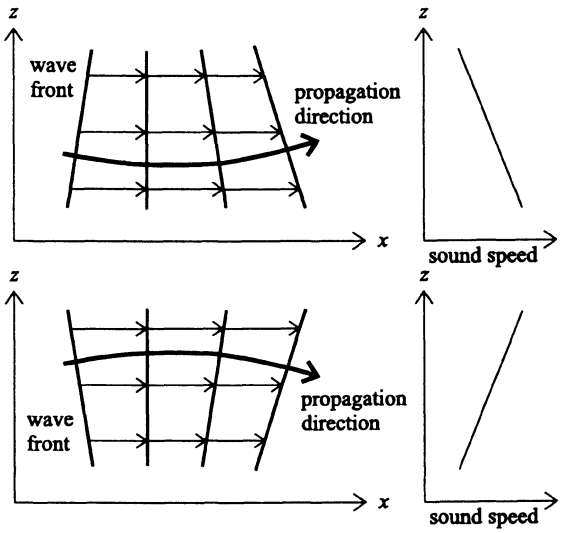

Figure 2.2. Top: illustration of *upward* refraction of sound, in a situation in which the sound speed *decreases* with increasing height z above the ground surface. Bottom: illustration of *downward* refraction of sound, in a situation in which the sound speed *increases* with increasing height z above the ground surface. A wave front moving to the right is shown at four successive times. The thick curve shows the propagation direction, defined at each point as the direction of the vector normal to the wavefront.

In the remainder of this chapter and the next, we will ignore the effect of refraction and assume a non-refracting, or homogeneous, atmosphere, with a constant sound speed. In subsequent chapters we will consider the effect of refraction.

2.3 Complex notation for harmonic waves

A sound signal $p(t)$ at a point in the atmosphere can always be written as a sum of harmonic components of the form

$$p(t) = A\cos(\phi - \omega t). \tag{2.2}$$

The harmonic components have different values of the amplitude A, the phase angle ϕ, and the angular frequency ω. The decomposition of a sound signal into harmonic components is called spectral decomposition (see Sec. B.4). Conversely, a sound field can be calculated by summing over all harmonic contributions. This is very useful in computational atmospheric acoustics, as many computational methods assume a harmonic sound field. Figure 2.3 shows a sim-

ple example of the spectral decomposition of a sound signal with three harmonic components. In practice the number of harmonic components is much larger than three, typically a few thousands.

In the example considered in the previous section, with the sound pressure given by Eq. (2.1), the amplitude A was a constant and the phase angle ϕ was equal to kx. In general, however, both A and ϕ are functions of position $\mathbf{r}$ in the atmosphere. Equation (2.2) can be written as

$$p(\mathbf{r}, t) = \mathrm{Re}\left[p_c(\mathbf{r}) \exp(-i\omega t)\right], \tag{2.3}$$

where $\mathrm{Re}(z)$ denotes the real part of complex number z and $p_c(\mathbf{r})$ is given by

$$p_c(\mathbf{r}) = A(\mathbf{r}) \exp[i\phi(\mathbf{r})]. \tag{2.4}$$

The quantity $p_c(\mathbf{r})$ is called the *complex pressure amplitude*.

2.4 Spherical waves

In the computational models described in this book we assume that the sound source is a monopole source. A monopole source is a point source which generates spherical waves, at least if the atmosphere is unbounded and homogeneous. In a spherical sound wave, the sound pressure (at a given time) is constant within each spherical surface with the source at the center. This is illustrated in Fig. 2.4, for a harmonic monopole source.

The sound pressure of a harmonic spherical wave can be represented by Eq. (2.3), with complex pressure amplitude given by (see Sec. A.4)

$$p_c(\mathbf{r}) = S \, \frac{\exp(ikr)}{r}, \tag{2.5}$$

where r is the radial distance from the source and S is a constant. From Eqs. (2.4) and (2.5) we find that the amplitude of a spherical wave is given by $A(r) = S/r$. The amplitude decreases with increasing distance from the source. At fixed position, the sound pressure oscillates between the values $A(r)$ and $-A(r)$ (see Fig. 2.4).

2.5 Atmospheric absorption

In the previous sections we assumed an ideal atmosphere. We found that the amplitude of a plane wave is a constant and the amplitude of a spherical wave decreases as $1/r$ with increasing distance r from the source. In a real atmosphere, however, the amplitude of a plane wave also decreases, and the decrease of the amplitude of a spherical wave is larger than in an ideal atmosphere. This is due to the effect of atmospheric absorption: a sound wave loses energy by dissipative processes in the atmosphere (see Sec. B.5). Atmospheric absorption

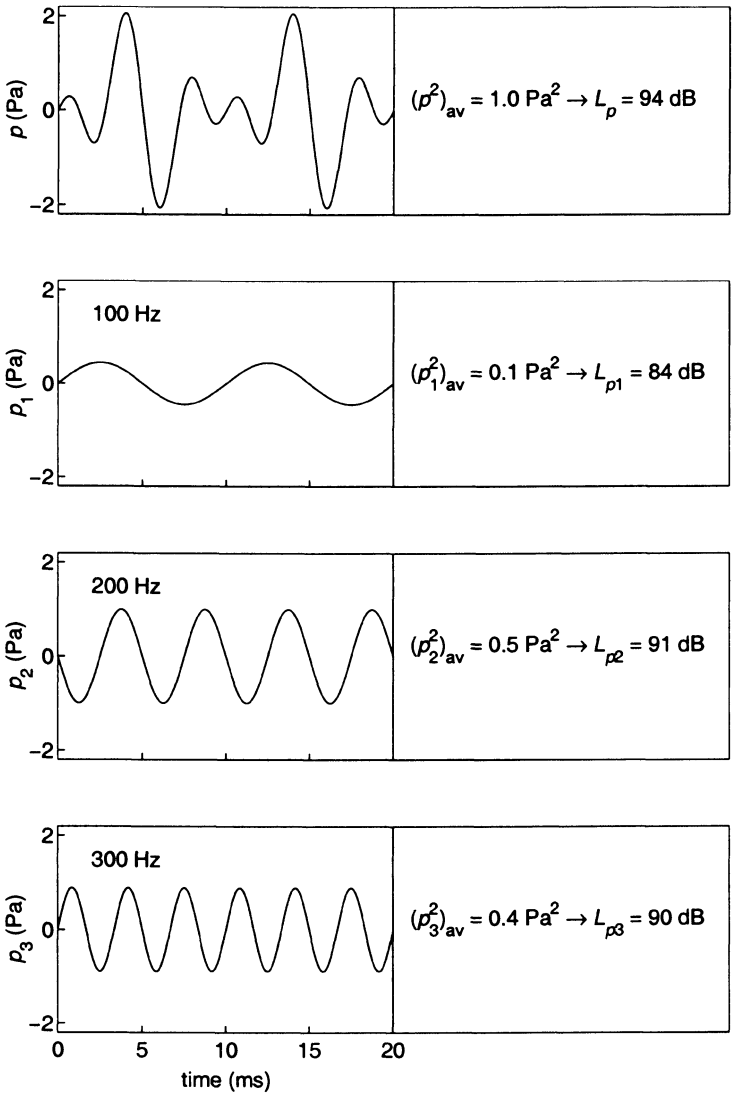

Figure 2.3. Simple example of the spectral decomposition of a sound signal. The signal $p(t)$ (upper graph) consists of three harmonic components $p_1(t)$, $p_2(t)$, and $p_3(t)$, with frequencies of 100 Hz, 200 Hz, and 300 Hz, respectively (lower three graphs). We have $p(t) = p_1(t) + p_2(t) + p_3(t)$. The calculation of the sound pressure levels on the right of the graphs is explained in Sec. 2.6.

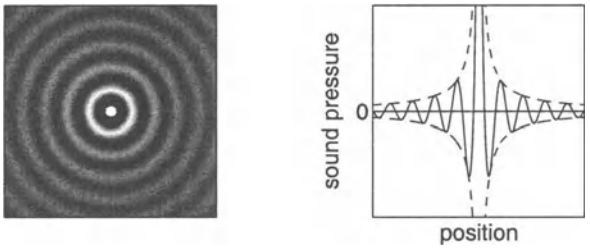

Figure 2.4. Left: cross-section of the spherical sound pressure field of a harmonic monopole source (the source is located at the center). Right: corresponding graph of the sound pressure along a line through the source. The dashed line in the graph represents the amplitude, which diverges at the source.

depends on the frequency of the sound wave, and on the temperature and the humidity of the atmosphere.

Atmospheric absorption causes an exponential decrease of the amplitude with distance (see Sec. B.5). This decrease can be taken into account by including a small imaginary term ik_i in the wave number k. Thus, we replace k by $k + ik_\mathrm{i}$, so the complex pressure amplitude given by Eq. (2.5) becomes

$$p_\mathrm{c}(\mathbf{r}) = S\,\frac{\exp(ikr)}{r}\exp(-k_\mathrm{i}r). \tag{2.6}$$

The factor $\exp(-k_\mathrm{i}r)$ represents the exponential decrease of the amplitude with distance r due to atmospheric absorption.

Atmospheric absorption also has an effect on the phase of a sound wave [106]. This effect varies with frequency, so waves with different frequencies travel with different speeds (this is called dispersion). Phase effects can be represented by including not only a small imaginary term but also a small real term in the wave number. For most practical applications, however, phase effects of atmospheric absorption can be neglected.

2.6 Sound pressure level and spectrum

The time average of the sound pressure of a harmonic sound signal, performed over an integral number of harmonic periods, is equal to zero [see Eq. (2.2)]. The time average of the squared sound pressure p^2 is not equal to zero, unless we have $p = 0$ for all times t. This time average is denoted as $(p^2)_\mathrm{av}$.

For an arbitrary sound signal, the quantity $(p^2)_\mathrm{av}$ is a measure of the loudness of the signal. We assume that the averaging period is sufficiently long, so $(p^2)_\mathrm{av}$

is independent of the averaging period. The *sound pressure level* is defined as

$$L_p = 10 \lg \left(\frac{(p^2)_{\text{av}}}{p_{\text{ref}}^2} \right) \tag{2.7}$$

with reference pressure $p_{\text{ref}} = 2\times10^{-5}$ Pa (or 20 μPa), where Pa is the symbol for pascals, the units of pressure (1 Pa = 1 N/m^2). For example, $(p^2)_{\text{av}} = 1$ Pa^2 corresponds to $L_p = 94$ dB, where we recall that dB stands for decibels. An increase of the sound pressure level by 1 dB corresponds to an increase of $(p^2)_{\text{av}}$ by a factor of $10^{0.1} \approx 1.26$. The choice $p_{\text{ref}} = 2\times10^{-5}$ Pa determines the zero point of the decibel scale: $(p^2)_{\text{av}} = p_{\text{ref}}^2$ corresponds to $L_p = 0$ dB.

For a harmonic sound signal, the time average in Eq. (2.7) can be performed over a single harmonic period. From Eq. (2.3) we find $(p^2)_{\text{av}} = \frac{1}{2}|p_{\text{c}}(\mathbf{r})|^2$ (see Sec. B.3). Substitution into Eq. (2.7) gives

$$L_p = 10 \lg \left(\frac{\frac{1}{2}|p_{\text{c}}(\mathbf{r})|^2}{p_{\text{ref}}^2} \right). \tag{2.8}$$

For a harmonic point source we find from Eqs. (2.6) and (2.8) the following expression for the sound pressure level as a function of distance r from the source (see Sec. B.5):

$$L_p = L_W - 10 \lg 4\pi r^2 - \alpha r, \tag{2.9}$$

where L_W is the sound power level and α is the atmospheric absorption coefficient (in dB per unit length). The sound power level L_W is a measure of the 'strength' of the sound source. The term αr is negligible for small r, so L_W is equal to the sound pressure level L_p at distance $r = (4\pi)^{-1/2} \approx 0.3$ m.

The term αr in Eq. (2.9) represents the attenuation of sound waves due to atmospheric absorption. The absorption coefficient α is related to the imaginary term ik_{i} used in Sec. 2.5 by $\alpha = k_{\text{i}} 20 \lg e$.

The term $10 \lg 4\pi r^2$ in Eq. (2.9) represents the attenuation due to the factor $1/r$ in Eq. (2.6) (the factor 4π is explained in Sec. B.3). This attenuation is called the geometrical attenuation, corresponding to spherical spreading of sound waves from a point source.

In the derivation of Eq. (2.9) we assumed that the source is harmonic. If the source is not harmonic, we decompose the sound pressure signal $p(t)$ into harmonic components: $p(t) = \sum p_f(t)$, where $p_f(t)$ is the sound pressure signal of a harmonic component with frequency f (see Fig. 2.3 and Sec. B.4). Equation (2.9) can be applied to the harmonic components:

$$L_p(f) = L_W(f) - 10 \lg 4\pi r^2 - \alpha(f) r. \tag{2.10}$$

The sound pressure level $L_p(f)$ is related to the harmonic signal $p_f(t)$ by Eq. (2.7): $L_p(f) = 10 \lg((p_f^2)_{\text{av}}/p_{\text{ref}}^2)$. The quantities $(p_f^2)_{\text{av}}$ satisfy the important relation $(p^2)_{\text{av}} = \sum (p_f^2)_{\text{av}}$, where the sum is over all harmonic components (this

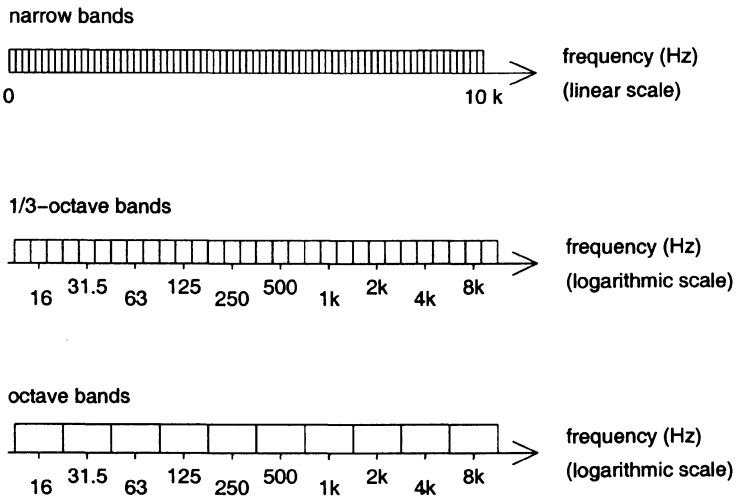

Figure 2.5. Illustration of frequency scales: narrow band scale, 1/3-octave band scale, and octave band scale. Each octave band covers several narrow bands. We assume that the narrow band width is a constant on a linear scale (for example equal to 1 Hz), so the number of narrow bands in an octave band increases with increasing octave band center frequency. Each octave band covers three 1/3-octave bands, with center frequencies that are approximately equal to $2^{-1/3}f_c$, f_c, and $2^{1/3}f_c$, where f_c is the octave band center frequency. The octave band with center frequency 125 Hz, for example, covers the 1/3-octave bands with center frequencies 100 Hz, 125 Hz, and 160 Hz.

follows from Parseval's theorem; see Sec. B.4). The corresponding relation in decibels is $L_p = 10\lg(\sum 10^{L_p(f)/10})$. We will call this *logarithmic summation* of the levels $L_p(f)$. In this context, the level L_p is called the broadband sound pressure level and the function $L_p(f)$ is called the spectrum of the sound pressure level (or narrow band spectrum of the sound pressure level, as will be explained later). The broadband level L_p is the logarithmic sum of the levels $L_p(f)$ of the spectrum. We assume here that the frequencies f of the harmonic components are equidistant on a linear scale (see Fig. 2.5).

The sound power level L_W was identified above as the sound pressure level at distance $r = (4\pi)^{-1/2}$, so we also have the expression $L_W = 10\lg(\sum 10^{L_W(f)/10})$ for the broadband sound power level L_W. The function $L_W(f)$ is called the spectrum of the sound power level. Equation (2.10) can be considered as the definition of $L_W(f)$.

Logarithmic summation is illustrated by the example shown in Fig. 2.3,

with three harmonic components. As indicated in the figure, the signal $p(t)$ corresponds to $(p^2)_{\text{av}} = 1.0$ Pa^2 and, by Eq. (2.7), $L_p = 94$ dB. The three harmonic components $p_j(t)$ with $j = 1,2,3$ correspond to $(p_j^2)_{\text{av}} = 0.1$, 0.5, 0.4 Pa^2 and $L_{pj} = 84$, 91, 90 dB. These values agree with the relations $(p^2)_{\text{av}} = (p_1^2)_{\text{av}} + (p_2^2)_{\text{av}} + (p_3^2)_{\text{av}}$ and $L_p = 10\lg(10^{L_{p1}/10} + 10^{L_{p2}/10} + 10^{L_{p3}/10})$, which represent logarithmic summation.

In practice the number of harmonic components is much larger than three, typically a few thousands. The frequencies of the harmonic components may be, for example, $f = 1,2,\ldots,5000$ Hz. The spectrum $L_p(f)$ is often a rather irregular function of frequency (an example will be shown in Fig. 2.6 later in this section). Therefore one replaces the large number of levels $L_p(f)$ by a much smaller number of *octave band levels* $L_p(f_c)$. Octave bands are contiguous frequency intervals that cover the complete frequency range (see Fig. 2.5). Each octave band is characterized by a center frequency, denoted by the symbol f_c. In atmospheric acoustics one uses the octave bands with the center frequencies 16, 31.5, 63, 125, 250, 500, 1000, 2000, 4000, and 8000 Hz. An octave band level $L_p(f_c)$ is calculated by logarithmic summation of the levels $L_p(f)$ of the harmonic components with frequencies in the octave band: $L_p(f_c) = 10\lg(\sum' 10^{L_p(f)/10})$, where the prime indicates that the sum is over the frequencies in the octave band. We assume here that the frequencies are equidistant on a linear scale (see Fig. 2.5 and Sec. B.4). The function $L_p(f_c)$ is called the octave band spectrum of the sound pressure level and, in this context, the function $L_p(f)$ is called the narrow band spectrum of the sound pressure level.

It is straightforward to show that logarithmic summation of the octave band levels $L_p(f_c)$ yields the broadband level L_p, so we have $L_p = 10\lg(\sum 10^{L_p(f_c)/10})$, where the sum is over the octave bands. This implies that the octave band spectrum can be considered as an intermediate stage in the logarithmic summation of the narrow band spectrum to the broadband level. Of course many details of the narrow band spectrum are lost in the octave band spectrum.

The octave band spectrum of the sound power level, denoted as $L_W(f_c)$, is defined in the same way as the octave band spectrum of the sound pressure level. An octave band sound power level is calculated from the narrow band spectrum $L_W(f)$ with the relation $L_W(f_c) = 10\lg(\sum' 10^{L_W(f)/10})$, where the sum is over the frequencies in the octave band.

Sometimes octave bands are too wide, and the narrower 1/3-octave bands, or one-third-octave bands, are used (see Fig. 2.5). A 1/3-octave band spectrum contains more details of the narrow band spectrum than an octave band spectrum does.

Equation (2.10) is a relation between the narrow band spectra $L_p(f)$ and $L_W(f)$. An analogous relation holds for the 1/3-octave or octave band spectra $L_p(f_c)$ and $L_W(f_c)$. If $L_W(f)$ is constant over a 1/3-octave or octave band we have $L_W(f_c) = 10\lg(N10^{L_W(f)/10})$, where N is the number of frequencies in

the band; logarithmic summation of Eq. (2.10) over the band gives

$$L_p(f_c) = L_W(f_c) - 10\lg 4\pi r^2 - \alpha(f_c)r, \tag{2.11}$$

where $-\alpha(f_c)r = 10\lg(\frac{1}{N}\sum' 10^{-\alpha(f)r/10})$ is the ***logarithmic average*** of the function $-\alpha(f)r$ over the band. In general, $L_W(f)$ is not constant over the band, but Eq. (2.11) is still used as an approximation, with $L_W(f_c)$ given by the logarithmic sum $10\lg(\sum' 10^{L_W(f)/10})$. Thus, while the 1/3-octave or octave band levels $L_p(f_c)$ and $L_W(f_c)$ are calculated from the narrow band spectra $L_p(f)$ and $L_W(f)$ by logarithmic summation, the term $-\alpha(f_c)r$ is calculated from the function $-\alpha(f)r$ by logarithmic averaging. In practice, however, the term $-\alpha(f_c)r$ is often approximated by the function $-\alpha(f)r$ evaluated at $f = f_c$ (see Sec. B.5).

It should be noted that the spectrum $L_p(f_c)$ and the broadband level L_p are calculated most accurately by logarithmic summation of the narrow band spectrum $L_p(f)$ given by Eq. (2.10). In practice one uses Eq. (2.11), however, because the sound emission of a source is usually represented by the 1/3-octave or octave band spectrum $L_W(f_c)$.

Equations (2.10) and (2.11) are important relations in atmospheric acoustics. The relations show that there is a clear distinction between ***sound emission*** and ***sound propagation.*** Sound emission is represented by the spectrum of the sound power level, *i.e.* the first term on the right-hand side of Eqs. (2.10) and (2.11). Sound propagation is represented by the remaining terms on the right-hand side. In this case we have an unbounded homogeneous atmosphere and the propagation terms are easily calculated; in the next chapter we will include an additional propagation term on the right-hand side to represent the effects of ground reflections, atmospheric refraction, and other propagation effects; we will describe numerical methods for the computation of this additional propagation term. After the computation of all propagation terms, Eq. (2.10) or Eq. (2.11) can be used to calculate the spectrum of the sound pressure level at the receiver, for an arbitrary source with a given spectrum of the sound power level.

In applications in which human perception is involved, one often applies the A-weighting to spectra of the sound pressure level. There are also B- and C-weightings, but these are rarely used. The A-weighting approximately represents the 'filter' that the human ear applies to sound (see Sec. B.4). The human ear is most sensitive to frequencies around 1 kHz. Therefore, the A-weighting assigns a larger weight to the part of a spectrum around 1 kHz than to the part of the spectrum around 100 Hz, for example. The broadband sound pressure level that results from logarithmic summation of an A-weighted spectrum of the sound pressure level is often called simply the ***sound level***, denoted by the symbol L_A and expressed in dB(A) ('A-weighted decibels').

Figure 2.6 shows an example of the spectral decomposition of a sound signal. The upper graph shows the sound pressure as a function of time, over a period of 1 s. Narrow band, 1/3-octave band, and octave band spectra are shown for the (unweighted, or linear) sound pressure level (left column) and the A-weighted

sound pressure level (right column). The broadband levels L_p and L_A are also indicated in the graphs.

Figures 2.7 and 2.8 show examples of A-weighted octave band spectra of the sound pressure level at various distances from a noise source. Spectra are shown for three types of noise source: a passenger car, a heavy truck, and a jet airplane. The spectra have been calculated with Eq. (2.11), using representative (experimental) sound power spectra for the sources and a temperature of 10°C and a relative humidity of 80% for the calculation of atmospheric absorption. The effects of ground reflections and atmospheric refraction are obviously not included in the spectra. These effects are studied in Chaps. 3 and 4. The graphs in Figs. 2.7 and 2.8 show that the frequency range from roughly 125 Hz to 4 kHz is most important for human perception of traffic noise and airplane noise. Frequencies below 125 Hz and above 4 kHz are relatively unimportant. With increasing distance from the source, low frequencies become increasingly important (see Fig. 2.8), due to the effect of atmospheric absorption: atmospheric absorption is larger at high frequency than at low frequency.

The spectrum of sound received from a moving source is affected by the motion of the source: frequencies are shifted by the Doppler effect (see Sec. B.6). In practice the Doppler frequency shift is often small and can be neglected. For a car with a speed of 100 km/h, for example, the frequency shift is less than 10%.

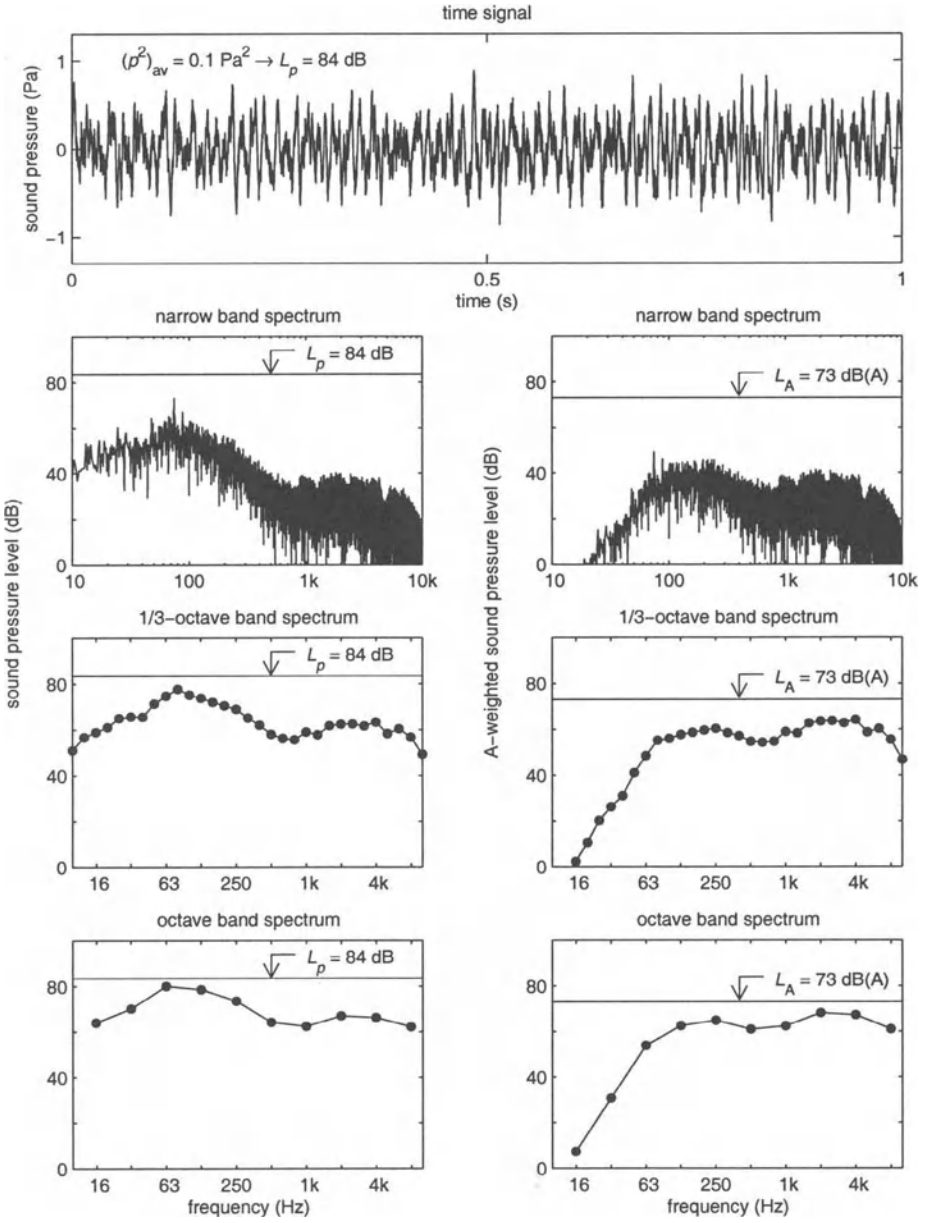

Figure 2.6. Example of the spectral decomposition of a sound signal (broadband noise). The figure shows the time signal (upper graph) and narrow band, 1/3-octave band, and octave band spectra of the unweighted (left column) and A-weighted (right column) sound pressure level.

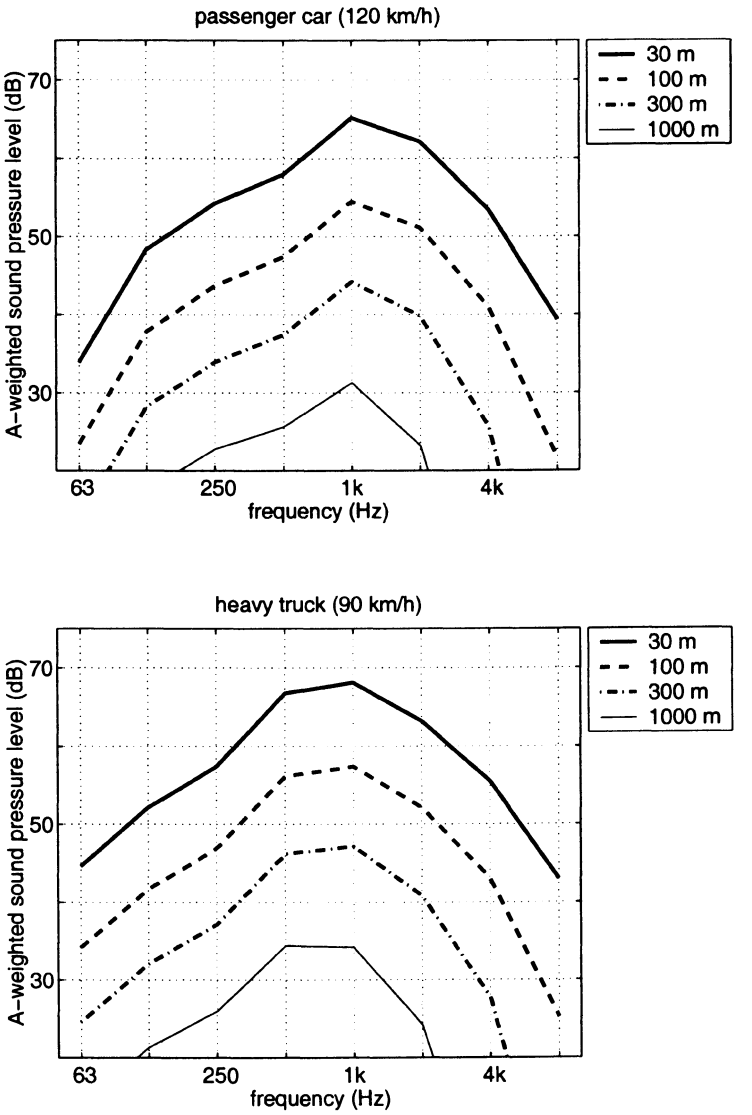

Figure 2.7. A-weighted octave band spectra of the sound pressure level of a noise source, at four distances from the source (see legend). The upper graph represents the noise from a passenger car with a speed of 120 km/h. The lower graph represents the noise from a heavy truck with a speed of 90 km/h. The spectra have been calculated with Eq. (2.11), so the effects of ground reflections and atmospheric refraction are not included. We used sound power spectra from Ref. [153], and a temperature of 10°C and a relative humidity of 80% for the calculation of atmospheric absorption. The term $-\alpha(f_c)r$ in Eq. (2.11) was approximated by the function $-\alpha(f)r$ evaluated at $f = f_c$.

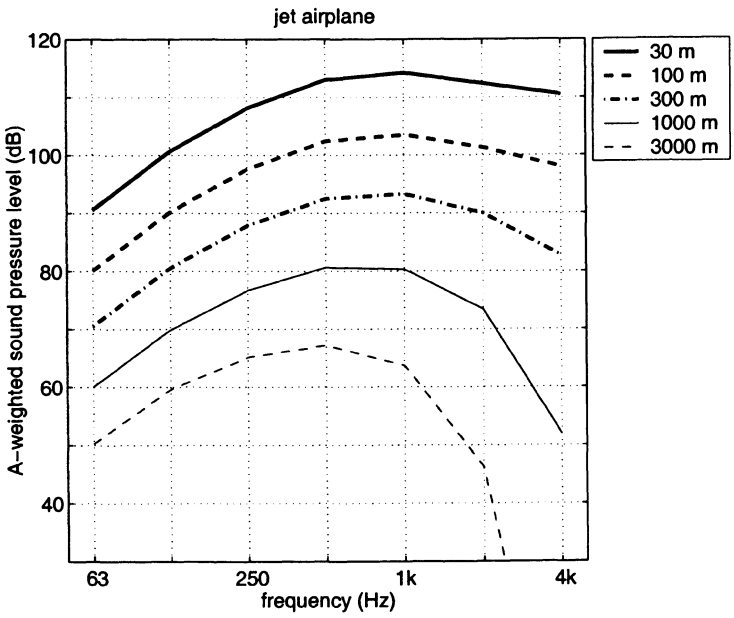

Figure 2.8. As Fig. 2.7, for the noise from a typical jet airplane, with a sound power spectrum from Ref. [110] and a broadband A-weighted sound power level of 160 dB(A). With increasing distance from the source, the maximum of the spectrum shifts to lower frequency due to the effect of atmospheric absorption.

Chapter 3

Homogeneous atmosphere above a ground surface

3.1 Introduction

In the previous chapter we have seen that a point source generates spherical waves in an unbounded homogeneous atmosphere. We showed that the sound pressure level at a receiver in the spherical sound field can be calculated from the sound power level of the source, taking into account the geometrical attenuation due to spherical spreading and the attenuation due to atmospheric absorption.

In practice the source or the receiver, or both, are often close to a ground surface. In this case the calculation of the sound pressure level at the receiver is more complex, as will be described in this chapter. The ground surface reflects sound waves, so there are not only direct sound waves from the source to the receiver but also reflected sound waves. The interference between direct waves and reflected waves has a considerable effect on the sound field (see Fig. 3.1). In Chaps. 4 and 5 we will see that the interference is affected by atmospheric gradients and atmospheric turbulence. For small distances between the source and the receiver, however, these atmospheric effects can be neglected.

For an acoustically hard ground surface, *e.g.* concrete, the calculation of the sound pressure level is relatively simple. For an acoustically absorbing ground surface, *e.g.* grassland, the calculation is more complex.

3.2 Reflection of spherical waves by a ground surface

We consider the geometry shown in Fig. 3.2, with a harmonic monopole source and a receiver in a homogeneous atmosphere above a ground surface. We use an rz coordinate system in the vertical plane through the source and the receiver;

E. M. Salomons, *Computational Atmospheric Acoustics*

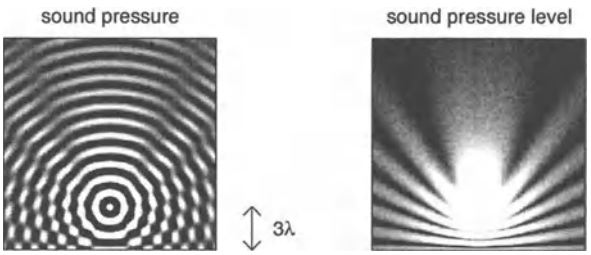

Figure 3.1. Fields of the sound pressure (left) and the sound pressure level (right), generated by a harmonic monopole source at a height of three wavelengths (3λ) above an acoustically hard ground surface, in a homogeneous atmosphere. Regions of low amplitude corresponding to destructive interference are clearly visible as dark regions in the field of the sound pressure level, but are also visible in the field of the sound pressure. The fields have been calculated with Eq. (3.2), using $Q = 1$ for a hard ground surface.

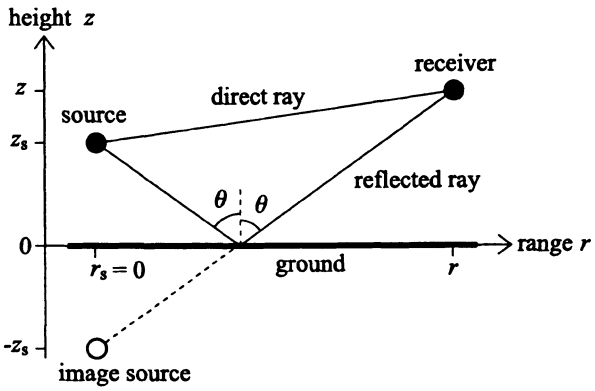

Figure 3.2. Geometry with a source and a receiver above a ground surface. Also indicated is the image source below the ground surface.

r is the horizontal range measured from the source and z is the height above the ground surface. The source is at position ($r_s = 0$,z_s) and the receiver is at position (r,z).

The source is characterized by the *free field*, *i.e.* the sound field of the source in an unbounded homogeneous atmosphere. The complex pressure amplitude of the free field is (see Sec. 2.4)

$$p_{\text{free}} = S \frac{\exp(ikR_1)}{R_1}, \tag{3.1}$$

where S is a constant, k is the wave number, and R_1 is the distance from the source.

The complex pressure amplitude at the receiver in the geometry shown in Fig. 3.2 can be written as (see Sec. D.4)

$$p_c = S \frac{\exp(ikR_1)}{R_1} + QS \frac{\exp(ikR_2)}{R_2}, \tag{3.2}$$

with $R_1 = \sqrt{r^2 + (z - z_s)^2}$ and $R_2 = \sqrt{r^2 + (z + z_s)^2}$. The quantity Q in this equation is called the spherical-wave reflection coefficient; this quantity can be calculated with Eq. (D.54), Eq. (D.58), or Eq. (D.72) in Appendix D. The value of Q is a complex number, in general. Equation (3.2) can be interpreted in terms of two sound rays: the direct ray and the ray reflected by the ground surface (see Fig. 3.2). The path length of the direct ray is R_1 and the path length of the reflected ray is R_2. Equation (3.2) can also be interpreted in terms of two sources: the real source above the ground surface and the image source below the ground surface (see Fig. 3.2). The distance between the receiver and the real source is R_1 and the distance between the receiver and the image source is R_2.

Atmospheric absorption is taken into account in Eqs. (3.1) and (3.2) by including a small imaginary term in the wave number (see Sec. 2.5).

The complex pressure amplitude given by Eq. (3.2) is unaffected if the positions of the source and the receiver are interchanged. This is called the principle of reciprocity [121, 106], which holds also in an inhomogeneous atmosphere without wind (and even in an inhomogeneous atmosphere with wind if the wind direction is reversed).

3.3 Spherical-wave reflection coefficient and ground impedance

The spherical-wave reflection coefficient Q in Eq. (3.2) is a function of the following four quantities (see Sec. D.4):

- wave number k (or frequency $f = kc/2\pi$),
- distance R_2,

- reflection angle θ (see Fig. 3.2),
- normalized ground impedance Z.

The normalized ground impedance Z is a quantity that characterizes the ground surface acoustically (see Appendix C). The value of Z is a complex number, which depends on the frequency of the sound waves and on the structure of the ground. Various models exist for the calculation of the normalized ground impedance from parameters that characterize the structure of the ground. The most important parameter is the flow resistivity, denoted by the symbol σ.

To define the flow resistivity, we consider a situation in which a pressure difference over a slab of porous material forces air to flow through the slab. The flow resistivity is equal to the ratio of the pressure difference to the flow velocity, divided by the thickness of the slab. This is analogous to the definition of electric resistance. We express flow resistivity in units of kPa·s·m^{-2}.

The concept of flow resistivity is also used for natural grounds such as grassland. Thus, grassland is modeled as a porous medium. A typical value of the flow resistivity for grassland is $\sigma = 200$ kPa·s·m^{-2}. The flow resistivity of a material can be measured directly, but is often determined indirectly from acoustic measurements [6, 8, 31, 32, 37, 15, 48, 50, 96, 127, 87]. In the latter case the flow resistivity is treated as an adjustable parameter, and is called the *effective* flow resistivity. Values of the effective flow resistivity of natural absorbing grounds, such as grassland, forest floors, and sandy grounds, range roughly from $\sigma = 10$ kPa·s·m^{-2} to $\sigma = 1000$ kPa·s·m^{-2}.

Delany and Bazley [39] developed an empirical model for the calculation of the impedance of fibrous absorbing materials. This model works well also for natural grounds such as grassland. Zwikker and Kosten [161] and Attenborough [4, 5, 6, 7, 10, 11] developed theoretical models for the calculation of the impedance. In the theoretical models, the ground is approximated as a semi-infinite porous medium, or as a porous layer with a rigid backing. In the numerical examples in this book, we model absorbing ground as a semi-infinite porous medium; unless indicated otherwise, we use the four-parameter model developed by Attenborough [5] for the calculation of the impedance; the parameters of the model are specified in Sec. C.4.

To gain insight into the ground reflection of spherical waves, we note that at high frequency the spherical-wave reflection coefficient Q is approximately equal to the plane-wave reflection coefficient R_p, which is given by (see Sec. D.2)

$$R_\mathrm{p} = \frac{Z\cos\theta - 1}{Z\cos\theta + 1}. \tag{3.3}$$

For an acoustically hard ground surface we have $Z = \infty$ (and $\sigma = \infty$) so we find $R_\mathrm{p} = 1$. In this case we also have $Q = 1$ (see Sec. D.4). An acoustically hard surface is usually referred to as a rigid surface. Examples are a concrete surface and a water surface.

An acoustically absorbing ground surface has a finite impedance. Let us consider a situation in which the ground surface has a finite impedance and

both the source height and the receiver height are very small compared with the horizontal distance between the source and the receiver. In this case the reflection angle θ approaches $\pi/2$ (see Fig. 3.3). The limit $\theta \to \pi/2$ is called the limit of grazing incidence. It follows from Eq. (3.3) that R_p approaches -1 in the limit of grazing incidence. Hence, the spherical-wave reflection coefficient at high frequency also approaches -1 in the limit of grazing incidence. The path lengths of the direct ray and the reflected ray are approximately equal in this case ($R_1 \approx R_2$), so the two terms on the right-hand side of Eq. (3.2) have approximately equal magnitudes but opposite signs. This corresponds to a destructive interference between direct sound waves and sound waves reflected by the ground surface. Thus, the sound pressure above a finite-impedance ground surface is very low in the limit of grazing incidence.

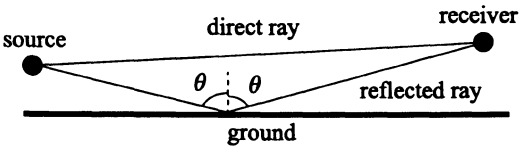

Figure 3.3. The reflection angle θ approaches $\pi/2$ in the limit of grazing incidence.

3.4 Relative sound pressure level

From Eqs. (3.1) and (3.2) we have

$$p_c = p_{free}\left[1 + Q\frac{R_1}{R_2}\exp(ikR_2 - ikR_1)\right]. \tag{3.4}$$

This relation between p_c and p_{free} can also be expressed in terms of the corresponding sound pressure levels L_p and $L_{p,free}$, respectively. From Eq. (2.8) we have $L_p = 10\lg(\frac{1}{2}|p_c|^2/p_{ref}^2)$ and $L_{p,free} = 10\lg(\frac{1}{2}|p_{free}|^2/p_{ref}^2)$. This gives

$$L_p = L_{p,free} + \Delta L, \tag{3.5}$$

with

$$\Delta L = 10\lg\left(|p_c|^2/|p_{free}|^2\right). \tag{3.6}$$

The quantity ΔL will be referred to as the *relative sound pressure level*, and plays an important role in this book. From Eqs. (3.4) and (3.6) we find

$$\Delta L = 10\lg\left|1 + Q\frac{R_1}{R_2}\exp(ikR_2 - ikR_1)\right|^2. \tag{3.7}$$

The relative sound pressure level ΔL represents the deviation from the free field sound pressure level due to the presence of the ground surface. Both positive and negative values of ΔL occur.

Negative values of ΔL occur in the case of destructive interference between direct sound waves and reflected sound waves. Complete destructive interference ($\Delta L = -\infty$) occurs if the second term in the argument of the logarithmic function in Eq. (3.7) is equal to -1.

Positive values of ΔL occur in the case of constructive interference between direct and reflected sound waves. For a rigid ground we have $Q = 1$ and the maximum value of ΔL is $10 \lg 2^2 \approx 6$ dB, as follows from Eq. (3.7) for $R_1 \approx R_2$. For absorbing ground we often have $|Q| < 1$, so the maximum value of ΔL is lower than 6 dB. In some situations, however, we have $|Q| > 1$ and values of ΔL higher than 6 dB occur; this can be attributed to the so-called surface wave [108, 51, 146] (see also Sec. H.5), which is contained implicitly in the expressions for the spherical-wave reflection coefficient Q given in Sec. D.4.

As noted before, atmospheric absorption is taken into account by including a small imaginary term in the wave number (see Sec. 2.5). In many practical situations, however, we have $R_1 \approx R_2$, and atmospheric absorption can be neglected in Eq. (3.7). Only in situations with a high source and a high receiver, the distances R_1 and R_2 may be considerably different, and atmospheric absorption should be taken into account in Eq. (3.7).

Substitution of Eq. (2.9) for $L_{p,\text{free}}$ into Eq. (3.5) gives

$$L_p = L_W - 10 \lg 4\pi R_1^2 - \alpha R_1 + \Delta L. \tag{3.8}$$

This equation, with relative sound pressure level ΔL defined by Eq. (3.6), is not restricted to the geometry shown in Fig. 3.2. Any deviation from the free field of a source can be represented by ΔL defined by Eq. (3.6). If the deviation is due to a ground reflection in a homogeneous atmosphere, ΔL is given by Eq. (3.7). The deviation may also be due to other effects. In Chaps. 4 to 7 we will use the relative sound pressure level to represent deviations due to atmospheric refraction, atmospheric turbulence, irregular terrain, and noise barriers.

Instead of the relative sound pressure level ΔL, the equivalent quantity 'excess attenuation' is also used in atmospheric acoustics. The excess attenuation is equal to $-\Delta L$.

The quantities L_p, L_W, α, and ΔL in Eq. (3.8) are functions of frequency, in general. The function $L_W(f)$, for example, is the narrow band spectrum of the sound power level of the source (see Sec. 2.6). The function $\Delta L(f)$ is the corresponding spectrum of the relative sound pressure level. The spectrum $\Delta L(f)$ should not be considered as a narrow band spectrum, as the value of $\Delta L(f)$ does not depend on a narrow band width [whereas the values of $L_p(f)$ and $L_W(f)$ do depend on the narrow band width]. The term 'continuous' spectrum is more appropriate for the spectrum $\Delta L(f)$.

The narrow band or continuous spectra in Eq. (3.8) can be converted to octave band spectra or 1/3-octave band spectra. Logarithmic summation of

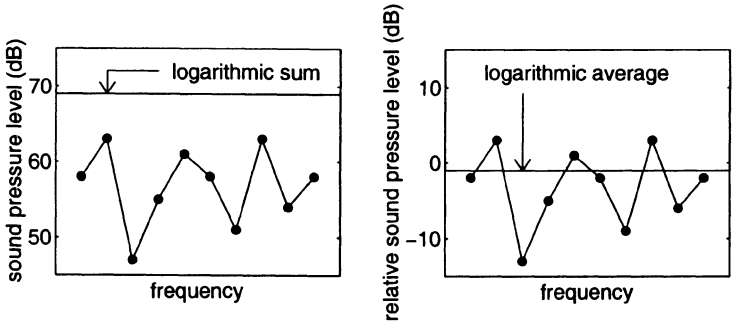

Figure 3.4. Example of logarithmic summation of the sound pressure level (left) and logarithmic averaging of the relative sound pressure level (right). The summation and averaging may be over the frequencies in an octave band or a 1/3-octave band.

Eq. (3.8) over a 1/3-octave or octave band yields the approximate relation

$$L_p(f_c) = L_W(f_c) - 10\lg 4\pi R_1^2 - \alpha(f_c)R_1 + \Delta L(f_c). \tag{3.9}$$

The quantities $L_p(f_c)$, $L_W(f_c)$, and $\alpha(f_c)R_1$ in this relation have been defined in Sec. 2.6 and the quantity $\Delta L(f_c)$ is equal to the 'logarithmic average' $10\lg(\frac{1}{N}\sum' 10^{\Delta L(f)/10})$, where the sum is over N frequencies in the band; we assume that the frequencies are equidistant on a linear scale (see Fig. 2.5 and Sec. B.4). To derive Eq. (3.9) from the narrow band relation (3.8) one neglects the variation of $L_W(f)$ and $-\alpha(f)R_1$ over the band. This variation can usually not be neglected, but Eq. (3.9) is still used as an approximation (see Sec. 2.6). Figure 3.4 shows an example of logarithmic summation of the sound pressure level and logarithmic averaging of the relative sound pressure level. The logarithmic average is dominated by the highest levels.

3.5 Examples

In this section we present graphs of the relative sound pressure level, calculated with Eq. (3.7) for the geometry shown in Fig. 3.2. We use the rz coordinate system shown in Fig. 3.2 to denote the positions of the source and the receiver. We use the following notation above the graphs:

- source ($r_s = 0$,z_s), where z_s is expressed in meters,
- receiver (r,z), where r and z are expressed in meters,
- frequency f in Hz,
- flow resistivity σ of the ground surface in kPa·s·m^{-2}.

Figure 3.5 shows the field of the relative sound pressure level ΔL for a harmonic monopole source of 500 Hz at a height of 2 m above a rigid ground surface ($\sigma = \infty$). The field contains distinct regions where the level ΔL is low (lower than the lower limit of -20 dB of the grey level scale). These regions correspond to destructive interference between direct sound waves and sound waves reflected by the ground surface. For a rigid ground surface we have $Q = 1$, and it follows from Eq. (3.7) that the minima of the relative sound pressure level occur for $\exp(ikR_2 - ikR_1) = -1$, or $k(R_2 - R_1) = (2n+1)\pi$, with $n = 0, 1, 2, \ldots$. Using $k = 2\pi f/c$, we find that the minima occur for

$$R_2 - R_1 = (n + \frac{1}{2})\lambda, \tag{3.10}$$

where $\lambda = c/f$ is the wavelength. Thus, destructive interference occurs if the path length difference $R_2 - R_1$ between the direct sound ray and the reflected sound ray is equal to $(n + \frac{1}{2})\lambda$, so that direct waves and reflected waves have a phase difference of 180°. With increasing height in Fig. 3.5, one successively passes the regions corresponding to $n = 0, 1, 2, \ldots$.

Figure 3.6 demonstrates the effect of 1/3-octave band averaging, both for a rigid ground surface and for an absorbing ground surface. For the rigid ground surface, deep interference minima occur in the continuous spectrum $\Delta L(f)$, while the minima in the 1/3-octave band spectrum are considerably less deep (*cf.* Fig. 3.4). For the absorbing ground surface, the interference minima in the continuous spectrum are considerably less pronounced than for the rigid ground surface, and consequently the effect of 1/3-octave band averaging on the minima is smaller than for the rigid ground surface.

For the rigid ground surface, the relative sound pressure level in Fig. 3.6 approaches 6 dB below a frequency of about 100 Hz (see Sec. 3.4). For the absorbing ground surface, the relative sound pressure level in Fig. 3.6 approaches 6 dB at very low frequencies, below about 16 Hz (at very low frequency the reflection coefficient Q approaches unity and the absorbing ground surface can be considered as a rigid ground surface); at frequencies around 100 Hz the relative sound pressure level is considerably lower for the absorbing ground surface than for the rigid ground surface. With increasing frequency in the graphs in Fig. 3.6, one successively passes the interference minima corresponding to $n = 0, 1, 2, \ldots$ (see above).

In Fig. 3.6, and in many practical situations, we have $z \ll r$ and $z_s \ll r$. In this case the frequencies of the interference minima can be calculated with Eqs. (3.11) and (3.12) below. Equation (3.11) is valid for a rigid ground surface and Eq. (3.12) is valid for an absorbing ground surface.

For a rigid ground surface we have from Eq. (3.10) the relation $R_2 - R_1 = (n + \frac{1}{2})\lambda$ at the interference minima, with $n = 0, 1, 2, \ldots$. From $z \ll r$ and $z_s \ll r$ we find $R_2 - R_1 \approx 2zz_s/r$. Using $\lambda = c/f$, we find that the interference minima for a rigid ground surface occur at the frequencies

$$f_n = (n + \frac{1}{2})\frac{rc}{2zz_s}. \tag{3.11}$$

Substitution of the values $z_s = 2$ m, $z = 2$ m, and $r = 30$ m, which were used for Fig. 3.6, gives the relation $f_n = (2n+1)f_0$ with $f_0 = 637.5$ Hz. The interference minima in Fig. 3.6 for the rigid ground surface occur at frequencies that agree with this relation.

For the absorbing ground surface, the interference minima occur at slightly lower frequencies. This is due to the fact that the reflection by a finite-impedance ground surface causes a phase change of a sound wave. The spherical-wave reflection coefficient Q in Eq. (3.7) is a complex number, and can be written as $Q = |Q|\exp(i\vartheta)$, where $|Q|$ is the absolute value and ϑ is the argument. For an absorbing ground surface, it follows from Eq. (3.7) that the minima of the level ΔL occur for $\exp(ikR_2 - ikR_1 + i\vartheta) = -1$, or $k(R_2 - R_1) + \vartheta = (2n+1)\pi$, with $n = 0, 1, 2, \ldots$. Using $R_2 - R_1 \approx 2zz_s/r$, we find that the interference minima for an absorbing ground surface occur at the frequencies

$$f_n = (n + \frac{1}{2} - \frac{\vartheta}{2\pi})\frac{rc}{2zz_s}. \tag{3.12}$$

The argument ϑ is a positive quantity; this can be seen from Eq. (3.3), using $Q \approx R_p$ and the fact that the imaginary part of the normalized impedance Z is positive (see Sec. C.4). Consequently, the interference minima for an absorbing ground surface occur at lower frequencies than for a rigid ground surface.

The interference minima in Fig. 3.6 are deeper for the rigid ground surface than for the absorbing ground surface. This can be explained as follows. For the rigid ground surface, direct waves and reflected waves have approximately equal amplitudes, so the waves cancel each other almost completely in regions where the phases are opposite. For the absorbing ground surface, the amplitude of reflected waves is smaller than the amplitude of direct waves, due to the absorption of acoustic energy by the ground, so only a partial cancellation occurs. This can also be seen from Eq. (3.7). For the rigid ground surface we have $Q = 1$, and the second term in the argument of the logarithm is approximately equal to -1 at the interference minima (using $R_1 \approx R_2$). For the absorbing ground surface we have $|Q| < 1$ at the interference minima, and the term is smaller (less negative) than -1.

Figure 3.7 illustrates the effect of the choice of the impedance model (see Sec. 3.3) on the spectrum of the relative sound pressure level. The model developed by Delany and Bazley [39] yields a slightly different spectrum than the model developed by Attenborough [5] does.

Figures 3.8 and 3.9 illustrate the effect of receiver range r (*i.e.* the horizontal distance between the source and the receiver) on the spectrum of the relative sound pressure level, for a rigid ground surface and an absorbing ground surface, respectively. For the rigid ground surface, the interference minima shift to higher frequency with increasing range r, in agreement with Eq. (3.11). For the absorbing ground surface, the first interference minimum becomes broader and deeper with increasing range r. This is a consequence of the destructive interference between direct sound waves and reflected sound waves, which occurs for grazing incidence on a finite-impedance ground surface (see Sec. 3.3).

Figures 3.10 and 3.11 illustrate the effect of receiver height z on the spectrum of the relative sound pressure level, for a rigid ground surface and an absorbing ground surface, respectively. For the rigid ground surface, the interference minima shift to lower frequency with increasing height z, in agreement with Eq. (3.11). For the absorbing ground surface, the first interference minimum becomes broader and deeper with decreasing height z. Again, this is a consequence of the destructive interference for grazing incidence on a finite-impedance ground surface.

Figure 3.12 illustrates the effect of flow resistivity σ of the ground surface on the spectrum of the relative sound pressure level. With increasing σ, the first interference minimum shifts to higher frequency.

Figure 3.13 illustrates the effect of finite dimensions of a sound source on the spectrum of the relative sound pressure level. For this figure we use a rectangular xyz coordinate system, where x and y are horizontal coordinates and z is the height above the ground surface. Source positions are denoted as $(x_s = 0, y_s, z_s)$ and the receiver position is $(x = 100, y = 0, z = 2)$, where coordinates are expressed in meters. The figure shows three spectra:

- a spectrum for a point source at position (0,0,2),
- a spectrum for a set of 256 incoherent point sources distributed uniformly over a square of 4 m^2 in the yz plane, with $-1 \leq y_s \leq 1$ and $1 \leq z_s \leq 3$,
- a spectrum for a set of 100 incoherent point sources distributed uniformly over a line segment with a length of 200 m, located above the y axis, with $x_s = 0$, $-100 \leq y_s \leq 100$, and $z_s = 2$.

By 'incoherent point sources' we mean that the contributions of the point sources to the received sound pressure level are summed logarithmically (see Sec. 2.6), corresponding to logarithmic averaging of ΔL. This approach is reasonable if the point sources have no phase relations with each other, or if the phase differences between the sources show random fluctuations. The set of point sources distributed uniformly over the line segment, for example, can be used to calculate the average noise from cars on a road, as the cars have no phase relations with each other. A continuous distribution of point sources over a line is called an incoherent line source [75]. The representation of a car by a point source is studied in Refs. [59, 60].

The differences between the three spectra shown in Fig. 3.13 are small. The second interference minimum in the spectrum for the single point source is absent in the spectrum for the set of point sources distributed over the square. In other situations, however, the effect of finite dimensions of a sound source may be larger.

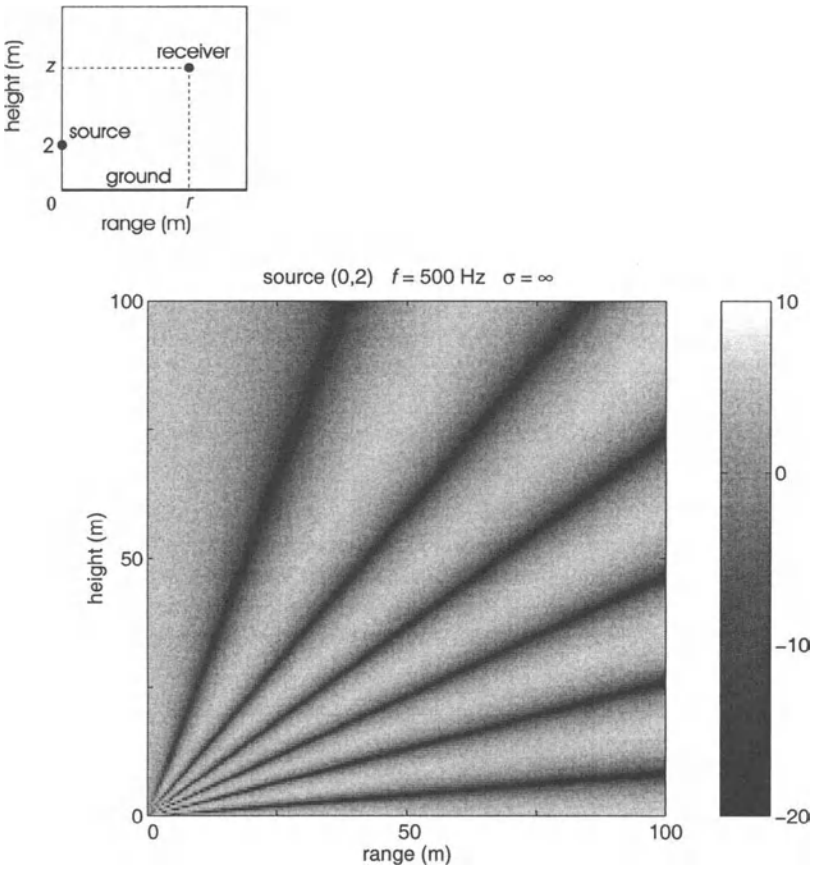

Figure 3.5. Field of relative sound pressure level ΔL as a function of receiver range r and receiver height z. The grey level represents the value of ΔL in dB, as indicated by the vertical bar. The geometry is shown above the graph. The source is a harmonic source with a frequency of 500 Hz. The source is located at range $r = 0$ and height $z = 2$ m. The ground surface is rigid ($\sigma = \infty$) and the atmosphere is homogeneous. The notation above the graph is explained in Sec. 3.5.

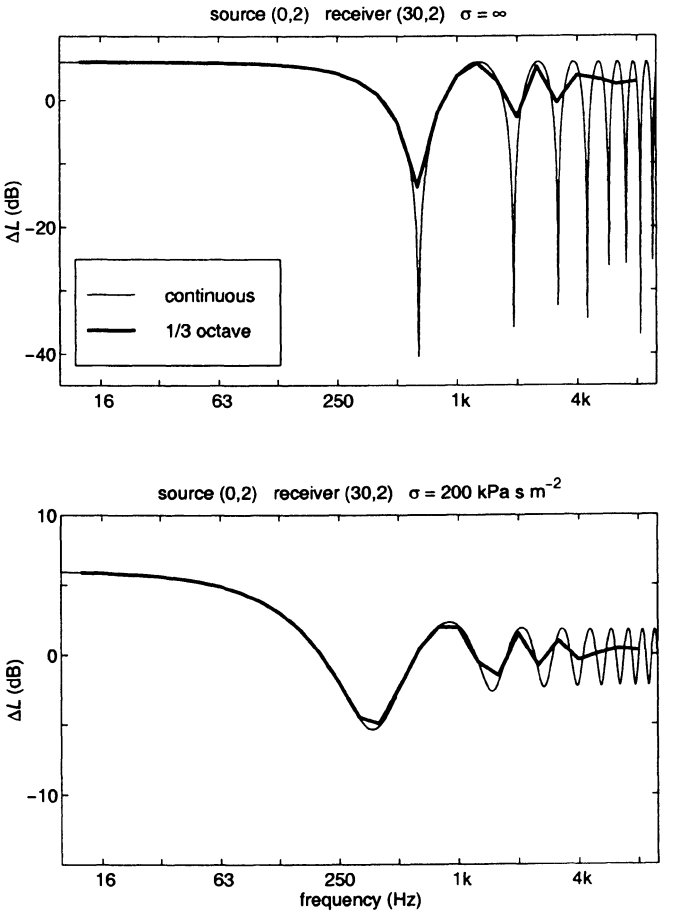

Figure 3.6. Continuous spectrum and one-third-octave band spectrum of the relative sound pressure level, for a rigid ground surface (upper graph) and an absorbing ground surface (lower graph). The impedance of the absorbing ground surface was calculated with a model developed by Attenborough [5], using a flow resistivity of 200 kPa·s·m^{-2}.

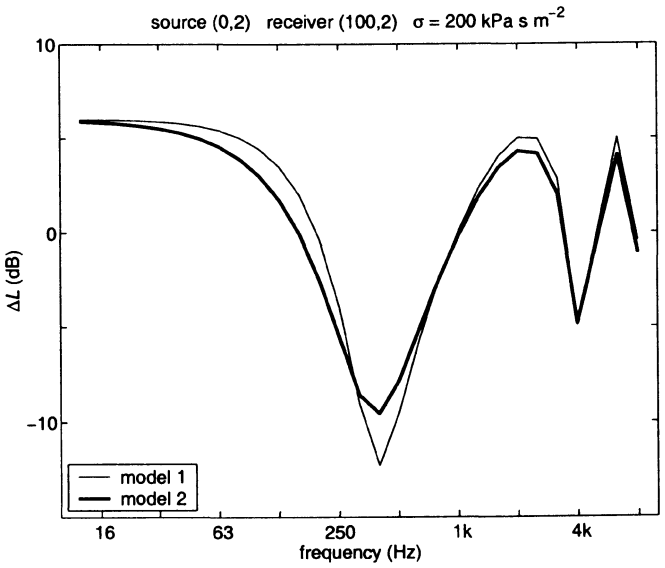

Figure 3.7. One-third-octave band spectrum of the relative sound pressure level, for an absorbing ground surface with a flow resistivity of 200 kPa·s·m^{-2}. The ground impedance was calculated from the flow resistivity with a model developed by Delany and Bazley [39] ('model 1') and a model developed by Attenborough [5] ('model 2').

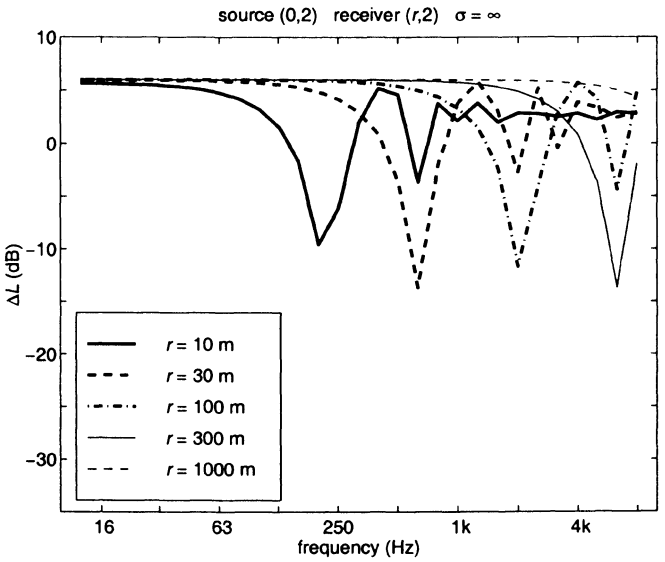

Figure 3.8. One-third-octave band spectrum of the relative sound pressure level, for five receiver ranges r (see legend) and a rigid ground surface.

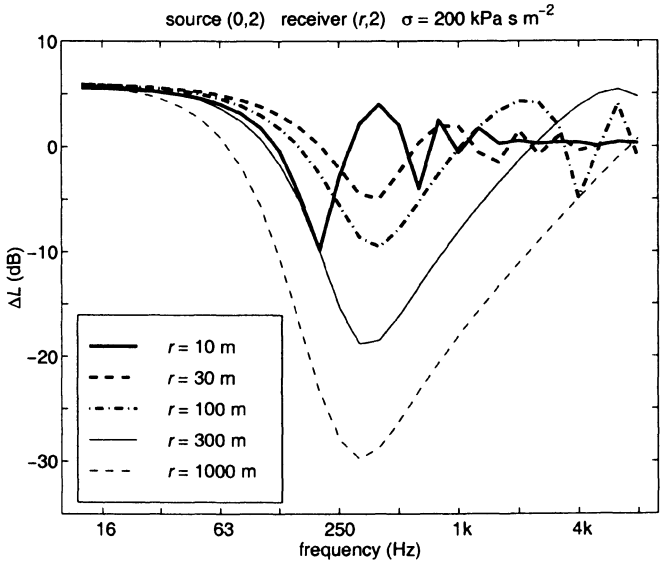

Figure 3.9. As Fig. 3.8, for an absorbing ground surface.

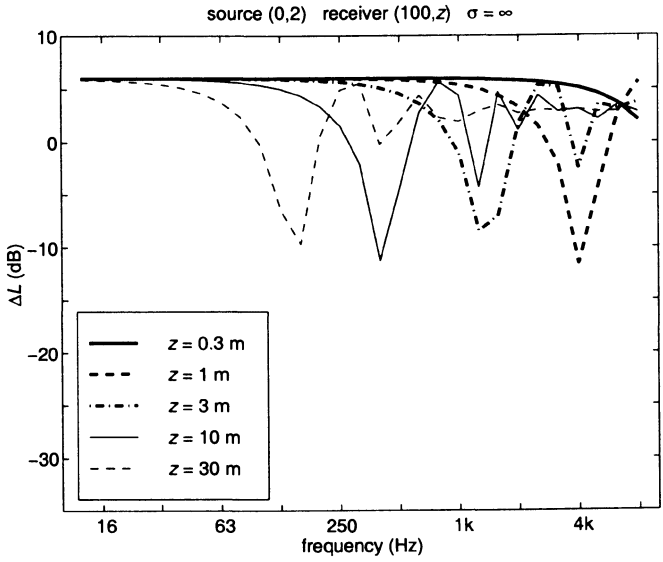

Figure 3.10. One-third-octave band spectrum of the relative sound pressure level, for five receiver heights z (see legend) and a rigid ground surface.

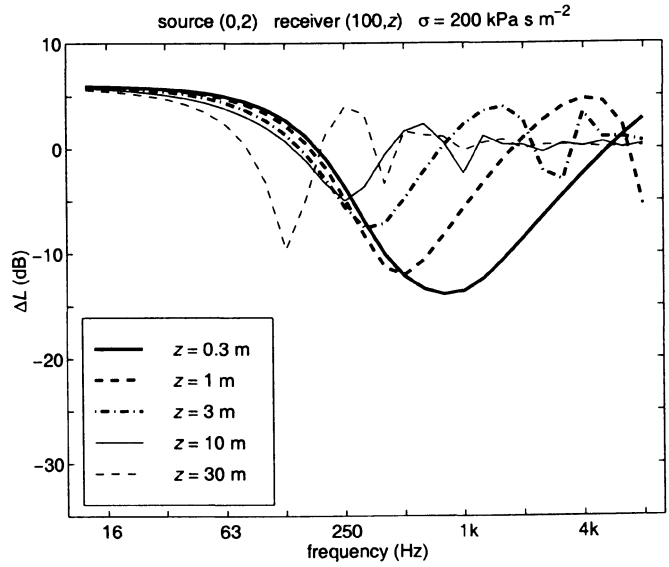

Figure 3.11. As Fig. 3.10, for an absorbing ground surface.

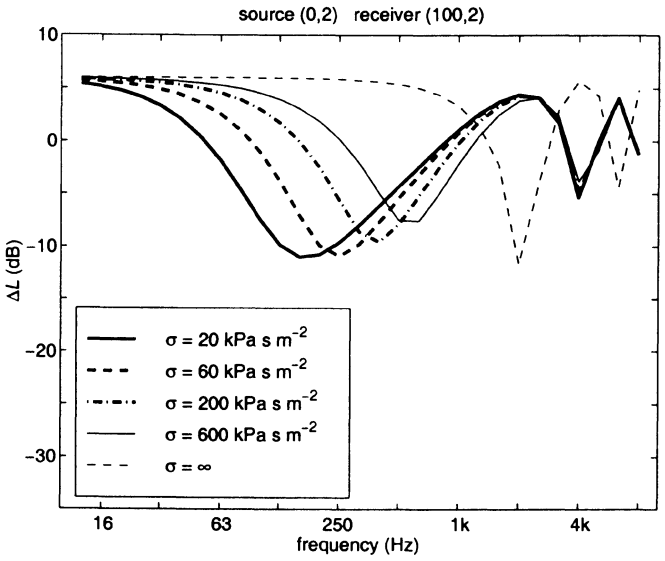

Figure 3.12. One-third-octave band spectrum of the relative sound pressure level, for five values of the flow resistivity σ of the ground surface (see legend).

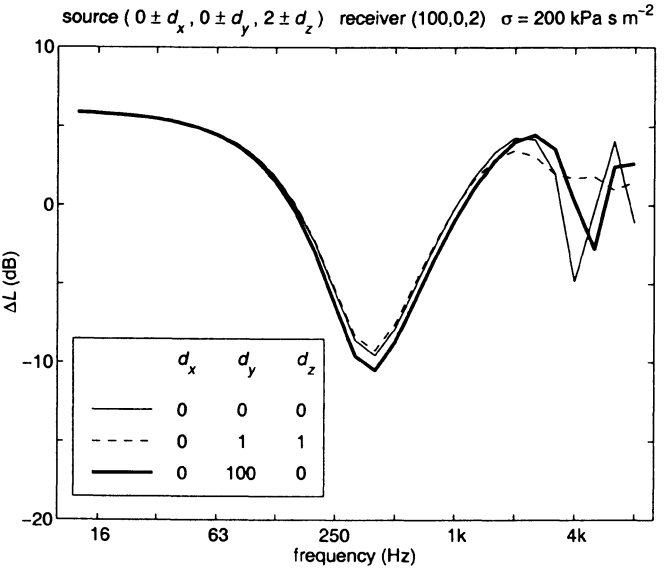

Figure 3.13. Example of the effect of finite dimensions of a source on the 1/3-octave band spectrum of the relative sound pressure level (see the text).

Chapter 4

Atmospheric refraction

4.1 Introduction

In the previous chapter we studied sound propagation in a non-refracting atmosphere over a ground surface. In general, the assumption of a non-refracting atmosphere is justified only for small propagation distances. For propagation distances of the order of 100 m or more, atmospheric refraction often has large effects on received sound pressure levels, in particular if the source and the receiver are close to the ground, at heights of a few meters or less.

In this chapter we study sound propagation in a refracting atmosphere over a ground surface. In Sec. 4.2 we describe the physical process of atmospheric refraction, which is caused predominantly by vertical gradients of the temperature and the wind speed. Empirical relations for the vertical profiles of the temperature and the wind speed in the atmospheric surface layer are given in Appendix N. In Sec. 4.3 we introduce the profile of the effective sound speed, which depends on the profiles of the temperature and the wind speed.

In Sec. 4.4 we describe the ray model for sound propagation in a refracting atmosphere. The ray model is useful for a qualitative understanding of atmospheric sound propagation. It is less useful for accurate computations of sound pressure levels, in particular in situations with irregular sound speed profiles, owing to complex effects such as the focusing of sound rays at so-called caustic points. A ray model for smooth sound speed profiles is described in Appendix L.

In Sec. 4.5 we describe three accurate numerical methods for sound propagation in a refracting atmosphere over a ground surface:

- the Fast Field Program (FFP),
- the Crank-Nicholson Parabolic Equation (CNPE) method,
- the Green's Function Parabolic Equation (GFPE) method.

The three methods are described in detail in Appendices F, G, and H, respectively.

E. M. Salomons, *Computational Atmospheric Acoustics*

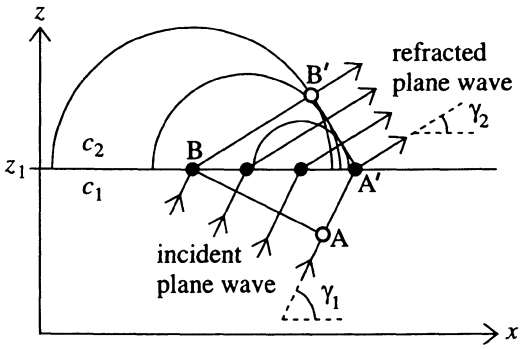

Figure 4.1. Refraction of a plane wave in an atmosphere with sound speed c_1 for $z \leq z_1$ and sound speed c_2 for $z > z_1$. Line segment AB is a wave front of the incident wave. Secondary sources (solid circles) at the interface $z = z_1$ generate spherical waves which form wave front A'B' of the refracted wave.

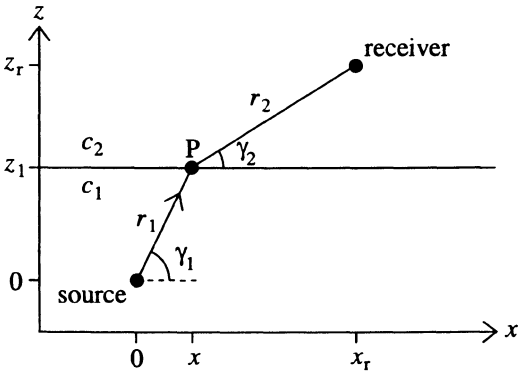

Figure 4.2. Refracted sound ray from a point source to a receiver, in the same atmosphere as in Fig. 4.1. The origin of the xz coordinate system is chosen at the position of the source. Point P is at position (x, z_1) and the receiver is at position (x_r, z_r).

In Sec. 4.6 we present numerical examples. The examples illustrate the accuracy of the computational methods in various situations.

4.2 Atmospheric refraction

Atmospheric refraction was described in Sec. 2.2 as a change of the propagation direction of a sound wave due to a sound speed gradient in the atmosphere. The propagation direction at a point was defined as the direction of the vector normal to the wave front through the point. The wave fronts of a plane wave in a non-refracting atmosphere are plane surfaces; in this case the propagation direction is independent of position. Refraction of a plane wave is illustrated in Fig. 4.1, for an atmosphere in which the sound speed c is a simple function of height z:

$$c(z) = \begin{cases} c_1 & \text{for } z \leq z_1 \\ c_2 & \text{for } z > z_1, \end{cases} \tag{4.1}$$

where c_1 and c_2 are constants and z_1 is the height indicated in Fig. 4.1. In general, the function $c(z)$ is called the (vertical) *sound speed profile*. The figure shows a plane wave in the region $z < z_1$ incident on the interface at height z_1. The elevation angle of a plane wave is defined as the angle between the propagation direction and the (horizontal) x axis; the elevation angle of the incident plane wave is γ_1. All points of the interface at height z_1 can be considered as secondary point sources (this is Huygen's principle [106]). Spherical waves generated by the secondary sources form a plane wave in the region $z > z_1$, with elevation angle γ_2.

We consider line segment AB of the wave front at time t, which has moved to A'B' at time $t + \delta t$. The time interval δt is equal to $|\mathrm{AA'}|/c_1$, and also equal to $|\mathrm{BB'}|/c_2$, where $|\mathrm{AA'}|$ and $|\mathrm{BB'}|$ are the lengths of line segments AA' and BB', respectively. From $|\mathrm{AA'}| = |\mathrm{A'B}| \cos\gamma_1$ and $|\mathrm{BB'}| = |\mathrm{A'B}| \cos\gamma_2$, where $|\mathrm{A'B}|$ is the length of line segment A'B, we find

$$\frac{\cos\gamma_1}{c_1} = \frac{\cos\gamma_2}{c_2}. \tag{4.2}$$

This is Snell's law of refraction (see also Sec. D.3). For an atmosphere with a continuous sound speed profile $c(z)$, instead of the discontinuous profile given by Eq. (4.1), Snell's law states that the elevation angle γ of a plane wave varies with z in such a way that the ratio $\cos\gamma(z)/c(z)$ is constant.

In Fig. 4.1 we have $\gamma_2 < \gamma_1$, corresponding to $c_2 > c_1$; the atmosphere is called a downward refracting atmosphere in this case. In the opposite case with $\gamma_2 > \gamma_1$ and $c_2 < c_1$, the atmosphere is called an upward refracting atmosphere.

The wave fronts of a point source in a non-refracting atmosphere are spheres. In a refracting atmosphere, the spheres are deformed by the effect of refraction. A curved wave front can be approximated locally by a plane wave front. The propagation of such a plane wave front obeys Snell's law of refraction. An

equivalent statement is that the curved sound rays from a point source, *i.e.* the curves perpendicular to the wave fronts of the point source, obey Snell's law for sound rays:

$$\frac{\cos\gamma(z)}{c(z)} = \text{constant along a sound ray,} \tag{4.3}$$

where $\gamma(z) = \arctan(dz/dx)$ is the elevation angle of the sound ray at height z. This is illustrated in Fig. 4.2 for an atmosphere with the sound speed profile given by Eq. (4.1). The sound ray consists of two straight segments, with a discontinuous slope at $z = z_1$. In an atmosphere with a continuous sound speed profile $c(z)$, instead of the discontinuous profile given by Eq. (4.1), the sound rays are curves with a continuous slope.

The travel time of a sound wave along the path represented by a sound ray is always smaller than the travel time along a slightly deformed path. In other words, a sound wave follows the path between the source and the receiver that corresponds to a (local) minimum of the travel time. This is Fermat's principle of minimum travel time (a more general statement is that a sound wave follows the path that corresponds to a stationary travel time; see Ref. [106]).

To illustrate Fermat's principle we consider a deformation of the path shown in Fig. 4.2 by varying the x coordinate of point P. The travel time t is given by $t = r_1/c_1 + r_2/c_2$, with $r_1 = \sqrt{x^2 + z_1^2}$ and $r_2 = \sqrt{(x_r - x)^2 + (z_r - z_1)^2}$. The derivative of the travel time with respect to the x coordinate of point P is $\partial t/\partial x = (x/r_1)/c_1 - [(x_r - x)/r_2]/c_2$, or $\partial t/\partial x = \cos\gamma_1/c_1 - \cos\gamma_2/c_2$. From Fermat's principle we have $\partial t/\partial x = 0$, which gives $\cos\gamma_1/c_1 = \cos\gamma_2/c_2$, *i.e.* Snell's law.

4.3 Effective sound speed

In a non-moving atmosphere, *i.e.* an atmosphere without wind, sound waves travel with the adiabatic sound speed, which is a function of the temperature of the atmosphere (see Secs. 2.2 and A.2). An atmosphere with wind is called a moving atmosphere. The computation of sound propagation in a moving atmosphere is more complex than the computation of sound propagation in a non-moving atmosphere. Fortunately, a moving atmosphere can be approximated by a non-moving atmosphere with an *effective sound speed* $c_{\text{eff}} = c + u$, where c is the adiabatic sound speed and u is the (horizontal) component of the wind velocity in the direction of sound propagation. The idea behind this approximation is that a sound wave travels faster if the atmosphere moves in the propagation direction ($u > 0$) and slower if the atmosphere moves in the opposite direction ($u < 0$) [40]. A more rigorous justification of the effective sound speed approximation is given in Sec. E.3. In general, the effective sound speed approximation is valid in situations in which sound waves travel with relatively small elevation angles, such as situations with the source and the receiver near the ground. For large elevation angles, the effective sound speed approximation

is not valid. The effective sound speed c_{eff} will often be referred to simply as the sound speed c.

Spatial variations of the temperature and the wind velocity in the atmosphere correspond to spatial variations of the effective sound speed. These variations cause atmospheric refraction. In situations with a flat, homogeneous ground surface, it is usually a good approximation to assume that the temperature, the wind velocity, and the effective sound speed are functions of height z only:

$$c_{\text{eff}}(z) = c(z) + u(z). \tag{4.4}$$

The atmosphere is called a layered atmosphere or a stratified atmosphere in this case. The function $c_{\text{eff}}(z)$ is called the (effective) sound speed profile.

Empirical expressions for the vertical profiles of the temperature and the wind speed are given in Appendix N. These profiles should be considered as average profiles, averaged over a period of typically ten minutes (variations of the profiles on smaller time scales are considered in Chap. 5). The expressions given in Appendix N are valid for the atmospheric surface layer, which has a height of typically 100 m. The profiles are characterized by large vertical gradients near the ground surface. At the ground surface, the wind speed is approximately zero, due to friction at the ground surface. With increasing height, the wind speed increases while the vertical derivative of the wind speed decreases. The variation of the wind speed is largest in the first few meters above the ground surface. The shape of the wind speed profile depends on the roughness of the ground surface. Air flowing over a ground surface is 'slowed down' more effectively by a rough surface, *e.g.* grassland, than by a smooth surface, *e.g.* a water surface.

The shape of the temperature profile is similar to the shape of the wind speed profile. The variation of the temperature is largest near the ground surface and decreases with increasing height. In the daytime, the temperature usually decreases with increasing height. At night, the temperature usually increases with increasing height.

A realistic profile of the effective sound speed in the atmospheric surface layer is the logarithmic profile

$$c_{\text{eff}}(z) = c_0 + b \ln\left(\frac{z}{z_0} + 1\right) \tag{4.5}$$

with parameters c_0, b, and z_0. Parameter c_0 is the sound speed at the ground surface; the precise value of c_0 is unimportant, and we use $c_0 = 340$ m/s. Parameter z_0 is called the (aerodynamic) roughness length of the ground surface; typical values are between 0.01 m and 0.1 m for grassland and between 10^{-4} m and 10^{-3} m for a water surface. We use $z_0 = 0.1$ m, unless indicated otherwise. Typical values of parameter b in Eq. (4.5) are 1 m/s for a downward refracting atmosphere and -1 m/s for an upward refracting atmosphere. Figure 4.3 shows the logarithmic profile (4.5) for $c_0 = 340$ m/s, $z_0 = 0.1$ m, and $b = 1$ m/s. For an

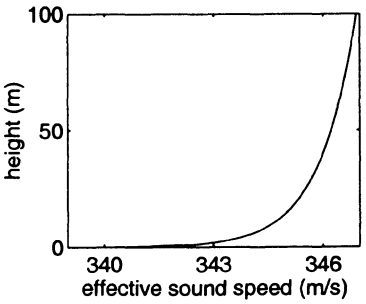

Figure 4.3. Logarithmic profile (4.5) of the effective sound speed, for $c_0 = 340$ m/s, $z_0 = 0.1$ m, and $b = 1$ m/s.

atmosphere with a constant temperature, the values $b = 1$ m/s and $z_0 = 0.1$ m correspond to a wind speed (component) of 4.6 m/s at a height of 10 m.

4.4 Ray model

Atmospheric sound propagation can be modeled with sound rays. Basically, the approach of a ray model consists of two steps:

i) calculation of the paths of all sound rays between the source and the receiver,

ii) calculation of the received sound pressure by summation of the contributions of all sound rays.

This approach is called geometrical acoustics. The principles of geometrical acoustics are described in Refs. [2, 17, 106].

The model described in Chap. 3 for sound propagation in a non-refracting atmosphere can be considered as a simple ray model. The complex pressure amplitude p_c was written in Eq. (3.2) as a sum of two terms:

$$p_c = \sum_{m=1}^{2} A_m \exp(i\phi_m), \tag{4.6}$$

with phases $\phi_m = kR_m$ and amplitudes A_m that follow by comparison with Eq. (3.2). In general, A_2 is complex, so ϕ_2 is not the total phase of the second term. The two terms can be interpreted as the contributions of sound rays. The first term represents the direct ray and the second term represents the ray reflected by the ground surface. In this case the ray model can be considered as a representation of the exact solution of the wave equation for a system with a non-refracting atmosphere and a finite-impedance ground surface (see Sec. D.4).

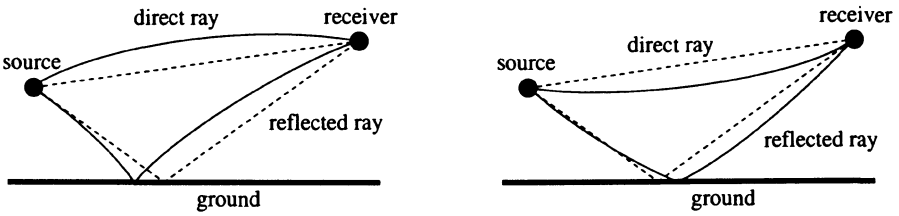

Figure 4.4. Direct ray and ray reflected by the ground surface, in a downward refracting atmosphere (left) and an upward refracting atmosphere (right). The dashed lines represented the straight rays in a non-refracting atmosphere.

In general, the assumption of a non-refracting atmosphere is justified only for small propagation distances, of the order of a few tens of meters. For larger distances, the effects of atmospheric refraction must be taken into account. In a refracting atmosphere, sound rays are curved and the number of rays is often different from two.

For small source-receiver distances, the number of rays is still equal to two, but the rays are curved as shown in Fig. 4.4. A solution of the wave equation for this situation, analogous to the exact solution for a non-refracting atmosphere, can be found in Ref. [82].

For larger distances, the number of rays is often different from two. This is illustrated in Figs. 4.5 and 4.6, for an upward refracting atmosphere and a downward refracting atmosphere, respectively. The figures show sound rays emitted by a point source within a limited interval of the elevation angle (a point source emits sound rays in all directions, but for graphical clarity we have omitted rays with large elevation angles in the figures). The rays were calculated for the logarithmic sound speed profile (4.5), with b = -1 m/s for Fig. 4.5 and b = 1 m/s for Fig. 4.6.

In an upward refracting atmosphere (Fig. 4.5), a region exists where no sound rays arrive. This region is called the shadow region. The location of the shadow region depends on the source height and the sound speed profile. The ray model predicts a vanishing sound pressure in a shadow region. In reality, the sound pressure is small but not zero, due to the effect of diffraction and the effect of scattering by atmospheric turbulence [89] (see Sec. 4.6.4 and Chap. 5).

In a downward refracting atmosphere (Fig. 4.6), sound rays with multiple ground reflections occur, so the number of rays arriving at a distant receiver is often much larger than two. The calculation of all ray paths to a receiver is called 'ray tracing'. One needs in general an iterative computational algorithm to 'trace' all ray paths. A ray tracing algorithm consists basically of the computation of many ray paths and the selection of those ray paths that arrive at the receiver. A ray path is computed by numerical integration of Snell's law (4.3), *i.e.* by making small steps along the ray path in such a way that the elevation angle satisfies Snell's law (4.3) at all points of the ray path. Figure 4.7 shows that the number of rays increases with increasing distance between the source

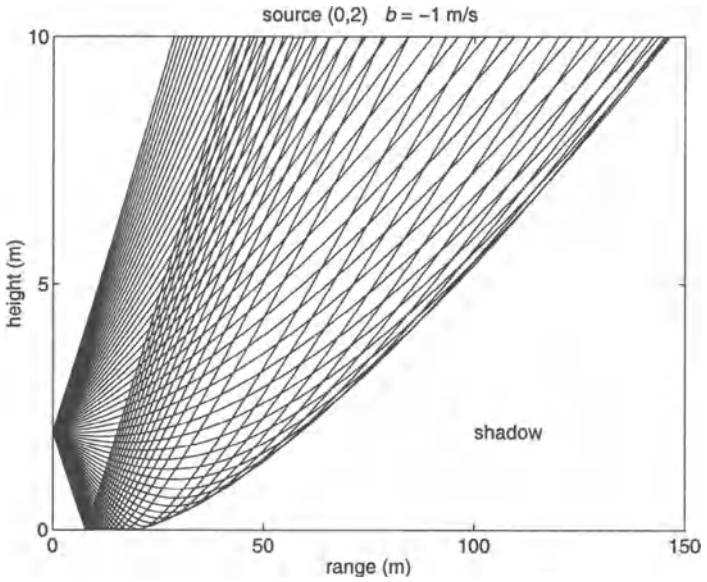

Figure 4.5. Sound rays in an upward refracting atmosphere.

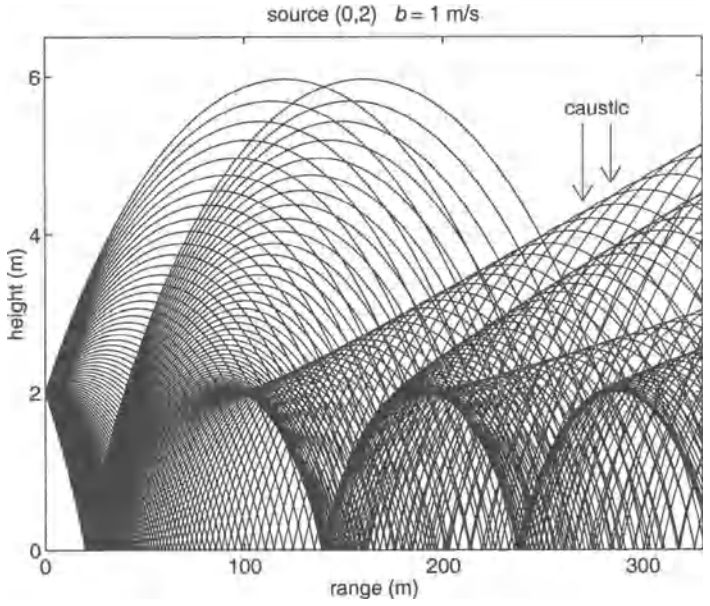

Figure 4.6. Sound rays in a downward refracting atmosphere.

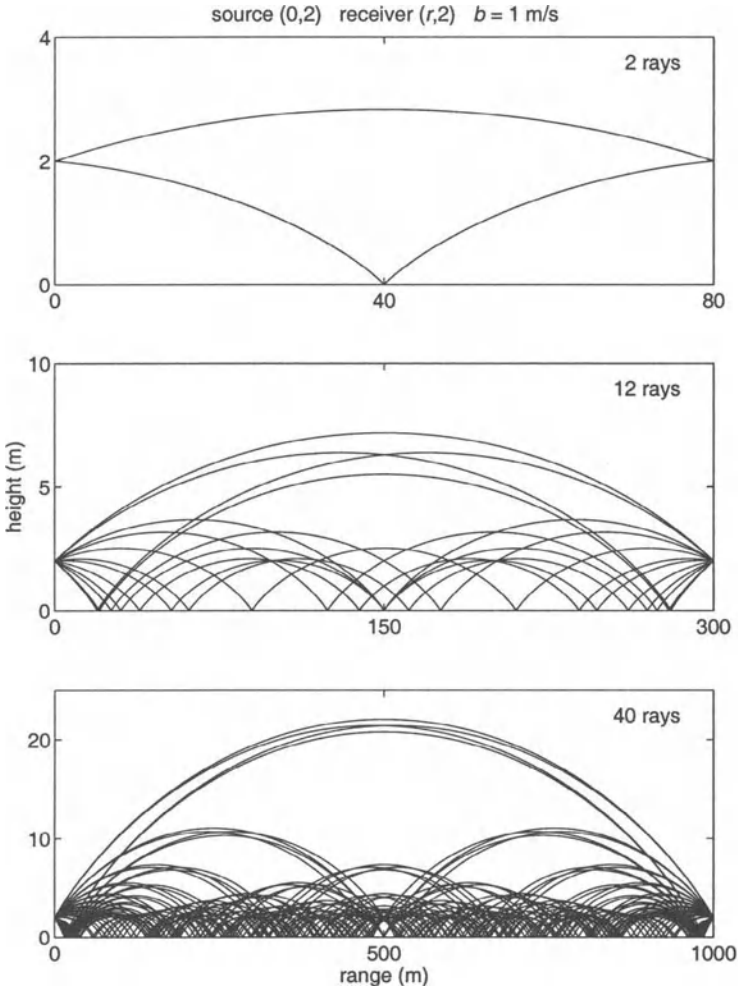

Figure 4.7. Sound rays between a source at position (0,2) and a receiver at position $(r,2)$, for $r = 80$ m (top), $r = 300$ m (middle), and $r = 1000$ m (bottom), in a downward refracting atmosphere with logarithmic sound speed profile (4.5) with $b = 1$ m/s. The lower graph for $r = 1000$ m illustrates the grouping of rays in sets of four rays.

Figure 4.8. The ray tube diameter D is the normal distance between two sound rays emitted by the source with a small difference in elevation angle.

and the receiver, for a logarithmic sound speed profile. The figure also shows that the rays are grouped in sets of four rays [49], except for small distances between the source and the receiver.

The generalization of Eq. (4.6) for a situation with two or more sound rays in a downward refracting atmosphere is [17, 81, 135]

$$p_c = \sum_{m=1}^{N_{\text{rays}}} A_m \exp(i\phi_m), \tag{4.7}$$

where N_{rays} is the number of sound rays. The phase ϕ_m of ray m is given by $\phi_m = \int k(z)ds$, where s is the path length along the ray; we assume a layered atmosphere here, with $k = k(z)$. This can also be written as $\phi_m = \omega t_m$, where $t_m = \int c^{-1}(z)ds$ is the travel time along the ray. The amplitude A_m of ray m can be written as (see Sec. L.3)

$$A_m = f_m C_m^{N_m} \frac{S}{R_1}, \tag{4.8}$$

where f_m is a focusing factor, C_m is a reflection coefficient, and N_m is the number of ground reflections. For the reflection coefficient C_m we use the spherical-wave reflection coefficient (see Sec. L.3.4). The focusing factor f_m accounts for the fact that, in a refracting atmosphere with curved sound rays, there are regions where the 'concentration' of sound rays is high and regions where the 'concentration' of sound rays is low (see Fig. 4.6). A measure of the ray concentration is the ray tube diameter D, which is defined as the normal distance between two sound rays emitted by the source with a small difference in elevation angle (see Fig. 4.8). The ray tube diameter is small in regions of high ray concentration (the rays are focused here) and the ray tube diameter is large in regions of low ray concentration (the rays are defocused here). The focusing factor is equal to $\sqrt{D_{\text{free}}/D}$, where D_{free} is the ray tube diameter in the free field, *i.e.* the field in an unbounded homogeneous atmosphere (see Sec. L.3.6). The focusing factor is equal to unity in the free field.

A problem with the ray model is caustics [18, 17, 106]. A caustic is a set of points where the ray tube diameter vanishes. In other words, two sound rays emitted by the source with a small (infinitesimal) difference in elevation angle, cross each other at a caustic point (see Fig. 4.6). Hence, the focusing factor diverges at a caustic point, and geometrical acoustics predicts an infinite

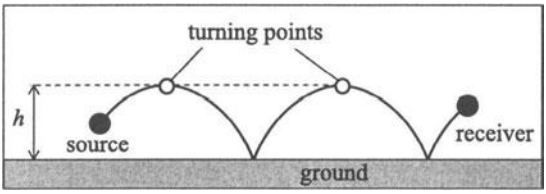

Figure 4.9. Example of a sound ray with two turning points ($n = 2$). The maximum height of the ray, denoted as h, is indicated.

amplitude at a caustic point. In reality, the amplitude of the sound pressure at a caustic point is relatively high but not infinite of course. The difference between the real sound pressure field and the geometrical acoustics prediction is called a caustic diffraction field. Caustic diffraction fields eliminate the infinite amplitudes. The computation of caustic diffraction fields is complex [85, 73], which makes the ray model less attractive for accurate computations of sound propagation, in particular for irregular sound speed profiles.

In Appendix L we describe a ray model that takes into account caustic diffraction fields. The model assumes a smooth sound speed profile, with a sound speed that increases monotonically with height; an example is the logarithmic profile (4.5). The rays shown in Figs. 4.6 and 4.7 for a downward refracting atmosphere were computed with this model (the rays shown in Fig. 4.5 for an upward refracting atmosphere were computed by straightforward integration of Snell's law).

In the remainder of this section we will use the ray model to provide insight into sound propagation in situations such as shown in the lower graph in Fig. 4.7 (for $r = 1000$ m), with a large distance between the source and the receiver and a large number of sound rays. The sound rays are grouped in sets of four rays. In the example shown in the lower graph in Fig. 4.7, there is a group of four rays that reach a height of about 22 m, a second group of four rays that reach a height of about 11 m, and so on. In general, the highest point of a sound ray is called the turning point, and the height of the turning point is called the maximum height of the ray; the maximum height is denoted as h (see Fig. 4.9). The four rays of a group have an equal number of turning points, which is denoted as n ($n = 1, 2, \ldots$). The maximum height h is approximately equal for the four rays of a group, and we denote the value of h for a group of rays with n turning points as h_n. For the logarithmic profile (4.5) we have (see Sec. L.3.1)

$$h_n \approx \frac{r}{n}\sqrt{\frac{b}{2\pi c_0}}. \tag{4.9}$$

For $r = 1000$ m and $b = 1$ m/s we find $h_n \approx 22/n$ m. Thus, we have $h_1 \approx 22$ m, $h_2 \approx 11$ m, and so on. These values are in agreement with the maximum heights of the rays shown in the lower graph in Fig. 4.7.

Equation (4.9) for the maximum height h_n is valid if the source height z_s and the receiver height z are small compared with h_n. With increasing n, the maximum height h_n decreases and deviations occur from Eq. (4.9). At a certain value of n, h_n given by Eq. (4.9) becomes smaller than z_s or z, and Eq. (4.9) should not be used anymore, as there are no sound rays with a maximum height smaller than z_s or z.

If we neglect the deviations from Eq. (4.9) and use this equation for all rays with h_n larger than z_s and z, we find that the total number of groups is given approximately by h_1/z_{sr}, where z_{sr} is, for example, the average of the source height and the receiver height. Each group consists of four rays, so the total number of rays is $N_{rays} \approx 4h_1/z_{sr}$. In the example in the lower graph in Fig. 4.7, $4h_1/z_{sr}$ is equal to 44, in good agreement with the actual number of rays (40).

The relation $N_{rays} \approx 4h_1/z_{sr}$ can be used to derive a simple expression for the relative sound pressure level ΔL for the case of sound propagation over a water surface in a downward refracting atmosphere with logarithmic sound speed profile (4.5). As the reflection coefficient for a water surface is equal to unity, all rays have approximately equal amplitudes at a distant receiver; here we neglect the effects of focusing and caustics. We further neglect the effects of interference between the rays, so we assume that the phases of the rays are random. In the free field there is only one ray, so we have $|p_c|^2 \approx N_{rays}|p_{free}|^2$ in the definition (3.6) of ΔL. This gives

$$\Delta L \approx 10 \lg N_{rays}, \tag{4.10}$$

where $N_{rays} = 4h_1/z_{sr}$ is the number of rays. It follows from Eq. (4.9) that N_{rays} is proportional to the receiver range r, so it follows from Eq. (4.10) that ΔL increases linearly with $\lg r$. In Sec. 4.6.4 we will illustrate this linear increase by a numerical example. In Chap. 6 we will see that the increase is not unlimited, as a consequence of the roughness of a water surface.

In the case of sound propagation over an absorbing ground surface, *e.g.* grassland, the above linear increase of ΔL with $\lg r$ does not occur. In this case, rays with many ground reflections have a small amplitude at a distant receiver. Consequently, most of the sound energy flows along the highest sound rays [131]. In this case the relative sound pressure level ΔL at a distant receiver is dominated by the highest sound rays.

4.5 FFP and PE methods

In this section we describe three accurate numerical methods for sound propagation in a refracting atmosphere over a ground surface:

- the Fast Field Program (FFP),
- the Crank-Nicholson Parabolic Equation (CNPE) method,
- the Green's Function Parabolic Equation (GFPE) method.

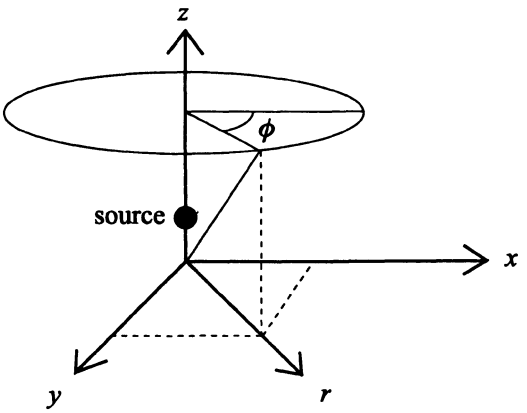

Figure 4.10. Rectangular xyz coordinates and cylindrical $rz\phi$ coordinates. In the axisymmetric approximation we neglect the variation of the sound field with azimuthal angle ϕ.

The three methods are described in detail in Appendices F, G, and H, respectively. References to the literature are given in the appendices. The three methods will be referred to as the FFP method, the CNPE method, and the GFPE method, respectively.

In general, the three methods yield a solution of the wave equation, or an approximation of the wave equation, for a system with a monopole source above an absorbing or rigid ground surface. The computation is performed in the frequency domain, *i.e.* for a harmonic sound field. The computation of a complete spectrum requires separate computations for all frequencies of the spectrum. In general, the computing time increases with increasing frequency, and the computing time for a complete spectrum is often considerable.

To keep the computing time acceptably small, the computations are usually performed in two dimensions, in the vertical plane through the source and the receiver. This approach is based on the axisymmetric approximation, which corresponds to a neglect of the variation of the sound field with azimuthal angle ϕ around the vertical axis through the source (see Fig. 4.10; see also Sec. E.4). The axisymmetric approximation is a good approximation in many practical situations, as wind and temperature variations with azimuthal angle are usually considerably smaller than wind and temperature variations with height. An example that illustrates the accuracy of the axisymmetric approximation is presented in Sec. 4.6.3.

The Fast Field Program (FFP method) is based on a Fourier transformation of the wave equation from the horizontal spatial domain to the horizontal wave number domain. The transformed wave equation is solved numerically, and the solution is transformed back to the spatial domain by an inverse Fourier

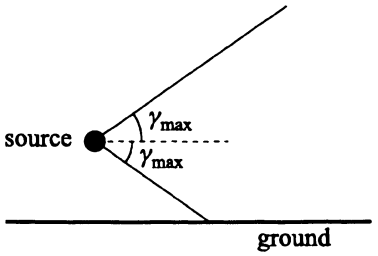

Figure 4.11. The PE method is valid for sound waves with elevation angles γ between $-\gamma_{max}$ and γ_{max}.

transformation. Thus, the solution in the spatial domain is an inverse Fourier integral over horizontal wave numbers. Therefore, the FFP method is sometimes called the 'wave number integration method' [69]. The FFP method is widely used in ocean acoustics. For simple sound speed profiles, the wave equation in the horizontal wave number domain can be solved analytically with the method of normal modes [69, 120, 9].

In Appendix F we describe a generalized formulation of the FFP method, which can be applied to both axisymmetric (two-dimensional) systems and three-dimensional systems, with either a non-moving atmosphere or a moving atmosphere with an arbitrary field of the (horizontal) wind vector. Results of the generalized FFP method will be used in Sec. 4.6.1 to illustrate moving-medium effects and the accuracy of the effective sound speed approximation.

As a consequence of the Fourier transformation to the horizontal wave number domain, the FFP method is restricted to systems with a layered atmosphere and a homogeneous ground surface. Systems with a range-dependent sound speed profile or a range-dependent ground impedance cannot be modeled with the FFP method.

In contrast to the FFP method, the Parabolic Equation (PE) method is not restricted to systems with a layered atmosphere and a homogeneous ground surface. The PE method is based on a parabolic equation, which is an approximate form of the wave equation. As described in Appendix G, different parabolic equations exist. A parabolic equation is valid for elevation angles that do not exceed a limiting angle γ_{max}. In other words, PE results are accurate only for receivers at elevation angles smaller than γ_{max} (see Fig. 4.11). This angular limitation will be studied quantitatively in Sec. 4.6.2.

For a moving atmosphere, the effective sound speed approximation is used in the PE method. Since the effective sound speed approximation is not valid for large elevation angles, the PE method should not be used for moving atmospheres and large elevation angles.

Back scattering of sound waves, *i.e.* scattering by sound speed gradients in the direction back to the source, is neglected by a parabolic equation. In other

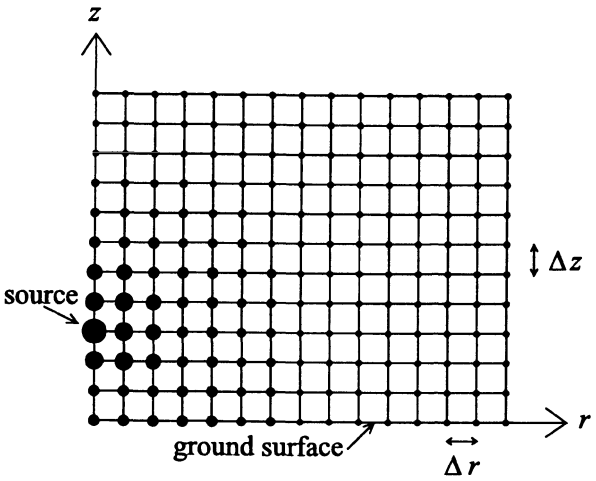

Figure 4.12. Grid in the rz plane used in two-dimensional PE methods, with horizontal grid spacing Δr and vertical grid spacing Δz. The amplitude of the sound pressure at a grid point is represented schematically by the size of the circle at the grid point.

words, a parabolic equation is a one-way wave equation, taking into account only sound waves traveling in the direction from the source to the receiver. As the sound speed is usually a smooth function of position in the atmosphere, the one-way wave propagation approximation is usually a good approximation.

The Crank-Nicholson Parabolic Equation (CNPE) method and the Green's Function Parabolic Equation (GFPE) method are two different methods of solving a parabolic equation. Two-dimensional CNPE and GFPE methods are based on the axisymmetric approximation, so the solution is performed in two dimensions, in the rz plane through the source and the receiver. Both methods make use of a rectangular grid in the rz plane (see Fig. 4.12). The source is represented by a starting function $p_c(r = 0, z)$ of the complex pressure amplitude at range $r = 0$. This starting function is extrapolated step-wise on the grid, in the positive r direction. An extrapolation step from range r to range $r + \Delta r$ can be expressed as

$$p_c(r, z) \rightarrow p_c(r + \Delta r, z). \tag{4.11}$$

By repeating this extrapolation step many times, the complete field $p_c(r, z)$ of the complex pressure amplitude is computed.

In the CNPE method, a Crank-Nicholson finite-difference scheme is used for the numerical evaluation of an extrapolation step. The horizontal and vertical grid spacings Δr and Δz in the CNPE method are limited to a maximum value of about $\lambda/10$, where λ is an average wavelength. Consequently, the number of

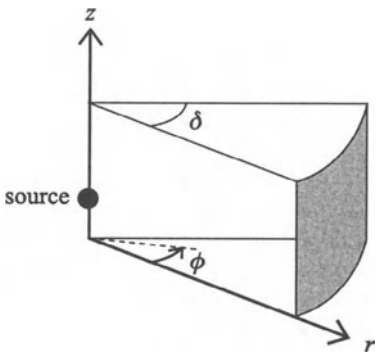

Figure 4.13. In the three-dimensional GFPE method, the field is computed in a pie slice region. Periodic boundary conditions are imposed on the straight sides at $\phi = 0$ and $\phi = \delta$.

grid points, and hence the computing time, increases with increasing frequency. In the GFPE method, the vertical grid spacing is also limited to about $\lambda/10$, but the horizontal grid spacing (or range step) may be chosen considerably larger, up to about 50λ. Consequently, computing times of the GFPE method are considerably smaller than computing times of the CNPE method.

As indicated before, the PE method is not restricted to systems with a layered atmosphere and a homogeneous ground surface. A range dependence of the sound speed profile or the ground impedance is taken into account by changing the profile or the impedance during the extrapolation of the field in the positive r direction. In Chap. 5 we will see that we can even take into account the effect of atmospheric turbulence with the PE method.

A three-dimensional GFPE method is described in Sec. H.12. In this case we compute the field in a pie slice region (see Fig. 4.13), by a step-wise extrapolation of the field in the positive r direction. Periodic boundary conditions are imposed on the straight sides at $\phi = 0$ and $\phi = \delta$. This approach is obviously correct for $\delta = 360°$. For $\delta < 360°$ it is an approximate approach. By choosing a low value for δ we keep the computation efficient.

4.6 Examples

In this section we present results that illustrate the application of the FFP method, the PE methods, and the ray model. Results are represented by the relative sound pressure level $\Delta L = 10\lg(|p_c|^2/|p_{\text{free}}|^2)$, in the same way as in Chap. 3 for a non-refracting atmosphere. Parameters are indicated above the graphs using the same notation as in Sec. 3.5. Unless indicated otherwise, we use the logarithmic sound speed profile (4.5) with $c_0 = 340$ m/s and $z_0 = 0.1$ m.

4.6.1 Moving-medium effects

The generalized formulation of the FFP method described in Appendix F can be used to study moving-medium effects and the accuracy of the effective sound speed approximation. In the three-dimensional FFP method, the atmosphere is represented by three profiles: the (adiabatic) sound speed profile $c(z)$ and the profiles $u(z)$ and $v(z)$ of horizontal wind velocity components; u and v are the components parallel and perpendicular to the direction of sound propagation, respectively. In the two-dimensional FFP method, the atmosphere is represented by the profiles $c(z)$ and $u(z)$. In this example, the profiles are given by logarithmic functions:

$$c(z) = c_0 + b_t \ln\left(\frac{z}{z_0} + 1\right) \tag{4.12}$$

$$u(z) = b_u \ln\left(\frac{z}{z_0} + 1\right) \tag{4.13}$$

$$v(z) = b_v \ln\left(\frac{z}{z_0} + 1\right) \tag{4.14}$$

with $c_0 = 340$ m/s and $z_0 = 0.1$ m. We consider different combinations of the parameters b_t, b_u, and b_v. For the two-dimensional FFP method we consider

i) $b_t = 1$ m/s, $b_u = 0$ m/s (non-moving atmosphere),

ii) $b_t = 0$ m/s, $b_u = 1$ m/s (moving atmosphere).

Both combinations correspond to the effective sound speed profile $c_{\text{eff}}(z) = c_0 + b\ln(1 + z/z_0)$ with $b = 1$ m/s. For the three-dimensional FFP method we consider

iii) $b_t = 1$ m/s, $b_u = 0$ m/s, $b_v = 0$ m/s (non-moving atmosphere),

iv) $b_t = 0$ m/s, $b_u = 1$ m/s, $b_v = 0$ m/s (moving atmosphere),

v) $b_t = 0$ m/s, $b_u = 1$ m/s, $b_v = 1$ m/s (moving atmosphere with cross-wind).

These three combinations also correspond to the effective sound speed profile $c_{\text{eff}}(z) = c_0 + b\ln(1 + z/z_0)$ with $b = 1$ m/s. If the combinations *i*) and *ii*) give equal results, and if the combinations *iii*), *iv*), and *v*) give equal results, we can conclude that the effective sound speed approximation is an accurate approximation. If two-dimensional results are equal to three-dimensional results, we can conclude that two-dimensional modeling, based on the axisymmetric approximation, is an accurate approach.

In this example the source height is 2 m, the frequency is 400 Hz, and the flow resistivity of the ground surface is 200 kPa·s·m^{-2}. Results are shown in Fig. 4.14 for a receiver height of 2 m and in Fig. 4.15 for a receiver height of 50 m, for the combinations *i*) to *v*) of the parameters b_t, b_u, and b_v. As a reference, the

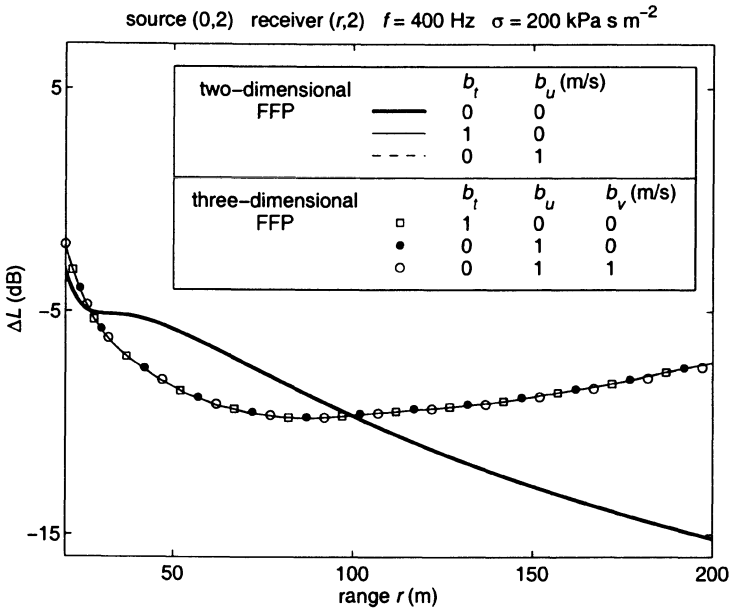

Figure 4.14. Relative sound pressure level as a function of range, computed with the two-dimensional FFP method and the three-dimensional FFP method, for a situation with $z_s = 2$ m, $f = 400$ Hz, $\sigma = 200$ kPa·s·m^{-2}, and $z = 2$ m. The legend shows values of the parameters used in Eqs. (4.12), (4.13), and (4.14) for the atmospheric profiles. The thick solid line represents a non-refracting atmosphere. The other lines and the symbols represent downward refracting atmospheres, which all correspond to the effective sound speed profile $c_{\text{eff}}(z) = c_0 + b\ln(1 + z/z_0)$ with $b = 1$ m/s. The dashed line is indistinguishable from the thin solid line.

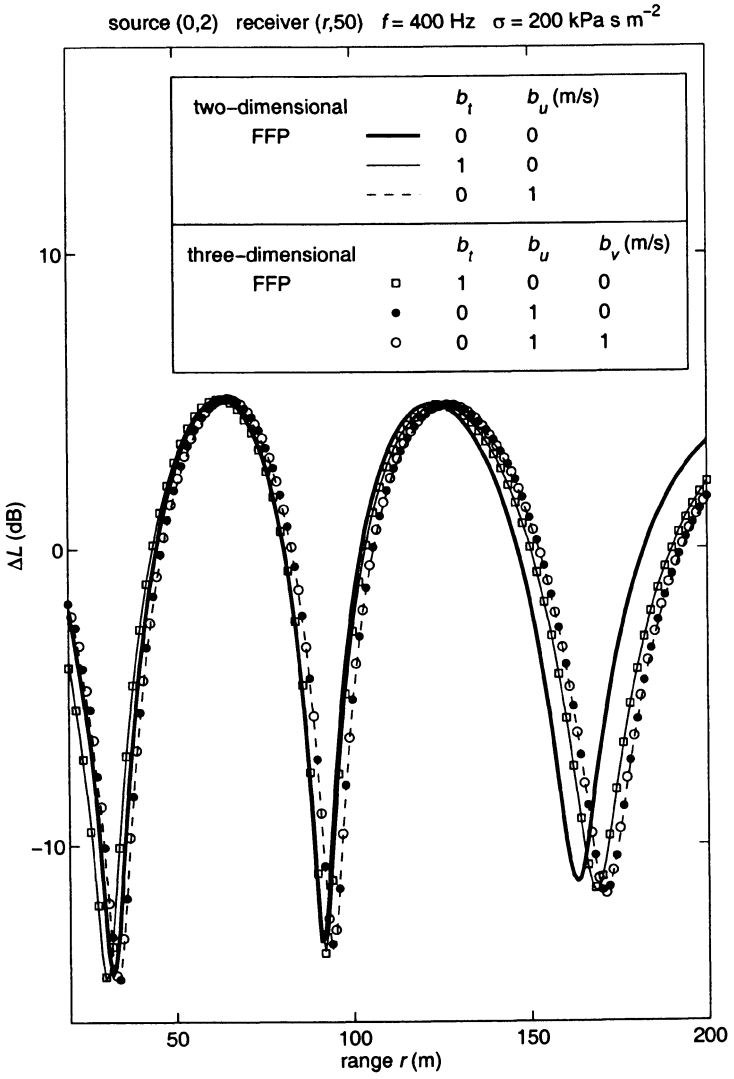

Figure 4.15. As Fig. 4.14, for $z = 50$ m.

figures show also the result for a non-refracting atmosphere, represented by a thick solid line.

Figure 4.14 shows that, for a receiver height of 2 m, the combinations *i*) to *v*) of b_t, b_u, and b_v give equal results. Consequently, the effective sound speed approximation is accurate and two-dimensional modeling is accurate.

Figure 4.15 shows that, for a receiver height of 50 m, small deviations occur between the results for the different combinations of b_t, b_u, and b_v. The effective sound speed approach gives slightly inaccurate results, in this case. Nevertheless, cross-wind has no effect and two-dimensional modeling is accurate.

4.6.2 Angular limitation of the PE method

In this section we present results that illustrate the angular limitation of the PE method (see Fig. 4.11). We first investigate how accurate the CNPE and GFPE methods can reproduce the exact field of the relative sound pressure level shown in Fig. 3.5, for a rigid ground surface and a non-refracting atmosphere ($b = 0$). The CNPE field is shown in Fig. 4.16 and the GFPE field is shown in Fig. 4.17. We see that the GFPE method is accurate up to high elevation angles, while the CNPE method is accurate only up to about 30° or 40°. Figure 4.18 shows the relative sound pressure level along a horizontal line at a height of 50 m in the fields shown in Figs. 3.5, 4.16, and 4.17.

It should be noted that we used a high-order starting function for the GFPE field (order 8, see Sec. H.10). The accuracy for large elevation angles decreases with decreasing order of the starting function.

From Figs. 4.16 to 4.18 we conclude that, for a non-refracting atmosphere, the GFPE method is more accurate than the CNPE method, at high elevation angles. Figure 4.19 shows an example which suggests that this conclusion is valid also for a refracting atmosphere. The figure shows a graph of the relative sound pressure level as a function of elevation angle, for a fixed receiver range of 400 m. In this example we used a linear sound speed profile $c(z) = c_0 + az$, with $c_0 = 340$ m/s and $a = 0.1$ s^{-1}. For comparison, the result for a non-refracting atmosphere ($a = 0$) is also included. FFP results and GFPE results agree up to high angles, while CNPE results deviate for angles larger than about 30°.

4.6.3 Accuracy of the axisymmetric approximation

With the three-dimensional GFPE method we can study the accuracy of the axisymmetric approximation, which is used in the two-dimensional methods (*cf.* Sec. 4.6.1). As an example, Fig. 4.20 shows the field of the relative sound pressure level at a height of 2 m, in a *horizontal* circular region around the source at position $(x, y) = (0, 0)$ and a height of 2 m. We assumed a wind vector in the positive x direction (as indicated in the figure) and a logarithmic wind speed profile $u(z) = b_u \ln(1 + z/z_0)$, with $b_u = 1$ m/s and $z_0 = 0.1$ m. The corresponding effective sound speed profile is $c(z) = c_0 + u(z)\cos\phi$, where $\phi = \arctan(y/x)$ is the azimuthal angle of the source-receiver line. The profile

is downward refracting for receivers in the region $x > 0$ and upward refracting for receivers in the region $x < 0$. This results in an acoustic shadow in the region $x < 0$, with low sound pressure levels, and higher levels in the region $x > 0$. In the shadow very low levels occur, much lower than the lower limit of the grey level scale of -30 dB. In Chap. 5 we will see that in reality the levels in the shadow are much higher, typically $\Delta L \approx -20$ dB, as a consequence of atmospheric turbulence.

The sound pressure field shown in Fig. 4.20 is clearly not axisymmetric. To study the effect of the axisymmetric approximation, we have also computed the field with the two-dimensional GFPE method. In this case the three-dimensional field was determined by combining two-dimensional fields in vertical rz planes with azimuthal angle ϕ varying between $\phi = 0°$ and $\phi = 360°$. If we ignore levels below -30 dB in the shadow region, the maximum deviation from the three-dimensional field shown in Fig. 4.20 is 0.4 dB. Therefore, the axisymmetric approximation is an accurate approximation in this case. In situations with larger azimuthal sound speed gradients, the axisymmetric approximation may be less accurate (*cf.* Sec. K.4).

4.6.4 Atmospheric refraction

Figure 4.21 shows the field of the relative sound pressure level for the logarithmic sound speed profile (4.5) with $b = 1$ m/s, computed with the GFPE method. The deviation from the field for $b = 0$ shown in Fig. 4.17 is small, except near the ground surface. Atmospheric refraction has large effects near the ground surface.

Figure 4.22 shows the field for the same situation with b = -1 m/s. In this case the atmosphere is upward refracting, which results in a sound shadow. In practice, the low levels in the shadow region are considerably affected by atmospheric turbulence (see Chap. 5).

Figure 4.23 shows 1/3-octave band spectra of ΔL for four receiver ranges (30, 100, 300, and 1000 m) and an absorbing ground surface. Figure 4.24 shows corresponding spectra for a rigid ground surface. We used the logarithmic sound speed profile (4.5) with $b = 1$ m/s, $b = 0$ m/s, and b = -1 m/s. For the absorbing ground surface we see that downward refraction has a considerable effect on the interference minimum. For the rigid ground surface we see that downward refraction causes high levels at the ranges 300 and 1000 m. Upward refraction causes low levels in the shadow region, both for the absorbing ground surface and for the rigid ground surface.

Figure 4.25 shows an example of the variation of the relative sound pressure level up to a range of 10 km, for an absorbing and a rigid ground surface, and $b = 0$ and $b = 1$ m/s. For the rigid ground surface and $b = 1$ m/s we see that the relative sound pressure level increases linearly with $\lg r$. This was explained at the end of Sec. 4.4 by the fact that the number of sound rays increases linearly with r. The figure shows also the simple prediction represented by Eq. (4.10): $\Delta L = 10 \lg N_{\text{rays}}$, where $N_{\text{rays}} = 4h_1/z_s$ is the number of rays. The simple

prediction is in fair agreement with the PE result for $b = 1$ m/s.

4.6.5 Accuracy of the ray model

Figures 4.26 and 4.27 show comparisons between PE results and results of the ray model described in Appendix L [135]. The CNPE and GFPE methods give equal results in this case. The PE results can be considered accurate, so the comparisons give an indication of the accuracy of the ray model.

Figure 4.26 shows 1/3-octave band spectra of ΔL for an absorbing ground surface and a downward refracting atmosphere with a linear sound speed profile $c(z) = c_0 + az$, with $a = 0.1$ s^{-1}. The agreement between the PE results and the results of the ray model is good.

Figure 4.27 shows 1/3-octave band spectra of ΔL for a linear sound speed profile (the same profile as used for Fig. 4.26) and a logarithmic sound speed profile [given by Eq. (4.5) with $b = 1$ m/s and $z_0 = 0.1$ m]. Again the agreement between PE results and results of the ray model is good for the linear profile, but for the logarithmic profile the results of the ray model deviate from the PE results below a frequency of about 300 Hz. The fact that the ray model is more accurate for the linear profile than for the logarithmic profile can be attributed to the large gradients of the logarithmic profile near the ground surface. The gradient of the logarithmic profile at $z = 0$ is 10 s^{-1}, which is a factor of 100 larger than the gradient $a = 0.1$ s^{-1} of the linear profile.

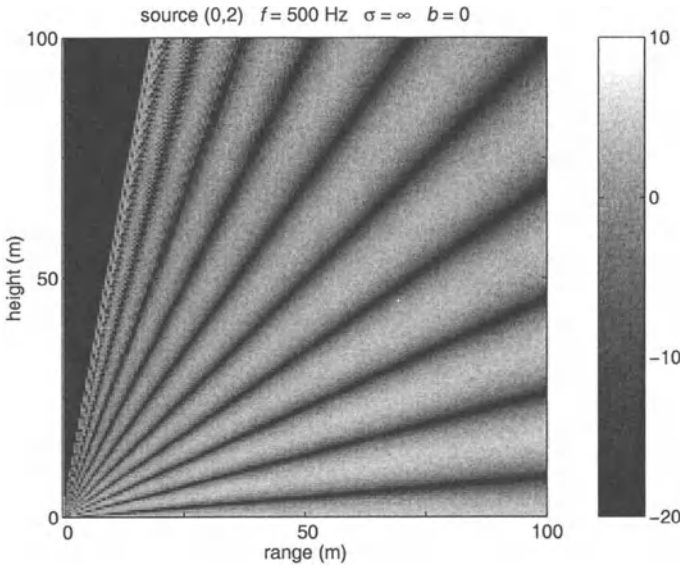

Figure 4.16. Field of the relative sound pressure level for $b = 0$, computed with the CNPE method. The level in dB is represented by the grey level scale.

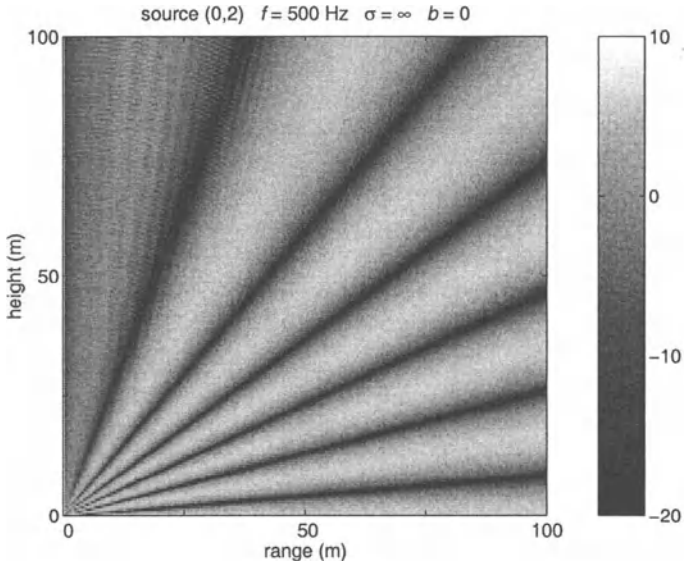

Figure 4.17. Field of the relative sound pressure level for $b = 0$, computed with the GFPE method.

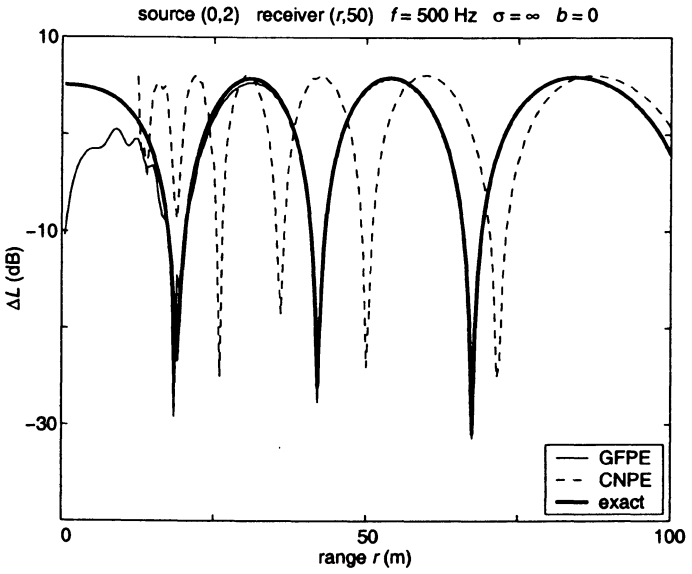

Figure 4.18. Relative sound pressure level as a function of range, for a receiver height of 50 m.

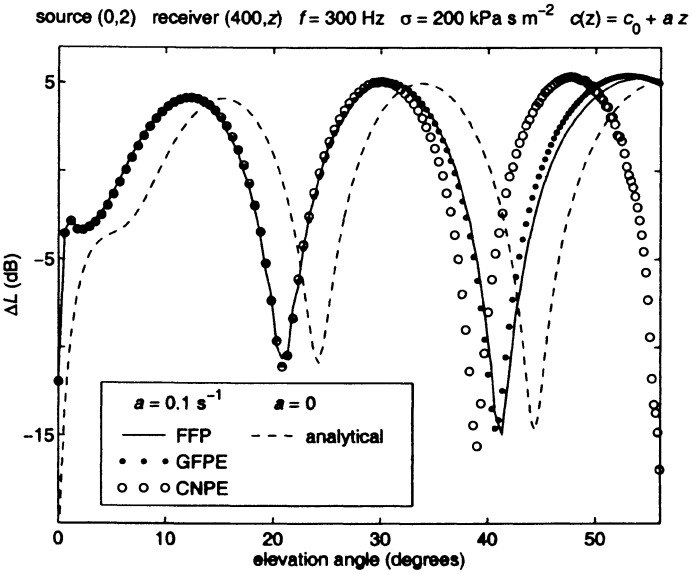

Figure 4.19. Relative sound pressure level as a function of elevation angle $\gamma = \arctan[(z - z_s)/r]$, for receiver range $r = 400$ m.

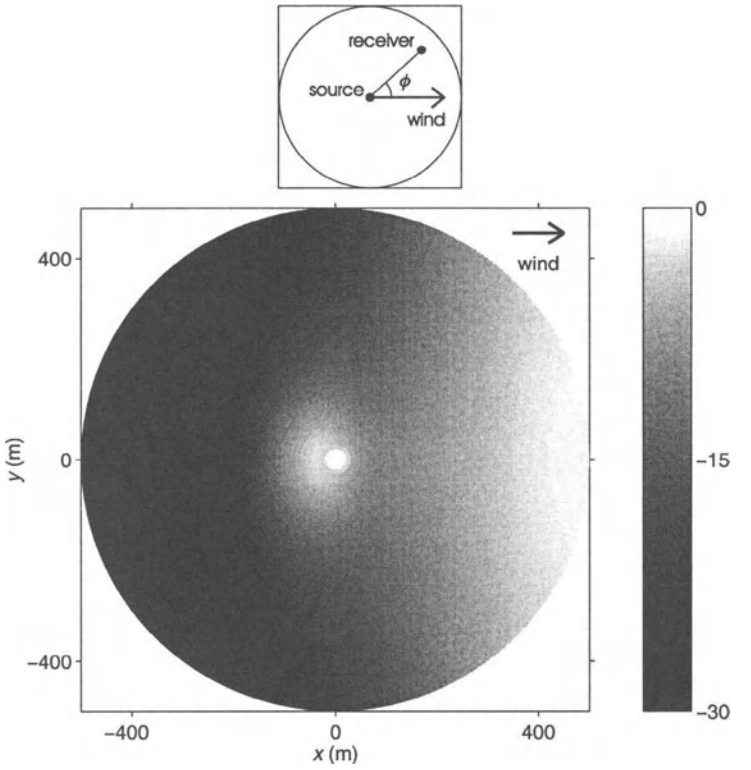

Figure 4.20. Field of the relative sound pressure level computed with the three-dimensional GFPE method, at a height of 2 m, in a ***horizontal*** circular region around the source at $(x, y) = (0, 0)$. The source height is 2 m, the frequency is 400 Hz, and the flow resistivity of the ground surface is 200 kPa·s·m^{-2}. The effective sound speed profile is $c(z) = c_0 + u(z)\cos\phi$, where $\phi = \arctan(y/x)$ is the azimuthal angle and $u(z) = b_u \ln(1 + z/z_0)$ is the wind speed profile, with $b_u = 1$ m/s and $z_0 = 0.1$ m. This profile corresponds to a wind vector in the positive x direction, as indicated in the figure.

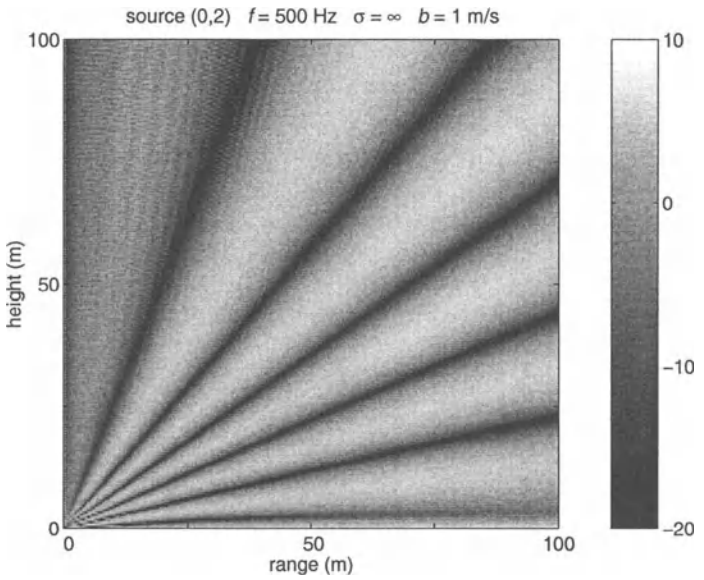

Figure 4.21. Field of the relative sound pressure level for $b = 1$ m/s, computed with the GFPE method.

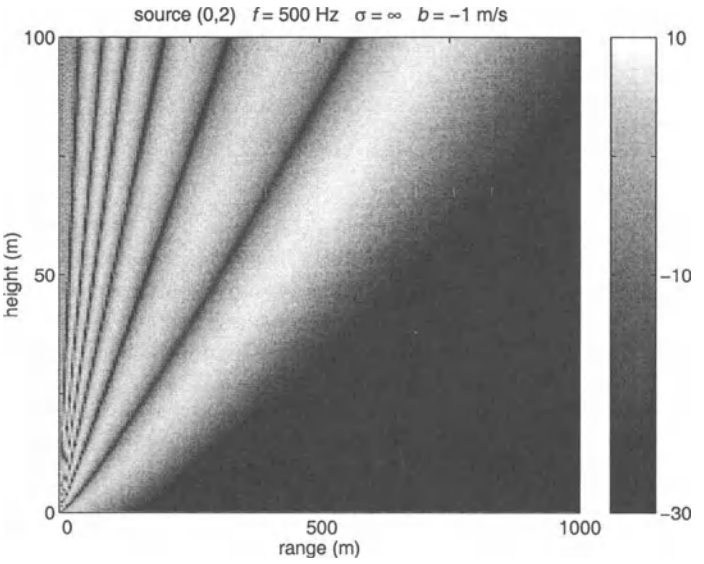

Figure 4.22. Field of the relative sound pressure level for $b = -1$ m/s, computed with the GFPE method. Note that the range scale is larger than in Fig. 4.21.

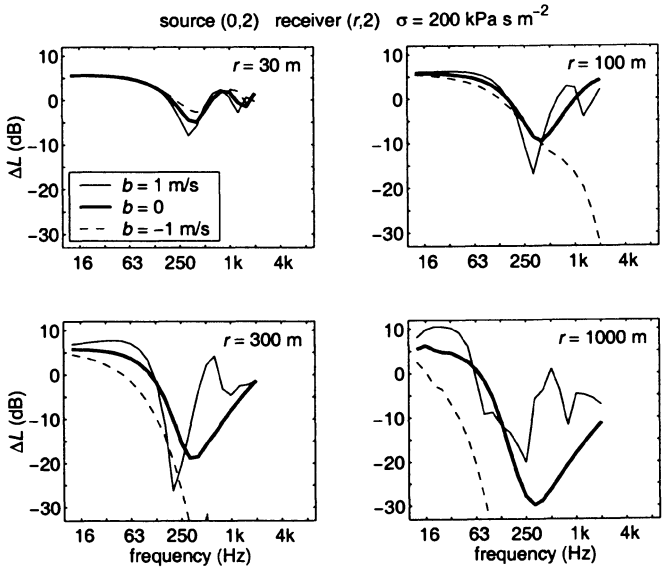

Figure 4.23. One-third-octave band spectra of the relative sound pressure level for an absorbing ground surface, computed with the CNPE method.

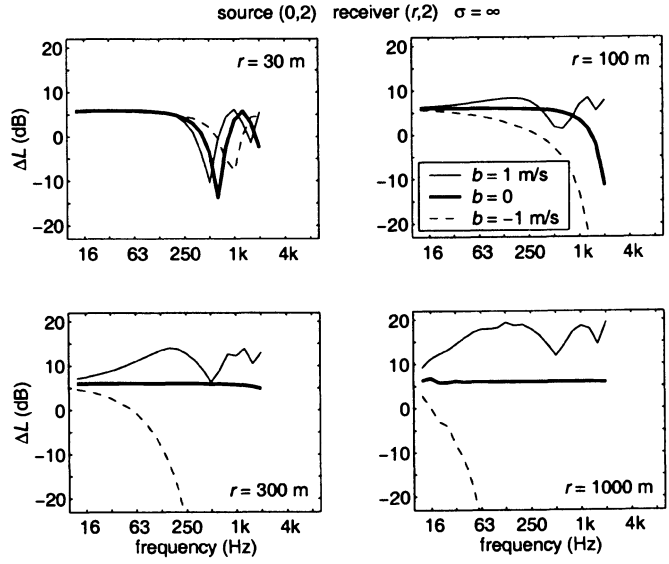

Figure 4.24. One-third-octave band spectra of the relative sound pressure level for a rigid ground surface, computed with the CNPE method.

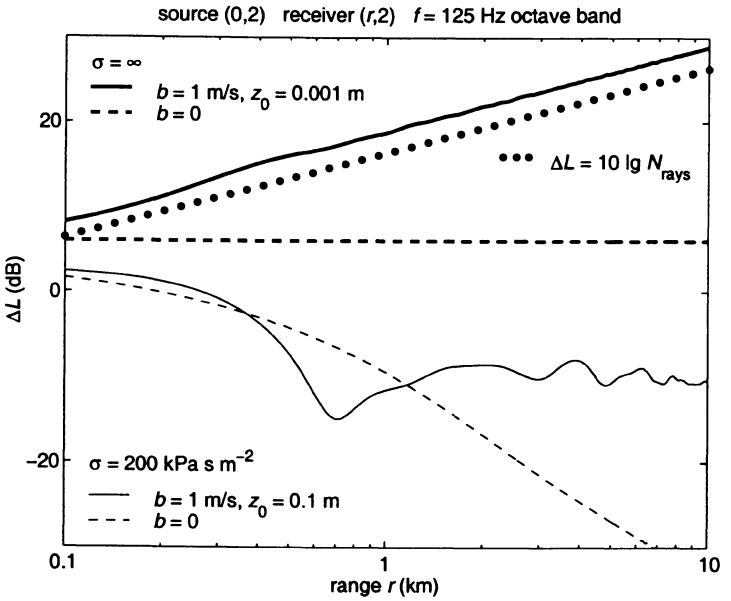

Figure 4.25. Relative sound pressure level as a function of range, computed with the CNPE method for the 125 Hz octave band. Thick lines are for a rigid ground surface and thin lines are for an absorbing ground surface, as indicated in the legends. The dotted line represents Eq. (4.10) for $b = 1$ m/s and a rigid ground surface. For the rigid ground surface we assumed a roughness length of $z_0 = 0.001$ m, appropriate for a water surface, instead of $z_0 = 0.1$ m.

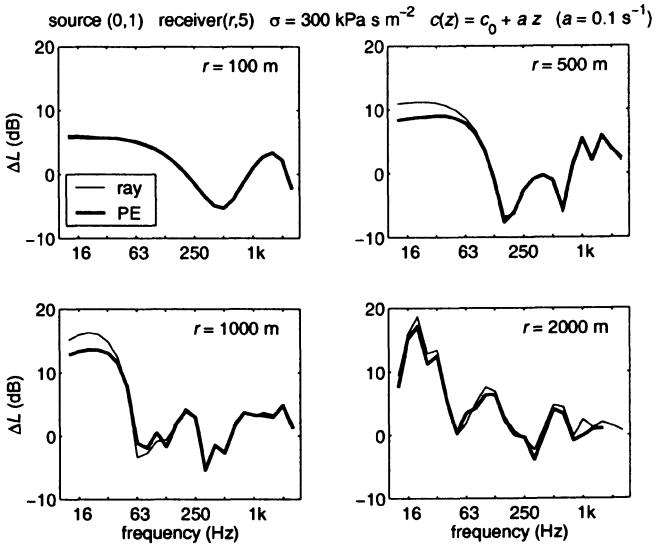

Figure 4.26. One-third-octave band spectra of the relative sound pressure level, computed with the ray model and with the PE method (the CNPE and GFPE methods give equal results), for a linear sound speed profile.

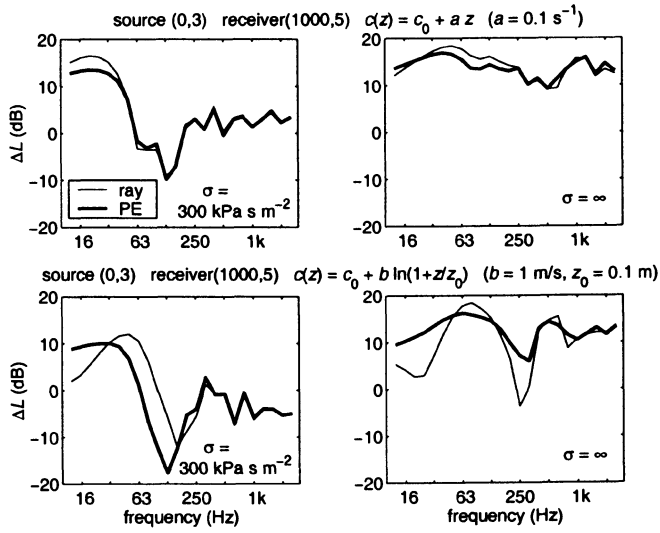

Figure 4.27. One-third-octave band spectra of the relative sound pressure level, computed with the ray model and with the PE method, for a linear sound speed profile (upper graphs) and a logarithmic sound speed profile (lower graphs).

Chapter 5

Atmospheric turbulence

5.1 Introduction

In the previous chapter we described sound propagation in a refracting atmosphere. For the vertical profiles of the temperature, the wind velocity, and the (effective) sound speed we used smooth functions of height [see Eqs. (4.5), (4.12), (4.13), and (4.14); see also Appendix N]. These profiles should be considered as average profiles, averaged over a period of typically ten minutes.

On time scales of seconds or minutes, the temperature and the wind velocity show considerable fluctuations around the average values. These fluctuations are commonly referred to as atmospheric turbulence (see Appendix I). Due to atmospheric turbulence, the instantaneous profiles of the temperature and the wind velocity are not smooth functions of height. The turbulent fluctuations of the temperature and the wind velocity have a considerable effect on atmospheric sound propagation, as will be described in this chapter.

In Sec. 5.2 we describe the effect of atmospheric turbulence on sound propagation in a non-refracting atmosphere. The description is based on an analytical model for sound propagation in a non-refracting turbulent atmosphere, which is described in detail in Appendix K. In Sec. 5.3 we study the effect of turbulence on sound propagation in a refracting atmosphere. We describe qualitatively how turbulence is taken into account in the PE method. A detailed description of the PE method for a turbulent atmosphere is given in Appendix J. In Sec. 5.4 we present numerical examples that illustrate the effects of turbulence on sound propagation.

5.2 Non-refracting turbulent atmosphere

In a non-refracting turbulent atmosphere, the *average* atmosphere (averaged over a period of typically ten minutes) is non-refracting, so the average (effective) sound speed is independent of position in the atmosphere. Turbulence causes

E. M. Salomons, *Computational Atmospheric Acoustics*

fluctuations of the instantaneous sound speed around the average value.

In Chaps. 3 and 4 we have seen that sound propagation in a non-refracting *non-turbulent* atmosphere can be modeled with two sound rays, the direct ray from the source to the receiver and the ray reflected by the ground surface (see Fig. 3.2). The interference between the direct ray and the reflected ray causes characteristic minima in the spectrum of the relative sound pressure level (see Sec. 3.5). Atmospheric turbulence reduces the depth of the interference minima [67], as will be explained in the following two paragraphs.

We assume that sound propagation in a non-refracting turbulent atmosphere can still be modeled with a straight direct sound ray and a straight reflected sound ray. This means that we neglect small deformations of the straight rays due to refraction by turbulent sound speed fluctuations. Turbulence is taken into account only by phase and amplitude fluctuations of the sound waves traveling along the ray paths.

The turbulent phase fluctuations are particularly important for the interference minima in the spectrum. An interference minimum occurs at a frequency for which direct and reflected waves have a phase difference of 180°, which means that the waves (partially) cancel each other. The phase fluctuations of the direct and reflected waves cause fluctuations of the frequency of the interference minimum. In other words, the interference minimum shifts more or less randomly within a limited frequency interval. Logarithmic averaging (see Sec. 3.4) over time results in a reduction of the depth of the interference minimum.

In Appendix K we describe an analytical model for the computation of the time-averaged sound pressure level in a non-refracting turbulent atmosphere. The model is based on a statistical method for averaging over the turbulent phase and amplitude fluctuations of the direct and reflected sound waves.

5.3 Refracting turbulent atmosphere

In the previous section we explained that, in a non-refracting atmosphere, atmospheric turbulence causes a reduction of the depth of the interference minima. In a downward refracting atmosphere, the effect of turbulence is similar. In a downward refracting atmosphere, the spectrum of the sound pressure level also has characteristic interference minima, due to interference between sound rays from the source to the receiver. The number of rays in a downward refracting atmosphere, however, is usually considerably larger than two.

Thus, the effect of turbulence in a downward refracting turbulent atmosphere is also a reduction of the depth of the interference minima. The analytical two-rays model for a non-refracting turbulent atmosphere described in Appendix K can be generalized to a multi-rays model for a downward refracting turbulent atmosphere [81, 131] (see Sec. L.5).

In an upward refracting atmosphere, the effect of turbulence is completely different. Upward refraction results in a shadow region, *i.e.* a region where no sound rays arrive (see Fig. 4.5). Figures 4.20 and 4.22 show that the relative

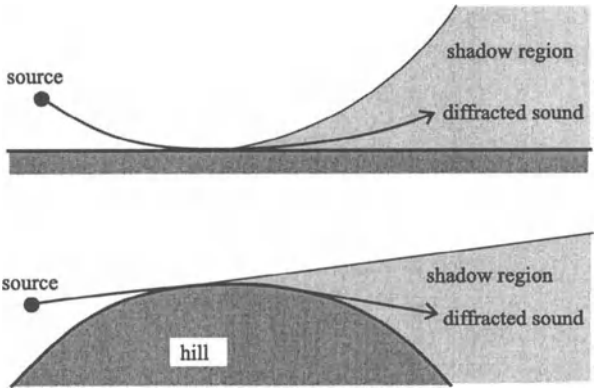

Figure 5.1. Diffraction of sound into a refractive shadow region is analogous to diffraction of sound into a shadow region behind a hill.

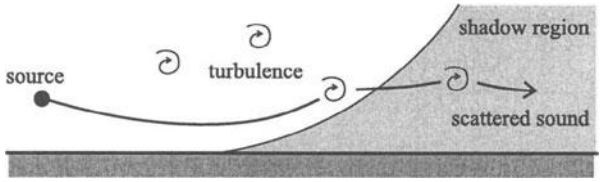

Figure 5.2. Scattering of sound into a refractive shadow region. Four turbulent inhomogeneities (eddies) are shown.

sound pressure level in a refractive shadow region in a non-turbulent atmosphere is very low; in fact, the level well inside the shadow region is much lower than the lower limit of −30 dB of the grey level scale used in the figures. Sound penetrates into a refractive shadow region in a non-turbulent atmosphere only by sound waves that can be considered as *diffracted* sound waves, as the penetration of sound waves into the refractive shadow region is analogous to the diffraction of sound waves into the shadow region behind a hill (see Fig. 5.1).

Atmospheric turbulence causes a large increase of the low levels in a refractive shadow region. The mechanism responsible for the effect of turbulence in a refractive shadow is usually described as scattering by turbulent inhomogeneities in the atmosphere (see Fig. 5.2). The scattering can be considered as small-scale refraction. Sound waves are scattered into a refractive shadow region by small random changes of the propagation direction.

The effect of turbulence in a refractive shadow region will be illustrated in Sec. 5.4 by numerical examples. Typically, we find relative sound pressure levels around −20 dB in a refractive shadow region, instead of the levels well below

−30 dB in a non-turbulent atmosphere. Experimental data confirm the typical value of −20 dB [157, 101, 102].

The PE methods described in Chap. 4 for sound propagation in a refracting non-turbulent atmosphere can also be applied to sound propagation in a refracting turbulent atmosphere. This is described in detail in Appendix J. Basically, the approach is as follows.

Using a random number generator, we calculate random fluctuations of the sound speed and add these to the average sound speed values corresponding to the average, smooth sound speed profile. In this way we generate random realizations of the fluctuating sound speed field in the turbulent atmosphere. The random realizations can be considered as 'snapshots' of the turbulent atmosphere.

First we compute sound propagation for the different random realizations with the PE method. Next we calculate average sound pressure levels by logarithmic averaging of the sound pressure levels computed for the different realizations. Thus, averaging over time is replaced by ensemble averaging over random realizations of the turbulent atmosphere.

For the calculation of the random realizations we make use of a quantity that is equivalent to the (effective) sound speed: the (acoustic) *refractive index* $n = c_0/c$, where c is the sound speed and c_0 is a constant sound speed. As sound speed fluctuations are relatively small, the value of the refractive index is of the order of unity and fluctuations of the refractive index are small compared to unity.

A statistical description of the refractive-index fluctuations is given in Appendix I. An important statistical quantity is the spatial correlation function of refractive-index fluctuations. In the literature on wave propagation in the turbulent atmosphere, various mathematical forms are given for this correlation function. The correlation function is used in the calculation of random realizations of the turbulent atmosphere (see Appendix J).

5.4 Examples

Figure 5.3 illustrates the effect of turbulence on sound propagation in a non-refracting atmosphere. The figure shows a graph of the relative sound pressure level as a function of receiver range, with a characteristic interference minimum (analogous to the interference minimum in the spectrum, *i.e.* the relative sound pressure level as a function of frequency). The interference minimum is considerably reduced by turbulence, as explained in Sec. 5.2. For the turbulence we used the Gaussian correlation function $B(r) = \mu_0^2 \exp(-r^2/a^2)$ of refractive-index fluctuations, with the values $a = 1.1$ m and $\mu_0^2 = 10^{-5}$, which represent relatively strong turbulence (see Secs. I.7.1 and I.7.2). The figure shows both PE results and analytical results. The PE results for the turbulent atmosphere were computed with the CNPE method, and were averaged over 500 random realizations [139]. The analytical results for the turbulent atmosphere were cal-

culated with the model described in Appendix K [Equation (K.6)]. The figure shows good agreement between PE results and analytical results.

Figures 5.4 and 5.5 illustrate the effect of turbulence on 1/3-octave band spectra of the relative sound pressure level in a non-refracting atmosphere, for a rigid ground surface and an absorbing ground surface, respectively. The spectra were calculated with the analytical model described in Appendix K [Equation (K.6)]. For the turbulence we used the von Kármán spectrum of refractive-index fluctuations, with parameters K_0^{-1}, C_T^2/T_0^2, and C_v^2/c_0^2 (see Sec. I.7.2).

Figure 5.6 illustrates the effect of turbulence for an upward refracting atmosphere with a shadow region. Comparison with the corresponding graph in Fig. 4.22 for a non-turbulent atmosphere shows that the level in the shadow region is enhanced by turbulence. The field was averaged over 50 random realizations of the turbulent atmosphere.

Figure 5.7 shows a graph of the relative sound pressure level along a horizontal line in the field shown in Fig. 5.6, at height $z = 2$ m. In the shadow region, the relative sound pressure level is constant, in good approximation. For comparison, the result for a non-turbulent atmosphere (from Fig. 4.22) is also shown.

Figure 5.8 shows a similar graph for the frequency of 125 Hz. For the computation of the levels shown in this graph we used the CNPE method with a range step Δr of 0.25 m and the GFPE method with two values of Δr: 10 and 20 m. All results are in good agreement with each other. The advantage of the GFPE method over the CNPE method that larger range steps are possible (see Sec. 4.5) is preserved in a turbulent atmosphere.

Figure 5.9 illustrates the effect of atmospheric turbulence on 1/3-octave band spectra that were presented for non-turbulent atmospheres in Figs. 4.23 and 4.24. In general, the effect of turbulence is larger for low levels than for high levels.

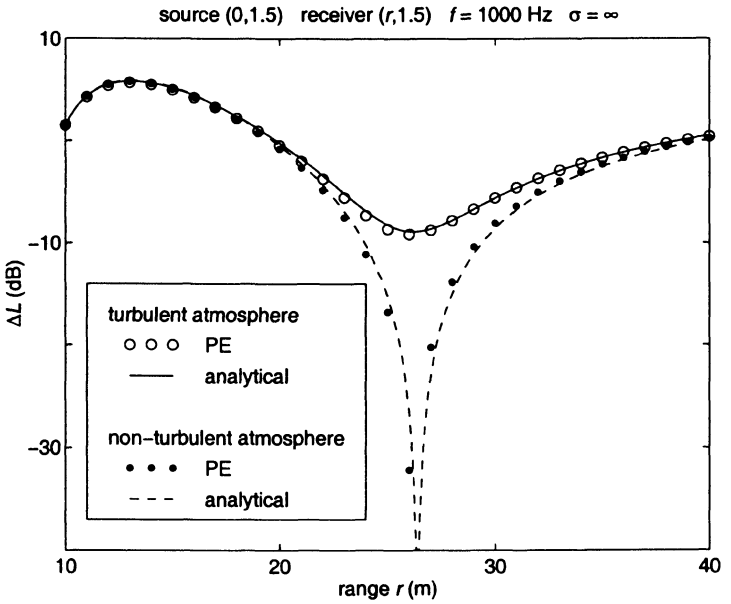

Figure 5.3. Relative sound pressure level as a function of range, for a non-refracting atmosphere with and without turbulence. Analytical results for the turbulent atmosphere were calculated with Eq. (K.6). PE results for the turbulent atmosphere were averaged over 500 random realizations. For the turbulence we used the Gaussian correlation function $B(r) = \mu_0^2 \exp(-r^2/a^2)$ with $a = 1.1$ m and $\mu_0^2 = 10^{-5}$.

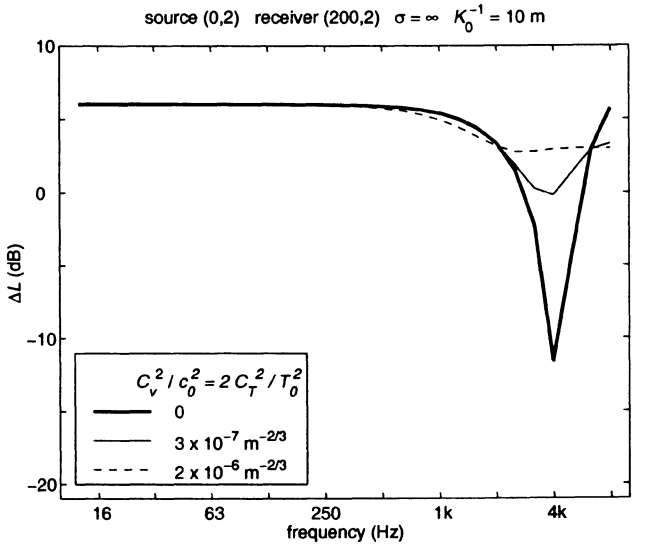

Figure 5.4. One-third-octave band spectra of the relative sound pressure level, for a non-refracting atmosphere and a rigid ground surface. The thick curve is for a non-turbulent atmosphere. The thin curves are for turbulent atmospheres with a von Kármán spectrum for a moving atmosphere with $C_v^2/c_0^2 = 2C_T^2/T_0^2$.

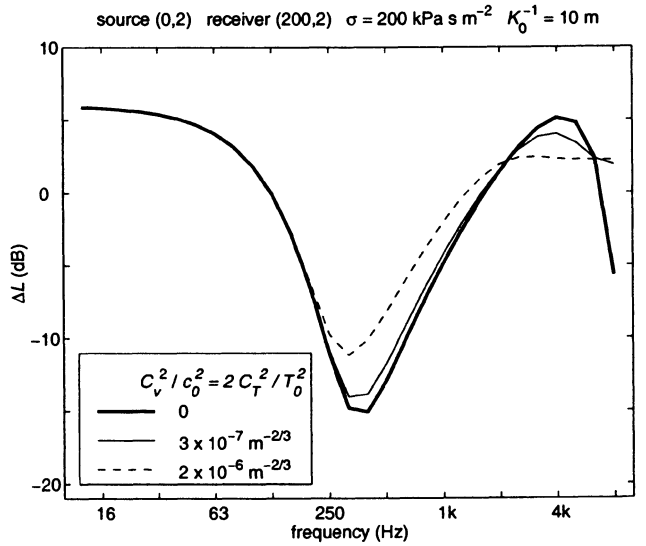

Figure 5.5. As Fig. 5.4, for an absorbing ground surface.

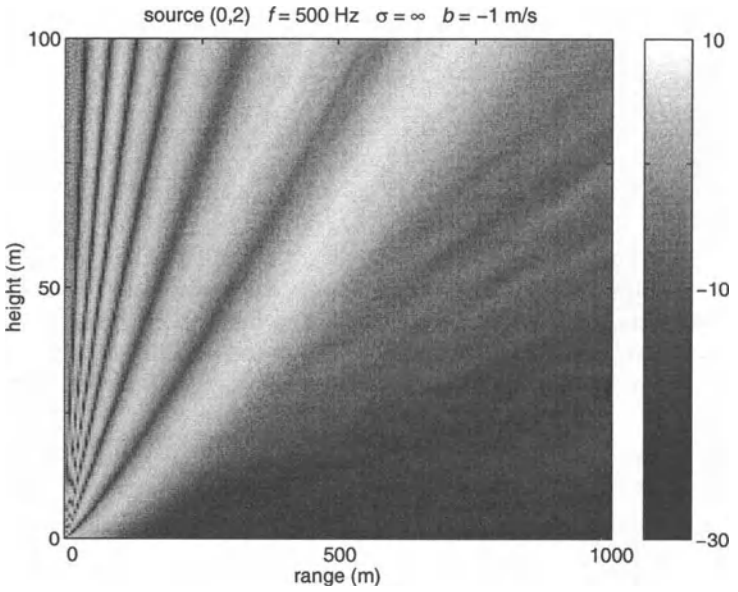

Figure 5.6. Field of the relative sound pressure level computed with the GFPE method for the logarithmic sound speed profile (4.5) with $b = -1$ m/s. The field was averaged over 50 random realizations of a turbulent atmosphere, with a von Kármán spectrum with parameters $K_0^{-1} = 10$ m, $C_T^2/T_0^2 = 2.5\times10^{-7}$ m$^{-2/3}$, and $C_v^2/c_0^2 = 1\times10^{-6}$ m$^{-2/3}$.

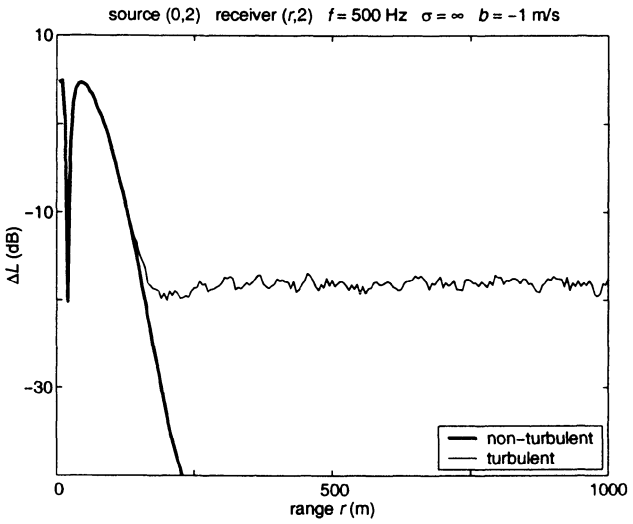

Figure 5.7. Relative sound pressure level along a horizontal line at height $z = 2$ m in the field shown in Fig. 5.6 for a turbulent atmosphere (thin line) and the field shown in Fig. 4.22 for a non-turbulent atmosphere (thick line).

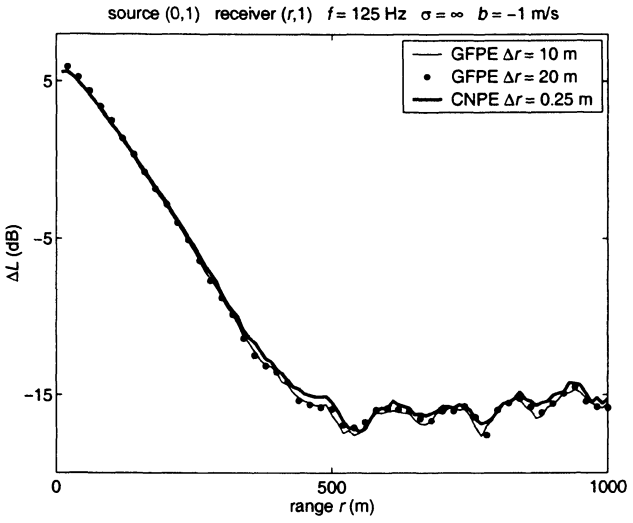

Figure 5.8. Relative sound pressure level as a function of range, computed with the CNPE and GFPE methods for different values of the range step Δr. The levels were averaged over 50 random realizations of a turbulent atmosphere with the same parameters as for Fig. 5.6.

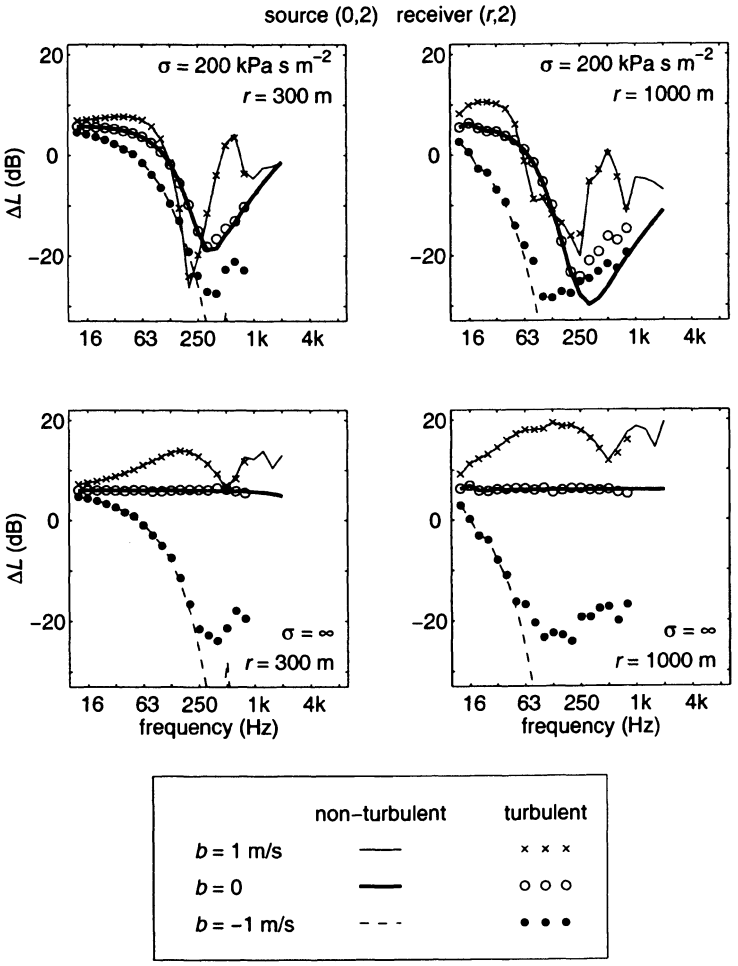

Figure 5.9. One-third-octave band spectra of the relative sound pressure level, computed with the CNPE method for an absorbing ground surface (upper graphs) and a rigid ground surface (lower graphs). Spectra are shown for turbulent atmospheres with the same turbulence parameters as for Fig. 5.6 (averaged over 16 random realizations) and for non-turbulent atmospheres (from Figs. 4.23 and 4.24). For the sound speed profile we used Eq. (4.5), with values of the parameter b indicated in the legend.

Chapter 6

Irregular terrain

6.1 Introduction

In the previous chapters we assumed that the ground surface is perfectly flat. In practice, a ground surface is never perfectly flat. Natural ground surfaces, *e.g.* grassland, always show small variations of the ground level, and sometimes larger variations, such as hills. In this chapter we study the effect of smooth variations of the ground level. In Appendix M we describe computational methods for sound propagation over a ground surface with a smooth terrain profile.

In Sec. 6.2 we describe qualitatively the effects of a terrain profile on sound propagation. In Sec. 6.3 we present numerical examples that illustrate the effects.

6.2 Hills and other terrain profiles

The effect of a hill on sound propagation from a source near the ground is illustrated in Fig. 6.1. The hill can be considered as a barrier for sound waves, with a shadow region behind the hill. The shadow region is limited by the shadow boundary, which is also shown in Fig. 6.1.

The sound pressure levels in the shadow region depend on the dimensions of the hill, the position of the source, the frequency, and the atmospheric conditions. In general, the levels are enhanced by downward atmospheric refraction: sound waves travel along curved paths over the hill if the atmosphere is downward refracting. The levels are also enhanced by atmospheric turbulence: sound waves are scattered into the shadow region by atmospheric turbulence (*cf.* Sec. 5.3). In Sec. 6.3 we will illustrate these atmospheric effects by a numerical example.

The effect of a hill can also be considered in a different way. The hill shown in Fig. 6.2 consists of two concave ground segments and one convex ground segment. The convex curvature and the concave curvature have opposite effects

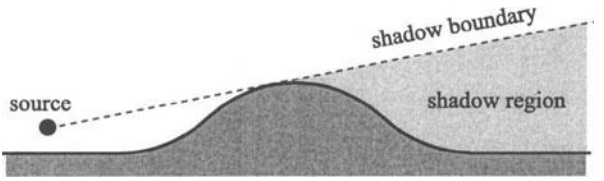

Figure 6.1. Shadow region behind a hill.

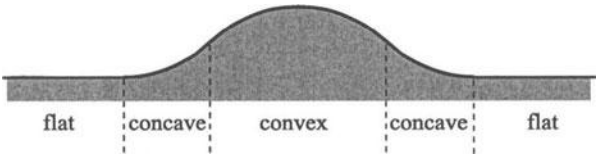

Figure 6.2. Hill consisting of two concave segments and one convex segment.

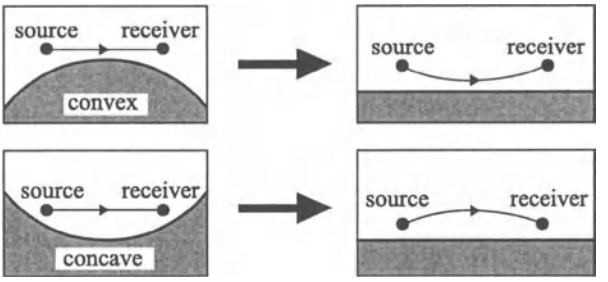

Figure 6.3. Ray illustration of the conformal mapping method for computing sound propagation over a curved ground surface. A convex ground curvature is transformed to an upward refracting contribution to the atmospheric sound speed profile; a concave ground curvature is transformed to a downward refracting contribution. To demonstrate the effect of the transformation on the sound speed profile, the figure shows the straight direct sound ray in the original systems and the corresponding curved sound rays in the transformed systems.

on sound propagation. This follows from the conformal mapping method, which is described in detail in Sec. M.2.

The conformal mapping method is based on a coordinate transformation that is called a conformal mapping. The conformal mapping transforms a system with a curved ground surface to a system with a flat ground surface and a modified sound speed profile. A convex curvature is transformed to an upward refracting contribution to the sound speed profile and a concave curvature is transformed to a downward refracting contribution to the sound speed profile. This is illustrated in Fig. 6.3.

Consequently, sound propagation over a convex or concave ground surface can be computed with the computational methods described in the previous chapters (the PE methods for example); first a conformal mapping is applied and next sound propagation is computed for the transformed system with a flat ground surface. This approach can also be applied to a terrain profile consisting of a 'chain' of convex and concave segments (*e.g.* the hill shown in Fig. 6.2), by applying a series of conformal mappings [43].

An alternate method for computing sound propagation over a smooth terrain profile is the Generalized Terrain PE (GTPE) method [129]. For a flat ground surface, the GTPE method is identical to the CNPE method (which is described in Appendix G). The GTPE method is described in Sec. M.3.

6.3 Examples

Figure 6.4 shows a comparison between results of the GTPE method and results of the conformal mapping method in combination with the GFPE method. The figure shows the relative sound pressure level as a function of receiver range, for sound propagation over a hill with a height of 10 m. The logarithmic sound speed profile (4.5) with $b = 1$ m/s was used (with height measured with respect to local ground level). This profile represents a downward refracting atmosphere. Other parameters are given in the figure. For comparison, the figure shows also results for the situation without the hill, *i.e.* for a flat ground surface. The agreement between the GTPE method and the conformal mapping method is good.

Figure 6.5 shows fields of the relative sound pressure level, computed with the conformal mapping method in combination with the GFPE method. The fields demonstrate that both downward refraction and atmospheric turbulence enhance sound pressure levels in the shadow region behind a hill.

Figure 6.6 illustrates the effect of surface roughness on sound propagation over water in a downward refracting atmosphere. For a flat water surface, the figure shows that the relative sound pressure level increases linearly with the logarithm of the range, as predicted by Eq. (4.10) (the curve for the flat surface in Fig. 6.6 was also shown in Fig. 4.25). For the rough surface we used a periodic oscillation with a wavelength of 25 m between $z = 0$ and $z = -0.5$ m. For ranges larger than about 1 km, the relative sound pressure level above the

rough surface is considerably lower than above the flat surface. This can be explained as follows. High levels above a flat surface are due to the fact that many rays with multiple reflections arrive at receiver positions near the surface. An example of such a ray is shown in Fig. 6.7. Above a rough surface the levels are lower, because many of the rays do not arrive at the receiver positions near the surface: rays that hit a surface section with a positive slope are reflected with large elevation angles. This is illustrated in Fig. 6.7.

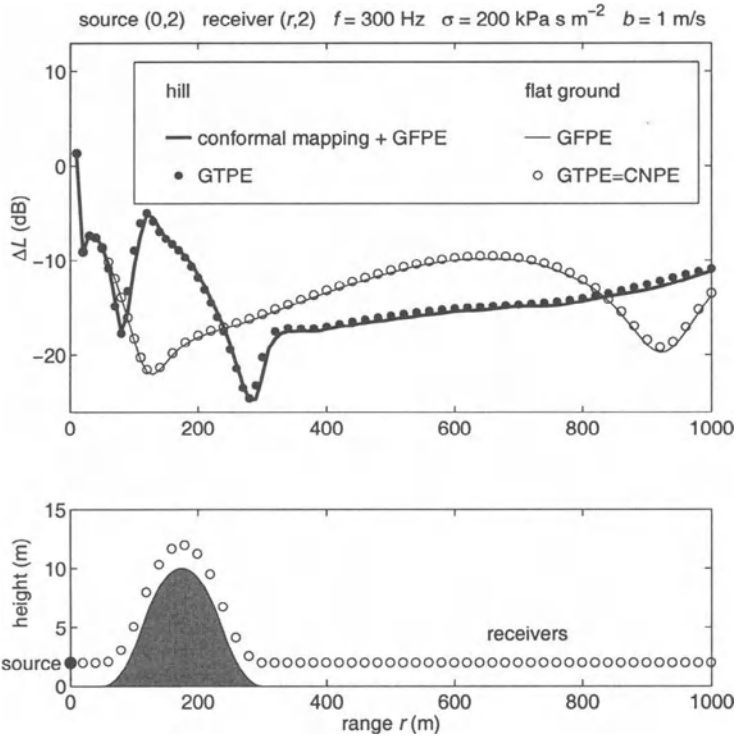

Figure 6.4. Comparison between results of the GTPE method and results of the conformal mapping method in combination with the GFPE method, for sound propagation over a hill. The geometry with the hill is indicated below the graph. For comparison, results for the situation without the hill (flat ground) are also shown. For a flat ground, the GTPE method is identical to the CNPE method. The receiver height is 2 m, measured with respect to local ground level.

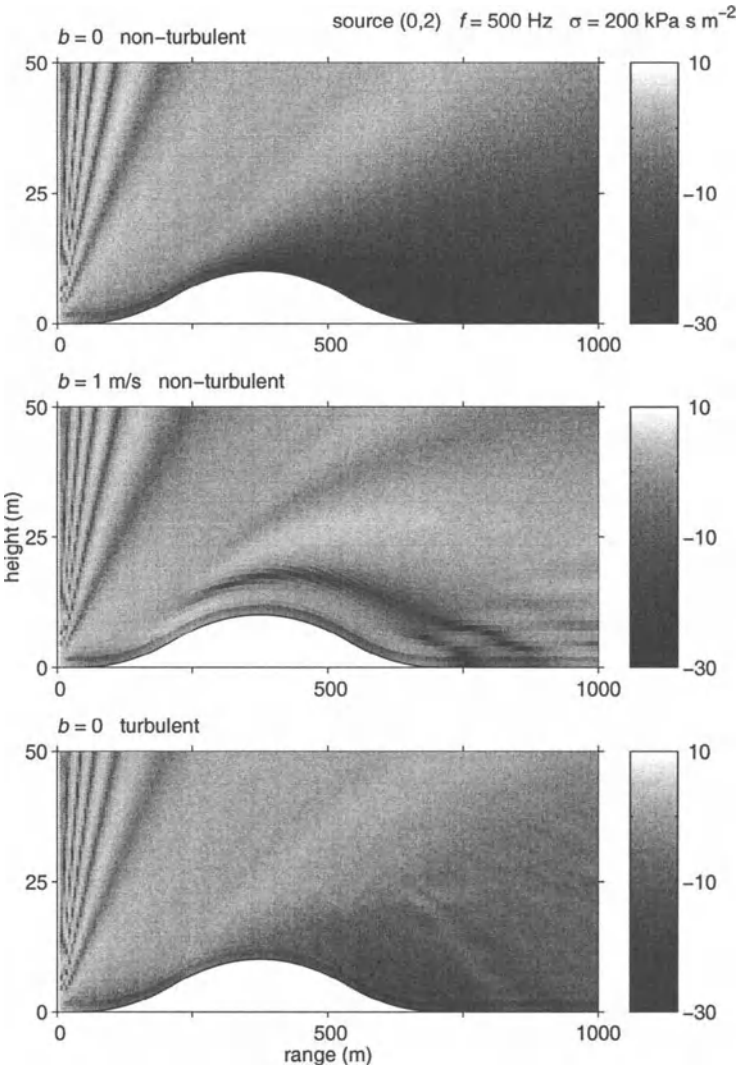

Figure 6.5. Fields of the relative sound pressure level, computed with the conformal mapping method in combination with the GFPE method, for a non-refracting non-turbulent atmosphere (upper graph), a downward refracting non-turbulent atmosphere (middle graph), and a non-refracting turbulent atmosphere (lower graph). For the refracting atmosphere we used the logarithmic profile (4.5) with $b = 1$ m/s. The sound field for the turbulent atmosphere was computed by averaging over 50 random realizations, using a von Kármán spectrum with parameters $K_0^{-1} = 10$ m, $C_T^2/T_0^2 = 2.5\times10^{-7}$ m$^{-2/3}$, and $C_v^2/c_0^2 = 1\times10^{-6}$ m$^{-2/3}$.

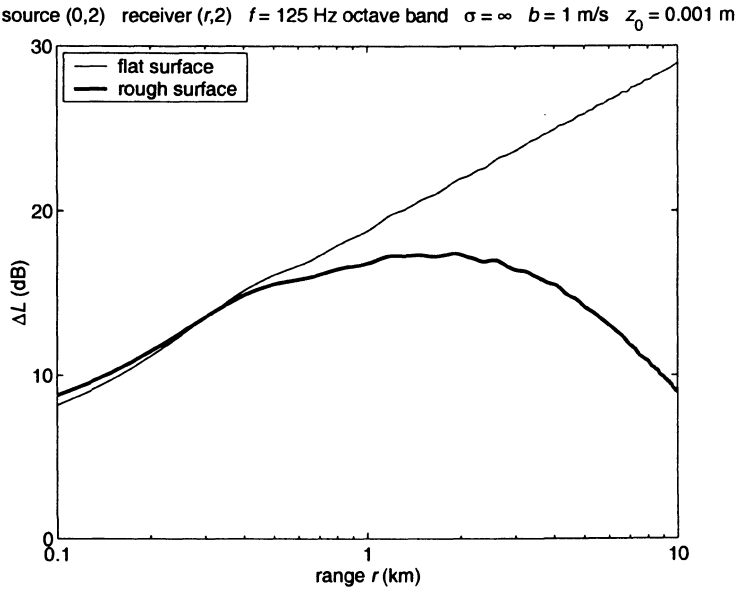

Figure 6.6. Relative sound pressure level as a function of range, averaged over the 125 Hz octave band, for propagation over a rigid flat surface and a rigid rough surface (*e.g.* water surfaces). For the rough surface we used a periodic oscillation with a wavelength of 25 m between $z = 0$ and $z = -0.5$ m. For the sound speed profile we used the logarithmic profile (4.5) with $b = 1$ m/s and $z_0 = 0.001$ m. For the computation we used the GTPE method.

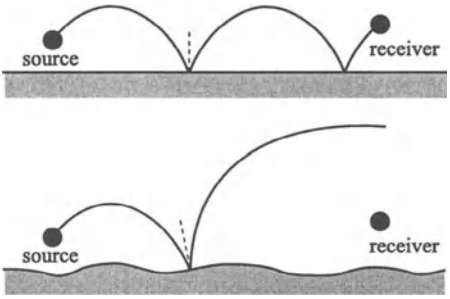

Figure 6.7. Top: example of a ray that reaches the receiver by two reflections at a flat surface. Bottom: the ray does not reach the receiver in a situation with a rough surface.

Chapter 7

Noise barriers

7.1 Introduction

Noise from a source near the ground can be reduced by means of a barrier between the source and the receiver. Noise barriers are widely used for the reduction of traffic noise. The simplest noise barrier is a vertical screen, *e.g.* a thin wall. In this chapter we describe computational methods for sound propagation over a vertical screen. In Appendix O we describe the computational methods in more detail. Experimental results for sound propagation over barriers can be found in Refs. [114, 71, 38, 117, 12].

In Sec. 7.2 we describe an analytical model for sound propagation over a screen in a non-refracting atmosphere. In Sec. 7.3 we describe the application of the PE method to sound propagation over a screen in a refracting atmosphere. In general, atmospheric refraction has large effects on sound propagation over a screen. The complex wind speed profile near a screen plays an important role in the refraction. This profile is also described in Sec. 7.3. In Sec. 7.4 we present numerical examples.

7.2 Non-refracting atmosphere

In Chap. 3 we have seen that sound propagation in a non-refracting atmosphere over a flat ground surface can be described with two sound rays: a direct ray and a ray reflected by the ground surface (see Fig. 3.2). We denote these rays as follows:
ray 1: source → receiver
ray 2: source → ground → receiver.
In a similar way, sound propagation over a screen on a ground surface, in a non-refracting atmosphere, can be described with four sound rays (see Fig. 7.1):
ray 1: source → screen top → receiver
ray 2: source → ground → screen top → receiver

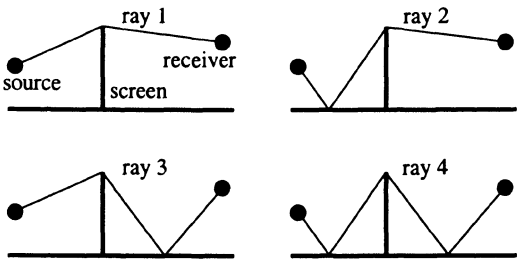

Figure 7.1. Four sound rays contributing to sound propagation over a screen on a ground surface, in a non-refracting atmosphere.

ray 3: source → screen top → ground → receiver
ray 4: source → ground → screen top → ground → receiver.
All four rays are diffracted by the screen top. Rays 2 and 3 are reflected once by the ground surface; ray 4 is reflected twice by the ground surface. In Sec. O.2 we give expressions for the contributions of the four rays to the complex pressure amplitude at the receiver. These expressions are based on a combination of the theory of reflection of spherical waves by a finite-impedance ground surface and the theory of diffraction of spherical waves by a screen.

We assume here that the receiver is below the shadow boundary of the source, *i.e.* the line through the source and the screen top. If the receiver is above the shadow boundary of the source, the direct ray (source → receiver) also contributes to the complex pressure amplitude at the receiver. If the receiver is above the shadow boundary of the image source (see Sec. O.2), the reflected ray (source → ground → receiver) also contributes.

7.3 Refracting atmosphere

In Chap. 4 we have seen that sound propagation in a refracting atmosphere over a ground surface can be computed with the PE method. Sound propagation over a screen on a ground surface, in a refracting atmosphere, can also be computed with the PE method. Both the CNPE method and the GFPE method can be used.

The basic approach of the PE method is a step-wise extrapolation of the field on a rectangular grid in the vertical plane through the source and the receiver. The effect of the screen can be taken into account by setting the field equal to zero at the grid points covered by the screen. This is equivalent to the Kirchhoff approximation of diffraction [142]. The application of the PE method to sound propagation over a screen is described in detail in Sec. O.3.

A noise screen has an effect not only on sound waves but also on the wind speed profile in the atmosphere. Wind speeds are low in the region behind the screen (on the downwind side) and high in the region just above the screen.

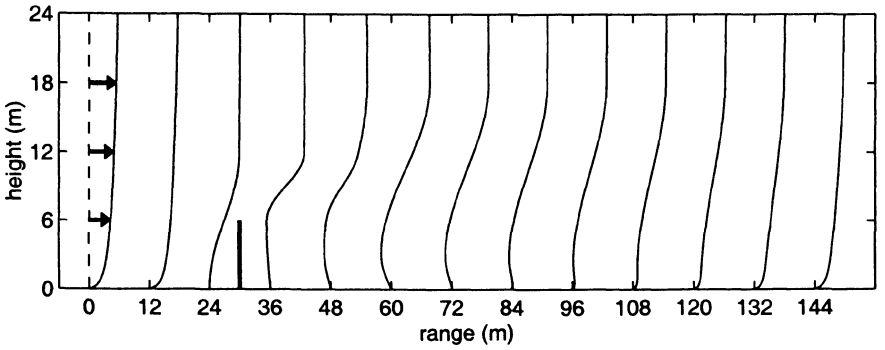

Figure 7.2. Wind speed profiles at ranges 0, 12, 24 ..., 144 m near a screen on a ground surface. The screen is located at range 30 m and has a height of 6 m. The profiles have been calculated with approximate relations given in Sec. O.4, for $z_0 = 0.1$ m and $u_{10} = 4$ m/s. The undisturbed logarithmic profile at range zero corresponds to a wind speed of 4 m/s at a height of 10 m.

This effect of a screen on the wind speed profile has an indirect effect on sound propagation over the screen.

Figure 7.2 shows an example of wind speed profiles near a screen. The profiles have been calculated with approximate analytical relations for the wind speed field near a screen [137], which are given in Sec. O.4. Far from the screen, an undisturbed logarithmic profile is assumed; this profile is shown in Fig. 7.2 at range zero. Near the screen, the profiles are disturbed by the screen. The profiles show large vertical wind speed gradients in the region near the screen top. These screen-induced wind speed gradients have a significant effect on sound propagation over a screen [118, 136, 137].

Sound propagation over a screen is also affected by atmospheric turbulence. The effect of turbulence is particularly important deep in the shadow region behind a screen [34, 53, 54]. This is analogous to the effect of turbulence in a refractive shadow (see Chap. 5). The PE method for a turbulent atmosphere (see Chap. 5) can be used to study the effect of turbulence on sound propagation over a screen.

7.4 Examples

Figure 7.3 shows 1/3-octave band spectra of the relative sound pressure level for sound propagation in a non-refracting atmosphere over a screen on a rigid ground surface. Figure 7.4 shows corresponding spectra for an absorbing ground surface. The figures show spectra for two screen heights, $H = 4$ m and $H = 8$ m. For comparison, the figures show also spectra for the situation without the

screen, indicated as $H = 0$. The spectra for $H > 0$ were computed with the analytical model described in Secs. 7.2 and O.2; the spectra for $H = 0$ were computed with the method described in Chap. 3.

As expected, the relative sound pressure levels for $H > 0$ are lower than for $H = 0$. In other words, the levels are reduced by the screens. The reduction is larger for $H = 8$ m than for $H = 4$ m (except in a narrow frequency interval in Fig. 7.3). At high frequency, the relative sound pressure level decreases with increasing frequency by (on average) 3 dB per octave; this simple behavior at high frequency can be derived from the diffraction solution used in the analytical model described in Sec. O.2 [106, 74], and also from well-known scale model results presented by Maekawa [86]. At lower frequency, around 250 Hz, the spectra show various interference minima, corresponding to interference between the four sound rays shown in Fig. 7.1. At very low frequency, all spectra approach the limiting value $\Delta L = 6$ dB, corresponding to a doubling of the acoustic pressure; in this frequency range, the wavelength is large compared with the screen height, so the screen is nearly 'invisible' for sound waves.

Figure 7.5 illustrates the effect of screen-induced wind speed gradients on sound propagation over a screen (see end of Sec. 7.3). The figure shows the relative sound pressure level as a function of range, computed with the CNPE method for three different sound speed profiles, indicated as (i), (ii), and (iii). Profile (i) is the profile shown in Fig. 7.2, with large wind speed gradients in the region near the screen top. Profile (ii) is the undisturbed logarithmic profile (also shown in Fig. 7.2, at range zero); profile (ii) ignores the effect of the screen on the wind speed profile. Profile (iii) represents a non-refracting atmosphere. For comparison, analytical results for the non-refracting atmosphere are also shown in Fig. 7.5; the analytical results are in good agreement with the PE results for the non-refracting atmosphere.

The PE results for the profiles (i) and (ii) deviate considerably from the results for the non-refracting atmosphere. This implies that atmospheric refraction has a significant effect on the propagation over the screen. Moreover, screen-induced wind speed gradients have a significant effect on the propagation over the screen, as the levels for profile (i) are considerably higher than the levels for profile (ii) (except for the 125 Hz octave band). The acronym RESWING (REfraction by Screen-induced WINd speed Gradients) is used for this effect [136].

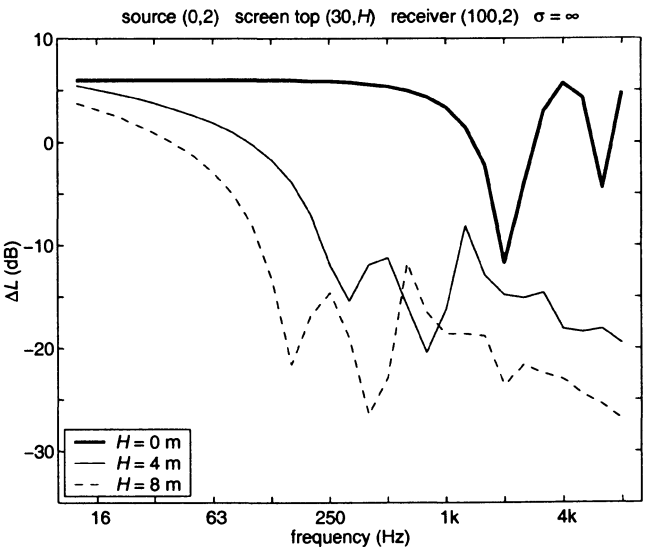

Figure 7.3. One-third-octave band spectrum of the relative sound pressure level, for sound propagation in a non-refracting atmosphere over a rigid ground surface with a screen. Results are shown for three screen heights H: 0, 4, and 8 m (see legend).

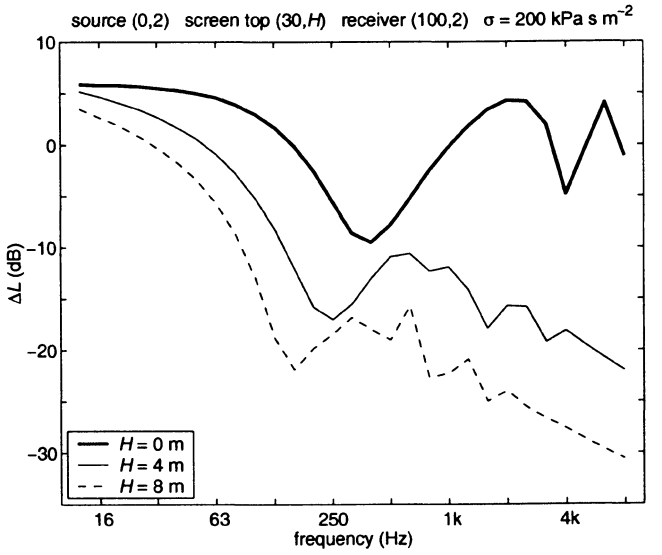

Figure 7.4. As Fig. 7.3, for an absorbing ground surface.

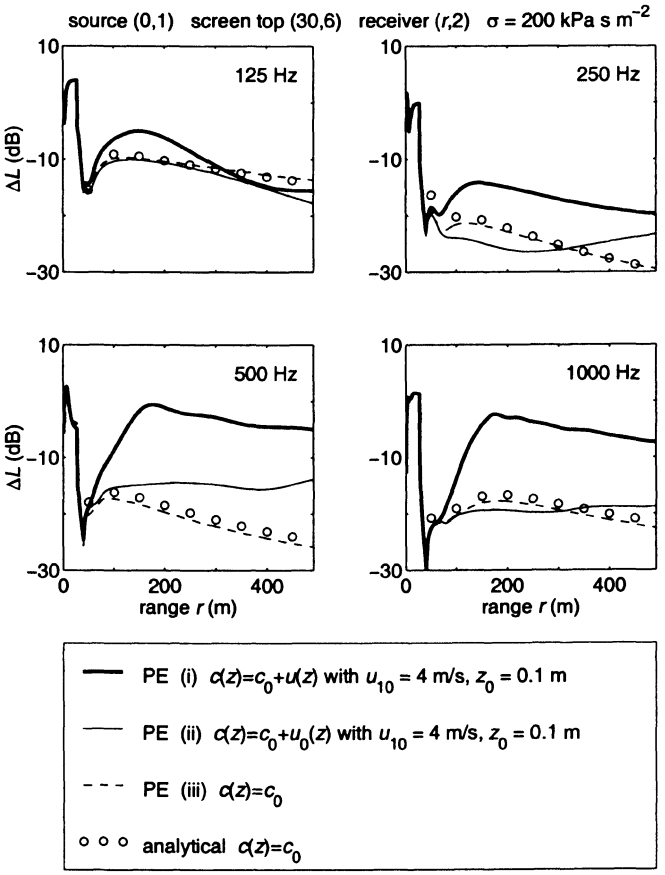

Figure 7.5. Relative sound pressure level as a function of range, for sound propagation over a screen on a ground surface [137]. PE results are shown for four octave bands and three sound speed profiles (see legend): (i) the profile $c(z) = c_0 + u(z)$ shown in Fig. 7.2, (ii) an 'undisturbed' logarithmic profile $c(z) = c_0 + u_0(z)$, and (iii) the profile $c(z) = c_0$ representing a non-refracting atmosphere. The functions $u(z)$ and $u_0(z)$, with parameters u_{10} and z_0, are given in Sec. O.4. A value of 340 m/s was used for c_0. For comparison, analytical results for the non-refracting atmosphere are also shown. The distance between the source and the screen is 30 m and the screen has a height of 6 m, as indicated above the graphs.

Appendix A

Basic acoustic equations for a homogeneous atmosphere

A.1 Introduction

The models described in this book are based on *linear acoustics*. In linear acoustics one assumes that the pressure fluctuations generated by a sound wave are small compared with the average pressure in the atmosphere. This is usually a good assumption. Nonlinear terms are important only for very loud sounds, such as the sound generated by an explosion.

In this appendix we derive the basic equations of linear acoustics for a homogeneous atmosphere [106, 107]. In Sec. A.2 we derive the *linear acoustic equations* and the *wave equation*, and we develop an expression for the adiabatic sound speed. In Sec. A.3 we derive the *Helmholtz equation* for harmonic sound waves. In Sec. A.4 we derive the inhomogeneous Helmholtz equation, which includes a Dirac delta function for a monopole source.

A.2 The linear acoustic equations and the wave equation

The atmosphere is modeled as a compressible fluid, *i.e.* a gaseous medium in which local pressure fluctuations cause local density fluctuations. When a sound wave travels through this medium, local pressure fluctuations and local density fluctuations are generated. The corresponding movement of the fluid is represented by a (fluctuating) fluid velocity.

The mathematical description of sound waves in the atmosphere follows from the equations of mass conservation and momentum conservation in a fluid. The

equation of mass conservation is

$$\frac{\partial \rho_a}{\partial t} + \nabla \cdot (\rho_a \mathbf{v}_a) = 0, \tag{A.1}$$

where ρ_a is the density of the atmosphere (mass per unit volume), $\mathbf{v}_a$ is the fluid velocity of the atmosphere, and t is the time. The index 'a', for 'atmosphere', is used to distinguish ρ_a and $\mathbf{v}_a$ from the quantities ρ and $\mathbf{v}$ used below. The derivation of Eq. (A.1) is a matter of keeping track of the mass in an infinitesimal fluid volume, and can be found in textbooks on fluid dynamics. The term $\partial \rho_a / \partial t$ represents the rate of change of the density of the volume. The term $\nabla \cdot (\rho_a \mathbf{v}_a)$ represents the net flow of fluid out of the volume.

The equation of momentum conservation is

$$\rho_a \frac{D\mathbf{v}_a}{Dt} = -\nabla p_a, \tag{A.2}$$

where p_a is the pressure in the atmosphere and the operator $D/Dt \equiv \partial/\partial t + \mathbf{v}_a \cdot \nabla$ is the time derivative in a frame moving with the local fluid velocity. This equation is of the form 'mass $\times$ acceleration = force', and represents the acceleration of the fluid by local pressure gradients.

In a sound wave in the atmosphere, the fluctuations of the pressure and the density are usually small compared with the average values (*i.e.* time averages) of these quantities. For example, the fluctuation of the pressure is typically smaller than 100 Pa, which is only 0.1 % of the average pressure in the atmosphere. The velocity fluctuation is linearly related to the pressure and density fluctuations, in the linear acoustic approximation, so the velocity fluctuation can also be considered as a small quantity.

We assume that the atmosphere is homogeneous, so the average pressure, the average density, and the average velocity are independent of position in the atmosphere (a generalization to inhomogeneous atmospheres is presented in Appendix E). We assume that there is no wind in the atmosphere, so the average velocity is zero everywhere in the fluid. We write

$$\begin{aligned} p_a &= p_{av} + p \\ \rho_a &= \rho_{av} + \rho \\ \mathbf{v}_a &= \mathbf{v}_{av} + \mathbf{v}, \end{aligned} \tag{A.3}$$

where p_{av}, ρ_{av}, and $\mathbf{v}_{av}$ are the constant average values, with $\mathbf{v}_{av} = 0$, and p, ρ, and $\mathbf{v}$ are the small fluctuating contributions, referred to as the acoustic contributions. The fluctuation p is called the acoustic pressure or sound pressure. We substitute Eqs. (A.3) into Eqs. (A.1) and (A.2), retain only terms linear in the small fluctuating contributions, and find

$$\rho_{av} \nabla \cdot \mathbf{v} = -\frac{\partial \rho}{\partial t} \tag{A.4}$$

$$\rho_{av} \frac{\partial \mathbf{v}}{\partial t} = -\nabla p. \tag{A.5}$$

Equations (A.4) and (A.5) are called the ***linear acoustic equations.*** To proceed, we have to specify the thermodynamic relation between the pressure p_a and the density ρ_a in the atmosphere. The fluctuations caused by a sound wave are so rapid that sound propagation can be considered as an adiabatic process, *i.e.* a process without heat flow. In adiabatic processes, the pressure and the density satisfy the relation

$$p_a = K\rho_a^\gamma, \tag{A.6}$$

where K is a constant and $\gamma = c_p/c_v$ is the specific-heat ratio; c_p and c_v are the specific-heat coefficients of air at constant pressure and constant volume, respectively. A relation between the pressure fluctuation p and the density fluctuation ρ is found from a first-order Taylor expansion of the function $p_a(\rho_a)$:

$$p_a(\rho_{av} + \rho) = p_{av} + \left(\frac{\partial p_a}{\partial \rho_a}\right)_{av} \rho, \tag{A.7}$$

where the derivative is evaluated under adiabatic conditions and at density ρ_{av}. Using $p = p_a - p_{av}$ and Eq. (A.6), we find

$$p = c^2\rho \tag{A.8}$$

with

$$c^2 \equiv \left(\frac{\partial p_a}{\partial \rho_a}\right)_{av} = \gamma\frac{p_{av}}{\rho_{av}}. \tag{A.9}$$

The constant c will be identified later as the sound speed. From the ideal-gas law

$$p_{av} = \rho_{av}RT \tag{A.10}$$

we find

$$c^2 = \gamma RT. \tag{A.11}$$

Here T is the absolute temperature and R is a constant. Using Eq. (A.8), we write the linear acoustic equations (A.4) and (A.5) as

$$\rho\nabla\cdot\mathbf{v} = -\frac{1}{c^2}\frac{\partial p}{\partial t} \tag{A.12}$$

$$\rho\frac{\partial \mathbf{v}}{\partial t} = -\nabla p, \tag{A.13}$$

where we have omitted the subscript of ρ_{av}; the subscript of ρ_{av} will be omitted when it is clear from the context that ρ represents the average atmospheric density (this is the case in all appendices except in Appendix E). We take the

time derivative of Eq. (A.12) and take the divergence of Eq. (A.13), eliminate $\partial(\nabla \cdot \mathbf{v})/\partial t$ from the two resulting equations, and find the wave equation

$$\nabla^2 p - \frac{1}{c^2}\frac{\partial^2 p}{\partial t^2} = 0. \tag{A.14}$$

From this equation we can identify the constant c as the sound speed. To show this, we consider the solution $p = g(x - ct)$ of Eq. (A.14), where g is an arbitrary function. This solution represents a plane wave traveling in the positive x direction, with constant values of the pressure p within planes normal to the x axis. As the solution depends only on $x - ct$, the pressure appears constant to an observer moving in the positive x direction with speed c. In other words, the wave travels with speed c.

For dry air we have $\gamma = 1.4$ and $R = 287$ J·kg^{-1}·K^{-1}, and we find from Eq. (A.11) a sound speed of 331 m/s at temperature 273 K, *i.e.* 0°C. Equation (A.11) can be written as

$$c = c_0\sqrt{T/T_0}, \tag{A.15}$$

where we use $T_0 = 273$ K and $c_0 = 331$ m/s (one may also use, for example, $T_0 = 288$ K and $c_0 = 340$ m/s). Values of the sound speed calculated with Eq. (A.15) agree with experimental values, which confirms our assumption that sound propagation can be considered as an adiabatic process. The sound speed given by Eq. (A.11) or Eq. (A.15) is referred to as the adiabatic sound speed. For comparison, the isothermal sound speed is a factor of $\gamma^{-1/2} \approx 0.85$ smaller than the adiabatic sound speed.

The value $c_0 = 331$ m/s for $T_0 = 273$ K was derived for dry air. The effect of humidity is a small increase of the sound speed, by a factor of $(1+0.16h)$, where h is the molar concentration of water vapour in the atmosphere ($0 \leq h \leq 1$; *cf.* Sec. B.5). At 20°C, an upper limit for h is about 0.02, corresponding to an increase of the sound speed by 0.3%.

For future reference we note that the ideal-gas law (A.10) gives the following expression for the density of air at a pressure of 1 atm (1 atm = 1.01325×10^5 Pa):

$$\rho = \rho_0 T_0/T, \tag{A.16}$$

where $\rho_0 = 1.29$ kg·m^{-3} is the density at temperature $T_0 = 273$ K.

A.3 Helmholtz equation for harmonic waves

A sound wave is harmonic if the time dependence of the sound pressure is given by a factor $\cos(\phi - \omega t)$, where $\omega = 2\pi f$ is the angular frequency (f is the frequency) and ϕ is a constant phase angle. The factor can also be written as $\sin(\phi' - \omega t)$, with $\phi' = \phi + \frac{1}{2}\pi$. In this case, the sound pressure and the other acoustic variables oscillate sinusoidally with time, at each position. This

is perceived as a pure tone. We write in this case

$$\begin{aligned} p &= \mathrm{Re}\left(p_c e^{-i\omega t}\right) \\ \mathbf{v} &= \mathrm{Re}\left(\mathbf{v}_c e^{-i\omega t}\right), \end{aligned} \tag{A.17}$$

where p_c and $\mathbf{v}_c$ are complex amplitudes and $\mathrm{Re}(z)$ is the real part of a complex number z. To explain this notation, we write the complex amplitude p_c as $Ae^{i\phi}$, where A and ϕ are real numbers. Substitution into Eq. (A.17) gives $p = A\cos(\phi - \omega t)$. The factor A is called the amplitude of the sound field and $\phi - \omega t$ is called the phase. The amplitude and the phase vary with position in the atmosphere, in general. A surface on which the phase is constant is called a wave front. In Sec. A.4 we will see that the wave fronts of a point source are spheres.

For harmonic sound waves we can simplify the linear acoustic equations (A.12) and (A.13) and the wave equation (A.14). From Eqs. (A.17) we have that the pressure p and the velocity $\mathbf{v}$ depend on time only through the factor $e^{-i\omega t}$. Consequently, the time derivative in Eqs. (A.12) to (A.14) reduces to a multiplication by the factor $-i\omega$. For example, substitution of Eqs. (A.17) into Eq. (A.12) gives $\mathrm{Re}\left[(\rho c^2 \nabla \cdot \mathbf{v}_c - i\omega p_c)e^{-i\omega t}\right] = 0$. This should hold for all values of time t, which implies $\rho c^2 \nabla \cdot \mathbf{v}_c - i\omega p_c = 0$. The same arguments can be used in Eqs. (A.13) and (A.14). The linear acoustic equations (A.12) and (A.13) become

$$\rho c^2 \nabla \cdot \mathbf{v}_c = i\omega p_c \tag{A.18}$$

$$i\omega \rho \mathbf{v}_c = \nabla p_c \tag{A.19}$$

and the wave equation (A.14) becomes

$$\nabla^2 p_c + k^2 p_c = 0, \tag{A.20}$$

where $k = \omega/c$ is the wave number. Equation (A.20) is called the Helmholtz equation.

A.4 Inhomogeneous Helmholtz equation for a harmonic monopole source

We consider a sound field generated by a point source, and assume that the field has spherical symmetry with respect to the source, *i.e.* depends only on the radial distance r from the source. In this case the source is called a monopole source. The Helmholtz equation (A.20) becomes

$$\frac{1}{r}\frac{\partial^2}{\partial r^2}(r p_c) + k^2 p_c = 0. \tag{A.21}$$

This implies that the product rp_c satisfies the one-dimensional Helmholtz equation $\partial^2(rp_c)/\partial r^2 + k^2(rp_c) = 0$. The solution is

$$p_c = S\,\frac{\exp(ikr)}{r}, \tag{A.22}$$

where S is a constant; we assume that S is real, for simplicity. This solution represents an 'outgoing' wave, *i.e.* a wave that travels away from the point source. This can be seen as follows. Substitution of Eq. (A.22) into Eq. (A.17) gives $p = S\cos(kr - \omega t)/r$. The corresponding wave fronts, *i.e.* surfaces of constant phase $kr - \omega t$, are spheres with radius r. The phase $kr - \omega t$ of a wave front remains constant in time only if the radius r increases with increasing time t.

A second solution of Eq. (A.21) is $p_c = S\exp(-ikr)/r$. This solution is non-physical, as it represents a wave in which the radius of a wave front decreases with increasing time.

The amplitude of the spherical sound field represented by Eq. (A.22) is S/r, which decreases with increasing r. The corresponding sound pressure $p = S\cos(kr - \omega t)/r$ is a periodic function of time with period $2\pi/\omega = 1/f$ and a periodic function of r with 'spatial period' $2\pi/k = c/f$, which is called the wavelength.

The field given by Eq. (A.22) diverges for $r \to 0$. This divergence can be represented by including a term $-4\pi S\delta(\mathbf{r} - \mathbf{r}_s)$ on the right-hand side of Eq. (A.20):

$$\nabla^2 p_c + k^2 p_c = -4\pi S\delta(\mathbf{r} - \mathbf{r}_s), \tag{A.23}$$

where $\mathbf{r}_s = (x_s, y_s, z_s)$ denotes the source position in a rectangular xyz coordinate system and $\delta(\mathbf{r} - \mathbf{r}_s) = \delta(x - x_s)\delta(y - y_s)\delta(z - z_s)$ is the product of three Dirac delta functions. The Dirac delta function is defined by the relation $\int g(x)\delta(x - a)dx = g(a)$, where $g(x)$ is an arbitrary function and the integration interval includes $x = a$ [91].

To prove Eq. (A.23), we integrate Eq. (A.23) over the volume of a sphere with radius ϵ around the source:

$$4\pi\epsilon^2 \left(\frac{\partial p_c}{\partial r}\right)_{r=\epsilon} + 4\pi k^2 \int_0^\epsilon p_c r^2 dr = -4\pi S. \tag{A.24}$$

In the first term on the left-hand side we have used Gauss' theorem

$$\iiint_V \nabla \cdot \mathbf{F}\, dV = \iint_{S_c} \mathbf{F} \cdot \mathbf{n}\, dS_c, \tag{A.25}$$

where $\mathbf{F}(\mathbf{r})$ is an arbitrary vector field, S_c is a closed surface, V is the volume enclosed by the surface S_c, and $\mathbf{n}$ is the outward unit normal vector at the surface S_c; in this case we have $\mathbf{F} = \nabla p_c$ and $\nabla p_c = (\partial p_c/\partial r)\mathbf{n}$, as we have

$p_c = p_c(r)$ in a spherically symmetric field. We substitute Eq. (A.22) into Eq. (A.24) and take the limit $\epsilon \to 0$. This gives an identity. Equation (A.23) is called an inhomogeneous Helmholtz equation, while Eq. (A.20) is called a homogeneous Helmholtz equation.

Appendix B

Free field of a point source

B.1 Introduction

The sound field of a source in an unbounded homogeneous atmosphere is called the *free field* of the source. The atmosphere is unbounded if there are no boundaries, such as a ground surface. The atmosphere is homogeneous, or non-refracting, if the sound speed is constant, *i.e.* independent of position in the atmosphere.

In this appendix we describe the free field of a point source. This field is used as a reference field in the definition of the relative sound pressure level (see Sec. 3.4).

The 'strength' of a source is represented by the acoustic power, which is defined in Sec. B.2. In Sec. B.3 we introduce the sound pressure level, and we derive a relation between the sound pressure level and the sound power level, taking into account the geometrical attenuation corresponding to spherical spreading of sound waves. In Sec. B.4 we describe the spectral decomposition of the sound field, using the mathematical technique of Fourier transformation. In Sec. B.5 we include the effect of atmospheric absorption in the description of the sound field. In Sec. B.6 we describe the Doppler effect for a moving source.

B.2 Acoustic power of a source

The sound field of a source is represented by the acoustic pressure $p(\mathbf{r},t)$ and the fluid velocity $\mathbf{v}(\mathbf{r},t)$, where $\mathbf{r}$ denotes position in the field and t denotes time. We assume that the source is harmonic, and write $p = \mathrm{Re}\left(p_c e^{-i\omega t}\right)$ and $\mathbf{v} = \mathrm{Re}\left(\mathbf{v}_c e^{-i\omega t}\right)$ with complex amplitudes $p_c = p_r + ip_i$ and $\mathbf{v}_c = \mathbf{v}_r + i\mathbf{v}_i$ (see Sec. A.3). The acoustic intensity is defined as $\mathbf{I} = p\mathbf{v}$, which can be written as follows in this case:

$$\mathbf{I} = (p_r \cos\omega t + p_i \sin\omega t)(\mathbf{v}_r \cos\omega t + \mathbf{v}_i \sin\omega t). \tag{B.1}$$

The intensity is a function of time. The time average of the intensity, denoted as $\mathbf{I}_{\mathrm{av}}$, is given by

$$\mathbf{I}_{\mathrm{av}} = \frac{1}{2} p_{\mathrm{r}} \mathbf{v}_{\mathrm{r}} + \frac{1}{2} p_{\mathrm{i}} \mathbf{v}_{\mathrm{i}} = \mathrm{Re}(\frac{1}{2} p_{\mathrm{c}}^{*} \mathbf{v}_{\mathrm{c}}), \tag{B.2}$$

as follows from Eq. (B.1) and the relation $(\cos 2\omega t)_{\mathrm{av}} = (\sin 2\omega t)_{\mathrm{av}} = 0$. Here the average is performed over an integral number of harmonic periods.

The average acoustic power of the source is defined as

$$W_{\mathrm{av}} = \iint_{S_{\mathrm{c}}} \mathbf{I}_{\mathrm{av}} \cdot \mathbf{n} \, dS_{\mathrm{c}}, \tag{B.3}$$

where S_{c} is an arbitrary surface that encloses the source and $\mathbf{n}$ is the outward unit normal vector at the surface. The integral in Eq. (B.3) is independent of the choice of the surface S_{c}, as long as it encloses the source. An equivalent statement is that the integral vanishes if the surface encloses no sources. This can be shown as follows. We have $\nabla \cdot \mathbf{I} = (\nabla p) \cdot \mathbf{v} + p \nabla \cdot \mathbf{v}$. Substitution of the linear acoustic equations (A.12) and (A.13) gives the relation $\nabla \cdot \mathbf{I} = -\partial w / \partial t$, where $w = \frac{1}{2} \rho v^2 + \frac{1}{2} p^2 / \rho c^2$ is called the acoustic energy density [106]. This relation is valid at all positions except source positions (at source positions, p and $\mathbf{v}$ diverge). As w depends on time through v^2 and p^2, we have $(\partial w / \partial t)_{\mathrm{av}} = 0$, where the average is performed over an integral number of harmonic periods [from $p = p_{\mathrm{r}} \cos \omega t + p_{\mathrm{i}} \sin \omega t$ we find $(\partial p^2 / \partial t)_{\mathrm{av}} = 0$]. Consequently, we have $\nabla \cdot \mathbf{I}_{\mathrm{av}} = 0$ at all positions except source positions. With Gauss' theorem (A.25) we find that the integral in Eq. (B.3) vanishes if the surface encloses no sources.

B.3 Sound pressure level and geometrical attenuation

We assume that the sound field has spherical symmetry with respect to the source, so the complex pressure amplitude p_{c} and the complex velocity amplitude $\mathbf{v}_{\mathrm{c}}$ depend on position only through the radial distance r from the source. In this case Eq. (B.3) gives

$$I_{\mathrm{av}} = \frac{W_{\mathrm{av}}}{4\pi r^2}, \tag{B.4}$$

where $I_{\mathrm{av}} = \mathbf{I}_{\mathrm{av}} \cdot \mathbf{n}$ is the magnitude of the average intensity, which has only a radial component in this case.

In practice the field of a sound source is often not spherical. The field is usually a smooth function of the direction of sound emission. In this case the analysis presented in this section can still be applied. The power W_{av} is a function of the direction of sound emission in this case, and Eq. (B.4) represents the decrease with distance r of the intensity within a cone, with the source at the apex of the cone.

The complex pressure amplitude is given by Eq. (A.22):

$$p_c = S \frac{\exp(ikr)}{r}, \tag{B.5}$$

where S is a constant. The corresponding fluid velocity has only a radial component, which follows from Eq. (A.19):

$$v_c = \frac{1}{i\omega\rho} \frac{\partial p_c}{\partial r}. \tag{B.6}$$

This gives

$$v_c = \left(1 + \frac{i}{kr}\right) \frac{p_c}{\rho c}. \tag{B.7}$$

For large r we have $kr \gg 1$, and we find $v_c \approx p_c/\rho c$. As ρc is a real number, this implies that the pressure and the fluid velocity are in phase with each other, at large distance from the source. For plane waves, the relation $v_c = p_c/\rho c$ holds exactly, as follows from Eq. (A.19) (see Sec. C.3). Thus, a spherical wave behaves locally as a plane wave, at large distance from the source. The region where we have $kr \gg 1$ is called the far-field region.

The average acoustic intensity given by Eq. (B.2) becomes, from Eq. (B.7),

$$I_{av} = \frac{1}{2} \frac{|p_c|^2}{\rho c}. \tag{B.8}$$

The near-field term i/kr in Eq. (B.7) does not contribute to I_{av}. Equation (B.8) can also be written as

$$I_{av} = \frac{(p^2)_{av}}{\rho c}, \tag{B.9}$$

where $(p^2)_{av}$ is the squared sound pressure averaged over an integral number of harmonic periods. The proof that $(p^2)_{av}$ is equal to $\frac{1}{2}|p_c|^2$ is analogous to the derivation of Eq. (B.2) from Eq. (B.1). From Eqs. (B.5) and Eq. (B.8) we find that I_{av} is proportional to r^{-2}, in agreement with Eq. (B.4); the quantity W_{av} in Eq. (B.4) is related to the constant S by the relation $W_{av} = 2\pi S^2/\rho c$. Equations (B.4) and (B.9) give the relation

$$(p^2)_{av} = \rho c \frac{W_{av}}{4\pi r^2}. \tag{B.10}$$

The *sound pressure level* is defined as

$$L_p = 10 \lg \frac{(p^2)_{av}}{p_{ref}^2} \tag{B.11}$$

with reference sound pressure $p_{\text{ref}} = 2\times10^{-5}$ Pa (or 20 μPa). The ***sound power level*** is defined as

$$L_W = 10\lg\frac{W_{\text{av}}}{W_{\text{ref}}} \tag{B.12}$$

with reference sound power $W_{\text{ref}} = 1\times10^{-12}$ W (or 1 pW). The values of p_{ref} and W_{ref} satisfy the relation

$$p_{\text{ref}}^2 \approx \rho c W_{\text{ref}}. \tag{B.13}$$

From Eqs. (B.10) to (B.13) we find

$$L_p = L_W - 10\lg 4\pi r^2. \tag{B.14}$$

The term $10\lg 4\pi r^2$ represents the attenuation of a spherical sound wave with increasing distance from the source, as a consequence of the spherical spreading of acoustic intensity. This attenuation is called geometrical attenuation.

The sound pressure level is a dimensionless number, but to indicate that the level is calculated with Eq. (B.11) one writes dB (*re* 20 μPa) after the number, where dB stands for decibel and *re* for 'reference'. For $(p^2)_{\text{av}} = 1$ Pa, for example, we have $L_p = 94$ dB (*re* 20 μPa). Analogously, one writes dB (*re* 1 pW) after a sound power level calculated with Eq. (B.12).

B.4 Spectral decomposition

The foregoing was restricted to a harmonic source, but the results can also be used for a non-harmonic source by decomposing the sound pressure signal $p(t)$ (at an arbitrary position) into harmonic components:

$$p(t) = \sum_n \text{Re}\left(p_{c,n}e^{-i\omega_n t}\right), \tag{B.15}$$

where $p_{c,n}$ are the complex pressure amplitudes and ω_n are the angular frequencies of the harmonic components, for $n = 0, 1, 2, \ldots$. In this section we will derive Eq. (B.15), using the mathematical technique of Fourier transformation [112].

The Fourier transform $P(f)$ of a time signal $p(t)$ is defined as

$$P(f) = \int_{-\infty}^{\infty} p(t)e^{i2\pi ft}\,dt. \tag{B.16}$$

The inverse transform is

$$p(t) = \int_{-\infty}^{\infty} P(f)e^{-i2\pi ft}\,df. \tag{B.17}$$

The variable f in these expressions will be identified later as the frequency of a harmonic component. As $p(t)$ is real, we have $P(-f) = P^*(f)$. The functions $p(t)$ and $P(f)$ satisfy the relation

$$\int_{-\infty}^{\infty} p^2(t)\,dt = \int_{-\infty}^{\infty} |P(f)|^2\,df, \tag{B.18}$$

which is known as Parseval's theorem [112].

In practice one works with a sampled signal, *i.e.* a set of values of the signal $p(t)$ at discrete times t_j given by

$$t_j = j\tau, \text{ with } j = 0, 1, \ldots, N-1, \tag{B.19}$$

where τ is the sample time and N is the number of samples; we assume that N is even. We define N frequencies

$$f_n = \frac{n}{N\tau}, \text{ with } n = -\frac{1}{2}N+1, -\frac{1}{2}N+2, \ldots, \frac{1}{2}N. \tag{B.20}$$

For a sampled signal, the infinite time integration interval in Eqs. (B.16) and (B.18) is replaced by the finite 'measurement period' from t_0 to t_{N-1}. We assume that the signal is nonzero only in a finite time interval that is contained in the measurement period. The signal is zero at the boundaries of the measurement period, *i.e.* at the times t_0 and t_{N-1}. For a continuous time signal this is not true; in this case one forces the signal to go to zero at the boundaries, by multiplying the signal by a 'time window' function; this function is equal to unity except in narrow regions near the boundaries, where the function goes continuously to zero.

The signal $p(t)$ is accurately represented by the N samples $p(t_j)$ only if the measurement period $N\tau$ is sufficiently long and if the sample frequency $1/\tau$ is sufficiently high. It proves that the sample frequency should be at least twice the highest frequency present in the signal. The infinite frequency integration interval in Eqs. (B.17) and (B.18) is replaced by the finite interval from $-1/2\tau$ to $1/2\tau$.

The discrete approximation of the Fourier transform (B.16) for a sampled signal is

$$P(f_n) = \tau P_n \tag{B.21}$$

with

$$P_n = \sum_{j=0}^{N-1} p(t_j) e^{i2\pi jn/N}. \tag{B.22}$$

The quantity P_n is called the Discrete Fourier Transform (DFT) of the signal $p(t_j)$. If we use a power of 2 for the number N, *e.g.* $N = 2^{10} = 1024$, the sum in

Eq. (B.22) can be evaluated efficiently with the Fast Fourier Transform (FFT) algorithm [112].

The discrete approximation of the inverse Fourier transform (B.17) is

$$p(t_j) = \frac{1}{N} \sum_{n=-\frac{1}{2}N+1}^{\frac{1}{2}N} P_n e^{-i2\pi jn/N}, \tag{B.23}$$

where Eq. (B.21) has been used. From Eq. (B.22) we have $P_n = P_{n+N}$, which implies that the set $n = -\frac{1}{2}N + 1, -\frac{1}{2}N + 2, \ldots, \frac{1}{2}N$ is equivalent to the set $n = 0, 1, \ldots, N-1$. From Eq. (B.23) we have $p(t_j) = p(t_{j+N})$. In particular, we have $p(t_0) = p(t_N)$. This is the reason why we assumed $p(t_0) = p(t_{N-1}) = 0$ below Eq. (B.20); for $p(t_0) \neq p(t_{N-1})$ we would have a pressure jump between t_{N-1} and t_N, which introduces spurious high-frequency components in the spectrum.

As $p(t)$ is real, we have $P_{-n} = P_n^*$. This implies that Eq. (B.23) can also be written as

$$p(t_j) = \sum_{n=0}^{\frac{1}{2}N} \mathrm{Re}\left(P_{\mathrm{c},n} e^{-i2\pi jn/N}\right) \tag{B.24}$$

with

$$\frac{P_n}{N} = \begin{cases} \frac{1}{2}P_{\mathrm{c},n} & \text{for } n = 1, 2, \ldots, \frac{1}{2}N - 1 \\ P_{\mathrm{c},n} & \text{for } n = 0 \text{ and } n = \frac{1}{2}N \\ \frac{1}{2}P_{\mathrm{c},-n}^* & \text{for } n = -1, -2, \ldots, -\frac{1}{2}N + 1. \end{cases} \tag{B.25}$$

Equation (B.24) is of the same form as Eq. (B.15) if we set $\omega_n = 2\pi f_n$ and use Eqs. (B.19) and (B.20); we identify ω_n as the angular frequency and f_n as the frequency of Fourier component n. Thus, we have shown that a time signal can always be decomposed into harmonic Fourier components.

We will now use Fourier decomposition to introduce the spectrum of the sound pressure level. The discrete form of Parseval's theorem (B.18) is

$$\tau \sum_{j=0}^{N-1} p^2(t_j) = \frac{1}{N\tau} \sum_{n=-\frac{1}{2}N+1}^{\frac{1}{2}N} |P(f_n)|^2. \tag{B.26}$$

Replacing the left-hand side by $\tau N (p^2)_{\mathrm{av}}$ and using P_n from Eq. (B.21) on the right-hand side, we find

$$(p^2)_{\mathrm{av}} = \sum_{n=-\frac{1}{2}N+1}^{\frac{1}{2}N} \frac{|P_n|^2}{N^2}. \tag{B.27}$$

This can be written as

$$(p^2)_{\mathrm{av}} = \frac{|P_0|^2}{N^2} + \sum_{n=1}^{\frac{1}{2}N-1} \frac{2|P_n|^2}{N^2} + \frac{|P_{\frac{1}{2}N}|^2}{N^2}. \tag{B.28}$$

The first term on the right-hand side represents the DC component, *i.e.* the component that is independent of time; this term is usually zero as the sound pressure is defined as the deviation from the DC component. The remaining terms represent the contributions to $(p^2)_{\mathrm{av}}$ from the Fourier components with frequencies f_n with $n = 1, 2, \ldots, \frac{1}{2}N$. The last term on the right-hand side for $n = \frac{1}{2}N$ can be neglected if the number of samples N is sufficiently large. For the contributions $2|P_n|^2/N^2$ from components $n = 1, 2, \ldots, \frac{1}{2}N - 1$ we find from Eq. (B.25)

$$\frac{2|P_n|^2}{N^2} = \frac{1}{2}|P_{\mathrm{c},n}|^2 \tag{B.29}$$

or

$$\frac{2|P_n|^2}{N^2} = (p_n^2)_{\mathrm{av}} \tag{B.30}$$

with $p_n(t_j) = \mathrm{Re}\left(P_{\mathrm{c},n}e^{-i2\pi jn/N}\right)$. Substitution of Eq. (B.30) into Eq. (B.28) gives

$$(p^2)_{\mathrm{av}} = \sum_{n=0}^{\frac{1}{2}N-1} (p_n^2)_{\mathrm{av}}, \tag{B.31}$$

where we have included the contribution $(p_0^2)_{\mathrm{av}} = P_0^2/N^2$ of the DC component $p_0(t_j) = P_{\mathrm{c},0} = P_0/N$, with real P_0, and the last term on the right-hand side of Eq. (B.28) has been neglected. The quantity $(p^2)_{\mathrm{av}}$ has been decomposed into contributions $(p_n^2)_{\mathrm{av}}$ of the Fourier components with frequencies f_n. The contributions $(p_n^2)_{\mathrm{av}}$ are related to the Fourier coefficients P_n by Eq. (B.30). The Fourier coefficients P_n are obtained from the signal $p(t)$ by the Discrete Fourier Transform (B.22).

The quantity $(p^2)_{\mathrm{av}}$ is related to the sound pressure level L_p by Eq. (B.11). The spectrum of the sound pressure level is defined as

$$L_p(f_n) = 10\lg\frac{(p_n^2)_{\mathrm{av}}}{p_{\mathrm{ref}}^2}, \tag{B.32}$$

so we have

$$L_p = 10\lg\sum_n 10^{L_p(f_n)/10}. \tag{B.33}$$

We use the notation $L_p(f_n)$ for the spectrum and L_p for the broadband level. From Eq. (B.14) we have $L_W = L_p + 10\lg 4\pi r^2$, so we define the spectrum of the sound power level as $L_W(f_n) = L_p(f_n) + 10\lg 4\pi r^2$, which is independent of r. We use here the spectrum $L_p(f_n)$ at a relatively small distance r from the source (for large r the effect of atmospheric absorption should be taken into account; see Sec. B.5). We have

$$L_W = 10\lg\sum_n 10^{L_W(f_n)/10}. \tag{B.34}$$

The frequencies f_n are given by $f_n = n/N\tau$, with $n = 0, 1, \ldots, \frac{1}{2}N - 1$. The frequencies are equidistant on a linear scale (see Fig. 2.5). A frequency interval between f_n and f_{n+1} is called a *narrow* frequency band. The width $f_{n+1} - f_n = 1/N\tau$ of a narrow frequency band is typically 1 Hz or smaller (for example, $1/N\tau \approx 1$ Hz for $N = 1024$ and $\tau = 1$ ms).

In practice one often uses 1/3-octave (one-third-octave) and octave bands. Each 1/3-octave band and each octave band is characterized by a center frequency, an upper frequency, and a lower frequency (see Fig. 2.5). The center frequencies are given approximately by $f_{c,m} \approx f_{c,30} 2^{-10+m/3}$ with $f_{c,30} = 1000$ Hz, where the band number m is a positive integer. For the 1/3-octave bands m runs over all positive integers ($m = 1, 2, 3, \ldots$), while for the octave bands m is a multiple of 3 ($m = 3, 6, 9, \ldots$). The center frequencies of two successive octave bands differ by a factor of 2. The upper and lower frequencies of an octave band m are $2^{1/2} f_{c,m}$ and $2^{-1/2} f_{c,m}$, respectively, so the octave bands are contiguous. The center frequencies of two successive 1/3-octave bands differ by a factor of $2^{1/3}$. The upper and lower frequencies of a 1/3-octave band m are $2^{1/6} f_{c,m}$ and $2^{-1/6} f_{c,m}$, respectively, so the 1/3-octave bands are also contiguous.

A problem with the approximate relation $f_{c,m} \approx f_{c,30} 2^{-10+m/3}$ is that it does not give round numbers for the center frequencies. For $m = 20$, for example, we find $f_{c,20} = 99.2$ Hz. One can also calculate the center frequencies with the relation $f_{c,m} = 10^{m/10}$ Hz, as follows from $2^{10/3} \approx 10$; the center frequencies calculated with this relation are sometimes referred to as the 'exact' center frequencies, for example in the International Standard IEC 651 (1993-09). Also the exact center frequencies are not all round numbers; only the frequencies 1, 10, 100, 1000, and 10 000 Hz are round numbers. For $m = 24$, for example, we find 251.2 Hz. In practice one often uses round numbers for all center frequencies. These round numbers are referred to as the 'preferred' center frequencies, and are specified in the International Standard ISO 266-1976(E).

The 'preferred' 1/3-octave band center frequencies between 10 Hz and 10 kHz are

10, 12.5, 16, 20, 25, 31.5, 40, 50, 63, 80 Hz	($m = 10, 11, \ldots, 19$)
100, 125, 160, 200, 250, 315, 400, 500, 630, 800 Hz	($m = 20, 21, \ldots, 29$)
1, 1.25, 1.6, 2, 2.5, 3.15, 4, 5, 6.3, 8, 10 kHz	($m = 30, 31, \ldots, 40$).

The 'preferred' octave band center frequencies between 10 Hz and 10 kHz are

16, 31.5, 63, 125, 250, 500 Hz	($m = 12, 15, \ldots, 27$)
1, 2, 4, 8 kHz	($m = 30, 33, \ldots, 39$).

There are also 'preferred' frequencies for the upper and lower frequencies of the 1/3-octave and octave bands. For most practical applications, however, the approximations $2^{1/2} f_{c,m}$ and $2^{-1/2} f_{c,m}$ for the octave bands, and $2^{1/6} f_{c,m}$ and $2^{-1/6} f_{c,m}$ for the 1/3-octave bands, are sufficiently accurate.

Narrow-band spectra $L_p(f_n)$ are converted to 1/3-octave or octave band

spectra with the relation

$$L_p(f_{c,m}) = 10\lg{\sum_n}' 10^{L_p(f_n)/10}, \tag{B.35}$$

where the prime indicates that the sum is over all narrow bands in 1/3-octave or octave band m (if only a fraction of a narrow band is covered by band m, the contribution of this narrow band in the sum should be multiplied by this fraction). Consequently, Eq. (B.33) also applies with a summation over 1/3-octave or octave bands, instead of narrow bands: $L_p = 10\lg(\sum_m 10^{L_p(f_{c,m})/10})$. The conversion of narrow-band sound power spectra $L_W(f_n)$ to 1/3-octave or octave band spectra is analogous.

The human ear is most sensitive to frequencies in the range between about 1 kHz and 6 kHz. A pure tone of 1 kHz, for example, appears about equally loud as a pure tone of 100 Hz with a 20 dB higher value of the sound pressure level. To account for this effect one employs the A-weighting, in applications in which human perception of sound is involved, *e.g.* noise control. The A-weighting is represented by the function $W_A(f_n)$ given in the International Standard IEC 651 (1993-09):

$$W_A(f_n) = 20\lg\frac{R_A(f_n)}{R_{A,1000}} \tag{B.36}$$

with

$$R_A(f) = \frac{12200^2 f^4}{(f^2+20.6^2)(f^2+12200^2)(f^2+107.7^2)^{1/2}(f^2+737.9^2)^{1/2}}, \tag{B.37}$$

where f is expressed in Hz and $R_{A,1000}$ is the value of $R_A(f_n)$ at $f_n = 1000$ Hz. The A-weighted spectrum $L_A(f_n)$ is defined as

$$L_A(f_n) = L_p(f_n) + W_A(f_n). \tag{B.38}$$

Pure tones with equal values of $L_A(f_n)$ are perceived with about equal loudness. From the A-weighted spectrum $L_A(f_n)$ the A-weighted sound pressure level L_A is calculated with the relation

$$L_A = 10\lg\sum_n 10^{L_A(f_n)/10}. \tag{B.39}$$

The level L_A is often referred to simply as the sound level. As an approximation, one can apply the A-weighting to the 1/3-octave or octave band spectrum (instead of the narrow-band spectrum). In this case one uses Eq. (B.38) with the frequency f_n replaced by a center frequency $f_{c,m}$ and calculates the sound level L_A from the A-weighted levels $L_A(f_{c,m})$. The values of the A-weighting $W_A(f_{c,m})$ for the 'preferred' center frequencies are given in Table B.1.

Table B.1. The A-weighting $W_A(f_{c,m})$ (in dB) for the 'preferred' 1/3-octave band center frequencies $f_{c,m}$ (in Hz).

$f_{c,m}$	12.5	25	50	100	200	400	800	1600	3150	6300
	16	31.5	63	125	250	500	1000	2000	4000	8000
	20	40	80	160	315	630	1250	2500	5000	10k
W_A	-63.6	-44.8	-30.3	-19.1	-10.8	-4.8	-0.8	1.0	1.2	-0.1
	-56.4	-39.5	-26.2	-16.2	-8.7	-3.2	0.0	1.2	1.0	-1.1
	-50.4	-34.5	-22.4	-13.2	-6.6	-1.9	0.6	1.3	0.6	-2.5

B.5 Atmospheric absorption

In the foregoing we have ignored the fact that a sound wave loses energy by atmospheric absorption. Atmospheric absorption originates from two effects [92, 106]:

i) thermal conduction and viscosity of air,

ii) relaxation losses of oxygen and nitrogen molecules in air.

Both effects cause an attenuation of a sound wave.

The attenuation due to the first effect is called classical attenuation. Temperature gradients present in a sound wave are partly reduced by heat flow, which depends on the thermal conductivity of air. Analogously, velocity gradients present in a sound wave are partly reduced by momentum transfer, which depends on the viscosity of air. In both processes the sound wave loses energy, which is converted into heat. As the gradients are proportional to the frequency of the sound wave, the attenuation is larger at high frequency than at low frequency. The classical attenuation of a sound wave can be derived from the equations of fluid dynamics including viscosity and thermal conductivity.

An analysis based on statistical mechanics is required for the attenuation due to molecular relaxation losses. A sound wave causes periodic compression and expansion of air. During the compression stage, the diatomic oxygen and nitrogen molecules in the air are brought into excited vibrational and rotational states. During the expansion stage, the molecules relax to their original states. In this process some energy is lost, which is converted into heat. Water molecules play an important role as a catalyst in these internal molecular processes of excitation and relaxation. Consequently, the attenuation by atmospheric absorption depends on the humidity of the air.

A spherical sound wave is attenuated by atmospheric absorption, in addition to the geometrical attenuation by spherical spreading described in Sec. B.3. The relative change in average acoustic intensity I_{av} over an infinitesimal propagation distance dr can be written as

$$\frac{dI_{av}}{I_{av}} = -\frac{2}{r}dr - \alpha' dr, \tag{B.40}$$

where the first term on the right-hand side represents spherical spreading [this term follows from Eq. (B.4)] and the second term represents atmospheric absorption; α' is the fraction of acoustic intensity that the wave loses per unit propagation distance due to atmospheric absorption. Integration of this equation gives

$$I_{\mathrm{av}} = \frac{W_{\mathrm{av}}}{4\pi r^2} e^{-\alpha' r}, \tag{B.41}$$

which agrees with Eq. (B.4) for $\alpha' = 0$. Using Eqs. (B.9) and (B.11) to (B.13) we find the following expression for the sound pressure level:

$$L_p = L_W - 10 \lg 4\pi r^2 - \alpha r, \tag{B.42}$$

where $\alpha = \alpha' 10 \lg e$ is the attenuation in dB per unit length. The term $-\alpha r$ is negligible for short distance r. For distances of the order of a hundred meters or more, however, this term can usually not be neglected, in particular at high frequencies. It should be noted that molecular relaxation losses affect not only the amplitude but also the phase of a sound wave [106]. The effect on the phase is small, however, and is neglected here.

The attenuation of a sound wave by atmospheric absorption varies considerably with the frequency f of the wave. We distinguish three regions in the frequency range, separated by the relaxation frequencies $f_{\mathrm{r,N}}$ and $f_{\mathrm{r,O}}$ of nitrogen and oxygen, respectively. At low frequency, $f < f_{\mathrm{r,N}}$, the attenuation is dominated by nitrogen relaxation. For $f_{\mathrm{r,N}} < f < f_{\mathrm{r,O}}$, oxygen relaxation dominates. At high frequency, $f > f_{\mathrm{r,O}}$, the attenuation approaches the classical attenuation. The three regions in the frequency range are clearly visible in a double-logarithmic graph of the absorption coefficient α versus frequency; an example is shown in Fig. B.1, for a temperature of 10°C, a relative humidity of 80%, and a pressure of 1 atm. In each region, the curve approaches a straight line with a slope equal to 2. A slope of 2 means that the absorption coefficient is proportional to the square of the frequency.

The curve shown in Fig. B.1 was calculated with the International Standard ISO 9613-1:1993(E). The formulas from this Standard are given below. The absorption coefficient is calculated from three atmospheric parameters: the absolute temperature T in K, the relative humidity r_h in %, and the atmospheric pressure p_{a} in Pa. The absorption coefficient in dB per meter is given by

$$\alpha = 8.686 f^2 \tau_{\mathrm{r}}^{1/2} \left(1.84 \times 10^{-11} \rho_{\mathrm{r}}^{-1} + \tau_{\mathrm{r}}^{-3} [b_1 + b_2]\right), \tag{B.43}$$

where $\tau_{\mathrm{r}} = T/T_{20}$ and $\rho_{\mathrm{r}} = p_{\mathrm{a}}/p_{\mathrm{r}}$ are dimensionless quantities, with $T_{20} = 293.15$ K and $p_{\mathrm{r}} = 101\,325$ Pa; the quantities b_1 and b_2 are given by

$$b_1 = 0.1068 \exp(-3352/T)/(f_{\mathrm{r,N}} + f^2/f_{\mathrm{r,N}}) \tag{B.44}$$

$$b_2 = 0.01275 \exp(-2239.1/T)/(f_{\mathrm{r,O}} + f^2/f_{\mathrm{r,O}}), \tag{B.45}$$

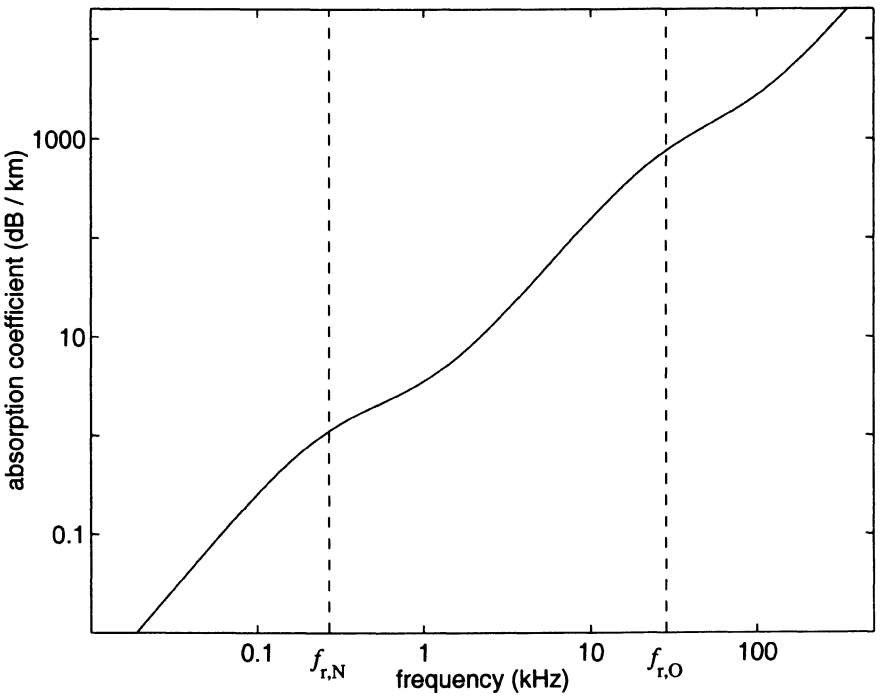

Figure B.1. Absorption coefficient α as a function of frequency f, calculated with the International Standard ISO 9613-1:1993(E) for a temperature of 10°C, a relative humidity of 80%, and a pressure of 1 atm. The relaxation frequencies $f_{r,N}$ and $f_{r,O}$ of nitrogen and oxygen, respectively, are also indicated.

where $f_{r,N}$ and $f_{r,O}$ are the relaxation frequencies of nitrogen and oxygen, respectively, which are given by

$$f_{r,N} = \rho_r \tau_r^{-1/2} \left(9 + 280h \exp(-4.17[\tau_r^{-1/3} - 1])\right) \tag{B.46}$$

$$f_{r,O} = \rho_r \left[24 + 40400h(0.02 + h)/(0.391 + h)\right]. \tag{B.47}$$

The quantity h in these expressions is the molar concentration of water vapour in the atmosphere, expressed as a percentage. The relative humidity r_h is defined as the ratio, expressed as a percentage, of the water vapour pressure in the atmosphere to the saturation vapour pressure p_{sat}. We have

$$h = r_h \rho_{sat} / \rho_r \tag{B.48}$$

with $\rho_{sat} = p_{sat}/p_r$. The quantity ρ_{sat} is written as

$$\rho_{sat} = 10^{C_{sat}} \tag{B.49}$$

with

$$C_{\text{sat}} = -6.8346(T_{01}/T)^{1.261} + 4.6151, \tag{B.50}$$

where $T_{01} = 273.16$ K is the triple-point temperature of water. The accuracy of the absorption coefficient α calculated with these expressions is estimated to be $\pm 10\%$ for $0.05\% < h < 5\%$, $253 < T < 323$ K, $p_{\text{a}} < 200$ kPa, and $4 \times 10^{-4} < f/p_{\text{a}} < 10$ Hz/Pa.

The above expressions are valid for pure-tone sounds, but the expressions can also be used for broadband sounds by spectral decomposition (it is indicated in Ref. [146] that the spectral decomposition into 1/3-octave or octave bands causes small errors in the calculation of atmospheric absorption). As an approximation, the absorption for a 1/3-octave or octave band can be calculated by evaluating the absorption coefficient at the center frequency of the band. Table B.2 gives the values of the absorption coefficient for a temperature of 10°C and a relative humidity of 80%, calculated with Eqs. (B.43) to (B.50) for the 1/3-octave band center frequencies.

Table B.2. Atmospheric absorption coefficient α (in dB per kilometer) at $T = 283.15$ K (10°C), $r_h = 80\%$, and $p_{\text{a}} = 1.01325 \times 10^5$ Pa (1 atm), for the 'preferred' 1/3-octave band center frequencies $f_{\text{c},m}$ (in Hz).

$f_{\text{c},m}$	12.5	25	50	100	200	400	800	1600	3150	6300
	16	31.5	63	125	250	500	1000	2000	4000	8000
	20	40	80	160	315	630	1250	2500	5000	10k
α	0.005	0.018	0.07	0.25	0.77	1.63	2.88	6.3	18.8	67
	0.007	0.028	0.11	0.37	1.02	1.96	3.57	8.8	29.0	105
	0.011	0.045	0.17	0.55	1.31	2.36	4.58	12.6	43.7	157

B.6 Doppler effect

The frequency of sound received from a moving harmonic source is affected by the motion of the source. This is the Doppler effect. As illustrated in Fig. B.2, the distance between wave fronts emitted at constant time intervals by a moving source is reduced in the region in front of the source (to the right in the figure) and enhanced in the region behind the source (to the left in the figure), simply because successive wave fronts are emitted at different source positions. The frequency of the sound at a stationary receiver is inversely proportional to the distance between successive wave fronts. Therefore, the frequency is enhanced in the region in front of the source and reduced in the region behind the source.

It is straightforward to show [46, 106] that source motion changes the observed frequency by a factor $f_{\text{D}} = c/(c - v_{\text{r}})$, where c is the sound speed and v_{r} is the radial component of the source velocity, *i.e.* the component along the line from the source to the receiver (see Fig. B.2). The radial velocity component v_{r} is positive for a receiver in the region in front of the source and negative for

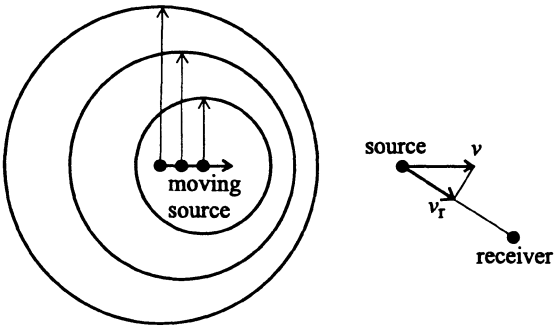

Figure B.2. Illustration of the Doppler effect. The circles represent spherical wave fronts emitted at constant time intervals by a moving source. The distance between the wave fronts is reduced in the region in front of the source and enhanced in the region behind the source. Also shown is the radial velocity component v_r, which determines the Doppler frequency shift at a receiver.

a receiver in the region behind the source; for positive v_r we have $f_D > 1$ and for negative v_r we have $f_D < 1$.

The amplitude is changed by the same factor f_D [46]. The compressed waves in the region in front of the source have an enhanced amplitude, while the decompressed waves in the region behind the source have a reduced amplitude.

In practice the Doppler effect can often be neglected. For $v_r = 100$ km/h, for example, we have $f_D = 1.09$, so the frequency and amplitude are enhanced by only 9%.

Appendix C

Acoustic impedance

C.1 Introduction

In computational models for atmospheric sound propagation, the ground surface is usually taken into account by a mathematical boundary condition to the solution for the field above the ground surface. This condition contains the acoustic impedance of the ground surface as a parameter. In this appendix we describe the concept of acoustic impedance of a ground surface.

In Sec. C.2 we introduce the impedance of a ground surface and explain the relation to the characteristic impedance of the ground material. Not only the impedance of the ground material but also the impedance of air plays a role in the interaction of sound waves with the ground. The impedance of air is evaluated in Sec. C.3. Many natural grounds can be modeled as porous media. In Sec. C.4 we describe various impedance models for porous media.

In Sec. C.5 we describe the normal reflection of plane waves, as a simple example of the use of ground impedance. In Appendix D we will describe the ground reflection of plane waves for an arbitrary angle of incidence, and the ground reflection of spherical waves.

Some grounds can be modeled as a homogeneous medium of porous material with a top layer that consists of a different porous material. The impedance of such a layered ground is described in Sec. C.6.

C.2 Impedance of a ground surface

When a sound wave strikes a ground surface, part of the wave is reflected and part of the wave is transmitted into the ground (see Fig. C.1). In general, the propagation speed of the wave in the ground is different from the sound speed in the air above the ground. The sound speed in the ground is often smaller than the sound speed in air. In Appendix D we will see that this implies $\theta' < \theta_{\mathrm{i}}$ (see Fig. C.1). We will also see that we have $\theta_{\mathrm{i}} = \theta_{\mathrm{r}}$.

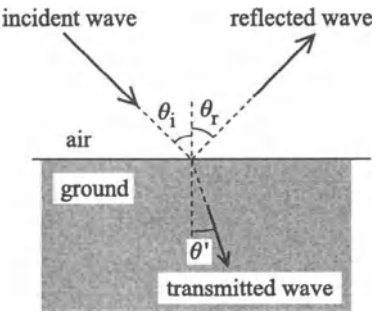

Figure C.1. Reflection of a sound wave by a ground surface.

Many natural grounds can be described as porous media. A sound wave causes a vibration of the air in the pores of a porous ground medium. Solid or liquid material in the ground may also vibrate.

In general, the ground is modeled as a continuous propagation medium for sound waves, *i.e.* as a fluid, so a sound pressure and a fluid velocity can be defined in the ground medium [92]. At the air-ground interface, *i.e.* at the ground surface, the sound pressure and the fluid velocity component normal to the ground surface are continuous, *i.e.* have equal values just above and just below the ground surface. This follows from mechanical equilibrium and mass conservation at the interface. The fluid velocity component parallel to the ground surface may be discontinuous at the ground surface.

The sound pressure and the normal velocity component at the ground surface depend of course on the incident sound field. If the amplitude of the incident field is doubled, for example, the amplitudes of the sound pressure and the normal velocity component at the ground surface are also doubled. The ratio of the sound pressure to the normal velocity component, however, is independent of the amplitude of the incident sound field, and is therefore a convenient quantity for the acoustic characterization of the ground surface. The ratio depends on the frequency of the sound field, but this is not a problem as we can always decompose a sound field into harmonic components.

We consider a harmonic sound field in the system shown in Fig. C.1, with complex pressure amplitude p_c and normal component $v_{c,n}$ of the complex velocity amplitude ($v_{c,n}$ is the normal component in downward direction). The quantities p_c and $v_{c,n}$ are functions of the (vertical) position. The (acoustic) *impedance of the ground surface* is defined as the ratio $p_c/v_{c,n}$ evaluated at the ground surface. The ratio $p_c/v_{c,n}$ is continuous at the ground surface, *i.e.* has equal values just above and just below the ground surface; this provides the boundary condition to the sound field above the ground surface.

The value of the ratio $p_c/v_{c,n}$ just below the ground surface is related to the *characteristic impedance of the ground material*. The characteristic impedance

of a medium is defined as the ratio p_c/v_c, where p_c and v_c are the complex pressure and velocity amplitudes, respectively, of a ***single*** harmonic sound wave traveling in the medium. It should be noted that in the system shown in Fig. C.1 there are *two* waves in the region above the ground surface (the incident wave and the reflected wave) and a single wave below the ground surface (the transmitted wave).

If the propagation direction of the incident wave is normal to the ground surface ($\theta_i = 0$ in Fig. C.1), the propagation direction of the transmitted wave is also normal to the ground surface ($\theta' = 0$). In this case we have $v_c = v_{c,n}$. Consequently, the impedance of a ground surface for normal incidence is equal to the value of p_c/v_c for the transmitted wave, *i.e.* the characteristic impedance of the ground material, evaluated at the surface. In general, the characteristic impedance is a function of depth in the ground, and the characteristic impedance should be evaluated at the surface; only if the ground medium is homogeneous, the characteristic impedance is independent of depth in the ground.

If the propagation direction of the incident wave is not normal to the ground surface, the propagation direction of the transmitted wave is also not normal to the ground surface, in general. For many ground surfaces, however, it is a good approximation to assume that the propagation direction of the transmitted wave *is* normal to the ground surface, irrespective of the propagation direction of the incident wave. These ground surfaces are called ***locally reacting*** ground surfaces (see also Sec. D.3). Thus we have $v_c \approx v_{c,n}$ for a locally reacting ground surface. Consequently, the impedance of a locally reacting ground surface is approximately equal to the characteristic impedance of the ground material. In Sec. D.3 we will derive a general relation between the impedance of a ground surface and the characteristic impedance of the ground material.

The impedance of an acoustically absorbing surface is a complex number (or rather, a complex function of frequency), as the pressure and the fluid velocity are not in phase with each other, in general. The impedance of an acoustically hard surface is infinite, as normal movement of air is not possible at a hard surface ($v_{c,n} = 0$). Thus, the impedance of a surface is a measure of the resistance of the surface against normal movement of air.

Not only the characteristic impedance of the ground material but also the characteristic impedance of air, *i.e.* the propagation medium above the ground surface, plays a role in the ground reflection of sound waves. The characteristic impedance of air is evaluated in Sec. C.3. Models for the characteristic impedance of porous ground media are described in Sec. C.4.

C.3 Impedance of air

We consider a harmonic plane sound wave traveling in air. The sound pressure p is written as

$$\begin{aligned} &p(x,t) = \mathrm{Re}\,[p_c(x)\exp(-i\omega t)] \\ &\text{with } p_c(x) = p_0\exp(ikx), \end{aligned} \tag{C.1}$$

where x is the propagation distance and p_0 is a constant. The function $p(x,t)$ satisfies the one-dimensional wave equation

$$\frac{\partial^2 p}{\partial x^2} - \frac{1}{c^2}\frac{\partial^2 p}{\partial t^2} = 0, \tag{C.2}$$

where $c = \omega/k$ is the adiabatic sound speed. This equation follows from the three-dimensional wave equation (A.14) and $\nabla^2 p = \partial^2 p/\partial x^2$. In this one-dimensional case, the linear acoustic equations (A.12) and (A.13) become

$$-\frac{\partial v}{\partial x} = \frac{1}{\rho c^2}\frac{\partial p}{\partial t} \tag{C.3}$$

$$\rho\frac{\partial v}{\partial t} = -\frac{\partial p}{\partial x}, \tag{C.4}$$

where ρ is the density of air ($\rho \equiv \rho_{\mathrm{av}}$) and $v = v(x,t)$ is the fluid velocity.

The sound pressure given by Eq. (C.1) corresponds to a fluid velocity v given by

$$\begin{aligned} &v(x,t) = \mathrm{Re}\,[v_c(x)\exp(-i\omega t)] \\ &\text{with } v_c(x) = v_0\exp(ikx), \end{aligned} \tag{C.5}$$

where v_0 is a constant. This follows from the wave equation (C.2) with p replaced by v, which can be derived from the linear acoustic equations (C.3) and (C.4). From Eqs. (C.1) and (C.5) we see that the ratio $p_c(x)/v_c(x)$ is constant, *i.e.* independent of x. This ratio is called the (specific) acoustic impedance ζ of the medium, air in this case. The value of the acoustic impedance of air, denoted as ζ_{air}, can be derived from the linear acoustic equations (C.3) and (C.4). Substitution of Eqs. (C.1) and (C.5) in either Eq. (C.3) or Eq. (C.4) yields

$$\zeta_{\mathrm{air}} = \rho c. \tag{C.6}$$

This equation can also be derived directly from Eqs. (A.19) and (C.1). From Eqs. (A.15) and (A.16) we find $\zeta_{\mathrm{air}} = 427\ \mathrm{kg{\cdot}m^{-2}{\cdot}s^{-1}}$ at temperature $T_0 = 273$ K.

For spherical waves, the ratio p_c/v_c approaches the value ρc in the far-field region (see Sec. B.3). Thus, the impedance for spherical waves is equal to the impedance for plane waves, except at small distance from the source.

C.4 Impedance of porous media

Many natural grounds can be modeled as porous media. The (specific) acoustic impedance ζ of a porous medium is defined in the same way as the impedance of the medium 'air' was defined in the previous section, *i.e.* as the ratio p_c/v_c, where p_c and v_c are the complex pressure and velocity amplitudes, respectively, of a harmonic plane wave traveling in the medium. The normalized (specific) acoustic impedance Z is defined as $Z = \zeta/\zeta_{air}$. This quantity plays an important role in the reflection of sound waves by a ground surface (see Sec. C.5 and Appendix D).

Zwikker and Kosten [161] and Attenborough [4, 5, 6, 7] developed various models for the impedance of porous materials. In this section we first follow the derivation by Zwikker and Kosten of the impedance of a porous material with a rigid frame. Next we give an expression for the impedance developed by Attenborough, and finally an empirical expression developed by Delany and Bazley [39].

We consider a plane sound wave traveling in a porous material with a rigid frame. The sound wave causes a vibration of the air in the pores of the material, while the rigid frame does not vibrate. The expressions (C.1) and (C.5) are also valid in this case, but the value of the wave number k is different from its value in free air. The wave number contains an imaginary part, which depends on the flow resistance, *i.e.* the resistance that the frame offers to an air flow through the material. The imaginary part corresponds to a reduction of the amplitude of the sound wave with increasing propagation distance, *i.e.* an attenuation of the sound wave.

The linear acoustic equations (C.3) and (C.4) can be generalized as follows for the porous material (Zwikker and Kosten [161]):

$$-\frac{\partial v}{\partial x} = \frac{\Omega}{\rho c^2}\frac{\partial p}{\partial t} \tag{C.7}$$

$$\frac{c_s}{\Omega}\rho\frac{\partial v}{\partial t} + \sigma v = -\frac{\partial p}{\partial x}, \tag{C.8}$$

where Ω is the porosity, c_s is the structure constant, and σ is the flow resistivity of the porous material. The porosity Ω is defined as the volume fraction of air in the material. Equation (C.7) shows that the pressure fluctuations generated by a velocity gradient $\partial v/\partial x$ are a factor of $1/\Omega$ larger in the porous material than in free air, simply because the available volume is a factor of Ω smaller. We assume that the air vibrations in the porous material are approximately adiabatic, so the constant c in Eq. (C.7) can be approximated by the adiabatic sound speed in free air, which is given by Eq. (A.9). The flow resistivity σ of a porous material is defined as the ratio $-(\partial p/\partial x)/v$ in a situation with a steady flow through the material, as follows from Eq. (C.8) with $\partial v/\partial t = 0$. The first term on the left-hand side of Eq. (C.8) differs from the corresponding term in Eq. (C.4) by the factor c_s/Ω. The factor $1/\Omega$ accounts for the reduced

available volume in the porous material. The structure constant c_s accounts for the specific structure of the pores and the frame of the material. Zwikker and Kosten [161] indicated that experimental values of c_s are often in the range between 3 and 7.

Substitution of Eqs. (C.1) and (C.5) into Eqs. (C.7) and (C.8) gives

$$k = \frac{\omega}{c}\sqrt{q_c \Omega} \tag{C.9}$$

$$Z = \sqrt{q_c/\Omega} \tag{C.10}$$

with

$$q_c = \frac{c_s}{\Omega} + i\frac{\sigma}{\rho\omega}. \tag{C.11}$$

We give here not only the expression for the impedance Z but also the expression for the complex wave number k, because the impedance of a layered ground depends on k and Z (see Sec. C.6).

If the sound propagation in the porous material is better approximated as an isothermal process than as an adiabatic process, the adiabatic sound speed c in Eq. (C.9) should be replaced by the isothermal sound speed $c\gamma^{-1/2}$. Figure C.2 shows two examples of the impedance as a function of frequency, calculated with Eqs. (C.10) and (C.11). For this figure we used the adiabatic sound speed, and the values $c_s = 3$, $\Omega = 0.3$, and $\rho = 1.19$ kg·m^{-3}. The figure shows also the impedance calculated with two other models, which are described below.

We note that the sign of the imaginary parts of k and Z is related to the (arbitrary) choice of the signs of the arguments of the exponential functions in Eqs. (C.1) and (C.5). One can also choose the opposite signs: $p(x,t) = \mathrm{Re}\,[p_c(x)\exp(+i\omega t)]$ with $p_c(x) = p_0\exp(-ikx)$, and similarly for the velocity. Both choices correspond to a wave traveling in the positive x direction. If the opposite signs are chosen instead of the signs chosen in Eqs. (C.1) and (C.5), then Eqs. (C.9) and (C.10) are obtained with q_c replaced by its complex conjugate q_c^*, *i.e.* with opposite imaginary part.

Attenborough [4, 5, 7, 10, 11] developed various more refined models for the impedance of porous materials (see also Ref. [144]). Here we give the expressions of Attenborough's four-parameter model [5]:

$$k = \frac{\omega}{c}\sqrt{\gamma\Omega}\sqrt{\left(\frac{4}{3} - \frac{\gamma-1}{\gamma}N_{\mathrm{pr}}\right)\frac{q^2}{\Omega} + i\frac{s_f^2\sigma}{\rho\omega}} \tag{C.12}$$

$$Z = \left(\frac{4q^2}{3\Omega} + i\frac{s_f^2\sigma}{\rho\omega}\right)\frac{\omega/c}{k}, \tag{C.13}$$

where $N_{\mathrm{pr}} \approx 0.7$ is the Prandtl number, s_f is the pore shape factor ratio, and $q^2 \equiv \Omega^{-g}$ is the square of the tortuosity q, where g is a grain shape factor.

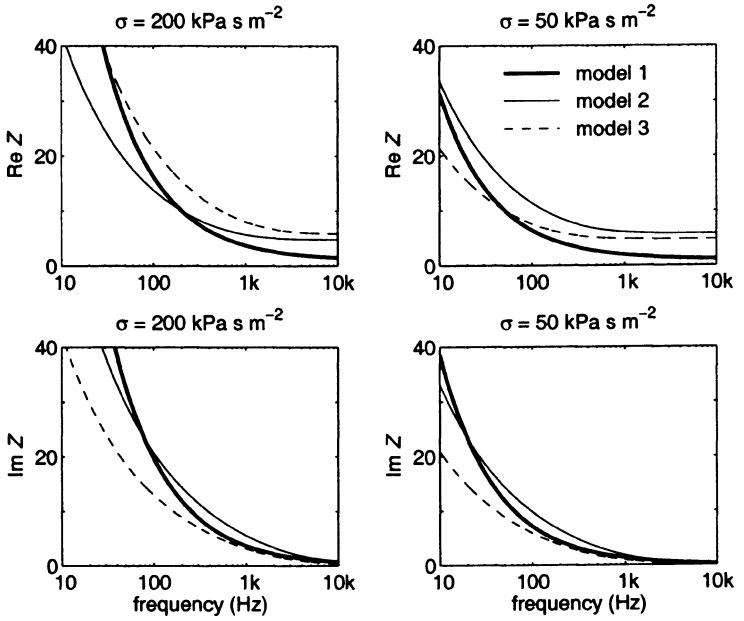

Figure C.2. Real and imaginary parts of the normalized impedance Z as a function of frequency, for flow resistivity $\sigma = 200$ kPa·s·m^{-2} (left column) and $\sigma = 50$ kPa·s·m^{-2} (right column). Model 1 represents Eq. (C.15) due to Delany and Bazley [39]. Model 2 represents Eq. (C.13) due to Attenborough [5]. Model 3 represents Eq. (C.10) due to Zwikker and Kosten [161].

Attenborough presents several comparisons of the four-parameter model with experimental data for grassland, sandy soil, and forest floors, treating the four parameters σ, g, s_f, and Ω as more or less adjustable parameters. The values of the parameters vary considerably for different types of natural ground. Typical values are $g = 0.5$, $s_f = 0.75$, and $\Omega = 0.3$, while σ varies in the range between roughly 10 and 1000 kPa·s·m^{-2}. For the numerical examples presented in this book we used the values $g = 0.5$, $\Omega = 0.3$, $N_{pr} = 0.7$, and $s_f^2/\rho = 0.75^2/1.19$ m^3·kg^{-1} in Eqs. (C.12) and (C.13).

An empirical impedance model for fibrous absorbing materials, *e.g.* glass-fiber and mineral-wool materials, was developed by Delany and Bazley [39]:

$$k = \frac{\omega}{c}\left[1 + 0.0858\left(\frac{\sigma}{f}\right)^{0.70} + i\,0.175\left(\frac{\sigma}{f}\right)^{0.59}\right] \tag{C.14}$$

$$Z = 1 + 0.0511\left(\frac{\sigma}{f}\right)^{0.75} + i\,0.0768\left(\frac{\sigma}{f}\right)^{0.73}. \tag{C.15}$$

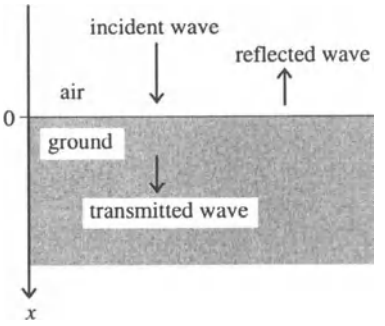

Figure C.3. Normal reflection of a plane wave by a ground surface.

These empirical relations are based on experimental data for values of f/σ ranging from 0.01 to 1.0 $m^3 \cdot kg^{-1}$. Chessel [23] showed that the relations also give good agreement with experimental data for grassland, with the flow resistivity σ varying between 100 and 300 $kPa \cdot s \cdot m^{-2}$, and f/σ ranging from 10^{-4} to 0.1 $m^3 \cdot kg^{-1}$ (see also Ref. [146]).

C.5 Normal reflection by a ground surface

The normalized impedance Z introduced in the previous section is used for the modeling of the reflection of sound waves by ground surfaces and other surfaces. As an example we consider the reflection of a harmonic plane wave by a homogeneous ground surface, with the propagation direction normal to the ground surface (see Fig. C.3). We choose the x axis along the propagation direction, with the ground surface at $x = 0$. In the air above the ground surface there is an incident wave and a reflected wave. In the (porous) ground there is only a transmitted wave.

The complex pressure amplitude p_c in the air above the ground surface is equal to the sum of the complex pressure amplitude of the incident wave and the complex pressure amplitude of the reflected wave:

$$p_c(x) = p_0[\exp(ikx) + R_p \exp(-ikx)], \tag{C.16}$$

where R_p is a complex quantity that is called the plane-wave reflection coefficient and p_0 is a constant. The corresponding complex velocity amplitude v_c in the air above the ground surface follows from Eq. (C.4):

$$v_c(x) = \frac{p_0}{\rho c}[\exp(ikx) - R_p \exp(-ikx)]. \tag{C.17}$$

The ratio $p_c(x)/v_c(x)$ is continuous at $x = 0$, so $p_c(x)/v_c(x)$ just above the ground surface is equal to $p_c(x)/v_c(x)$ just below the ground surface. The

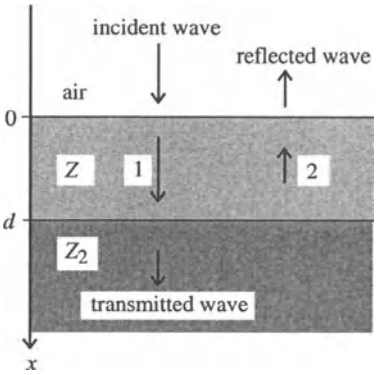

Figure C.4. Normal reflection of a plane wave by a layer with thickness d and normalized impedance Z, backed by a second material with normalized impedance Z_2. The waves traveling in the layer in the positive and negative x directions are labeled with 1 and 2, respectively.

ratio $p_c(x)/v_c(x)$ just below the ground surface is equal to the characteristic impedance ρcZ of the ground. From Eqs. (C.16) and (C.17) for $x = 0$ we find

$$Z = \frac{1 + R_p}{1 - R_p}, \tag{C.18}$$

which implies

$$R_p = \frac{Z - 1}{Z + 1}. \tag{C.19}$$

We see that the plane-wave reflection coefficient for normal incidence depends only on the normalized ground impedance.

C.6 Normal reflection by a layered ground

In the previous section we modeled a ground surface as a semi-infinite porous material. One can also model a ground surface (or any other reflecting surface) as a layer of porous material with normalized impedance Z, backed by a second material with normalized impedance Z_2 (see Fig. C.4). In this case we will see that the ratio $p_c(x)/v_c(x)$ varies with x, in the layer between $x = 0$ and $x = d$ (d is the thickness of the layer). We denote this ratio as $\rho cZ_{\text{layer}}(x)$. While the normalized impedance Z is a (frequency-dependent) material constant, the normalized impedance Z_{layer} is not a material constant, as Z_{layer} varies with x.

The normalized impedance Z in expression (C.19) for the reflection coefficient should now be replaced by the normalized impedance $Z_{\text{layer}}(x = 0)$ at

the ground surface at $x = 0$. An expression for $Z_{\text{layer}}(x = 0)$ is derived in the remainder of this section.

The incident wave in Fig. C.4 is a harmonic plane wave traveling in the positive x direction. Part of the wave is reflected at the interface at $x = 0$ and part of the wave is transmitted into the porous material. Part of the transmitted wave is reflected at the interface at $x = d$. The total complex pressure amplitude in the layer between $x = 0$ and $x = d$ is written as

$$p_c(x) = p_1 \exp(ik[x - d]) + p_2 \exp(-ik[x - d]), \tag{C.20}$$

where p_1 and p_2 are constants and k is the (complex) wave number in the layer [given by Eq. (C.9), Eq. (C.12), or Eq. (C.14), for example]. The corresponding complex velocity amplitude is

$$v_c(x) = \frac{p_1}{\rho c Z} \exp(ik[x - d]) - \frac{p_2}{\rho c Z} \exp(-ik[x - d]). \tag{C.21}$$

At $x = d$ we have $p_c(d)/v_c(d) = \rho c Z_2$. Substitution of $p_c(d)$ and $v_c(d)$ from Eqs. (C.20) and (C.21) gives the relation

$$\frac{p_2}{p_1} = \frac{Z_2 - Z}{Z_2 + Z}. \tag{C.22}$$

The impedance of the layer $\rho c Z_{\text{layer}}$ was defined as the ratio $p_c(x)/v_c(x)$. From Eqs. (C.20) to (C.22) we find

$$Z_{\text{layer}}(x = 0) = Z \frac{Z_2 \cosh(-ikd) + Z \sinh(-ikd)}{Z_2 \sinh(-ikd) + Z \cosh(-ikd)}. \tag{C.23}$$

For a rigid backing we have $Z_2 = \infty$ and we find $Z_{\text{layer}}(x = 0) = Z \coth(-ikd)$ from Eq. (C.23).

For $d \to \infty$, we find $Z_{\text{layer}}(x = 0) \to Z$ from Eq. (C.23). In practice the difference between $Z_{\text{layer}}(x = 0)$ and Z is negligible for layers with a thickness larger than typically 0.1 m. For thin layers ($d < 0.1$ m), however, the normalized impedance $Z_{\text{layer}}(x = 0)$ may deviate considerably from Z.

Appendix D

Reflection of sound waves

D.1 Introduction

The reflection of sound waves by a ground surface in a non-refracting atmosphere can be described with a reflection coefficient, which is a function of the ground impedance. The reflection coefficient for plane waves is called the plane-wave reflection coefficient; the reflection coefficient for spherical waves is called the spherical-wave reflection coefficient. In this appendix we derive expressions for these reflection coefficients.

In Sec. D.2 we describe the reflection of plane waves by a ground surface. We derive an expression for the plane-wave reflection coefficient for an arbitrary angle of incidence [in Secs. C.5 and C.6 we described the reflection of plane waves for normal incidence].

In Sec. D.3 we describe the local reaction approximation, which was mentioned before in Sec. C.2. The impedance of a locally reacting ground surface is equal to the characteristic impedance of the ground medium, evaluated at the surface. If the local reaction approximation is not valid, the ground surface is called an extended reacting ground surface. For many natural ground surfaces, however, the local reaction approximation is a good approximation.

In Sec. D.4 we describe the reflection of spherical waves by a ground surface; in Sec. D.4.1 we consider a locally reacting ground surface and in Sec. D.4.2 we consider an extended reacting ground surface. The derivation presented in Sec. D.4 can be considered as an analytical application of the FFP method (see Appendix F) for the case of a non-refracting atmosphere.

D.2 Reflection of plane waves

In this section we describe the ground reflection of a harmonic plane sound wave for an arbitrary angle of incidence. We use a rectangular xyz coordinate system with the ground surface at $x = 0$ and the propagation direction in the

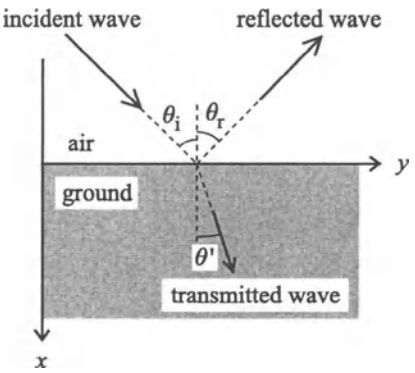

Figure D.1. Oblique reflection of a plane wave by a ground surface.

xy plane (see Fig. D.1).

We write the complex pressure amplitude of the incident sound wave as $p_{c,i}(\mathbf{r}) = p_0 \exp(iks)$, where p_0 is a constant, $k = \omega/c$ is the wave number, and s is the propagation distance. We have $s = \mathbf{r}\cdot\mathbf{n}$, where $\mathbf{r} = (x, y, z)$ is the position vector and $\mathbf{n} = (\cos\theta_i, \sin\theta_i, 0)$ is the unit vector in the propagation direction; θ_i is the angle of incidence. This gives

$$p_{c,i} = p_0 \exp(ik_x x + ik_y y) \tag{D.1}$$

with $k_x = k\cos\theta_i$ and $k_y = k\sin\theta_i$.

The incident wave is partly reflected and partly transmitted into the ground, in general. The complex pressure amplitude of the reflected wave is denoted as $p_{c,r}(\mathbf{r})$. The total complex pressure amplitude in the air above the ground is $p_c = p_{c,i} + p_{c,r}$. As the incident wave satisfies the Helmholtz equation (A.20), the reflected wave must also be a solution of the Helmholtz equation.

We first consider a rigid ground surface. In this case no fluid movement is possible in the direction normal to the surface. Therefore the x component of the fluid velocity amplitude, denoted as $v_{c,x}$, vanishes at the surface. Equation (A.5) gives in this case $\partial p_c/\partial x = 0$, or $\partial p_{c,r}/\partial x = -\partial p_{c,i}/\partial x$, for $x = 0$. We find

$$\partial p_{c,r}/\partial x = -ik_x p_0 \exp(ik_y y) \tag{D.2}$$

for $x = 0$. The solution $p_{c,r}$ must satisfy this equation and the Helmholtz equation. We write

$$p_{c,r} = p_0' \exp(-ik_x' x + ik_y' y) \tag{D.3}$$

with $k_x' = k\cos\theta_r$ and $k_y' = k\sin\theta_r$, where p_0' is a constant and θ_r is the angle of reflection (see Fig. D.1). As we have $k_x'^2 + k_y'^2 = k^2$, the complex pressure

amplitude $p_{c,r}$ given by Eq. (D.3) satisfies the Helmholtz equation. Substitution of Eq. (D.3) into Eq. (D.2) gives

$$-ik'_x p'_0 \exp(ik'_y y) = -ik_x p_0 \exp(ik_y y). \tag{D.4}$$

This equation and the equation $k'^2_x + k'^2_y = k^2$ can only be satisfied for arbitrary y if we have $k'_x = k_x$, $k'_y = k_y$, and $p'_0 = p_0$. This implies $\theta_i = \theta_r$, so the angle of incidence is equal to the angle of reflection. Equation (D.3) becomes

$$p_{c,r} = p_0 \exp(-ik_x x + ik_y y). \tag{D.5}$$

It should be noted that we assume here that the surface is perfectly flat. In the case of a rough surface, sound is reflected in all directions instead of a single direction [68, 143, 154]. As described in Refs. [10, 11], surface roughness can be taken into account by using an effective impedance.

For a ground surface that is not rigid, *e.g.* the surface of a porous material, the boundary condition $v_{c,x} = 0$ is replaced by the condition that the complex pressure amplitude p_c and the x component $v_{c,x}$ of the complex velocity amplitude must be continuous at $x = 0$. This implies

$$\left(\frac{p_c}{v_{c,x}}\right)_{x=-\epsilon} = \left(\frac{p_c}{v_{c,x}}\right)_{x=+\epsilon} \tag{D.6}$$

with $\epsilon > 0$, $\epsilon \to 0$. In Sec. C.2 we defined the right-hand side of Eq. (D.6) as the impedance of the ground surface. We denote this impedance as $\zeta_s = Z_s \rho c$, where Z_s is the normalized impedance of the ground surface. The boundary condition (D.6) becomes

$$\left(\frac{p_c}{v_{c,x}}\right)_{x=-\epsilon} = Z_s \rho c \tag{D.7}$$

with $\epsilon > 0$, $\epsilon \to 0$.

For many natural ground surfaces we have $\theta' \approx 0$ (see Fig. D.1). These surfaces are called *locally reacting* surfaces (see Sec. D.3). From $\theta' \approx 0$ we have $v_{c,x} \approx v_c$ for $x > 0$. This implies that the impedance $Z_s \rho c$ of a locally reacting ground surface is equal to the characteristic impedance $Z \rho c$ of the ground medium [which can be calculated with Eq. (C.10), Eq. (C.13), Eq. (C.15), or Eq. (C.23)].

With Eq. (A.19) and $p_c = p_{c,i} + p_{c,r}$, Eq. (D.7) gives

$$p_{c,i} + p_{c,r} = \frac{Z_s \rho c}{i\omega\rho}\left(\frac{\partial p_{c,i}}{\partial x} + \frac{\partial p_{c,r}}{\partial x}\right) \tag{D.8}$$

for $x = 0$. Substitution of Eq. (D.1) into this equation gives

$$p_0 \exp(ik_y y) + p_{c,r}(x = 0) = Z_s \cos\theta_i p_0 \exp(ik_y y) + \frac{Z_s}{ik}\left(\frac{\partial p_{c,r}}{\partial x}\right)_{x=0}. \tag{D.9}$$

As before, the solution $p_{c,r}$ must satisfy this equation and the Helmholtz equation. We write

$$p_{c,r} = p_0 R_p \exp(-ik'_x x + ik'_y y) \tag{D.10}$$

with $k'_x = k\cos\theta_r$ and $k'_y = k\sin\theta_r$. The quantity R_p is called the plane-wave reflection coefficient, which will be determined below (the plane-wave reflection coefficient has already been introduced in Sec. C.5 for the special case of normal reflection of a plane wave). Substitution of Eq. (D.10) into Eq. (D.9) gives

$$p_0 \exp(ik_y y) + p_0 R_p \exp(ik'_y y) = \\ Z_s \cos\theta_i p_0 \exp(ik_y y) - Z_s \cos\theta_r p_0 R_p \exp(ik'_y y). \tag{D.11}$$

This can only be satisfied for arbitrary y if we have $k'_y = k_y$, so we find again $\theta_i = \theta_r$. The angles θ_i and θ_r will be denoted as θ. Equation (D.11) gives

$$Z_s = \frac{1}{\cos\theta}\,\frac{1+R_p}{1-R_p}, \tag{D.12}$$

which implies

$$R_p = \frac{Z_s\cos\theta - 1}{Z_s\cos\theta + 1}. \tag{D.13}$$

We see that the reflection coefficient R_p varies with the angle of incidence. The reflection coefficient approaches -1 if θ approaches $\frac{1}{2}\pi$ (grazing incidence). For a rigid ground surface we have $Z_s = \infty$ and $R_p = 1$.

D.3 Local reaction approximation

From the previous section we have the following expression for the complex pressure amplitude p_c in the region above the ground surface ($x < 0$):

$$p_c = p_0[\exp(ik_x x + ik_y y) + R_p \exp(-ik_x x + ik_y y)] \text{ for } x < 0. \tag{D.14}$$

The corresponding complex amplitude of the normal velocity follows from Eq. (A.19):

$$v_{c,x} = \frac{\cos\theta}{\rho c} p_0[\exp(ik_x x + ik_y y) - R_p \exp(-ik_x x + ik_y y)] \text{ for } x < 0. \tag{D.15}$$

In the region below the ground surface ($x > 0$), the transmitted wave travels at an angle θ' with the x axis (see Fig. D.1). We write the complex amplitudes of the pressure and the normal velocity of the transmitted wave as follows:

$$p_c = p_0 T_p \exp(ik'_x x + ik'_y y) \text{ for } x > 0 \tag{D.16}$$

$$v_{c,x} = \frac{\cos\theta'}{\rho' c'} p_0 T_p \exp(ik'_x x + ik'_y y) \text{ for } x > 0 \tag{D.17}$$

with $k'_x = k' \cos\theta'$ and $k'_y = k' \sin\theta'$; we have used Eq. (A.19) to derive Eq. (D.17) from Eq. (D.16). The quantity T_p is called the plane-wave transmission coefficient. We have introduced here a density ρ', a wave number k', and a sound speed c' for the ground material, with $k' = \omega/c'$. We assume that ρ', k', and c' are real quantities, so the characteristic impedance $\rho' c'$ of the ground material is also real. Later we will generalize the results for grounds with a complex wave number and a complex impedance, such as the porous media considered in Sec. C.4.

Continuity of the pressure at $x = 0$ implies that Eqs. (D.14) and (D.16) should give equal values of p_c at $x = 0$. This yields

$$(1 + R_p) \exp(ik_y y) = T_p \exp(ik'_y y). \tag{D.18}$$

Continuity of the normal velocity at $x = 0$ implies that Eqs. (D.15) and (D.17) should give equal values of $v_{c,x}$ at $x = 0$. This yields

$$\frac{\cos\theta}{\rho c}(1 - R_p) \exp(ik_y y) = \frac{\cos\theta'}{\rho' c'} T_p \exp(ik'_y y). \tag{D.19}$$

Equations (D.18) and (D.19) should hold for arbitrary y, which implies $k_y = k'_y$, or

$$\frac{\sin\theta}{c} = \frac{\sin\theta'}{c'}. \tag{D.20}$$

This is Snell's law of refraction. Using $k_y = k'_y$ in Eqs. (D.18) and (D.19), we find

$$R_p = \frac{\rho' c' \cos\theta - \rho c \cos\theta'}{\rho' c' \cos\theta + \rho c \cos\theta'}. \tag{D.21}$$

The normalized impedance of the ground surface, $Z_s = (p_c/v_{c,x})/\rho c$, follows from Eqs. (D.16) and (D.17):

$$Z_s = \frac{1}{\cos\theta'} \frac{\rho' c'}{\rho c}. \tag{D.22}$$

If we use Eq. (D.22), we find that Eqs. (D.21) and (D.13) for the reflection coefficient are identical.

In the case of normal incidence ($\theta = 0$ and $\theta' = 0$), the normalized impedance Z_s of the ground surface is equal to the normalized characteristic impedance Z of the ground material (see Sec. C.2). Hence, Eq. (D.22) implies $Z = \rho' c'/\rho c$ and $Z_s = Z/\cos\theta'$. From Snell's law (D.20) we have $\sin\theta' = (k/k')\sin\theta$, and we find

$$Z_s = \frac{Z}{\sqrt{1 - (k/k')^2 \sin^2\theta}}. \tag{D.23}$$

We assume a homogeneous ground medium here, with normalized characteristic impedance Z. If the ground consists of a thin layer on top of a different material, the normalized impedance Z in Eq. (D.23) should be replaced by the normalized impedance $Z_{\text{layer}}(x = 0)$, as described in Sec. C.6.

It is instructive to consider the trivial case in which there is no difference between the ground medium and the air above the ground, so that we have $\rho' = \rho$ and $c' = c$. In this case, Eqs. (D.18) to (D.21) imply $\theta' = \theta$, $R_{\text{p}} = 0$, and $T_{\text{p}} = 1$, so there is no reflected wave and the transmitted wave is equal to the incident wave. In all other cases, with $\rho' \neq \rho$ or $c' \neq c$ (or both), there is a reflected wave ($R_{\text{p}} \neq 0$) and the transmitted wave is different from the incident wave ($T_{\text{p}} \neq 1$).

If the sound speed c' in the ground material is small compared with the sound speed c in the air above the ground, Eq. (D.20) implies $\theta' \approx 0$, so the propagation direction of the transmitted wave is approximately parallel to the x axis. In this case the ground surface is called a *locally reacting* ground surface [92]. Equation (D.22) implies that the normalized impedance of a locally reacting ground surface is $Z_{\text{s}} = \rho' c'/\rho c$, which is independent of the angle of incidence θ.

In general, however, the normalized impedance of a ground surface depends on the angle of incidence, as follows from Eq. (D.23). This means that the incident wave causes a 'reaction' at a point on the ground surface that depends on the pressure distribution in a region around this point. Such a reaction is called an *extended reaction.*

If the normalized impedance of a ground surface is independent of the angle of incidence, the 'reaction' at a point on the ground surface depends only on the pressure at this point, *i.e.* the local pressure. This explains the name *local reaction.*

The above results can be generalized for a ground with complex characteristic impedance $\rho c Z$ and complex wave number k'. These complex quantities can be calculated with the models described in Sec. C.4 for porous media (k' was denoted as k in Sec. C.4). We define a complex sound speed $c' = \omega/k'$ and a complex density $\rho' = \rho c Z/c'$ of the ground, so we have $Z = \rho' c'/\rho c$. The derivation of Eqs. (D.20) to (D.23) remains valid if we consider $\cos\theta'$ and $\sin\theta'$ as complex quantities that satisfy the relation $\cos^2\theta' + \sin^2\theta' = 1$. From Snell's law (D.20) we have $k_y = k'_y$, so k'_y is real, as $k_y = k\sin\theta$ is real. The relation $k_x'^2 + k_y'^2 = k'^2$ implies that k'_x is complex, as k' is complex. If we write $k'_x = \text{Re}k'_x + i\text{Im}k'_x$, the imaginary part $\text{Im}k'_x$ yields an exponential attenuation factor $\exp(-x\,\text{Im}k'_x)$ in Eqs. (D.16) and (D.17). The propagation angle of the plane attenuating wave below the ground surface is equal to $\arctan(k'_y/\text{Re}k'_x)$, which differs from θ' unless k'_x is real. The plane-wave reflection coefficient is given by Eq. (D.21), or by Eq. (D.13) with normalized impedance Z_{s} of the ground surface given by Eq. (D.23). The local reaction approximation corresponds to the approximation $|k/k'| \ll 1$ in this case. For many natural ground surfaces this is a good approximation, as can be verified with the models described in Sec. C.4.

Unless indicated otherwise, we will assume that the ground surface is locally

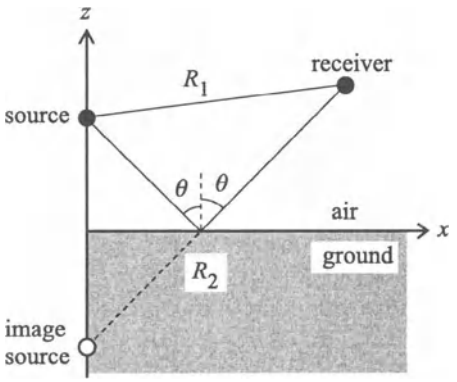

Figure D.2. Point source and receiver above a ground surface. R_1 is the length of the direct path from the source to the receiver. R_2 is the length of the reflected path, which is equal to the distance from the image source to the receiver.

reacting, so that we have $Z_s = Z$.

D.4 Reflection of spherical waves

In this section we develop an analytical solution for the sound field of a point source in a non-refracting atmosphere above a ground surface. We consider a locally reacting ground surface in Sec. D.4.1 and an extended reacting ground surface in Sec. D.4.2.

D.4.1 Locally reacting ground surface

We consider the geometry shown in Fig. D.2. We use a rectangular xyz coordinate system, with horizontal x and y coordinates; the z coordinate represents height above the ground surface. The source is at position $\mathbf{r}_s = (0, 0, z_s)$ and the receiver is at position $\mathbf{r} = (x, y, z)$ (Figure D.2 shows the geometry for the case $y = 0$). The source is a harmonic monopole source, with angular frequency ω. The source is characterized by the free field, with complex pressure amplitude $p_c = S \exp(ikR_1)/R_1$, where $R_1 = |\mathbf{r} - \mathbf{r}_s|$ is the radial distance from the source. We choose $S = 1$ Pa·m, so we have $p_c = \exp(ikR_1)/R_1$; we note that the right-hand side has not the dimension of a pressure, due to the omission of S. Atmospheric absorption is ignored (see Sec. 3.4).

In this section, the wave number, sound speed, and density in the air above the ground are denoted as k_1, c_1, and ρ_1, respectively; we have $c_1 = \omega/k_1$. The ground is characterized by wave number k_2 and normalized impedance Z. We define $c_2 \equiv \omega/k_2$ as the complex sound speed in the ground, and $\rho_2 \equiv Z\rho_1 c_1/c_2$ as the complex density of the ground, so we have $Z = \rho_2 c_2/\rho_1 c_1$ (*cf.* Sec. D.3).

The complex pressure amplitude $p_c(x,y,z) \equiv p_c(\mathbf{r})$ is written as

$$p_c = \begin{cases} p_1 & \text{for } z \geq 0 \\ p_2 & \text{for } z \leq 0 \end{cases} \tag{D.24}$$

with $p_1 = p_1(x,y,z)$ and $p_2 = p_2(x,y,z)$. We have (see Secs. A.3 and A.4)

$$(\nabla^2 + k_1^2)p_1 = -4\pi\delta(\mathbf{r} - \mathbf{r}_s) \qquad \text{for } z \geq 0 \tag{D.25}$$

$$(\nabla^2 + k_2^2)p_2 = 0 \qquad \text{for } z \leq 0. \tag{D.26}$$

We apply a double Fourier transformation $(x,y) \to (k_x, k_y)$ to these equations:

$$\left[\frac{\partial^2}{\partial z^2} + (k_1^2 - k_x^2 - k_y^2)\right] P_1 = -4\pi\delta(z - z_s) \qquad \text{for } z \geq 0 \tag{D.27}$$

$$\left[\frac{\partial^2}{\partial z^2} + (k_2^2 - k_x^2 - k_y^2)\right] P_2 = 0 \qquad \text{for } z \leq 0, \tag{D.28}$$

where the Fourier transform pairs (p_j, P_j) with $j = 1, 2$ are defined by

$$P_j(k_x, k_y, z) = \int_{-\infty}^{\infty}\int_{-\infty}^{\infty} \exp(-ik_x x - ik_y y) p_j(x,y,z)\, dx\, dy \tag{D.29}$$

$$p_j(x,y,z) = \frac{1}{(2\pi)^2}\int_{-\infty}^{\infty}\int_{-\infty}^{\infty} \exp(ik_x x + ik_y y) P_j(k_x, k_y, z)\, dk_x\, dk_y. \tag{D.30}$$

The solution of Eqs. (D.27) and (D.28) must satisfy four boundary conditions:

$$P_1(k_x, k_y, 0) = P_2(k_x, k_y, 0) \tag{D.31}$$

$$\frac{1}{\rho_1}\left(\frac{\partial P_1}{\partial z}\right)_{z=0} = \frac{1}{\rho_2}\left(\frac{\partial P_2}{\partial z}\right)_{z=0} \tag{D.32}$$

$$P_1(k_x, k_y, z_s + \epsilon) = P_1(k_x, k_y, z_s - \epsilon) \tag{D.33}$$

$$\left(\frac{\partial P_1}{\partial z}\right)_{z=z_s+\epsilon} - \left(\frac{\partial P_1}{\partial z}\right)_{z=z_s-\epsilon} = -4\pi \tag{D.34}$$

with $\epsilon > 0$, $\epsilon \to 0$. Equation (D.31) represents continuity of the pressure at the ground surface. Equation (D.32) represents continuity of the normal velocity at the ground surface; here Eq. (A.19) has been used. Equation (D.33) represents continuity of the pressure at the source height. Equation (D.34) shows that the fluid velocity is discontinuous at the source height, as the directions of the velocities just above the source and just below the source are opposite to each other. To prove Eq. (D.34), we integrate Eq. (D.27) over z from $z_s - \epsilon$ to $z_s + \epsilon$:

$$\int_{z_s-\epsilon}^{z_s+\epsilon} \frac{\partial}{\partial z}\left(\frac{\partial P_1}{\partial z}\right) dz + (k_1^2 - k_x^2 - k_y^2)\int_{z_s-\epsilon}^{z_s+\epsilon} P_1 dz = -4\pi. \tag{D.35}$$

For $\epsilon \to 0$, the second term on the left-hand side vanishes and we find Eq. (D.34).

We write the solution of Eqs. (D.27) and (D.28) as follows:

$$\begin{aligned} P_1 &= C_1 \exp(ik_{1z}z) && \text{for } z \geq z_s \\ P_1 &= C_2 \exp(ik_{1z}z) + C_3 \exp(-ik_{1z}z) && \text{for } 0 \leq z \leq z_s \\ P_2 &= C_4 \exp(-ik_{2z}z) && \text{for } z \leq 0, \end{aligned} \tag{D.36}$$

where C_1, C_2, C_3, and C_4 are constants and the vertical wave number components k_{1z} and k_{2z} are defined by

$$k_{jz}^2 = k_j^2 - k_x^2 - k_y^2 \tag{D.37}$$

for $j = 1, 2$. The constants C_1, C_2, C_3, and C_4 follow from the boundary conditions (D.31) to (D.34), and Eq. (D.36) becomes

$$P_1 = A\{\exp(ik_{1z}|z - z_s|) + R(k_{1z})\exp(ik_{1z}[z + z_s])\} \quad \text{for } z \geq 0 \tag{D.38}$$

$$P_2 = A[1 + R(k_{1z})]\exp(ik_{1z}z_s - ik_{2z}z) \quad \text{for } z \leq 0 \tag{D.39}$$

with

$$A = \frac{2\pi i}{k_{1z}} \tag{D.40}$$

and

$$R(k_{1z}) = \frac{\rho_2 k_{1z} - \rho_1 k_{2z}}{\rho_2 k_{1z} + \rho_1 k_{2z}}. \tag{D.41}$$

The local reaction approximation corresponds to $k_{2z} \approx k_2$, and we find

$$R(k_{1z}) = \frac{\rho_2 k_{1z} - \rho_1 k_2}{\rho_2 k_{1z} + \rho_1 k_2} \tag{D.42}$$

or

$$R(k_{1z}) = \frac{k_{1z} - k_1/Z}{k_{1z} + k_1/Z}, \tag{D.43}$$

where $Z = \rho_2 c_2/\rho_1 c_1$ is the normalized ground impedance. It is easily verified that we have $P_j/V_{n,j} = Z\rho c$, where $V_{n,j} = -(\partial P_j/\partial z)/(i\omega\rho_j)$ is the Fourier transform of the component of the complex velocity amplitude in the negative z direction; this is in agreement with Eq. (D.7).

We write Eq. (D.38) as

$$P_1 = P_s + P_{is} \tag{D.44}$$

with

$$P_s = A\exp(ik_{1z}|z - z_s|) \tag{D.45}$$

$$P_{is} = AR(k_{1z})\exp(ik_{1z}[z + z_s]). \tag{D.46}$$

The term P_s represents the direct field of the source (indicated by index 's' for source), so the term P_{is} must represent the contribution of the ground reflection to the field, or equivalently, the contribution of the image source (indicated by index 'is'). The quantity $R(k_{1z})$ is identified as a reflection coefficient.

If we apply the inverse Fourier transformation $(k_x, k_y) \rightarrow (x, y)$ to Eq. (D.45), we find of course the solution for a spherical wave in an unbounded atmosphere:

$$p_s = \frac{\exp(ik_1\sqrt{r^2 + (z - z_s)^2})}{\sqrt{r^2 + (z - z_s)^2}} \tag{D.47}$$

with $r^2 = x^2 + y^2$. The inverse Fourier transformation cannot be applied directly to Eq. (D.46), owing to the factor $R(k_{1z})$.

Therefore we write the reflection coefficient $R(k_{1z})$ as a Laplace transform [83, 84, 42]:

$$R(k_{1z}) = \int_0^\infty s(q) \exp(-qk_{1z}) dq, \tag{D.48}$$

where $s(q)$ is an image source distribution, which is given by

$$s(q) = \delta(q) - 2\frac{k_1}{Z} \exp\left(-\frac{qk_1}{Z}\right). \tag{D.49}$$

Equation (D.48) agrees with Eq. (D.43), as follows from substitution of Eq. (D.49) into Eq. (D.48).

Substitution of Eq. (D.48) into Eq. (D.46) gives

$$P_{is} = \int_0^\infty s(q) A \exp(ik_{1z}[z + (z_s + iq)]) dq. \tag{D.50}$$

Now the inverse Fourier transformation can be performed, by using the fact that the dependence on k_{1z} is through an exponential factor similar to the factor in Eq. (D.45). The result is

$$p_{is} = \int_0^\infty s(q) \frac{\exp(ik_1\sqrt{r^2 + (z + z_s + iq)^2})}{\sqrt{r^2 + (z + z_s + iq)^2}} dq, \tag{D.51}$$

where the square root is in the first quadrant of the complex plane. The inverse Fourier transformation and the Laplace transformation have been interchanged. The field given by Eq. (D.51) can be interpreted as the field of an image line source distribution $s(q)$ in a complex space, located at $(0, 0, -z_s - iq)$. By substitution of Eq. (D.49) into Eq. (D.51) we find the following expression for

the complex pressure amplitude $p_1 = p_s + p_{is}$:

$$p_1 = \frac{\exp(ik_1R_1)}{R_1} + \frac{\exp(ik_1R_2)}{R_2} - 2\frac{k_1}{Z}\int_0^\infty \exp\left(-\frac{qk_1}{Z}\right)\frac{\exp(ik_1\sqrt{r^2+(z+z_s+iq)^2})}{\sqrt{r^2+(z+z_s+iq)^2}}dq \quad \text{(D.52)}$$

with $R_1 = \sqrt{r^2+(z-z_s)^2}$ and $R_2 = \sqrt{r^2+(z+z_s)^2}$. We write this expression as

$$p_1 = \frac{\exp(ik_1R_1)}{R_1} + Q\frac{\exp(ik_1R_2)}{R_2}, \quad \text{(D.53)}$$

where

$$Q = 1 - 2\frac{k_1}{Z}\frac{R_2}{\exp(ik_1R_2)}\int_0^\infty \exp\left(-\frac{qk_1}{Z}\right)\frac{\exp(ik_1\sqrt{r^2+(z+z_s+iq)^2})}{\sqrt{r^2+(z+z_s+iq)^2}}dq \quad \text{(D.54)}$$

is the spherical-wave reflection coefficient.

As k_1 is real and Z is a complex number with a positive real part, the integral in Eq. (D.54) is dominated by relatively small values of q. For numerical calculations the upper limit of the integral can be set at $q_{max} = \lambda(Z_r^2 + Z_i^2)/Z_r$, where λ is the wavelength and Z_r and Z_i are the real and imaginary parts of Z, respectively [42].

In practice we often have $R_2 \gg z + z_s$. This corresponds to a reflection angle $\theta \approx \pi/2$ (see Fig. D.2). The limit $(z+z_s)/R_2 \to 0$ and $\theta \to \pi/2$ is called the limit of *grazing incidence*. In this limiting case we can simplify Eq. (D.54). In the numerator of the integrand in Eq. (D.54) we use the approximation

$$\sqrt{r^2+(z+z_s+iq)^2} \approx R_2 + iq\cos\theta - \frac{q^2}{2R_2} \quad \text{(D.55)}$$

with $\cos\theta = (z+z_s)/R_2$. In the denominator of the integrand in Eq. (D.54) we use $\sqrt{r^2+(z+z_s+iq)^2} \approx R_2$. Equation (D.54) becomes

$$Q = 1 - 2\frac{k_1}{Z}\exp(-d^2)\int_0^\infty \exp\left[-\left(q\sqrt{\frac{ik_1}{2R_2}} - id\right)^2\right]dq, \quad \text{(D.56)}$$

where

$$d = \sqrt{\frac{ik_1R_2}{2}}\left(\frac{1}{Z} + \cos\theta\right) \quad \text{(D.57)}$$

is called the numerical distance. Equation (D.56) can also be written as

$$Q = R_p + (1 - R_p)F(d), \tag{D.58}$$

where

$$R_p = \frac{Z\cos\theta - 1}{Z\cos\theta + 1} \tag{D.59}$$

is the plane-wave reflection coefficient (D.13) and

$$F(d) = 1 + id\sqrt{\pi}\exp(-d^2)\mathrm{erfc}(-id) \tag{D.60}$$

is called the boundary loss factor; here $\mathrm{erfc}(z) = 2\pi^{-1/2}\int_z^\infty \exp(-t^2)dt$ is the complementary error function [1].

The spherical-wave reflection coefficient for a locally reacting ground surface can be calculated with Eq. (D.54) or Eq. (D.58). Equation (D.54) is a general expression and Eq. (D.58) is valid only in the limit of grazing incidence ($R_2 \gg z + z_s$). In many situations, even situations with $R_2 \sim z + z_s$, the grazing incidence approximation (D.58) proves to be sufficiently accurate. The grazing incidence approximation (D.58) has been derived by several authors (see the review article [3]); the derivation presented here is based on Ref. [42].

For the calculation of the boundary loss factor $F(d)$ one can use series expansions of the complementary error function [1]. For small values of $|d^2|$, smaller than 8 for example, the series

$$\mathrm{erfc}(z) = 1 - \frac{2}{\sqrt{\pi}}\sum_{n=0}^{\infty}\frac{(-1)^n z^{2n+1}}{n!(2n+1)} \tag{D.61}$$

can be used. This gives

$$F(d) = 1 + id\sqrt{\pi}\exp(-d^2)\left[1 + \frac{2id}{\sqrt{\pi}}\sum_{n=0}^{\infty}\frac{(d^2)^n}{n!(2n+1)}\right]. \tag{D.62}$$

The series can be truncated at the point where the summand is smaller than 10^{-6}, for example. For large values of $|d^2|$, larger than 8 for example, the series

$$\sqrt{\pi}z\exp(z^2)\mathrm{erfc}(z) = 1 + \sum_{m=1}^{\infty}(-1)^m\frac{1\cdot 3\cdot 5\ldots(2m-1)}{(2z^2)^m} \tag{D.63}$$

can be used. This series is valid for $z \to \infty$ and $|\arg z| < \frac{3}{4}\pi$. For $z \to -\infty$ we use the relation $\mathrm{erfc}(-z) = 2 - \mathrm{erfc}(z)$. This gives

$$F(d) = 2id\sqrt{\pi}\exp(-d^2)H(-\mathrm{Im}d) - \sum_{m=1}^{\infty}\frac{1\cdot 3\cdot 5\ldots(2m-1)}{(2d^2)^m}, \tag{D.64}$$

where H is the Heaviside step function [$H(x) = 1$ for $x \geq 0$ and $H(x) = 0$ for $x < 0$] and $\mathrm{Im}d$ is the imaginary part of d. In practice the series can be truncated at $m = 8$.

D.4.2 Extended reacting ground surface

For an extended reacting ground surface, the approach is similar to the approach for a locally reacting ground surface, but the local reaction approximation $k_{2z} \approx k_2$ is not used in Eq. (D.41). Instead, we use Snell's law in the form

$$k_1^2 - k_{1z}^2 = k_2^2 - k_{2z}^2, \tag{D.65}$$

which follows from Eq. (D.37) and the pressure continuity condition $p_1(x, y, 0) = p_2(x, y, 0)$, where p_1 and p_2 are given by Eq. (D.30) (*cf.* Sec. D.3). Hence, Eq. (D.41) can be written as [83, 84, 42]

$$\begin{aligned} R(k_{1z}) &= \frac{\rho_2 k_{1z} - \rho_1 \sqrt{(k_2^2 - k_1^2) + k_{1z}^2}}{\rho_2 k_{1z} + \rho_1 \sqrt{(k_2^2 - k_1^2) + k_{1z}^2}} \\ &= \frac{\rho_2 (\epsilon k_{1z}) - \rho_1 \sqrt{(\epsilon k_{1z})^2 + 1}}{\rho_2 (\epsilon k_{1z}) + \rho_1 \sqrt{(\epsilon k_{1z})^2 + 1}} \end{aligned} \tag{D.66}$$

with $\epsilon = 1/\sqrt{k_2^2 - k_1^2}$. This can also be written as

$$\begin{aligned} R(k_{1z}) = \frac{\rho_2 - \rho_1}{\rho_2 + \rho_1} &- \frac{\rho_2 - \rho_1}{\rho_2 + \rho_1} \frac{\rho_2}{\rho_1} \frac{\gamma^2}{(\epsilon k_{1z})^2 - \gamma^2} \\ &+ \frac{\rho_2}{\rho_1} \frac{\gamma^2}{(\epsilon k_{1z})^2 - \gamma^2} \left[(\epsilon k_{1z}) - \sqrt{(\epsilon k_{1z})^2 + 1} \right]^2 \end{aligned} \tag{D.67}$$

with $\gamma = \rho_1/\sqrt{\rho_2^2 - \rho_1^2}$. The Laplace transform (D.48) is replaced by the following Laplace transform:

$$R(k_{1z}) = \int_0^\infty s(q) \exp(-q\, \epsilon k_{1z}) dq. \tag{D.68}$$

The inverse Laplace transform of the function $R(k_{1z})$ given by Eq. (D.67) yields the following expression for $s(q)$ [84, 1]:

$$s(q) = \frac{\rho_2 - \rho_1}{\rho_2 + \rho_1} \delta(q) - \gamma \frac{\rho_2}{\rho_1} \frac{\rho_2 - \rho_1}{\rho_2 + \rho_1} \sinh(\gamma q) + 2\gamma \frac{\rho_2}{\rho_1} \int_0^q \sinh\left[\gamma(q - q')\right] \frac{J_2(q')}{q'} dq', \tag{D.69}$$

where J_2 is the Bessel J-function of order 2. Substitution of Eq. (D.68) into Eq. (D.46) gives

$$P_{\mathrm{is}} = \int_0^\infty s(q) A \exp(i k_{1z} [z + (z_{\mathrm{s}} + i\, \epsilon q)]) dq. \tag{D.70}$$

The inverse Fourier transformation gives

$$p_{\mathrm{is}} = \int_0^\infty s(q) \frac{\exp(ik_1\sqrt{r^2 + (z + z_{\mathrm{s}} + i\,\epsilon q)^2})}{\sqrt{r^2 + (z + z_{\mathrm{s}} + i\,\epsilon q)^2}}\, dq. \tag{D.71}$$

The solution is given by $p_1 = p_{\mathrm{s}} + p_{\mathrm{is}}$, where p_{s} is given by Eq. (D.47) and p_{is} is given by Eq. (D.71). The solution can be written as in Eq. (D.53), if we write the spherical-wave reflection coefficient Q as

$$Q = p_{\mathrm{is}} \frac{R_2}{\exp(ik_1 R_2)}, \tag{D.72}$$

where p_{is} is given by Eq. (D.71). The image source distribution $s(q)$ in Eq. (D.71) is given by Eq. (D.69), which contains an integral, so the calculation of Q requires the calculation of a double integral.

As an example, Fig. D.3 shows a spectrum of the relative sound pressure level calculated with the above (general) solution for an extended reacting ground surface, and the corresponding spectrum calculated with the solution based on the local reaction approximation, which was described in Sec. D.4.1 [Equations (D.54) and (D.58) give equal results in this case]. The spectra were calculated for a situation with $z_{\mathrm{s}} = 2$ m, $z = 2$ m, and $r = 100$ m. For the ground impedance we used the four-parameter model developed by Attenborough (see Sec. C.4), with a flow resistivity $\sigma = 200$ kPa·s·m^{-2}. The figure shows that the effect of the local reaction approximation is small. In general, the local reaction approximation is a good approximation for ground surfaces.

The solution for the extended reacting ground surface shown in Fig. D.3 was calculated by straightforward numerical evaluation of the double integral in the expression for p_{is}. In some cases, however, straightforward numerical integration gives inaccurate results; more accurate numerical approaches are described in Ref. [84]. Alternately, one can use the FFP method for an extended reacting ground surface (see Appendix F).

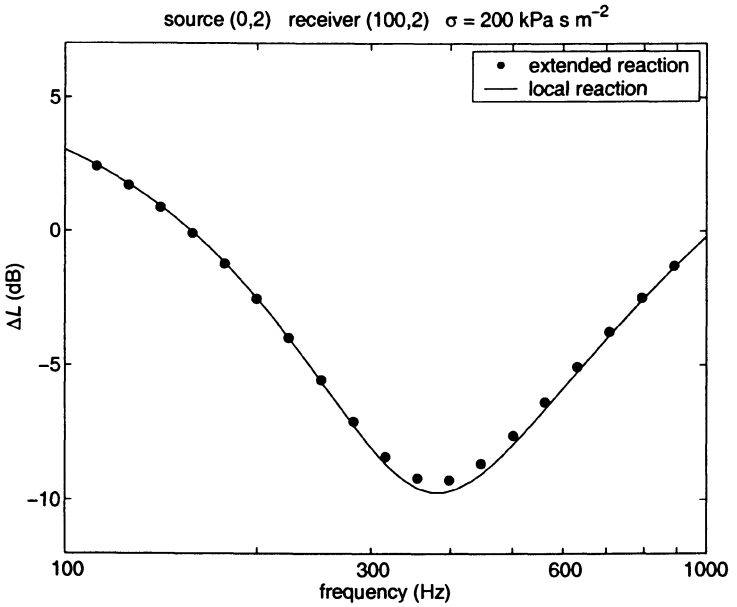

Figure D.3. Relative sound pressure level as a function of frequency, for an absorbing ground surface with a flow resistivity of 200 kPa·s·m^{-2}. The dots represent the solution described in Sec. D.4.2 for an extended reacting ground surface. The line represents the solution described in Sec. D.4.1 for a locally reacting ground surface. The differences between the dots and the line are small, so the local reaction approximation is a good approximation in this case.

Appendix E

Basic acoustic equations for a layered refracting atmosphere

E.1 Introduction

In Appendix A we derived the basic equations of linear acoustics for a homogeneous non-moving atmosphere. The atmosphere was homogeneous because we assumed that the average pressure p_{av} and the average density ρ_{av} are constants (*i.e.* independent of position); the atmosphere was non-moving because we assumed that the average fluid velocity $\mathbf{v}_{\text{av}}$ is zero. The atmosphere was also non-refracting, as the adiabatic sound speed

$$c = \sqrt{\gamma p_{\text{av}} / \rho_{\text{av}}} \tag{E.1}$$

(see Sec. A.2) is a constant in a homogeneous atmosphere.

In this appendix we derive linear acoustic equations for a refracting moving atmosphere. In such an atmosphere, the quantities ρ_{av}, p_{av}, $\mathbf{v}_{\text{av}}$, and c are functions of position in the atmosphere. We assume that the quantities ρ_{av}, p_{av}, $\mathbf{v}_{\text{av}}$, and c are functions of height only; the atmosphere is called a layered atmosphere or a stratified atmosphere in this case. The assumption of a layered atmosphere is a reasonable approximation for the atmospheric surface layer, as horizontal variations of atmospheric parameters are usually much smaller than vertical variations. Furthermore, we assume that the wind vector is horizontal, as vertical wind velocity components are usually much smaller than horizontal wind velocity components.

In Sec. E.2 we derive general linear acoustic equations for a refracting moving atmosphere. In Sec. E.3 we describe how a moving atmosphere can be represented approximately by a non-moving atmosphere with an effective sound

speed. In Secs. E.4 and E.5 we describe the axisymmetric approximation, which is the basis of a two-dimensional representation of the three-dimensional atmosphere. In Sec. E.6 we describe how atmospheric absorption can be included in the equations.

E.2 Moving atmosphere

E.2.1 Helmholtz equation in the horizontal wave number domain

In this section we derive a Helmholtz equation for a layered moving atmosphere [113, 98]. We use a rectangular xyz coordinate system, with horizontal x and y axes and a vertical z axis.

We write [*cf.* Eqs. (A.3)]

$$\begin{aligned} p_\mathrm{a} &= p_\mathrm{av}(z) + p \\ \rho_\mathrm{a} &= \rho_\mathrm{av}(z) + \rho \\ \mathbf{v}_\mathrm{a} &= (u_\mathrm{av}(z) + u, v_\mathrm{av}(z) + v, w) \end{aligned} \tag{E.2}$$

for the total pressure, density, and fluid velocity, respectively. The average quantities p_av, ρ_av, u_av, and v_av are functions of height z only. The acoustic fluctuations p, ρ, u, v, and w are functions of position $\mathbf{r}$ and time t.

The equation of mass conservation is

$$\frac{\partial \rho_\mathrm{a}}{\partial t} + \nabla \cdot (\rho_\mathrm{a} \mathbf{v}_\mathrm{a}) = 0, \tag{E.3}$$

and the first-order approximation for linear acoustics is

$$\frac{\partial \rho}{\partial t} + u_\mathrm{av}\frac{\partial \rho}{\partial x} + v_\mathrm{av}\frac{\partial \rho}{\partial y} + w\frac{\partial \rho_\mathrm{av}}{\partial z} + \rho_\mathrm{av}\left(\frac{\partial u}{\partial x} + \frac{\partial v}{\partial y} + \frac{\partial w}{\partial z}\right) = 0. \tag{E.4}$$

The equation of momentum conservation is

$$\rho_\mathrm{a}\frac{D\mathbf{v}_\mathrm{a}}{Dt} = -\nabla p_\mathrm{a} - \rho_\mathrm{a} g \mathbf{e}_z, \tag{E.5}$$

where $D/Dt \equiv \partial/\partial t + \mathbf{v}_\mathrm{a} \cdot \nabla$ is the derivative in a frame that follows the flow, g is the gravitational acceleration ($g \approx 9.8$ m/s^2), and $\mathbf{e}_z = (0,0,1)$ is the unit vector in the z direction. The second term on the right-hand side represents the gravitational force per unit volume, which accelerates a fluid element in the negative z direction. If we take $p = 0$, $\rho = 0$, $u = 0$, $v = 0$, and $w = 0$ in Eq. (E.5) we find the following equilibrium equations for the average pressure:

$$\frac{\partial p_\mathrm{av}}{\partial x} = 0, \quad \frac{\partial p_\mathrm{av}}{\partial y} = 0, \quad \frac{\partial p_\mathrm{av}}{\partial z} = -\rho_\mathrm{av} g. \tag{E.6}$$

Hence, gravity causes a decrease of the average atmospheric pressure p_av with increasing height z. For sound propagation this vertical pressure variation can

usually be neglected; we will come back to this neglect later in this section. The first-order approximation of Eq. (E.5) is

$$\frac{\partial u}{\partial t} + u_{\mathrm{av}}\frac{\partial u}{\partial x} + v_{\mathrm{av}}\frac{\partial u}{\partial y} + w\frac{\partial u_{\mathrm{av}}}{\partial z} + \frac{1}{\rho_{\mathrm{av}}}\frac{\partial p}{\partial x} = 0 \tag{E.7}$$

$$\frac{\partial v}{\partial t} + u_{\mathrm{av}}\frac{\partial v}{\partial x} + v_{\mathrm{av}}\frac{\partial v}{\partial y} + w\frac{\partial v_{\mathrm{av}}}{\partial z} + \frac{1}{\rho_{\mathrm{av}}}\frac{\partial p}{\partial y} = 0 \tag{E.8}$$

$$\frac{\partial w}{\partial t} + u_{\mathrm{av}}\frac{\partial w}{\partial x} + v_{\mathrm{av}}\frac{\partial w}{\partial y} + \frac{1}{\rho_{\mathrm{av}}}\frac{\partial p}{\partial z} + \frac{\rho}{\rho_{\mathrm{av}}}g = 0. \tag{E.9}$$

Pressure fluctuations and density fluctuations are related to each other by the fact that sound propagation can be considered as an adiabatic process. For a homogeneous non-moving atmosphere we have from $p = c^2\rho$ (see Sec. A.2) the relation

$$\frac{\partial p}{\partial t} = c^2\frac{\partial \rho}{\partial t}. \tag{E.10}$$

For an inhomogeneous moving atmosphere this relation is replaced by the relation

$$\frac{Dp_{\mathrm{a}}}{Dt} = c^2\frac{D\rho_{\mathrm{a}}}{Dt}, \tag{E.11}$$

or, using Eqs. (E.2),

$$\frac{\partial p}{\partial t} + \mathbf{v}_{\mathrm{a}}\cdot\nabla p_{\mathrm{a}} = c^2\left(\frac{\partial \rho}{\partial t} + \mathbf{v}_{\mathrm{a}}\cdot\nabla\rho_{\mathrm{a}}\right), \tag{E.12}$$

as the pressure and the density of a volume element moving through an inhomogeneous atmosphere are also affected by spatial variations of p_{a} and ρ_{a}. For a non-moving atmosphere ($\mathbf{v}_{\mathrm{a}} = 0$), Eq. (E.12) agrees with Eq. (E.10). The first-order approximation of Eq. (E.12) is

$$\frac{\partial p}{\partial t} + u_{\mathrm{av}}\frac{\partial p}{\partial x} + v_{\mathrm{av}}\frac{\partial p}{\partial y} + w\frac{\partial p_{\mathrm{av}}}{\partial z} = c^2\left(\frac{\partial \rho}{\partial t} + u_{\mathrm{av}}\frac{\partial \rho}{\partial x} + v_{\mathrm{av}}\frac{\partial \rho}{\partial y} + w\frac{\partial \rho_{\mathrm{av}}}{\partial z}\right). \tag{E.13}$$

We consider a harmonic sound field, with sound pressure

$$p(x,y,z,t) = \mathrm{Re}\left[p_{\mathrm{c}}(x,y,z)e^{-i\omega t}\right]. \tag{E.14}$$

We apply a double Fourier transformation from the spatial domain (x,y,z) to the horizontal wave number domain (k_x,k_y,z):

$$p_{\mathrm{c}}(x,y,z) = \frac{1}{(2\pi)^2}\int_{-\infty}^{\infty}\int_{-\infty}^{\infty}\exp(ik_x x + ik_y y)P(k_x,k_y,z)\,dk_x\,dk_y, \tag{E.15}$$

where $P(k_x, k_y, z)$ is the Fourier transform of $p_c(x, y, z)$. We write Eqs. (E.14) and (E.15) symbolically as

$$p \to P. \tag{E.16}$$

The Fourier transformation is also applied to the other acoustic variables:

$$\begin{aligned} \rho &\to \Omega \\ u &\to U \\ v &\to V \\ w &\to W. \end{aligned} \tag{E.17}$$

Application of the Fourier transformation to Eqs. (E.4), (E.7), (E.8), (E.9), and (E.13) gives

$$\eta\Omega + \rho'_{\mathrm{av}} W + \rho_{\mathrm{av}}(ik_x U + ik_y V + W') = 0 \tag{E.18}$$

$$\eta U + u'_{\mathrm{av}} W + \rho_{\mathrm{av}}^{-1} ik_x P = 0 \tag{E.19}$$

$$\eta V + v'_{\mathrm{av}} W + \rho_{\mathrm{av}}^{-1} ik_y P = 0 \tag{E.20}$$

$$\eta W + \rho_{\mathrm{av}}^{-1} P' + g\rho_{\mathrm{av}}^{-1}\Omega = 0 \tag{E.21}$$

$$\eta P - \rho_{\mathrm{av}} g W = c^2(\eta\Omega + \rho'_{\mathrm{av}} W), \tag{E.22}$$

where we have introduced $\eta = -i\omega + ik_x u_{\mathrm{av}} + ik_y v_{\mathrm{av}}$, the derivative dg/dz of a function g is denoted as g', and Eq. (E.6) has been used. From Eqs. (E.19) to (E.22) we find expressions for U, V, W, and Ω in terms of P; substitution into Eq. (E.18) gives

$$\begin{aligned} P'' - \left\{ \frac{d}{dz} \ln\left[\eta^2 \rho_{\mathrm{av}}(1 - gQ)\right] \right\} P' - \left\{ \frac{\eta^2}{c^2} + (1 - gQ)(k_x^2 + k_y^2) \right. \\ \left. + \frac{g}{c^2} \frac{d}{dz} \ln\left[\eta^2 c^2 (1 - gQ)\right] \right\} P = 0, \end{aligned} \tag{E.23}$$

where we have introduced $Q = \eta^{-2}(gc^{-2} + \rho'_{\mathrm{av}}\rho_{\mathrm{av}}^{-1})$. In this equation, gQ can be neglected with respect to unity and the term $gc^{-2}\frac{d}{dz}\ln(\eta^2 c^2)$ can also be neglected; this will be shown in the following two paragraphs.

We have

$$gQ = -\frac{g}{\omega^2}\left(\frac{g}{c^2} + \frac{\rho'_{\mathrm{av}}}{\rho_{\mathrm{av}}}\right)\left(1 - \frac{k_x}{k}\frac{u_{\mathrm{av}}}{c} - \frac{k_y}{k}\frac{v_{\mathrm{av}}}{c}\right)^{-2}, \tag{E.24}$$

with $k = \omega/c$. The last factor on the right-hand side can be approximated by unity, as we have $u_{\mathrm{av}} \ll c$ and $v_{\mathrm{av}} \ll c$ in practice, and the Fourier integral (E.15) is dominated by values of k_x and k_y with $k_x^2 + k_y^2 \lesssim k^2$ (see Sec. E.3). The second factor on the right-hand side of Eq. (E.24) contains the term $\rho'_{\mathrm{av}}/\rho_{\mathrm{av}}$. To estimate the order of magnitude of this term we note that the ideal-gas law (A.10) implies

$$\frac{\rho'_{\mathrm{av}}}{\rho_{\mathrm{av}}} = \frac{p'_{\mathrm{av}}}{p_{\mathrm{av}}} - \frac{T'}{T}. \tag{E.25}$$

For an ideal atmosphere with only hydrostatic pressure gradients, *i.e.* pressure gradients given by Eq. (E.6), we find from Eq. (E.1)

$$\frac{p'_{\mathrm{av}}}{p_{\mathrm{av}}} = -\frac{g\gamma}{c^2}, \tag{E.26}$$

which is of the order of 10^{-4} m^{-1}. The term T'/T is usually largest near the ground surface; we assume an upper limit of 0.1 m^{-1} for $|T'/T|$, corresponding to a temperature change of 3°C over a height interval of 10 cm. A safe upper limit for $|gQ|$ is therefore of the order of ω^{-2} if ω is expressed in s^{-1}. For frequencies above 10 Hz this implies $|gQ| \leq 3 \times 10^{-4}$, so gQ can be neglected with respect to unity.

The term $gc^{-2}\frac{d}{dz}\ln(\eta^2 c^2)$ in Eq. (E.23) can be written as

$$\frac{g}{c^2}\frac{d}{dz}\ln(\eta^2 c^2) = \frac{2g}{c^2}\left(\frac{\eta'}{\eta} + \frac{c'}{c}\right). \tag{E.27}$$

We have $|\eta'/\eta| \lesssim (u'_{\mathrm{av}} + v'_{\mathrm{av}})/c$ from $k_x^2 + k_y^2 \lesssim k^2$ (see Sec. E.3). The gradients u'_{av}, v'_{av}, and c' are usually largest near the ground surface; we assume an upper limit of 0.1 m^{-1} for the ratios $|u'_{\mathrm{av}}/c|$, $|v'_{\mathrm{av}}/c|$, and $|c'/c|$. From Eq. (E.27) we find an upper limit of the order of 6×10^{-5} m^{-2} for the magnitude of the term $gc^{-2}\frac{d}{dz}\ln(\eta^2 c^2)$, so this term can be neglected in Eq. (E.23).

Equation (E.23) becomes

$$P'' - \left(\frac{2\eta'}{\eta} + \frac{\rho'_{\mathrm{av}}}{\rho_{\mathrm{av}}}\right)P' - \left(\frac{\eta^2}{c^2} + k_x^2 + k_y^2\right)P = 0, \tag{E.28}$$

or

$$P'' - \left(2\frac{k'_{\mathrm{m}}}{k_{\mathrm{m}}} - \frac{\gamma g}{c^2}\right)P' + k_{\mathrm{m}z}^2 P = 0, \tag{E.29}$$

where wave number k_{m} is defined by

$$k_{\mathrm{m}} = k - k_x m_x - k_y m_y \tag{E.30}$$

with $m_x = u_{\mathrm{av}}/c$ and $m_y = v_{\mathrm{av}}/c$, and wave number $k_{\mathrm{m}z}$ is defined by

$$k_{\mathrm{m}z}^2 = k_{\mathrm{m}}^2 - k_x^2 - k_y^2. \tag{E.31}$$

In practice the term $\gamma g/c^2$ in Eq. (E.29) can be neglected. We find

$$P'' - 2\frac{k'_{\mathrm{m}}}{k_{\mathrm{m}}}P' + k_{\mathrm{m}z}^2 P = 0. \tag{E.32}$$

This equation can also be written as

$$k_{\mathrm{m}}^2 \frac{\partial}{\partial z}\left(k_{\mathrm{m}}^{-2}\frac{\partial P}{\partial z}\right) + k_{\mathrm{m}z}^2 P = 0. \tag{E.33}$$

Equations (E.32) and (E.33) can be considered as Helmholtz equations in the horizontal wave number domain. The corresponding inhomogeneous Helmholtz equation for a monopole source of unit amplitude at position $\mathbf{r}_s = (0, 0, z_s)$ is (see Sec. D.4)

$$k_m^2 \frac{\partial}{\partial z}\left(k_m^{-2}\frac{\partial P}{\partial z}\right) + k_{mz}^2 P = -4\pi\delta(z - z_s). \tag{E.34}$$

This is the basic equation of the FFP method described in Appendix F.

E.2.2 Alternate derivation

Equations (E.28) and (E.29) can also be derived from the following generalized wave equation for an inhomogeneous moving atmosphere [105]:

$$\frac{1}{\rho_{av}}\nabla\cdot(\rho_{av}\nabla\phi_v) - \frac{1}{c^2}\frac{D^2\phi_v}{Dt^2} = 0, \tag{E.35}$$

where ϕ_v is the velocity potential, which is related to the acoustic pressure p by

$$p = -\rho_{av}\frac{D\phi_v}{Dt}, \tag{E.36}$$

where $D/Dt \equiv \partial/\partial t + \mathbf{v}_{av}\cdot\nabla$ is the derivative in a frame that moves with fluid velocity $\mathbf{v}_{av} = (u_{av}, v_{av}, 0)$. We apply a Fourier transformation to Eqs. (E.35) and (E.36), as in Eqs. (E.14) to (E.16). With $\phi_v \to \Phi_v$ and $D/Dt \to \eta$, Eq. (E.35) becomes

$$\frac{1}{\rho_{av}}\frac{\partial}{\partial z}\left(\rho_{av}\frac{\partial}{\partial z}\Phi_v\right) - \left(\frac{\eta^2}{c^2} + k_x^2 + k_y^2\right)\Phi_v = 0, \tag{E.37}$$

and Eq. (E.36) becomes

$$\Phi_v = -\frac{P}{\eta\rho_{av}}. \tag{E.38}$$

Substitution of Eq. (E.38) into Eq. (E.37) yields Eq. (E.28) if one neglects second derivatives and squared first derivatives of $\mathbf{v}_{av}$ and ρ_{av}; this neglect is consistent with the derivation of Eq. (E.35) in Ref. [105].

E.2.3 Helmholtz equation in the spatial domain

For a non-moving atmosphere we can derive a Helmholtz equation for $p_c(\mathbf{r})$ in the spatial domain from Eq. (E.33). In this case we have $m_x = 0$, $m_y = 0$, and $k_m = k$. Equation (E.33) becomes

$$k^2\frac{\partial}{\partial z}\left(k^{-2}\frac{\partial P}{\partial z}\right) + (k^2 - k_x^2 - k_y^2)P = 0. \tag{E.39}$$

We multiply this equation by $(2\pi)^{-2}\exp(ik_x x + ik_y y)$ and integrate over k_x and k_y. Using Eq. (E.15) we find

$$k^2\nabla\cdot(k^{-2}\nabla p_c) + k^2 p_c = 0. \tag{E.40}$$

For a moving atmosphere, with wave number k replaced by k_m, this approach does not work, as k_m depends on k_x and k_y.

For a non-moving isobaric atmosphere Eq. (E.40) reduces to

$$\rho_{av}\nabla\cdot(\rho_{av}^{-1}\nabla p_c) + k^2 p_c = 0, \tag{E.41}$$

where we have used Eq. (E.1). This equation is also valid if the density ρ_{av} is a function of x, y, and z, instead of a function of z only [13, 106].

E.3 Non-moving atmosphere with an effective sound speed

To gain insight into the solution of Eqs. (E.32) to (E.34) we first consider the case of a homogeneous non-moving atmosphere. In this case we have $k_m = k$ and $k_m' = 0$, so $k_{mz}^2 = k^2 - k_x^2 - k_y^2$ is a constant. We ignore the ground surface for the moment. The solution of Eq. (E.34) is then (see Sec. D.4)

$$P = \frac{2\pi i}{k_{mz}}\exp(ik_{mz}|z - z_s|). \tag{E.42}$$

Substitution of this expression into Eq. (E.15) gives

$$p_c = \frac{i}{2\pi}\int_{-\infty}^{\infty}\int_{-\infty}^{\infty}\frac{\exp[ig(k_x,k_y,z)]}{k_{mz}}\,dk_x\,dk_y, \tag{E.43}$$

where

$$g(k_x,k_y,z) = k_x x + k_y y + |z - z_s|\sqrt{k^2 - k_x^2 - k_y^2} \tag{E.44}$$

is a phase function. The right-hand side of Eq. (E.43) is of course equal to $\exp(ikR)/R$, with $R = \sqrt{x^2 + y^2 + (z - z_s)^2}$. The integral in Eq. (E.43) is dominated by values of k_x and k_y near the point of stationary phase, *i.e.* the point where we have

$$\frac{\partial g}{\partial k_x} = 0 \text{ and } \frac{\partial g}{\partial k_y} = 0 \tag{E.45}$$

(see Appendix P). From Eq. (E.44) we find $k_x = kx/R$, $k_y = ky/R$, and $k_x^2 + k_y^2 = k^2(x^2 + y^2)/R^2$ at the point of stationary phase. In the case of sound propagation under relatively small elevation angles we have $|z - z_s| \ll \sqrt{x^2 + y^2}$, so we have $k_x^2 + k_y^2 \approx k^2$ at the point of stationary phase.

We choose the xyz coordinate system in such a way that the receiver is located in the xz plane, so we have $y = 0$. We assume $|z - z_s| \ll x$ and $x > 0$. In this case we find

$$k_x \approx k \quad \text{and} \quad k_y = 0 \tag{E.46}$$

at the point of stationary phase.

For an inhomogeneous moving atmosphere above a ground surface the solution of Eq. (E.34) is not given by Eq. (E.42), but the conclusion (E.46) remains approximately valid. This implies that $k_m = k - k_x m_x - k_y m_y$ can be replaced by $k_m = k - k m_x$ (we still assume $y = 0$), or

$$k_m = \frac{\omega}{c}\left(1 - \frac{u_{av}}{c}\right) \approx \frac{\omega}{c + u_{av}} = \frac{\omega}{c_{eff}} = k_{eff}, \tag{E.47}$$

where $c_{eff} = c + u_{av}$ is called the *effective sound speed* and k_{eff} is the corresponding wave number. Consequently, for sound propagation calculations one can replace a moving layered atmosphere by a non-moving atmosphere with an effective sound speed, which is the sum of the adiabatic sound speed c and the wind velocity component u_{av} in the direction of sound propagation. This is an approximate approach [98, 99], which is valid for small elevation angles (as we assumed $|z - z_s| \ll \sqrt{x^2 + y^2}$). Equation (E.32) becomes

$$P'' - 2\frac{k'_{eff}}{k_{eff}} P' + (k_{eff}^2 - k_x^2 - k_y^2) P = 0. \tag{E.48}$$

The inverse Fourier transformation yields the following Helmholtz equation for the complex pressure amplitude $p_c(\mathbf{r})$ (see Sec. E.2.3):

$$k_{eff}^2 \nabla \cdot (k_{eff}^{-2} \nabla p_c) + k_{eff}^2 p_c = 0. \tag{E.49}$$

E.4 Axisymmetric approximation

In this section we describe the axisymmetric approximation for sound fields in a layered atmosphere with an effective sound speed accounting for wind. This approximation is the basis of a two-dimensional representation of the atmosphere, which is used in the two-dimensional computational methods described in Appendices F, G, and H.

We assume that the sound field is generated by a point source, and use cylindrical $rz\phi$ coordinates with the z axis along the vertical line through the source (see Fig. E.1). Equation (E.49) becomes

$$\frac{1}{r}\frac{\partial}{\partial r}\left(r\frac{\partial p_c}{\partial r}\right) + k_{eff}^2 \frac{\partial}{\partial z}\left(k_{eff}^{-2}\frac{\partial p_c}{\partial z}\right) + \frac{1}{r^2}\frac{\partial^2 p_c}{\partial \phi^2} + k_{eff}^2 p_c = 0. \tag{E.50}$$

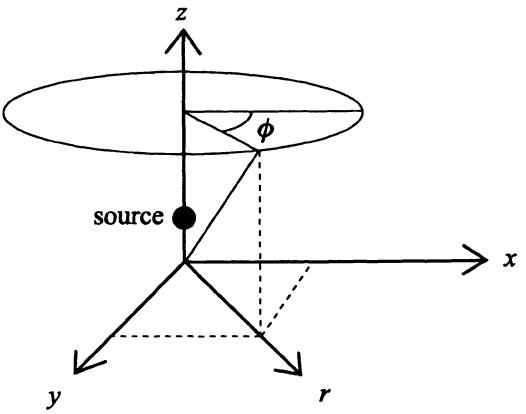

Figure E.1. Rectangular xyz coordinates and cylindrical $rz\phi$ coordinates. In the axisymmetric approximation we neglect the variation of the sound field with the azimuthal angle ϕ.

In the axisymmetric approximation we neglect the variation of the sound field with the azimuthal angle ϕ, so the third term on the left-hand side of Eq. (E.50) vanishes. We replace p_c by the quantity

$$q_c = p_c\sqrt{r}, \tag{E.51}$$

and Eq. (E.50) becomes

$$\frac{\partial^2 q_c}{\partial r^2} + \frac{1}{4r^2}q_c + k_{\text{eff}}^2 \frac{\partial}{\partial z}\left(k_{\text{eff}}^{-2}\frac{\partial q_c}{\partial z}\right) + k_{\text{eff}}^2 q_c = 0. \tag{E.52}$$

We apply the far-field approximation $r \gg k_{\text{eff}}^{-1}$, so the second term on the left-hand side can be neglected, and we find the two-dimensional Helmholtz equation

$$\frac{\partial^2 q_c}{\partial r^2} + k_{\text{eff}}^2 \frac{\partial}{\partial z}\left(k_{\text{eff}}^{-2}\frac{\partial q_c}{\partial z}\right) + k_{\text{eff}}^2 q_c = 0. \tag{E.53}$$

This is the basic equation of the two-dimensional PE methods described in Appendices G and H. In the remainder of this section we derive the corresponding inhomogeneous Helmholtz equation in the horizontal wave number domain, which is the basic equation of the two-dimensional FFP method described in Appendix F.

For the field of a monopole source we have from Eq. (E.34)

$$k_{\text{eff}}^2 \frac{\partial}{\partial z}\left(k_{\text{eff}}^{-2}\frac{\partial P}{\partial z}\right) + (k_{\text{eff}}^2 - k_x^2 - k_y^2)P = -4\pi\delta(z - z_s), \tag{E.54}$$

where Fourier transform P is given by

$$P(k_x, k_y, z) = \int_{-\infty}^{\infty} \int_{-\infty}^{\infty} \exp(-ik_x x - ik_y y)\, p_c(\mathbf{r})\, dx\, dy. \tag{E.55}$$

In the axisymmetric approximation, p_c is a function of r and z only. With $x = r\cos\phi$ and $y = r\sin\phi$, Eq. (E.55) becomes

$$P(k_x, k_y, z) = \int_0^{2\pi} \int_0^{\infty} \exp(-ik_x r\cos\phi - ik_y r\sin\phi)\, p_c(\mathbf{r})\, r\, dr\, d\phi. \tag{E.56}$$

Substitution into Eq. (E.54) gives, with $q_c = p_c\sqrt{r}$,

$$\int_0^{2\pi} \int_0^{\infty} \exp(-ik_x r\cos\phi - ik_y r\sin\phi) \left[k_{\text{eff}}^2 \frac{\partial}{\partial z}\left(k_{\text{eff}}^{-2}\frac{\partial q_c}{\partial z}\right) + (k_{\text{eff}}^2 - k_x^2 - k_y^2)q_c\right] \times \sqrt{r}\, dr\, d\phi = -4\pi\delta(z - z_s). \tag{E.57}$$

We write $k_x = k_r\cos\psi$ and $k_y = k_r\sin\psi$. This gives

$$\int_0^{\infty} \left[k_{\text{eff}}^2 \frac{\partial}{\partial z}\left(k_{\text{eff}}^{-2}\frac{\partial q_c}{\partial z}\right) + (k_{\text{eff}}^2 - k_r^2)q_c\right] \sqrt{r} \int_0^{2\pi} \exp(-ik_r r\cos[\phi - \psi])\, d\phi\, dr = -4\pi\delta(z - z_s). \tag{E.58}$$

The integral over ϕ can be written as

$$\int_0^{2\pi} \exp(-ik_r r\cos\alpha)\, d\alpha = 2\pi J_0(k_r r), \tag{E.59}$$

where J_0 is the Bessel J-function of order zero [1]. For large $k_r r$ we have the asymptotic relation

$$J_0(k_r r) = \sqrt{\frac{2}{\pi k_r r}}\cos(k_r r - \tfrac{1}{4}\pi). \tag{E.60}$$

Equation (E.58) becomes, for large $k_r r$,

$$\int_0^{\infty} \left[k_{\text{eff}}^2 \frac{\partial}{\partial z}\left(k_{\text{eff}}^{-2}\frac{\partial q_c}{\partial z}\right) + (k_{\text{eff}}^2 - k_r^2)q_c\right] 2\sqrt{\frac{2\pi}{k_r}}\cos(k_r r - \tfrac{1}{4}\pi)\, dr = -4\pi\delta(z - z_s). \tag{E.61}$$

With the definition

$$Q(k_r, z) = \int_0^\infty q_c \cos(k_r r - \frac{1}{4}\pi)\, dr = \int_0^\infty \left[\frac{q_c}{\sqrt{2}} \cos(k_r r) + \frac{q_c}{\sqrt{2}} \sin(k_r r) \right] dr \tag{E.62}$$

we find

$$k_{\text{eff}}^2 \frac{\partial}{\partial z} \left(k_{\text{eff}}^{-2} \frac{\partial Q}{\partial z} \right) + (k_{\text{eff}}^2 - k_r^2) Q = -\sqrt{2\pi k_r}\, \delta(z - z_s). \tag{E.63}$$

The function $Q(k_r, z)$ can be computed by numerically solving this equation with the FFP method (see Appendix F). The field $q_c(r, z)$ is obtained from $Q(k_r, z)$ by the inverse Fourier transformation corresponding to Eq. (E.62):

$$\frac{q_c}{\sqrt{2}} = \frac{1}{\pi} \int_{-\infty}^\infty Q(k_r, z) \cos(k_r r)\, dk_r = \frac{1}{\pi} \int_{-\infty}^\infty Q(k_r, z) \sin(k_r r)\, dk_r. \tag{E.64}$$

We have reduced the three-dimensional problem to a two-dimensional problem by evaluating the integral over the azimuthal angle ϕ in Eq. (E.58) analytically. In the derivation we have assumed that p_c is independent of the angle ϕ. This assumption is valid for a *non-moving* layered atmosphere. The assumption is not valid for a *moving* atmosphere, *i.e.* an atmosphere with wind, as sound waves travel faster in downwind directions than in upwind directions. As an approximation, however, the moving atmosphere can be replaced by a non-moving atmosphere with an effective sound speed, so that the assumption of axial symmetry can still be used.

An alternate approximate approach for a *moving* atmosphere is as follows. We assume that the variation of p_c with the azimuthal angle ϕ is small, so Eq. (E.58) can still be used as an approximation, with k_{eff} replaced by $k_m = k - k_x u_{av}/c - k_y v_{av}/c$. As shown in Sec. E.3, the field is dominated by wave numbers k_x and k_y near the stationary phase values kx/R and ky/R, respectively, where $R = \sqrt{x^2 + y^2 + (z - z_s)^2}$ is the distance between the source at position $(0, 0, z_s)$ and the receiver at position (x, y, z). Using $k_r^2 = k_x^2 + k_y^2$ we find $k_r = kr/R$ at the stationary phase point, where $r = \sqrt{x^2 + y^2}$ is the horizontal distance between the source and the receiver. This gives $k_m = k - k_r(u_{av}x/r + v_{av}y/r)/c$ at the stationary phase point, where $(u_{av}x/r + v_{av}y/r)$ is the wind velocity component in the direction from the source to the receiver. If we choose the xyz coordinate system in such a way that the receiver is located in the xz plane, so that the receiver is at position $(x, 0, z)$, we have $k_m = k - k_r u_{av}/c$ at the stationary phase point. Hence, Eqs. (E.62) to (E.64) can be used as an approximation for a moving atmosphere if we replace k_{eff} by $k_m = k - k_r u_{av}/c$.

E.5 Alternate approach

In the previous section we derived the inhomogeneous Helmholtz equation (E.63) in the horizontal wave number domain by using the axisymmetric approximation and the asymptotic relation (E.60). An alternate approach is to replace Eqs. (E.51) and (E.62) by the Fourier-Bessel transform

$$Q(k_r, z) = \int_0^\infty p_c(r, z) J_0(k_r r)\, r\, dr \tag{E.65}$$

(see Ref. [55]). One starts from Eq. (E.50) with $\partial^2 p_c / \partial \phi^2 = 0$ and replaces the right-hand side by the monopole source term in cylindrical coordinates, which is $-4\pi r^{-1}\delta(r)\delta(\phi)\delta(z - z_s)$. The resulting equation is integrated over ϕ from 0 to 2π, and as p_c is independent of ϕ this gives

$$\frac{1}{r}\frac{\partial}{\partial r}\left(r\frac{\partial p_c}{\partial r}\right) + k_{\text{eff}}^2 \frac{\partial}{\partial z}\left(k_{\text{eff}}^{-2}\frac{\partial p_c}{\partial z}\right) + k_{\text{eff}}^2 p_c = -\frac{2}{r}\delta(r)\delta(z - z_s). \tag{E.66}$$

With the Fourier-Bessel transform given by Eq. (E.65), we find from Eq. (E.66)

$$k_{\text{eff}}^2 \frac{\partial}{\partial z}\left(k_{\text{eff}}^{-2}\frac{\partial Q}{\partial z}\right) + (k_{\text{eff}}^2 - k_r^2)Q = -2\delta(z - z_s). \tag{E.67}$$

To prove this, Eq. (E.66) is multiplied by $J_0(k_r r)r$ and integrated over r from $r = 0$ to $r = \infty$, as in Eq. (E.65). Integration by parts yields Eq. (E.67). Equation (E.67) differs from Eq. (E.63) only by a factor $\sqrt{2/\pi k_r}$ on the right-hand side. The function $Q(k_r, z)$ can be computed by numerically solving Eq. (E.67) with the FFP method. The field $p_c(r, z)$ is given by the inverse transform:

$$p_c(r, z) = \int_0^\infty Q(k_r, z) J_0(k_r r)\, k_r\, dk_r. \tag{E.68}$$

To calculate the integral in this equation one replaces $J_0(k_r r)$ by a far-field approximation; the resulting expression is equivalent to Eq. (E.64).

E.6 Representation of atmospheric absorption

In the previous sections of this appendix we ignored the effect of atmospheric absorption. This effect can be included, however, simply by replacing the wave number k by $k + i\beta$, with $\beta = \alpha/(20 \lg e)$, where α is the absorption coefficient in dB per unit length (see Sec. B.5). The imaginary term $i\beta$ yields a factor $\exp(-s\beta)$ in the sound pressure amplitude, where s is the propagation distance. This corresponds to a contribution $-s\alpha$ to the sound pressure level. One might even include phase effects of atmospheric absorption [106] by using a complex

term $i\beta + \gamma$ instead of the imaginary term $i\beta$. In general, the coefficients β and γ vary with height z, so the profile $k(z)$ should be replaced by the profile $k(z) + i\beta(z) + \gamma(z)$.

In many practical situations it is sufficiently accurate to account for the effect of atmospheric absorption by a simple reduction of the sound pressure level by $s\alpha$, where s is the distance between the source and the receiver and α is an average absorption coefficient. In these situations it is not necessary to include atmospheric absorption in the numerical computation of sound propagation.

Appendix F

Generalized Fast Field Program (FFP)

F.1 Introduction

The Fast Field Program (FFP) is a numerical method for computing the sound field of a monopole source in a layered atmosphere above a ground surface. The ground surface is characterized by the ground impedance and the atmosphere is represented by the vertical profiles of the wind velocity and the temperature. The profiles are approximated by dividing the atmosphere into a number of horizontal homogeneous layers with constant wind velocity and temperature. The sound field in each layer is computed in the horizontal wave number domain, taking into account the appropriate continuity equations at the interfaces between the layers. The sound field in the spatial domain is computed from the field in the horizontal wave number domain by an inverse Fourier transformation. Therefore the FFP method is sometimes called the 'wave number integration method' [69].

The FFP method was originally developed for underwater acoustics [45, 69]. Raspet *et al.* [119] and Lee *et al.* [79] developed an FFP method for atmospheric acoustics (see also Refs. [55, 155]); this is a two-dimensional method, for an axisymmetric atmosphere, with the effective sound speed accounting for wind (see Sec. E.3). Nijs and Wapenaar [94] and Wilson [158] developed three-dimensional computational methods for a moving atmosphere, which can be considered as generalized FFP methods.

In this appendix we describe a generalized FFP method, which can be applied both in three dimensions to a moving atmosphere and in two dimensions to an axisymmetric non-moving atmosphere with the effective sound speed accounting for wind.

F.2 Solution of the Helmholtz equation

Equation (E.34) is the basic equation of the FFP method for a monopole source in a layered moving atmosphere. Equation (E.63) is the corresponding equation for a layered non-moving atmosphere with the effective sound speed accounting for wind. Equation (E.34) corresponds to a three-dimensional representation of the atmosphere and Eq. (E.63) corresponds to a two-dimensional representation of the atmosphere. Both equations can be written as

$$k^2 \frac{\partial}{\partial z}\left(k^{-2}\frac{\partial P}{\partial z}\right) + k_z^2 P = -S_\delta \delta(z - z_s), \tag{F.1}$$

where we have

$$S_\delta = 4\pi \text{ and } k_z^2 = k^2 - k_x^2 - k_y^2 \text{ with } k \equiv k_m \tag{F.2}$$

in the three-dimensional case, and

$$S_\delta = \sqrt{2\pi k_r} \text{ and } k_z^2 = k^2 - k_r^2 \text{ with } k \equiv k_{eff} \tag{F.3}$$

in the two-dimensional case; P represents the quantity Q in the two-dimensional case. The wave number in the three-dimensional case is $k_m = \omega/c - k_x u_{av}/c - k_y v_{av}/c$, where u_{av} and v_{av} are the x and y components of the wind velocity, respectively. The wave number in the two-dimensional case is $k_{eff} = \omega/c_{eff}$, where $c_{eff} = c + u_{av}$ is the effective sound speed; u_{av} is now the wind velocity component in the r direction, *i.e.* the direction from the source to the receiver. As described in Sec. E.4, moving-medium effects can be studied approximately in the two-dimensional case by using $k \equiv k_m = \omega/c - k_r u_{av}/c$ instead of $k \equiv k_{eff}$.

The atmosphere is represented by the vertical profile of the wave number $k(z)$. We approximate the profile by dividing the atmosphere into a number of horizontal homogeneous layers with constant wave number k (see Fig. F.1). The heights of the interfaces between the layers are denoted as z_j $(j = 1, 2, \ldots, N)$, where $z_1 = 0$ is the height of the ground surface. The source is at height z_s, which coincides with the height of interface m, so we have $z_s = z_m$.

As the wave number k is constant within a layer, Eq. (F.1) reduces to

$$\frac{\partial^2 P}{\partial z^2} + k_z^2 P = -S_\delta \delta(z - z_s). \tag{F.4}$$

The effect of wave number gradients in the first term on the left-hand side of Eq. (F.1) is taken into account in the FFP method only by wave number differences between the layers; rapid variations of the wave number with height require thin layers. The solution of Eq. (F.4) in layer j is written as

$$P_j = A_j \exp(ik_{zj}z) + B_j \exp(-ik_{zj}z) \quad \text{for } z_j \le z \le z_{j+1}, \tag{F.5}$$

where k_{zj} is the value of k_z in the layer and A_j and B_j are constants. At the top of the highest layer between z_{N-1} and z_N we assume $B_{N-1} = 0$, so only an

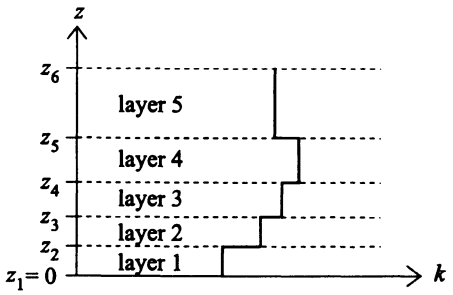

Figure F.1. The profile $k(z)$ is approximated by dividing the atmosphere into a number of horizontal homogeneous layers with constant wave number k.

upward traveling wave is present here. This implies that the highest layer must be chosen above the region where sound is refracted downward to the receiver; the height of this region usually increases with increasing distance between the source and the receiver. The solution of Eq. (F.4) in the region below the ground surface ($z \leq 0$) is written as

$$P_0 = B_0 \exp(-ik_0 z) \quad \text{for } z \leq 0, \tag{F.6}$$

where B_0 is a constant and k_0 is the (complex) wave number in the ground (*cf.* Sec. D.4).

The constants A_j and B_j follow from the boundary conditions at the interfaces. The acoustic pressure and normal velocity are continuous at all interfaces, except at the interface at the source height $z_s = z_m$, where the pressure is continuous but the normal velocity is discontinuous (see Sec. D.4). The Fourier transform W of the normal velocity is given by $W = -\eta^{-1}\rho_{\text{av}}^{-1}P'$, as follows from Eq. (E.21) with gravity neglected. This gives the following boundary conditions:

$$P_j(z_j) = P_{j-1}(z_j) \qquad \text{for } j = 1, 2, \ldots, N, \tag{F.7}$$

$$\eta_j^{-1}\rho_j^{-1}\frac{\partial P_j(z_j)}{\partial z} = \eta_{j-1}^{-1}\rho_{j-1}^{-1}\frac{\partial P_{j-1}(z_j)}{\partial z} \qquad \text{for } j = 2, 3, \ldots, N \ (j \neq m), \tag{F.8}$$

$$\frac{\partial P_j(z_j)}{\partial z} = \frac{\partial P_{j-1}(z_j)}{\partial z} - S_\delta \qquad \text{for } j = m, \tag{F.9}$$

$$\rho_j^{-1}\frac{\partial P_j(z_j)}{\partial z} = \rho_{j-1}^{-1}\frac{\partial P_{j-1}(z_j)}{\partial z} \qquad \text{for } j = 1, \tag{F.10}$$

where η_j is the value of η in layer j (see below), ρ_j is the value of ρ_{av} in layer j, and ρ_0 is the (complex) density of the ground material (see Sec. D.4). The derivation of Eq. (F.9) is analogous to the derivation of Eq. (D.34); the discontinuity at $z = z_m$ of the 'staircase approximation' of the profile $k(z)$ (see Fig. F.1) is ignored in the derivation, as the real profile is continuous at $z = z_m$.

The effect of the factors η_j^{-1}, η_{j-1}^{-1}, ρ_j^{-1}, and ρ_{j-1}^{-1} in Eqs. (F.8) and (F.10) is often small, so these factors may be omitted. In the two-dimensional case of a non-moving atmosphere with an effective sound speed we have $\eta = -i\omega$ and $\eta_j^{-1} = \eta_{j-1}^{-1}$. In the three-dimensional case we have $\eta = -ick_m$, and $\eta_j^{-1} \approx \eta_{j-1}^{-1}$ from $u_{av} \ll c$ and $v_{av} \ll c$. Equation (F.10) is consistent with Eq. (F.8) as we have $\eta_1 = \eta_0$ from $u_{av} = v_{av} = 0$ at $z_1 = 0$.

The boundary conditions for $z_1 = 0$ give the relation

$$A_1 = R(k_{z1})B_1, \tag{F.11}$$

where

$$R(k_{z1}) = \frac{k_{z1} - k(z_1)/Z_s}{k_{z1} + k(z_1)/Z_s} \tag{F.12}$$

is the plane-wave reflection coefficient (see Appendix D); Z_s is the normalized impedance of the ground surface. For a locally reacting ground surface, Z_s is equal to the normalized characteristic impedance Z of the ground material. For an extended reacting ground surface, Z_s is given by Eq. (D.23).

The other boundary conditions can be used to derive a set of equations that can be solved for the constants A_j and B_j. It is easier, however, to follow a different approach. From Eq. (F.5) we find the relations

$$\begin{aligned} P_j(z + \Delta z) &= \cos(k_{zj}\Delta z)P_j(z) + k_{zj}^{-1}\sin(k_{zj}\Delta z)P_j'(z) \\ P_j'(z + \Delta z) &= -k_{zj}\sin(k_{zj}\Delta z)P_j(z) + \cos(k_{zj}\Delta z)P_j'(z) \end{aligned} \tag{F.13}$$

for z and $z + \Delta z$ in layer j, where $\cos w$ and $\sin w$ are defined for complex w as $\frac{1}{2}(e^{iw} + e^{-iw})$ and $\frac{1}{2i}(e^{iw} - e^{-iw})$, respectively. These relations will be used to determine the quantities $P_j(z_j)$.

F.3 Extrapolation from the ground and the top to the source

We start at the ground surface at height $z_1 = 0$. We arbitrarily set $B_1 = 1$ for the moment. From Eqs. (F.5) and (F.11) we find

$$\begin{aligned} P_1(z_1) &= R(k_{z1}) + 1 \\ P_1'(z_1) &= ik_{z1}\left[R(k_{z1}) - 1\right]. \end{aligned} \tag{F.14}$$

The values of the quantities $P_{j-1}(z_j)$ and $P_{j-1}'(z_j)$ are determined successively for $j = 2, 3, \ldots, m$ by using Eqs. (F.14), Eqs. (F.13) with $z = z_j$ and $\Delta z = z_{j+1} - z_j$, and Eqs. (F.7) and (F.8). The final values of $P_{m-1}(z_m)$ and $P_{m-1}'(z_m)$ at the source height z_m are denoted as P_{ml} and P_{ml}', respectively, where index 'l' denotes 'lower region', *i.e.* region below the source.

Next we start at the top at height z_N. Here we choose $P_{N-1}(z_N) = 1$ for the moment. From Eq. (F.5) with $B_{N-1} = 0$ we find

$$\begin{aligned} P_{N-1}(z_N) &= 1 \\ P'_{N-1}(z_N) &= ik_{zN}. \end{aligned} \tag{F.15}$$

The values of the quantities $P_j(z_j)$ and $P'_j(z_j)$ are determined successively for $j = N-1, N-2, \ldots, m$ by using Eqs. (F.15), Eqs. (F.13) with $z = z_{j+1}$ and $\Delta z = z_j - z_{j+1}$, and Eqs. (F.7) and (F.8). The final values of $P_m(z_m)$ and $P'_m(z_m)$ at the source height z_m are denoted as P_{mu} and P'_{mu}, respectively, where index 'u' denotes 'upper region'.

F.4 Field at the receiver

Numerical values of P_j and P'_j are not yet correct, only the ratios P'_j/P_j are correct, as we have arbitrarily set $B_1 = 1$ and $P_{N-1}(z_N) = 1$. At the source height z_m we have from Eq. (F.9)

$$\left(\frac{P'_{mu}}{P_{mu}}\right) P_m - \left(\frac{P'_{ml}}{P_{ml}}\right) P_m = -S_\delta, \tag{F.16}$$

where P_m is the correct value of P at the source height z_m. This gives

$$P_m = \frac{-S_\delta}{(P'_{mu}/P_{mu}) - (P'_{ml}/P_{ml})}. \tag{F.17}$$

Now the values of P_j, as determined by the calculation described in Sec. F.3, can be scaled to the correct values, by multiplication of P_j by the factor

$$\begin{aligned} &(P_m/P_{mu}) \quad \text{for } z_j > z_m, \\ &(P_m/P_{ml}) \quad \text{for } z_j < z_m. \end{aligned} \tag{F.18}$$

Finally, an inverse Fourier transformation of the quantities P_j yields the complex pressure amplitude in the spatial domain. In the three-dimensional case we have

$$p_c(x, y, z) = \frac{1}{(2\pi)^2} \int_{-\infty}^{\infty} \int_{-\infty}^{\infty} \exp(ik_x x + ik_y y) P(k_x, k_y, z)\, dk_x\, dk_y. \tag{F.19}$$

In the two-dimensional case we have from Eq. (E.64), returning to the notation Q instead of P,

$$q_c(r, z) = \frac{1}{\pi\sqrt{2}} \int_{-\infty}^{\infty} [\exp(ik_r r) + \exp(-ik_r r)] Q(k_r, z)\, dk_r. \tag{F.20}$$

Numerical aspects of these Fourier integrals are discussed in the next section.

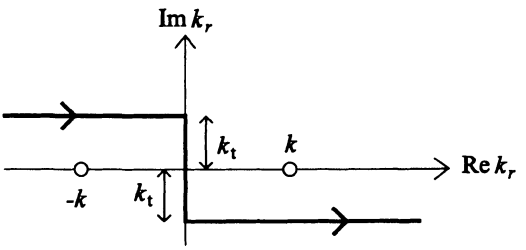

Figure F.2. Integration path that avoids the poles at $k_r = \pm k$ on the real axis.

F.5 Deformation of the integration path

We first consider Eq. (F.20) for the two-dimensional case. The integrand has poles on the integration path near $k_r = -k$ and $k_r = k$. This can be seen from the analytical solution for a homogeneous atmosphere without a ground surface (see Sec. F.7):

$$Q(k_r, z) = i\sqrt{\frac{\pi}{2}}\frac{\sqrt{k_r}}{k_z}\exp(ik_z|z - z_s|) \tag{F.21}$$

with $k_z^2 = k^2 - k_r^2$. The solution is of course (slightly) different for an inhomogeneous atmosphere, but the regions near the poles still dominate the integral in Eq. (F.20). To avoid the poles we do not integrate along the real axis in Eq. (F.20) but along the integration path shown in Fig. F.2. For positive k_r we include a small imaginary term $-ik_t$, and for negative k_r we include the opposite imaginary term $+ik_t$, where k_t is a small positive number. This choice corresponds to a positive imaginary part of k_z for $k_r^2 > k^2$, so that we have $Q \to 0$ for $k_r \to \pm\infty$ [see Eq. (F.21)]. It should be noted that the factors $\exp(\pm k_t r)$ can be taken out of the integrals $\int \exp(\pm ik_r r)Q\,dk_r$ in Eq. (F.20), so the integrals can still be performed with standard Fourier techniques (see Sec. B.4).

The integral in Eq. (F.20) can be transformed to an integral over positive wave numbers k_r only, by using the relation $Q(-k_r, z) = \pm iQ(k_r, z)$, which follows from Eqs. (F.3) and (F.4). It follows from the analytical example presented in Sec. F.7 that we must use the minus sign here. Equation (F.20) can therefore be written as

$$q_c(r, z) = \frac{1 - i}{\pi\sqrt{2}}\int_0^\infty [\exp(ik_r r) + \exp(-ik_r r)]Q(k_r, z)\,dk_r. \tag{F.22}$$

For the numerical evaluation of this integral we discretize the integration variable k_r as follows:

$$k_{r,n} = k_{s,n} - ik_t \quad (n = 1, 2, \ldots, M), \tag{F.23}$$

where k_t is the small positive number described before, and

$$k_{s,n} = \frac{1}{2}\Delta k, \frac{3}{2}\Delta k, \ldots, k_{s,M} \tag{F.24}$$

is the real part; Δk is the wave number spacing. The solution q_c given by Eq. (F.22) becomes periodic in r by the discretization, with periodic distance $2\pi/\Delta k$. The wave number spacing Δk should be chosen small enough to ensure that the value of q_c at the receiver is not affected by this periodicity; one can use, for example, $2\pi/\Delta k \geq 3r$. The choice of the maximum wave number $k_{s,M}$ depends on the frequency, as we have seen that the integral is dominated by wave numbers near the pole at $k_r = k = \omega/c_{\text{eff}}$. One can use $k_{s,M} \approx 3\omega/c_0$, where c_0 is the sound speed at $z = 0$. For the small positive number k_t one can use the value of Δk.

The truncation of the integration interval in Eq. (F.22) at the maximum wave number $k_{s,M}$ induces small, rapid oscillations of q_c as a function of r. These are easily eliminated by including a window function as a factor in the integrand of Eq. (F.22); this function is equal to unity except near the integration limits where the function goes smoothly to zero.

Next we consider the integral (F.19) for the three-dimensional case. As in the two-dimensional case, the solution for a homogeneous atmosphere is proportional to k_z^{-1} (see Sec. D.4). This implies that there are poles in the real $k_x k_y$ integration plane. The location of the poles depends on the receiver coordinates x and y. For $y = 0$ the poles are on the k_x axis, at $(k_x, k_y) = (-k, 0)$ and $(k_x, k_y) = (k, 0)$. In this case the k_x integration interval can be chosen as $[-3k_0, 3k_0]$ and the k_y integration interval as $[-k_0, k_0]$, with $k_0 = \omega/c_0$. As in the two-dimensional case, the integration variables are discretized and the poles must be avoided by including a small imaginary term in k_x and k_y. For $y = 0$ the poles are on the k_x axis and we know from the two-dimensional case that the imaginary part of k_x must be negative for $k_x > 0$ and positive for $k_x < 0$ (see Fig. F.2). A possible choice is therefore [158]

$$\begin{aligned} k_{x,m} &= k_{sx,m} - ik_t \cos\theta_{mn} \\ k_{y,n} &= k_{sy,n} - ik_t \sin\theta_{mn}, \end{aligned} \tag{F.25}$$

where $k_{sx,m}$ and $k_{sy,n}$ are the discretized variables in the real $k_x k_y$ plane, $\theta_{mn} = \arctan(k_{sy,n}/k_{sx,m})$ is the polar angle of the vector $(k_{sx,m}, k_{sy,n})$ running from 0 to 2π, and k_t is a small positive number. As in the two-dimensional case, a window function must be used to eliminate spurious effects from the truncation of the integration intervals.

F.6 Improvement of numerical accuracy

The efficiency of the computational method described in the previous sections depends on the number of horizontal layers that is used. This number depends on the vertical profiles of the adiabatic sound speed and the wind velocity.

At heights where the vertical gradients are large (near the ground surface for example), thin layers must be used. At heights where the gradients are small, thick layers can be used. In the case of a homogeneous atmosphere, two layers are sufficient (see Sec. D.4).

If the number of layers is large, one should be aware of numerical errors in the calculation of the quantities P_j by repeated application of Eqs. (F.13). These errors originate predominantly from the factors $\exp(\pm ik_{zj}\Delta z)$ in Eqs. (F.13). In the calculation of the (unscaled) quantities P_j for $j = 2, 3, \ldots, m$ (see Sec. F.3), P_j may become large with increasing j owing to the factors $\exp(-ik_{zj}\Delta z)$ with imaginary k_{zj}. Similarly, in the calculation of P_j for $j = N-1, N-2, \ldots, m$, P_j may become large near the source owing to the factors $\exp(+ik_{zj}\Delta z)$ with imaginary k_{zj}. This problem can be solved by multiplying the quantities P_j and P'_j by a factor

$$\begin{array}{ll} \exp(ik_{z0}\Delta z) & \text{for } \Delta z > 0 \\ \exp(-ik_{z0}\Delta z) & \text{for } \Delta z < 0 \end{array} \tag{F.26}$$

after each step $z \to z + \Delta z$ (see Sec. F.3). These factors do not affect the ratios P'_j/P_j. In the final scaling to the correct values of P_j, the reciprocal factors should be included; this gives an additional factor $\exp(ik_{z0}|z - z_s|)$ in the scale factors (F.18). For the wave number k_{z0} one can use, for example, the vertical wave number at the source height. An even better approach can be applied in the layers above the highest location where the field is to be computed. Here one can simply divide P_j and P'_j by P_j after the downward calculation in a layer, so P_j and P'_j are replaced by 1 and P'_j/P_j, respectively. This approach is equivalent to the admittance extrapolation approach described in Ref. [155].

F.7 Analytical example

As an example we will calculate the FFP solution for the two-dimensional case with a homogeneous atmosphere. In this case we use only two layers: layer 1 between $z_1 = 0$ and $z_2 = z_s$ ($m = 2$), and layer 2 between z_2 and $z_3 > z_2$ ($N = 3$).

Equations (F.14) are written as $Q_1(z_1) = R + 1$ and $Q'_1(z_1) = ik_z(R - 1)$. Application of Eqs. (F.13) with $z = z_1$ and $\Delta z = z_s - z_1 = z_s$ gives

$$\begin{aligned} Q_{ml} &= \exp(ik_z z_s)R + \exp(-ik_z z_s) \\ Q'_{ml} &= ik_z[\exp(ik_z z_s)R - \exp(-ik_z z_s)]. \end{aligned} \tag{F.27}$$

Equations (F.15) are written as $Q_{N-1}(z_N) = 1$ and $Q'_{N-1}(z_N) = ik_z$. Application of Eqs. (F.13) with $z = z_N$ and $\Delta z = z_s - z_N$ gives

$$\begin{aligned} Q_{mu} &= \exp[ik_z(z_s - z_N)] \\ Q'_{mu} &= ik_z \exp[ik_z(z_s - z_N)]. \end{aligned} \tag{F.28}$$

Equation (F.17) gives

$$Q_m = i\sqrt{\frac{\pi}{2}}\frac{\sqrt{k_r}}{k_z}[1 + R\exp(2ik_z z_s)]. \tag{F.29}$$

With the scale factors (F.18), the correct values of $Q_j(z_j)$ become

$$Q_j(z) = i\sqrt{\frac{\pi}{2}}\frac{\sqrt{k_r}}{k_z}\left\{\exp[ik_z|z - z_s|] + R\exp[ik_z(z + z_s)]\right\}. \tag{F.30}$$

This expression is valid for arbitrary $z > 0$.

We consider the case without a ground surface, so we have $R = 0$. Equation (F.30) becomes

$$Q_j = i\sqrt{\frac{\pi}{2}}\frac{\sqrt{k_r}}{k_z}\exp(ik_z|z - z_s|). \tag{F.31}$$

Equation (F.22) gives

$$q_c = \frac{i(1-i)}{2\sqrt{\pi}}\int_0^\infty \exp(ik_r r + ik_z|z - z_s|)\frac{\sqrt{k_r}}{k_z}dk_r + \frac{i(1-i)}{2\sqrt{\pi}}\int_0^\infty \exp(-ik_r r + ik_z|z - z_s|)\frac{\sqrt{k_r}}{k_z}dk_r. \tag{F.32}$$

We first consider the first integral on the right-hand side, which we write as

$$I_1 = \int_0^\infty \exp[iF(k_r)]G(k_r)dk_r \tag{F.33}$$

with $F(k_r) = k_r r + |z - z_s|\sqrt{k^2 - k_r^2}$ and $G(k_r) = \sqrt{k_r}/\sqrt{k^2 - k_r^2}$. For large $k_r r$, the integral (F.33) can be calculated with the method of stationary phase (see Appendix P):

$$I_1 \approx \sqrt{\frac{2\pi}{|F''(k_{r,0})|}}G(k_{r,0})\exp[iF(k_{r,0}) + i\mu\frac{1}{4}\pi], \tag{F.34}$$

with $\mu = \text{sign}[F''(k_{r,0})]$, where sign$(x)$ is 1 for $x > 0$ and -1 for $x < 0$; the quantity $k_{r,0}$ is the wave number at the stationary phase point, *i.e.* the solution of the equation $F'(k_{r,0}) = 0$. We find $k_{r,0} = rk/R_1$ with $R_1 = \sqrt{r^2 + (z - z_s)^2}$, and the integral becomes

$$I_1 = \sqrt{\pi}(1-i)\sqrt{r}\frac{\exp(ikR_1)}{R_1}. \tag{F.35}$$

The second integral on the right-hand side of Eq. (F.32) can be treated in a similar way. In this case the stationary phase point is at $k_{r,0} = -rk/R_1$, which

is outside the integration interval. This means that the integral can be neglected with respect to the first integral on the right-hand side of Eq. (F.32). Equations (F.32) and (F.35) give

$$q_c = \sqrt{r}\frac{\exp(ikR_1)}{R_1}, \tag{F.36}$$

which is the correct expression for q_c, corresponding to $p_c = \exp(ikR_1)/R_1$. Thus, we have shown that the FFP solution agrees with the analytical solution for the two-dimensional case with a homogeneous atmosphere.

Appendix G

Parabolic Equation (PE) method

G.1 Introduction

The Parabolic Equation (PE) method is a numerical method for computing the sound field of a monopole source in a refracting atmosphere above a ground surface. In contrast to the Fast Field Program (see Appendix F), the PE method is not limited to a layered atmosphere and a homogeneous ground surface. In the PE method, the sound speed profile and the ground impedance may vary along the propagation path. Furthermore, effects of atmospheric turbulence and irregular terrain can be taken into account in the PE method.

In the PE method, the sound field is computed by solving a parabolic equation, which follows from the wave equation by neglecting contributions to the field from sound waves with large elevation angles. Consequently, the PE method gives accurate results in a region limited by a maximum elevation angle (see Fig. 4.11). The value of the maximum elevation angle ranges from typically 10° to 70° or higher, depending on the small-angle approximation used in the derivation of the parabolic equation [69] (*cf.* Secs. 4.6 and G.12). A maximum elevation angle of 10° is often sufficient for situations with the source and the receiver near the ground.

The PE method has been widely used in underwater acoustics [148, 45, 69, 78]. In 1989, Gilbert and White presented a PE method for atmospheric acoustics [56]. This method is called the Crank-Nicholson PE (CNPE) method. In this appendix we describe the CNPE method, following a description by West *et al.* [156]. In Appendix H we describe an alternate PE method: the Green's Function PE (GFPE) method [58].

Both PE methods are two-dimensional methods, based on the axisymmetric approximation (see Sec. E.4). Recently a three-dimensional GFPE method has been developed [44], which is also described in Appendix H. Three-dimensional

CNPE methods are described in Refs. [41, 22, 77].

The CNPE method yields a finite-difference solution of a wide-angle parabolic equation; the solution is accurate up to elevation angles of about 35°. The GFPE method is less accurate than the CNPE method in situations with wide-angle propagation and large sound speed gradients; for most applications, however, the GFPE method is sufficiently accurate. The advantage of the GFPE method is that this method is more efficient, *i.e.* faster, than the CNPE method.

A flat, locally reacting ground surface is assumed in the PE methods described in this appendix and in Appendix H. In Appendix M we describe the application of the PE methods to propagation over hills and other terrain profiles. In Appendix J we describe how the effect of atmospheric turbulence can be taken into account in the PE methods.

G.2 Basic approach of the CNPE method

The CNPE method described in this appendix is based on the axisymmetric approximation, which was described in Sec. E.4. The axisymmetric approximation implies that the three-dimensional Helmholtz equation (E.49) reduces to the two-dimensional Helmholtz equation (E.53):

$$\frac{\partial^2 q_c}{\partial r^2} + \frac{\partial^2 q_c}{\partial z^2} + k_{\text{eff}}^2 q_c = 0, \tag{G.1}$$

where we use the rz coordinates shown in Fig. E.1. The term $\partial_z^2 q_c$ in Eq. (G.1) is an approximation of the term $k_{\text{eff}}^2 \partial_z (k_{\text{eff}}^{-2} \partial_z q_c)$ in Eq. (E.53) (with the notation $\partial_z \equiv \partial/\partial z$). This approximation is often used in the PE method; numerical computations show that the effect of the approximation is usually negligible. In Sec. G.10 we will show how the term $k_{\text{eff}}^2 \partial_z (k_{\text{eff}}^{-2} \partial_z q_c)$ can be implemented in the PE method.

We recall that the quantity $q_c(r, z)$ in Eq. (G.1) is related to the complex pressure amplitude $p_c(r, z)$ by Eq. (E.51):

$$q_c = p_c \sqrt{r}. \tag{G.2}$$

The wave number k_{eff} in Eq. (G.1) is equal to ω/c_{eff}, where ω is the angular frequency and c_{eff} is the effective sound speed. The subscript 'eff' will be omitted, so we have $k_{\text{eff}} \equiv k$ and $c_{\text{eff}} \equiv c$. The subscript 'c' of q_c will also be omitted, so we have $q_c \equiv q$.

In the CNPE method, the field $q(r, z)$ is computed on a grid in the rz plane (see Fig. G.1). The computation starts at $r = 0$ with a starting function $q(0, z)$, which represents a monopole source. This function is extrapolated step-wise in the positive r direction, which yields the complete field $q(r, z)$. An extrapolation step from range r to range $r + \Delta r$ is written as

$$q(r, z) \rightarrow q(r + \Delta r, z). \tag{G.3}$$

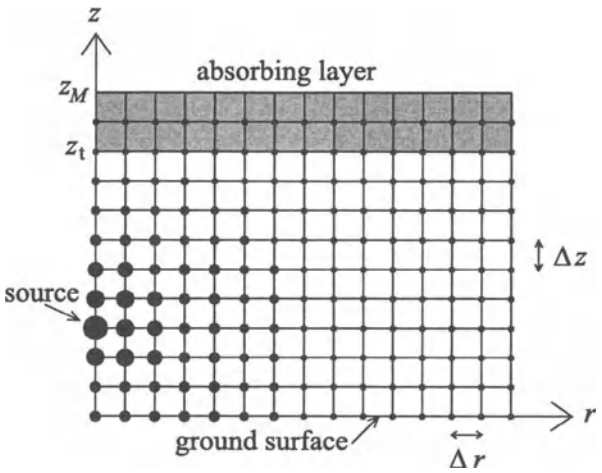

Figure G.1. Grid in the rz plane used in the PE method, with horizontal grid spacing Δr, vertical grid spacing Δz, a ground surface at $z = 0$, and an absorbing layer at the top ($z_t \leq z \leq z_M$). The amplitude of the sound pressure at a grid point is represented schematically by the size of the circle at the grid point. In practice the number of grid points along the z axis is typically 1000 or more (see Sec. G.9).

Thus, the values of q at the grid points at range $r + \Delta r$ are computed from the values at range r. Accurate results are obtained only if the horizontal grid spacing Δr and the vertical grid spacing Δz do not exceed about $\lambda/10$, where λ is an average wavelength.

The grid has a finite height. At the top of the grid we use an artificial absorbing layer to eliminate reflections from the top of the grid. The ground surface is taken into account by a boundary condition, with the complex ground impedance as a parameter.

The range dependence of the wave number k in Eq. (G.1) is taken into account step-wise. Within an extrapolation step, the range dependence is neglected, so k is a function of z only.

G.3 Narrow-angle parabolic equation

We write the solution of Eq. (G.1) as

$$q(r, z) = \psi(r, z) \exp(ik_a r), \tag{G.4}$$

where k_a is the value of the wave number $k(z)$ at some average height or at the ground surface; for the numerical examples in this book we used the value at the ground surface. The factor $\exp(ik_a r)$ in Eq. (G.4) represents a plane wave

traveling in the positive r direction, and oscillates rapidly as a function of r; the function $\psi(r,z)$ usually varies slowly with r. Substitution of Eq. (G.4) into Eq. (G.1) gives

$$\frac{\partial^2\psi}{\partial r^2} + 2ik_a\frac{\partial\psi}{\partial r} + \frac{\partial^2\psi}{\partial z^2} + (k^2 - k_a^2)\psi = 0. \tag{G.5}$$

As ψ usually varies slowly with r, the first term on the left-hand side can be neglected with respect to the second term, so we find

$$2ik_a\frac{\partial\psi}{\partial r} + \frac{\partial^2\psi}{\partial z^2} + (k^2 - k_a^2)\psi = 0. \tag{G.6}$$

This equation is called the narrow-angle parabolic equation.

G.4 Alternate derivation of the narrow-angle parabolic equation

The narrow-angle parabolic equation can be derived in a different way. We write Eq. (G.1) as

$$\partial_r^2 q + H_2(z)q = 0, \tag{G.7}$$

where we use the notation $\partial_r \equiv \partial/\partial r$ and the operator $H_2(z)$ is defined as

$$H_2(z) = k^2(z) + \partial_z^2. \tag{G.8}$$

We define the quantity $\delta k^2(z)$ as

$$\delta k^2(z) = k^2(z) - k_a^2, \tag{G.9}$$

so we have

$$H_2(z) = k_a^2 + \delta k^2(z) + \partial_z^2 \equiv k_a^2(1+s) \tag{G.10}$$

with

$$s = k_a^{-2}\delta k^2(z) + k_a^{-2}\partial_z^2. \tag{G.11}$$

Equation (G.7) can be written as

$$[\partial_r - iH_1(z)]\,[\partial_r + iH_1(z)]\,q = 0, \tag{G.12}$$

where

$$H_1(z) = k_a\sqrt{1+s} \tag{G.13}$$

is the square-root operator. The square-root of the differential operator $1+s$ is defined by the expansion $\sqrt{1+s} = 1 + \frac{1}{2}s - \frac{1}{8}s^2 + \ldots$, which is analogous to

the expansion of a common square-root function [26]. It is readily verified that, with this definition, H_1 satisfies $H_1^2 = H_2$. We will consider different ways of truncating the expansion of the square-root operator.

In the derivation of Eq. (G.12) from Eq. (G.7) we have assumed that the operators H_1 and ∂_r commute, which means that we have $H_1\partial_r = \partial_r H_1$. Strictly speaking this is valid only for a layered atmosphere with $k = k(z)$. For an atmosphere with a range-dependent wave number $k(r, z)$ it is an approximation.

The factor $[\partial_r - iH_1(z)]$ in Eq. (G.12) represents waves traveling in the positive r direction and the factor $[\partial_r + iH_1(z)]$ represents waves traveling in the negative r direction, as we assume a harmonic time factor $\exp(-i\omega t)$ (see Secs. A.3 and A.4). In the PE method we choose the source at $r = 0$ and the receiver at $r > 0$, and we take into account only waves traveling in the positive r direction; back scattering is neglected. Equation (G.12) reduces to the one-way wave equation

$$\partial_r q - iH_1(z)q = 0. \tag{G.14}$$

If we approximate the square-root operator (G.13) by

$$H_1(z) = k_a(1 + \frac{1}{2}s), \tag{G.15}$$

we find the narrow-angle parabolic equation

$$\partial_r q - ik_a q - \frac{i}{2k_a}\left(\partial_z^2 + \delta k^2(z)\right) q = 0. \tag{G.16}$$

If we replace the quantity q by the quantity ψ defined by Eq. (G.4) we find

$$\partial_r \psi = \frac{1}{2} ik_a s\psi, \tag{G.17}$$

which is equivalent to Eq. (G.6).

G.5 Wide-angle parabolic equation

The approximation (G.15) for the square-root operator is accurate only for propagation at small elevation angles, up to about 10°. A more accurate expansion of the square-root operator is [26]

$$H_1(z) = k_a \frac{1 + \frac{3}{4}s}{1 + \frac{1}{4}s}, \tag{G.18}$$

where $1/(1 + \frac{1}{4}s)$ is the inverse of the operator $1 + \frac{1}{4}s$. This expansion has quadratic accuracy in s, while Eq. (G.15) has linear accuracy in s. This can be verified by showing that $(1 + \frac{1}{4}s)^2 H_2 q$ agrees to second order in s with $(1 + \frac{1}{4}s)^2 H_1^2 q$. The reason for writing H_1 as a quotient instead of the expansion

$H_1 = k_a(1 + \frac{1}{2}s - \frac{1}{8}s^2)$ is that Eq. (G.18) leads to a tridiagonal matrix equation for a PE step (see Sec. G.6), which is easily solved, while $H_1 = k_a(1 + \frac{1}{2}s - \frac{1}{8}s^2)$ would lead to a matrix equation with more nonzero elements. With Eq. (G.18), the one-way wave equation (G.14) becomes

$$(1 + \frac{1}{4}s)\partial_r q = ik_a(1 + \frac{3}{4}s)q. \tag{G.19}$$

This is the wide-angle parabolic equation. The corresponding equation for the quantity ψ defined by Eq. (G.4) is

$$(1 + \frac{1}{4}s)\partial_r \psi = \frac{1}{2}ik_a s\psi. \tag{G.20}$$

G.6 Finite-difference solution of the narrow-angle parabolic equation

The narrow-angle and wide-angle parabolic equations derived in the previous sections can be solved numerically by approximating the derivatives in the equations with finite differences [156]. We first describe the finite-difference solution of the narrow-angle parabolic equation (G.6), which we write as

$$\partial_r \psi = \alpha \partial_z^2 \psi + \beta\psi \tag{G.21}$$

with $\alpha = \frac{1}{2}i/k_a$ and $\beta = \frac{1}{2}i(k^2 - k_a^2)/k_a = \frac{1}{2}i\,\delta k^2/k_a$. We use the grid shown in Fig. G.1, with grid points at heights

$$z_j = j\Delta z \quad \text{with } j = 1, 2, \ldots, M. \tag{G.22}$$

We denote the field ψ at range r as a vector $\vec{\psi}(r)$ with elements $\psi_j = \psi(r, z_j)$. Using the central difference formula

$$(\partial_z^2 \psi)_{z_j} = \frac{\psi_{j+1} - 2\psi_j + \psi_{j-1}}{(\Delta z)^2}, \tag{G.23}$$

we can write Eq. (G.21) as

$$\partial_r \begin{pmatrix} \psi_1 \\ \psi_2 \\ \psi_3 \\ \vdots \\ \psi_{M-1} \\ \psi_M \end{pmatrix} = \left[\gamma \begin{pmatrix} -2 & 1 & & & & \\ 1 & -2 & 1 & & & \\ & 1 & -2 & 1 & & \\ & & \ddots & \ddots & \ddots & \\ & & & 1 & -2 & 1 \\ & & & & 1 & -2 \end{pmatrix} + \begin{pmatrix} \beta_1 & & & & & \\ & \beta_2 & & & & \\ & & \beta_3 & & & \\ & & & \ddots & & \\ & & & & \beta_{M-1} & \\ & & & & & \beta_M \end{pmatrix} \right] \begin{pmatrix} \psi_1 \\ \psi_2 \\ \psi_3 \\ \vdots \\ \psi_{M-1} \\ \psi_M \end{pmatrix} + \gamma \begin{pmatrix} \psi_0 \\ 0 \\ 0 \\ \vdots \\ 0 \\ \psi_{M+1} \end{pmatrix} \tag{G.24}$$

with $\gamma = \alpha/(\Delta z)^2$ and $\beta_j = \beta(z_j)$; in the matrices on the right-hand side we have indicated only the nonzero elements. The vector equation (G.24) represents a set of M equations; each equation relates an element $\partial_r \psi_j$ to the elements ψ_{j-1}, ψ_j, and ψ_{j+1}. The last term on the right-hand side of Eq. (G.24) contains the field ψ_0 at the ground level $z_0 = 0$ and the field ψ_{M+1} at height $z_{M+1} = (M+1)\Delta z$. This term accounts for the two terms that are 'missing' in the first term on the right-hand side.

For the field ψ_0 at the ground level we use the relation

$$\psi_0 = \sigma_1 \psi_1 + \sigma_2 \psi_2 \tag{G.25}$$

with coefficients σ_1 and σ_2, which depend on the ground impedance (see Sec. G.8). For the field ψ_{M+1} we use the relation

$$\psi_{M+1} = \tau_1 \psi_M + \tau_2 \psi_{M-1} \tag{G.26}$$

with coefficients τ_1 and τ_2 (see Sec. G.9).

Using Eqs. (G.25) and (G.26), we write Eq. (G.24) as

$$\partial_r \vec{\psi} = (\gamma T + D)\vec{\psi}, \tag{G.27}$$

where T is a tridiagonal matrix and D is a diagonal matrix; T is given by

$$T = \begin{pmatrix} -2+\sigma_1 & 1+\sigma_2 & & & & \\ 1 & -2 & 1 & & & \\ & 1 & -2 & 1 & & \\ & & \ddots & \ddots & \ddots & \\ & & & 1 & -2 & 1 \\ & & & & 1+\tau_2 & -2+\tau_1 \end{pmatrix} \tag{G.28}$$

and D is given by

$$D = \begin{pmatrix} \beta_1 & & & & & \\ & \beta_2 & & & & \\ & & \beta_3 & & & \\ & & & \ddots & & \\ & & & & \beta_{M-1} & \\ & & & & & \beta_M \end{pmatrix}. \tag{G.29}$$

Integration of Eq. (G.27) from range r to range $r + \Delta r$ gives

$$\vec{\psi}(r + \Delta r) - \vec{\psi}(r) = (\gamma T + D) \int_r^{r+\Delta r} \vec{\psi}\, dr. \tag{G.30}$$

We approximate the integral on the right-hand side by $\frac{1}{2}[\vec{\psi}(r+\Delta r)+\vec{\psi}(r)]\Delta r$, *i.e.* the product of the average value of the integrand and the integration interval Δr. This approximation is called the Crank-Nicholson approximation. We find

$$M_2 \vec{\psi}(r + \Delta r) = M_1 \vec{\psi}(r), \tag{G.31}$$

where M_1 and M_2 are tridiagonal matrices given by

$$\begin{aligned} M_1 &= 1 + \tfrac{1}{2}\Delta r(\gamma T + D) \\ M_2 &= 1 - \tfrac{1}{2}\Delta r(\gamma T + D). \end{aligned} \tag{G.32}$$

A PE step $\vec{\psi}(r) \to \vec{\psi}(r + \Delta r)$ is reduced to the solution of Eq. (G.31), which is a set of M linear equations for M unknowns $\psi_j(r + \Delta r)$. As M_1 and M_2 are tridiagonal matrices, the solution can be performed efficiently by Gauss elimination [112].

G.7 Finite-difference solution of the wide-angle parabolic equation

The wide-angle parabolic equation (G.20) differs from the narrow-angle parabolic equation (G.17) by the factor $(1+\frac{1}{4}s)$ on the left-hand side. Comparison of Eqs. (G.17) and (G.27) shows that the finite-difference matrix form of the operator $\frac{1}{2}ik_a s$ is $\gamma T + D$. Consequently, the factor $(1 + \frac{1}{4}s)$ in the wide-angle parabolic equation yields a factor $[1+(\gamma T+D)/(2ik_a)]$ on the left-hand side of Eq. (G.30). This leads to the matrix equation (G.31) with modified matrices M_1 and M_2 given by

$$\begin{aligned} M_1 &= 1 + \frac{1}{2}\Delta r(\gamma T + D) + \frac{\gamma T + D}{2ik_a} \\ M_2 &= 1 - \frac{1}{2}\Delta r(\gamma T + D) + \frac{\gamma T + D}{2ik_a}. \end{aligned} \tag{G.33}$$

The PE method based on Eqs. (G.31) and (G.33) is called the Crank-Nicholson PE (CNPE) method.

G.8 Boundary condition at the ground surface

In this section we determine the coefficients σ_1 and σ_2 in Eq. (G.25). At the ground surface we have the boundary condition (see Sec. D.2)

$$\left(\frac{p_c}{v_{c,n}}\right)_{z=0} = Z\rho c, \tag{G.34}$$

where Z is the normalized impedance of the locally reacting ground surface, ρc is the impedance of air (evaluated just above the ground surface), p_c is the complex pressure amplitude, and $v_{c,n}$ is the normal component of the complex fluid velocity amplitude; the normal component is the component in the negative z direction. From Eq. (A.19) we have

$$v_{c,n} = -\frac{1}{i\omega\rho}\frac{\partial p_c}{\partial z}. \tag{G.35}$$

If we use the first-order finite-difference approximation

$$\frac{\partial p_c}{\partial z} = \frac{p_1 - p_0}{\Delta z} \tag{G.36}$$

with the notation $p_j = p_c(z_j)$ and $z_0 = 0$, we find from Eqs. (G.34) and (G.35) the following relation between p_0 and p_1:

$$p_0 = \left(1 - \frac{ik_0\Delta z}{Z}\right)^{-1} p_1, \tag{G.37}$$

where k_0 is the wave number at the ground surface. For the wide-angle parabolic equation it is preferable to use a second-order approximation for $\partial p_c/\partial z$, instead of the first-order approximation (G.36). Equation (G.36) represents a first-order estimate of the derivative centered at $z = \frac{1}{2}\Delta z$. For a second-order estimate we use the second derivative $\partial^2 p_c/\partial z^2 \approx (p_2 - 2p_1 + p_0)/(\Delta z)^2$ to estimate the change of the first derivative over the height interval from $z = \frac{1}{2}\Delta z$ to $z = 0$:

$$\frac{\partial p_c}{\partial z} = \frac{p_1 - p_0}{\Delta z} - \frac{1}{2}\Delta z\,\frac{p_2 - 2p_1 + p_0}{(\Delta z)^2} = \frac{-\frac{3}{2}p_0 + 2p_1 - \frac{1}{2}p_2}{\Delta z}. \tag{G.38}$$

This gives the following relation between p_0, p_1, and p_2:

$$p_0 = \left(3 - \frac{2ik_0\Delta z}{Z}\right)^{-1}(4p_1 - p_2). \tag{G.39}$$

This relation also holds with p_j replaced by ψ_j, so the coefficients σ_1 and σ_2 in Eq. (G.25) follow from this relation.

We assume that the impedance is constant within a range step. A range dependence of the ground impedance is taken into account in the PE method by changing the impedance between successive range steps [123, 30].

G.9 Boundary condition at the top of the grid

The numerical grid is truncated at height $z = z_M$. In this section we describe how the effects of the truncation are minimized.

At the top surface at $z = z_M$ we use a similar boundary condition as at the ground surface. Instead of the ground impedance we use $Z = 1$ for the normalized impedance of the top surface ($Z = 1$ is the normalized impedance of air). From Eq. (G.39) we find

$$p_{M+1} = (3 + 2ik_0\Delta z)^{-1}(4p_M - p_{M-1}). \tag{G.40}$$

The coefficients τ_1 and τ_2 in Eq. (G.26) follow from this relation.

The impedance $Z = 1$ at the top surface corresponds to a vanishing reflection coefficient only for vertically traveling plane waves. Other waves are partially reflected back into the region $z < z_M$. An absorbing layer just below the top surface, between $z = z_t$ and $z = z_M$ (see Fig. G.1), eliminates these reflections. We add an imaginary term to the wave number $k(z)$ for $z_t \le z \le z_M$, so that waves are gradually attenuated in the absorbing layer. Numerical tests show that a good choice for the imaginary term is $iA_t(z - z_t)^2/(z_M - z_t)^2$, where A_t is a constant. The optimum choice for A_t varies with frequency. Good results are obtained with $A_t = 1, 0.5, 0.4, 0.2$ at the frequencies 1000, 500, 125, 30 Hz, respectively; for intermediate frequencies, linear interpolation can be used. A safe value for the thickness $z_M - z_t$ of the absorbing layer is 50 wavelengths. An alternate boundary condition at the top surface is described in Ref. [122].

The sound field should not be influenced by the absorbing layer, so the height z_M of the top surface should not be chosen too small. A general rule for the choice of z_M cannot be given. The optimum choice depends on the geometry, the frequency, and the sound speed profile [134]. Usually z_M is at least equal to 1000 vertical grid spacings.

In the case of a downward refracting atmosphere, all curved sound rays from the source to the receiver should have their maximum heights below the absorbing layer. As an example we consider the logarithmic sound speed profile $c(z) = c_0 + b\ln(1 + z/z_0)$ [see Eq. (4.5)], where the roughness length z_0 should not be confused with the height $z_0 = 0$ used in previous sections. Downward refraction corresponds to $b > 0$. If the source and the receiver are close to the ground surface, the maximum height of the highest ray is given by $h \approx r/\sqrt{2\pi c_0/b}$ [see Eq. (4.9)]. A typical value of b is 1 m/s, so we find $h \approx 0.02r$. For $r = 10$ km, for example, this gives $h = 200$ m.

G.10 Density profile

In Eq. (G.1) we used the approximation $\partial_z^2 q$ for the term $k^2\partial_z(k^{-2}\partial_z q)$ (we recall that we use the notation $k \equiv k_{\text{eff}}$ and $q \equiv q_c$). It is straightforward to repeat the formulation of the PE method, presented in the previous sections, for the case that the term $k^2\partial_z(k^{-2}\partial_z q)$ is not approximated by $\partial_z^2 q$. For a non-moving

isobaric atmosphere, $k^2\partial_z(k^{-2}\partial_z q)$ is equal to $\rho\partial_z(\rho^{-1}\partial_z q)$, where $\rho = \rho(z)$ is the vertical density profile in the atmosphere [this follows from $k = \omega/c$ and Eq. (A.9)]. In this section we describe how the PE method is modified if $\partial_z^2 q$ in Eq. (G.1) is replaced by $\rho\partial_z(\rho^{-1}\partial_z q)$:

$$\frac{\partial^2 q}{\partial r^2} + \rho\frac{\partial}{\partial z}\left(\rho^{-1}\frac{\partial q}{\partial z}\right) + k^2 q = 0. \tag{G.41}$$

If the term $k^2\partial_z(k^{-2}\partial_z q)$ is used instead of $\rho\partial_z(\rho^{-1}\partial_z q)$, the density ρ should be replaced by k^2 in the equations in this section.

Equation (G.41) differs from Eq. (G.1) by the replacement of the differential operator ∂_z^2 by the differential operator $\rho\partial_z(\rho^{-1}\partial_z)$. The finite-difference form of the operator $\rho\partial_z(\rho^{-1}\partial_z)$ is given by

$$\rho\partial_z(\rho^{-1}\partial_z\psi)_{z_j} = \frac{1}{(\Delta z)^2}\left[\frac{1}{2}\left(1+\frac{\rho_j}{\rho_{j+1}}\right)\psi_{j+1} - \frac{1}{2}\left(\frac{\rho_j}{\rho_{j+1}} + 2 + \frac{\rho_j}{\rho_{j-1}}\right)\psi_j + \frac{1}{2}\left(1+\frac{\rho_j}{\rho_{j-1}}\right)\psi_{j-1}\right]. \tag{G.42}$$

The only effect of the replacement of ∂_z^2 by $\rho\partial_z(\rho^{-1}\partial_z)$ is that the matrix T in Eqs. (G.32) and (G.33) is modified:

$$T = \begin{pmatrix} -2\gamma_{0,1} & \gamma_{1,1} & & & & & \\ \gamma_{-1,2} & -2\gamma_{0,2} & \gamma_{1,2} & & & & \\ & \gamma_{-1,3} & -2\gamma_{0,3} & \gamma_{1,3} & & & \\ & & \ddots & \ddots & \ddots & & \\ & & & \gamma_{-1,M-1} & -2\gamma_{0,M-1} & \gamma_{1,M-1} & \\ & & & & \gamma_{-1,M} & -2\gamma_{0,M} & \end{pmatrix} + \begin{pmatrix} \gamma_{-1,1}\sigma_1 & \gamma_{-1,1}\sigma_2 & & & & & \\ 0 & 0 & 0 & & & & \\ & 0 & 0 & 0 & & & \\ & & \ddots & \ddots & \ddots & & \\ & & & 0 & 0 & 0 & \\ & & & & \gamma_{1,M}\tau_2 & \gamma_{1,M}\tau_1 & \end{pmatrix} \tag{G.43}$$

with

$$\begin{aligned} \gamma_{1,j} &= \frac{1}{2}\left(1+\frac{\rho_j}{\rho_{j+1}}\right) \\ \gamma_{0,j} &= \frac{1}{4}\left(\frac{\rho_j}{\rho_{j+1}} + 2 + \frac{\rho_j}{\rho_{j-1}}\right) \\ \gamma_{-1,j} &= \frac{1}{2}\left(1+\frac{\rho_j}{\rho_{j-1}}\right). \end{aligned} \tag{G.44}$$

Numerical computations show that the effect of the approximation of the term $\rho\partial_z(\rho^{-1}\partial_z q)$ in Eq. (G.41) by $\partial_z^2 q$ is very small. The effect of atmospheric gradients on sound propagation is determined almost completely by the term $k^2 q$ in Eq. (G.41).

G.11 Finite-element solution

In the previous sections we described a finite-difference approach to the solution of the wide-angle parabolic equation. Gilbert and White [56] presented a slightly more accurate finite-element approach; with this approach it is possible to use a non-uniform vertical grid spacing, which means that $z_j - z_{j-1}$ may vary with j. The finite-element approach is based on Eq. (G.41), so density gradients are included in the solution.

The finite-difference approach resulted in the tridiagonal matrix equation (G.31). The finite-element approach also leads to a tridiagonal matrix equation of the form (G.31), which we write as

$$M^- \vec{\psi}(r + \Delta r) = M^+ \vec{\psi}(r). \tag{G.45}$$

The tridiagonal matrices $M^\pm$ of the finite-element approach are given by (see Ref. [56])

$$M^\pm = \begin{pmatrix} M^\pm_{0,1} & M^\pm_{1,1} & & & & & \\ M^\pm_{-1,2} & M^\pm_{0,2} & M^\pm_{1,2} & & & & \\ & M^\pm_{-1,3} & M^\pm_{0,3} & M^\pm_{1,3} & & & \\ & & \ddots & \ddots & \ddots & & \\ & & & M^\pm_{-1,M-1} & M^\pm_{0,M-1} & M^\pm_{1,M-1} & \\ & & & & M^\pm_{-1,M} & M^\pm_{0,M} & \end{pmatrix} + \begin{pmatrix} M^\pm_{-1,1}\sigma_1 & M^\pm_{-1,1}\sigma_2 & & & & & \\ 0 & 0 & 0 & & & & \\ & 0 & 0 & 0 & & & \\ & & \ddots & \ddots & \ddots & & \\ & & & 0 & 0 & 0 & \\ & & & & M^\pm_{1,M}\tau_2 & M^\pm_{1,M}\tau_1 & \end{pmatrix}, \tag{G.46}$$

where the quantities $M^\pm_{m,j}$ are given by

$$M^\pm_{m,j} = \sum_{n=1}^{3} c_n^\pm H^{(n)}_{j,j+m} \tag{G.47}$$

for $m = -1, 0, 1$ and $j = 1, 2, \ldots, M$. The coefficients $c_n^{\pm}$ are given by

$$\begin{aligned} c_1^{\pm} &= \tfrac{3}{4} \mp \tfrac{1}{4} i k_a \Delta r \\ c_2^{\pm} &= \tfrac{1}{4} \pm \tfrac{1}{4} i k_a \Delta r \\ c_3^{\pm} &= c_2^{\pm} / k_a^2. \end{aligned} \tag{G.48}$$

The quantities $H_{j,j+m}^{(n)}$ for $n = 1, 2$ are given by

$$\begin{aligned} H_{j,j}^{(n)} &= \tfrac{1}{12} \left[(z_j - z_{j-1}) f_n(z_{j-1}) + 3(z_{j+1} - z_{j-1}) f_n(z_j) + (z_{j+1} - z_j) f_n(z_{j+1}) \right] \\ H_{j,j\pm1}^{(n)} &= \pm \tfrac{1}{12} \left[f_n(z_j) + f_n(z_{j\pm1}) \right] (z_{j\pm1} - z_j) \end{aligned} \tag{G.49}$$

and for $n = 3$ by

$$\begin{aligned} H_{j,j\pm1}^{(3)} &= \pm \tfrac{1}{2} \left[f_1(z_j) + f_1(z_{j\pm1}) \right] / (z_{j\pm1} - z_j) \\ H_{j,j}^{(3)} &= - \left[H_{j,j+1}^{(3)} + H_{j,j-1}^{(3)} \right] \end{aligned} \tag{G.50}$$

with $f_1(z) = \rho^{-1}(z)$ and $f_2(z) = \rho^{-1}(z) k^2(z) / k_a^2$.

As indicated in Sec. G.10, the density ρ should be replaced by k^2 in the above expressions if the second term in Eq. (G.41) is replaced by the term $k^2 \partial_z (k^{-2} \partial_z q)$.

G.12 Starting field

The numerical solution of the narrow-angle or wide-angle parabolic equation has been reduced to the repeated solution of the tridiagonal matrix equation (G.31) for a PE step $\vec{\psi}(r) \to \vec{\psi}(r + \Delta r)$. The computation starts at the source at $r = 0$, where a starting field $\vec{\psi}(0) \equiv \psi(0, z)$ is required. The starting field should represent a monopole source.

From Eq. (G.4) we have $\psi(0, z) = q(0, z)$. The exact expression for the field $q(r, z)$ of a monopole source in an unbounded non-refracting atmosphere is

$$q(r, z) = \frac{\exp(ikR)}{R} \sqrt{r}, \tag{G.51}$$

where R is the radial distance from the source. We cannot use this expression for the starting field, for two reasons: *i*) the expression diverges at the source, and *ii*) the expression produces sound waves with large elevation angles (outside the interval for which the PE method is valid), which generate numerical errors in a PE computation.

In Sec. G.12.1 we derive a starting field for the narrow-angle parabolic equation and in Sec. G.12.2 we derive a starting field for the wide-angle parabolic equation. In the derivation we assume a non-refracting atmosphere. The starting field is chosen in such a way that a PE computation for a non-refracting

atmosphere yields a far field that agrees with Eq. (G.51). In Sec. G.12.3 we include the effect of the ground surface in the starting field.

The derivation of the starting field in Secs. G.12.1 and G.12.2 is based on the work of Greene [62]. A different approach was presented by Collins [28].

G.12.1 Narrow-angle parabolic equation

In this section we derive a starting field for the narrow-angle parabolic equation. The ground surface is ignored and the source is located at $(r, z) = (0, 0)$.

We assume that $k(z)$ is a constant, so we have $k(z) = k_a$. The narrow-angle parabolic equation (G.16) reduces to

$$\partial_r q - ik_a q - \frac{i}{2k_a}\partial_z^2 q = 0. \tag{G.52}$$

We write the solution as a plane-wave expansion:

$$q = \int_{-\infty}^{\infty} S(k_z) \exp(ik_z z + ik_r r) dk_z, \tag{G.53}$$

where k_z is an integration variable and k_r and $S(k_z)$ will be determined below. Substitution of Eq. (G.53) into Eq. (G.52) gives

$$k_r = k_a - \frac{k_z^2}{2k_a}. \tag{G.54}$$

We write Eq. (G.53) as

$$q = \int_{-\infty}^{\infty} S(k_z) \exp[iF(k_z)] dk_z \tag{G.55}$$

with

$$F(k_z) = k_z z + \left(k_a - \frac{k_z^2}{2k_a}\right) r, \tag{G.56}$$

where we have used Eq. (G.54). To evaluate the integral in Eq. (G.55) we use the method of stationary phase (see Appendix P). At the stationary phase point we have $F'(k_{z,0}) = 0$, which gives

$$k_{z,0} = k_a z/r. \tag{G.57}$$

The stationary phase approximation of Eq. (G.55) is

$$q \approx \sqrt{\frac{2\pi}{|F''(k_{z,0})|}} S(k_{z,0}) \exp[iF(k_{z,0}) - i\tfrac{1}{4}\pi], \tag{G.58}$$

and we find

$$q \approx \frac{1}{\sqrt{r}}\sqrt{\frac{2\pi k_a}{i}}S(k_{z,0})\exp(ik_aR) \tag{G.59}$$

with $R = \sqrt{r^2+z^2} \approx r(1+\frac{1}{2}z^2/r^2)$. If we compare this with the exact expression $q = \sqrt{r}\exp(ik_aR)/R$ for a monopole source we find

$$S(k_{z,0}) = \sqrt{\frac{i}{2\pi k_a}}\frac{r}{R}, \tag{G.60}$$

or, from Eq. (G.57),

$$S(k_{z,0}) = \sqrt{\frac{i}{2\pi k_a}}\left(1+\frac{k_{z,0}^2}{k_a^2}\right)^{-1/2}. \tag{G.61}$$

Therefore we use

$$S(k_z) = \sqrt{\frac{i}{2\pi k_a}}\left(1+\frac{k_z^2}{k_a^2}\right)^{-1/2}. \tag{G.62}$$

Using $(1+x)^{-1/2} \approx 1-\frac{1}{2}x \approx \exp(-\frac{1}{2}x)$ for $x \ll 1$, this expression can be approximated as

$$S(k_z) = \sqrt{\frac{i}{2\pi k_a}}\exp\left(-\frac{k_z^2}{2k_a^2}\right). \tag{G.63}$$

Substitution of this expression into Eq. (G.53) for $r = 0$ gives a standard integral, and we find

$$q(0,z) = \sqrt{ik_a}\exp(-\frac{1}{2}k_a^2z^2). \tag{G.64}$$

This is a well-known Gaussian starting field for the PE method [148].

One may use a higher-order approximation of Eq. (G.62) instead of the first-order approximation (G.63). We will not do this here for the narrow-angle parabolic equation, but we will do this in the next section for the wide-angle parabolic equation.

G.12.2 Wide-angle parabolic equation

For an atmosphere with a constant wave number $k(z) = k_a$, the wide-angle parabolic equation (G.19) reduces to

$$(1+\frac{1}{4}k_a^{-2}\partial_z^2)\partial_r q - ik_a(1+\frac{3}{4}k_a^{-2}\partial_z^2)q = 0. \tag{G.65}$$

Substitution of the plane-wave expansion (G.53) into Eq. (G.65) gives

$$k_r = k_a \frac{1 - \frac{3}{4}k_z^2/k_a^2}{1 - \frac{1}{4}k_z^2/k_a^2}. \tag{G.66}$$

We proceed as in the previous section. For the function $F(k_z)$ in Eq. (G.55) we find

$$F(k_z) = k_z z + r k_a \frac{1 - \frac{3}{4}k_z^2/k_a^2}{1 - \frac{1}{4}k_z^2/k_a^2}. \tag{G.67}$$

This gives

$$F'(k_z) = z - r \frac{k_z/k_a}{(1 - \frac{1}{4}k_z^2/k_a^2)^2} \tag{G.68}$$

and

$$F''(k_z) = -\frac{r}{k_a} \frac{1 + \frac{3}{4}k_z^2/k_a^2}{(1 - \frac{1}{4}k_z^2/k_a^2)^3}. \tag{G.69}$$

At the stationary phase point we have $F'(k_{z,0}) = 0$. This gives

$$k_{z,0}/k_a \approx z/r, \tag{G.70}$$

where terms of the order of $(z/r)^3$ and higher-order terms have been neglected. The stationary phase approximation of Eq. (G.55) becomes

$$q \approx \frac{1}{\sqrt{r}} \sqrt{\frac{2\pi k_a}{i}} \frac{(1 - \frac{1}{4}z^2/r^2)^{3/2}}{(1 + \frac{3}{4}z^2/r^2)^{1/2}} S(k_{z,0}) \exp(ik_a R), \tag{G.71}$$

where we have used $R = \sqrt{r^2 + z^2} \approx r(1 + \frac{1}{2}z^2/r^2 - \frac{1}{8}z^4/r^4 \ldots)$ in the exponential, neglecting terms of the order of $r(z/r)^6$ and higher-order terms. This agrees with the exact expression $q = \sqrt{r}\exp(ik_a R)/R$ if we use

$$S(k_z) = \sqrt{\frac{i}{2\pi k_a}} \frac{1}{(1 + k_z^2/k_a^2)^{1/2}} \frac{(1 + \frac{3}{4}k_z^2/k_a^2)^{1/2}}{(1 - \frac{1}{4}k_z^2/k_a^2)^{3/2}}. \tag{G.72}$$

This function can be represented approximately by the expression

$$S(k_z) = \sqrt{\frac{i}{2\pi k_a}} \left(1 + a_2 \frac{k_z^2}{k_a^2}\right) \exp\left(-b_2 \frac{k_z^2}{k_a^2}\right) \tag{G.73}$$

with adjustable parameters a_2 and b_2. If we choose $a_2 = 0$ we find the following expression for the starting field:

$$q(0, z) = \sqrt{\frac{ik_a}{2b_2}} \exp\left(-\frac{k_a^2 z^2}{4b_2}\right). \tag{G.74}$$

For $b_2 = \frac{1}{2}$ we find the starting field derived in the previous section, given by Eq. (G.64). Equations (G.72) and (G.73) with $a_2 = 0$ and $b_2 = \frac{1}{2}$ agree with each other only for k_z between zero and about $0.2k_a$, corresponding to elevation angles between zero and about 10° [the elevation angle is $\arctan(z/r)$, which is equal to $\arctan(k_z/k_a)$ from Eq. (G.70)]. With increasing k_z, the agreement decreases. The agreement can be improved by choosing a smaller value of b_2, but if b_2 is chosen too small, high-angle waves are generated which cause errors in a PE computation. A better approach is to improve the agreement by adjusting the parameter a_2. For $a_2 = 1.02$ and $b_2 = 0.75$, Eqs. (G.72) and (G.73) agree with each other up to elevation angles of about 30°. This corresponds to the starting field

$$q(0,z) = \sqrt{ik_a}(A_0 + A_2 k_a^2 z^2) \exp\left(-\frac{k_a^2 z^2}{B}\right) \tag{G.75}$$

with $A_0 = 1.3717$, $A_2 = -0.3701$, and $B = 3$.

Use of the second-order starting field (G.75) instead of the zeroth-order starting field (G.74) is expected to improve the accuracy of the computed sound pressure field, but the improvement proves to be very small (see end of Sec. G.12.3). Apparently, the high-angle accuracy of CNPE results is not limited by the starting field but by the small-angle approximation used in the derivation of the CNPE method. The disagreement between Eqs. (G.72) and (G.73) for elevation angles between about 10° and about 30° has a relatively small effect on the sound pressure field.

The situation is different for the GFPE method described in Appendix H. The high-angle accuracy of GFPE results is limited by the starting field, and use of a higher-order starting field improves the accuracy of GFPE results (see Sec. H.10).

G.12.3 Source near a finite-impedance ground surface

If the source is at position $(r,z) = (0,z_s)$ above a finite-impedance ground surface at $z = 0$, the following starting field can be used:

$$q(0,z) = q_0(z - z_s) + Cq_0(z + z_s), \tag{G.76}$$

where the function $q_0(z)$ is defined as the starting field for a source at position $(r,z) = (0,0)$ in an unbounded atmosphere, and C is a reflection coefficient. For the narrow-angle parabolic equation we have shown that Eq. (G.64) can be used for the function $q_0(z)$. For the wide-angle parabolic equation, Eq. (G.74) or Eq. (G.75) can be used.

The first term on the right-hand side of Eq. (G.76) represents the direct field of the source; the second term represents the field reflected by the ground surface or, equivalently, the field of the image source at position $(0,-z_s)$. For the reflection coefficient C in Eq. (G.76) one usually employs the plane-wave

reflection coefficient for normal incidence:

$$C_p = \frac{Z-1}{Z+1}, \tag{G.77}$$

where Z is the normalized ground impedance. The most obvious choice for C, however, is the spherical-wave reflection coefficient C_s, which is given by the general integral expression (D.54) ($Q \equiv C_s$), with $R_2 = \sqrt{r^2 + (z+z_s)^2}$. For the PE starting field we must set $r = 0$ in this expression, so we have $R_2 = z + z_s$ and find

$$C_s = 1 - 2\frac{k_a}{Z}\frac{R_2}{i}\int_0^\infty \frac{\exp[-qk_a(Z+1)/Z]}{q + R_2/i}dq \tag{G.78}$$

or

$$C_s = 1 - 2\frac{k_a}{Z}\frac{R_2}{i}\exp\left(k_a\frac{Z+1}{Z}\frac{R_2}{i}\right)E_1\left(k_a\frac{Z+1}{Z}\frac{R_2}{i}\right), \tag{G.79}$$

where E_1 is the exponential integral function (see Eq. 5.1.28 in Ref. [1]). This expression for C_s is easily evaluated numerically.

A relation between C_p and C_s for $r = 0$ follows from the following asymptotic expansion of Eq. (G.78):

$$C_s = C_p - \frac{2}{Z+1}\sum_{n=1}^{\infty}(-1)^n n!\left(\frac{i}{k_a R_2}\frac{Z}{Z+1}\right)^n, \tag{G.80}$$

which can be derived by repeated integration by parts in Eq. (G.78). Equation (G.80) implies $C_s \approx C_p$ for $k_a(z+z_s) \gg 1$, or $(z+z_s) \gg \lambda/2\pi$, where λ is the wavelength. Numerical computations indicate, however, that $C_s \approx C_p$ is a reasonable approximation for the PE starting field even when the condition $(z+z_s) \gg \lambda/2\pi$ is not met.

For the field shown in Fig. 4.16 in Chap. 4 we used Eq. (G.74) with $b_2 = \frac{1}{2}$ for $q_0(z)$ and the plane-wave reflection coefficient C_p. We found no significant change of the field when we used Eq. (G.75) for $q_0(z)$ and the spherical-wave reflection coefficient C_s.

Appendix H

Green's Function Parabolic Equation (GFPE) method

H.1 Introduction

In this appendix we describe the Green's Function Parabolic Equation (GFPE) method, which was developed by Gilbert and Di [58] (see Sec. G.1). The GFPE method is more efficient, *i.e.* faster, than the Crank-Nicholson Parabolic Equation (CNPE) method, because in the GFPE method considerably larger extrapolation steps (*i.e.* range steps Δr) can be used than in the CNPE method. An alternate Parabolic Equation method with large extrapolation steps is described in Ref. [130].

The GFPE method developed in Ref. [58] is a two-dimensional method, based on the axisymmetric approximation. Recently a three-dimensional GFPE method was developed [44]. The two-dimensional GFPE method is described in Secs. H.2 to H.11 and the three-dimensional GFPE method is described in Sec. H.12.

The derivation of the basic equations of the two-dimensional GFPE method starts with Eq. (G.1), which we repeat here:

$$\frac{\partial^2 q}{\partial r^2} + \frac{\partial^2 q}{\partial z^2} + k^2 q = 0, \tag{H.1}$$

with $q = q(r, z)$ and $k = k(z)$. We have omitted the subscripts of q_c and k_{eff}, as in Appendix G.

H.2 Unbounded non-refracting atmosphere

It is instructive to formulate the GFPE method first for the trivial case of an unbounded non-refracting atmosphere. In this case the wave number k is a

constant. We apply a Fourier transformation $z \to k_z$ to Eq. (H.1), *i.e.* we multiply the equation by $\exp(-ik_z z)$ and integrate over z from $-\infty$ to ∞. This gives

$$\frac{\partial^2 Q}{\partial r^2} + (k^2 - k_z^2)Q = 0, \tag{H.2}$$

where

$$Q(r, k_z) = \int_{-\infty}^{\infty} \exp(-ik_z z) q(r, z)\, dz \tag{H.3}$$

is the Fourier transform of q. We write Eq. (H.2) as

$$\left(\frac{\partial}{\partial r} - i\sqrt{k^2 - k_z^2}\right)\left(\frac{\partial}{\partial r} + i\sqrt{k^2 - k_z^2}\right) Q = 0. \tag{H.4}$$

The first factor yields the solution $Q(r, k_z) = Q(0, k_z)\exp(ir\sqrt{k^2 - k_z^2})$, which represents waves traveling in the positive r direction [as we assume a harmonic time factor $\exp(-i\omega t)$]. The second factor yields the solution $Q(r, k_z) = Q(0, k_z)\exp(-ir\sqrt{k^2 - k_z^2})$, which represents waves traveling in the negative r direction. We restrict ourselves to sound propagation in the positive r direction, so we use the solution $Q(r, k_z) = Q(0, k_z)\exp(ir\sqrt{k^2 - k_z^2})$. This solution can also be written as

$$Q(r + \Delta r, k_z) = Q(r, k_z)\exp(i\Delta r\sqrt{k^2 - k_z^2}). \tag{H.5}$$

The function $q(r + \Delta r, z)$ is obtained by an inverse Fourier transformation:

$$q(r + \Delta r, z) = \frac{1}{2\pi}\int_{-\infty}^{\infty} \exp(ik_z z)\exp(i\Delta r\sqrt{k^2 - k_z^2})Q(r, k_z)\, dk_z. \tag{H.6}$$

Thus, the field is extrapolated from range r to range $r + \Delta r$ by a forward Fourier transformation [Equation (H.3)] and an inverse Fourier transformation [Equation (H.6)]. In Sec. H.8 we will show that Eq. (H.6) is closely related to the Fourier split-step algorithm for the parabolic equation. This algorithm is used in underwater acoustics.

Equation (H.6) is valid for an unbounded non-refracting atmosphere. Gilbert and Di [58] generalized Eq. (H.6) for a refracting atmosphere above a finite-impedance ground surface. The derivation by Gilbert and Di is based on the spectral theorem of functional analysis (see Sec. H.7). Here we present a different approach that leads to the same result [134]. This approach is based on the two-dimensional version of the Kirchhoff-Helmholtz integral equation, which is derived in the next section.

H.3 Kirchhoff-Helmholtz integral equation

The complex pressure amplitude $p(\mathbf{R}_1)$ at a point $\mathbf{R}_1 = (x_1, y_1, z_1)$ in a three-dimensional volume V without sources, enclosed by a surface S_c, can be calculated with the Kirchhoff-Helmholtz integral equation [91]

$$p(\mathbf{R}_1) = \frac{1}{4\pi} \iint_{S_c} [g_3(\mathbf{R}, \mathbf{R}_1) \nabla p(\mathbf{R}) - p(\mathbf{R}) \nabla g_3(\mathbf{R}, \mathbf{R}_1)] \cdot \mathbf{n} \, dS_c, \tag{H.7}$$

where the integral is over positions $\mathbf{R} = (x, y, z)$ on the surface S_c, the operator ∇ is $\partial/\partial\mathbf{R} = (\partial/\partial x, \partial/\partial y, \partial/\partial z)$, $\mathbf{n}$ is the outward unit normal vector at the surface S_c, the Green's function $g_3(\mathbf{R}, \mathbf{R}_1)$ is a solution of the inhomogeneous Helmholtz equation

$$\nabla^2 g_3(\mathbf{R}, \mathbf{R}_1) + k^2(\mathbf{R}) g_3(\mathbf{R}, \mathbf{R}_1) = -4\pi\delta(\mathbf{R} - \mathbf{R}_1), \tag{H.8}$$

and the complex pressure amplitude $p(\mathbf{R})$ in the volume V satisfies the homogeneous Helmholtz equation

$$\nabla^2 p(\mathbf{R}) + k^2(\mathbf{R}) p(\mathbf{R}) = 0. \tag{H.9}$$

To prove Eq. (H.7), the surface integral is converted to a volume integral with Gauss' theorem

$$\iiint_V \nabla \cdot \mathbf{F} \, dV = \iint_{S_c} \mathbf{F} \cdot \mathbf{n} \, dS_c, \tag{H.10}$$

where $\mathbf{F}$ is an arbitrary vector field. If we use Eqs. (H.8) and (H.9) in the resulting equation we find an identity.

There is still a considerable freedom for the choice of the Green's function g_3. The only condition is that g_3 must satisfy Eq. (H.8), so that g_3 contains a contribution from a monopole source at position $\mathbf{R}_1$. We may include additional contributions from sources outside the volume V; these contributions satisfy Eq. (H.9) within V, so g_3 still satisfies Eq. (H.8).

The two-dimensional version of the Kirchhoff-Helmholtz integral equation in the xz plane is

$$p(\mathbf{r}_1) = \frac{1}{4\pi} \int_C [g_2(\mathbf{r}, \mathbf{r}_1) \nabla p(\mathbf{r}) - p(\mathbf{r}) \nabla g_2(\mathbf{r}, \mathbf{r}_1)] \cdot \mathbf{n} \, ds, \tag{H.11}$$

with $\mathbf{r} = (x, z)$ and $\mathbf{r}_1 = (x_1, z_1)$; the operator ∇ is $\partial/\partial\mathbf{r} = (\partial/\partial x, \partial/\partial z)$, the integral is over positions $\mathbf{r}$ on the closed contour C, and $g_2(\mathbf{r}, \mathbf{r}_1)$ is a two-dimensional Green's function. Equation (H.11) can be derived as follows from the three-dimensional Kirchhoff-Helmholtz integral equation (H.7). We assume that $p(\mathbf{R})$ and $k(\mathbf{R})$ are independent of the y coordinate. For the surface S_c we choose the surface illustrated in Fig. H.1 (the figure is for the special case

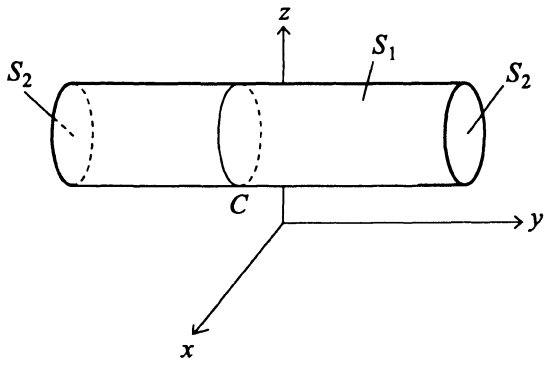

Figure H.1. Example of the closed surface S_c for the case that the contour C is a circle. The surface S_c consists of the cylindrical surface S_1 and the two circular surfaces S_2 at $y = -\infty$ and $y = +\infty$. The projection of the surface S_1 on the xz plane is the closed contour C.

that the contour C is a circle). The closed surface S_c consists of the cylindrical surface S_1 and the two surfaces S_2 at $y = -\infty$ and $y = +\infty$. The projection of the cylindrical surface S_1 on the xz plane is the contour C. We write the unit normal vector in Eq. (H.7) as $\mathbf{n} = (n_x, n_y, n_z)$, so Eq. (H.7) can be written as

$$p(\mathbf{R}_1) = \frac{1}{4\pi} \iint_{S_c} [g_3(n_x \partial_x p + n_y \partial_y p + n_z \partial_z p) - p(n_x \partial_x g_3 + n_y \partial_y g_3 + n_z \partial_z g_3)]\, dS_c, \tag{H.12}$$

with $\partial_x \equiv \partial/\partial x$, $\partial_y \equiv \partial/\partial y$, and $\partial_z \equiv \partial/\partial z$. At the surface S_1 we have $n_y = 0$. The contribution to the integral from the two surfaces S_2 vanishes, as we have $g_3(\mathbf{R}, \mathbf{R}_1) \to 0$ for $y \to \pm\infty$. If we choose $y_1 = 0$, Eq. (H.12) reduces to Eq. (H.11) with the two-dimensional Green's function g_2 defined by

$$g_2(\mathbf{r}, \mathbf{r}_1) = \int_{-\infty}^{\infty} g_3(\mathbf{R}, \mathbf{r}_1)\, dy. \tag{H.13}$$

As we assumed that $p(\mathbf{R})$ is independent of y, Eq. (H.9) gives the following two-dimensional Helmholtz equation for $p(\mathbf{r})$:

$$\nabla^2 p(\mathbf{r}) + k^2(\mathbf{r}) p(\mathbf{r}) = 0. \tag{H.14}$$

The Green's function g_2 defined by Eq. (H.13) satisfies the two-dimensional inhomogeneous Helmholtz equation

$$\nabla^2 g_2(\mathbf{r}, \mathbf{r}_1) + k^2(\mathbf{r}) g_2(\mathbf{r}, \mathbf{r}_1) = -4\pi\delta(\mathbf{r} - \mathbf{r}_1), \tag{H.15}$$

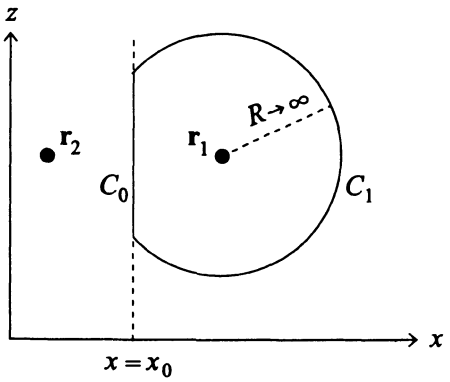

Figure H.2. Geometry for the two-dimensional Kirchhoff-Helmholtz integral equation. The contour C consists of line segment C_0 at $x = x_0$ and circular curve C_1 with radius $R \to \infty$ and point $\mathbf{r}_1$ at the center. In the text we use a Green's function that corresponds to a monopole source at point $\mathbf{r}_1$ and an opposite monopole source at point $\mathbf{r}_2$, so the Green's function vanishes on C_0. The points $\mathbf{r}_1$ and $\mathbf{r}_2$ are at equal distances from C_0.

as follows from integration of Eq. (H.8) over y from $y = -\infty$ to $y = +\infty$, using $\int_{-\infty}^{\infty} \partial_y^2 g_3 dy = [\partial_y g_3]_{-\infty}^{\infty} = 0$. As an example we consider the three-dimensional Green's function for a homogeneous atmosphere:

$$g_3(\mathbf{R}, \mathbf{R}_1) = \exp(ikr)/r \tag{H.16}$$

with $r = |\mathbf{R} - \mathbf{R}_1|$. To derive the corresponding two-dimensional Green's function, we substitute Eq. (H.16) into Eq. (H.13) and use $r = \sqrt{\rho^2 + (y - y_1)^2}$ with $\rho = |\mathbf{r} - \mathbf{r}_1|$. This gives

$$g_2(\mathbf{r}, \mathbf{r}_1) = i\pi H_0^{(1)}(k\rho), \tag{H.17}$$

where $H_0^{(1)}$ is the Hankel function of the first kind and order zero [1].

Now we choose the geometry shown in Fig. H.2 for the two-dimensional Kirchhoff-Helmholtz equation (H.11). The contour C consists of the line segment C_0 at $x = x_0$ and the circular curve C_1 with radius $R \to \infty$ and point $\mathbf{r}_1$ at the center. The contribution from the curve C_1 to the contour integral in Eq. (H.11) vanishes, as we have $p \to 0$ and $g_2 \to 0$ for $R \to \infty$. As in the three-dimensional case, there is a considerable freedom for the choice of the Green's function g_2; the only condition is that g_2 must satisfy Eq. (H.15), so that g_2 contains a contribution from a (two-dimensional) monopole source at position $\mathbf{r}_1$. We may include additional contributions from sources outside the region enclosed by the contour C. Here we choose the Green's function g_2 so that we have $g_2 = 0$ on C_0. This is achieved by using the field of two opposite

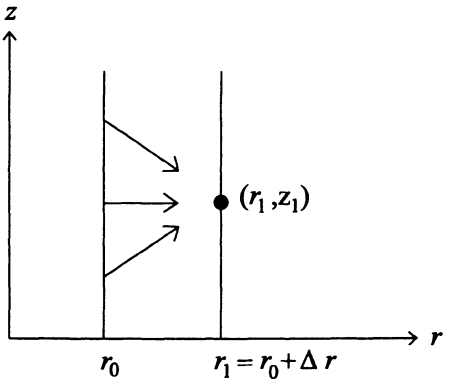

Figure H.3. Geometry for Eq. (H.20), which gives the field at point (r_1, z_1) as an integral over the line $r = r_0$.

monopole sources at the points $\mathbf{r}_1$ and $\mathbf{r}_2$:

$$g_2(\mathbf{r}, \mathbf{r}_1) = g(\mathbf{r}, \mathbf{r}_1) - g(\mathbf{r}, \mathbf{r}_2), \tag{H.18}$$

where $g(\mathbf{r}, \mathbf{r}_1)$ is the field of a monopole source at $\mathbf{r}_1$ and $-g(\mathbf{r}, \mathbf{r}_2)$ is the field of the opposite monopole source at $\mathbf{r}_2$. The field $g(\mathbf{r}, \mathbf{r}_1)$ is a solution of Eq. (H.15). The field $g(\mathbf{r}, \mathbf{r}_2)$ is a solution of Eq. (H.15) with $\mathbf{r}_1$ replaced by $\mathbf{r}_2$. For the field $g(\mathbf{r}, \mathbf{r}_2)$ we assume that the atmosphere, represented by the wave number $k(\mathbf{r})$, is symmetric with respect to the line $x = x_0$.

As we have $g_2 = 0$ on C_0, the first term in the integrand of Eq. (H.11) vanishes. In the second term we have $\nabla g_2 \cdot \mathbf{n} = -\partial_x g_2 = -2\partial_x g$ on C_0, where we have used Eq. (H.18). Equation (H.11) becomes

$$p(\mathbf{r}_1) = \frac{1}{2\pi} \int_{-\infty}^{\infty} \left(p(\mathbf{r}) \frac{\partial g(\mathbf{r}, \mathbf{r}_1)}{\partial x} \right)_{x=x_0} dz. \tag{H.19}$$

This integral is known as a Rayleigh integral [106, 14] (see also Sec. 278 of Rayleigh's book 'The Theory of Sound' [121]).

H.4 General Green's function approach to wave propagation

We return to the notation $q(r, z)$ for the field, as used in Sec. H.2. For the geometry shown in Fig. H.3, with a ground surface at $z = 0$, Eq. (H.19) becomes

$$q(r_1, z_1) = \frac{1}{2\pi} \int_{0}^{\infty} \left(q(r, z) \frac{\partial g(r, z; r_1, z_1)}{\partial r} \right)_{r=r_0} dz. \tag{H.20}$$

The lower integration limit is $z = 0$ as the effect of the ground reflection will be represented by a term in the Green's function (see Sec. H.5); the ground reflection corresponds to an image atmosphere below the ground surface. The Green's function $g(r, z; r_1, z_1)$ is the field at (r, z) generated by a monopole source at (r_1, z_1), and satisfies the equation

$$\left[\partial_r^2 + \partial_z^2 + k^2(z)\right] g(r, z; r_1, z_1) = -4\pi\delta(r - r_1)\delta(z - z_1). \tag{H.21}$$

The wave number k is a function of z only. The range dependence of the wave number is taken into account by changing the function $k(z)$ between successive range steps, as indicated in Sec. G.2. Consequently, the Green's function depends on r and r_1 only through the difference $\Delta r = r_1 - r$. Therefore the Green's function will be denoted as $g(\Delta r, z, z_1)$. We introduce the Fourier transform

$$G(\kappa, z, z_1) = \int_{-\infty}^{\infty} g(\Delta r, z, z_1) \exp(-i\kappa\Delta r)\, d(\Delta r), \tag{H.22}$$

where κ is a horizontal wave number. The inverse Fourier transform is

$$g(\Delta r, z, z_1) = \frac{1}{2\pi} \int_{-\infty}^{\infty} G(\kappa, z, z_1) \exp(i\kappa\Delta r)\, d\kappa. \tag{H.23}$$

Substitution of Eq. (H.23) into Eq. (H.20) gives, with $\partial_r = -\partial_{\Delta r}$ and the notation z for z_1 and z' for z,

$$q(r + \Delta r, z) = \frac{1}{4\pi^2 i} \int_{-\infty}^{\infty} \exp(i\kappa\Delta r)\, \kappa\, d\kappa \int_0^{\infty} G(\kappa, z', z) q(r, z')\, dz'. \tag{H.24}$$

The Green's function $G(\kappa, z', z)$ is the solution of the Fourier transformed version of Eq. (H.21), which we find by multiplying this equation by $\exp(-i\kappa\Delta r)$ and integrating over Δr:

$$\left[\partial_z^2 + k^2(z) - \kappa^2\right] G(\kappa, z', z) = -4\pi\delta(z - z'). \tag{H.25}$$

From Eqs. (H.24) and (H.25) we will derive the basic equations of the GFPE method. In Sec. H.5 we present the derivation for a non-refracting atmosphere above a finite-impedance ground surface. In Sec. H.6 we take atmospheric refraction into account.

H.5 Non-refracting atmosphere

For a non-refracting atmosphere we have $k(z) = k_0$, where k_0 is a constant. In this case the solution of Eq. (H.25) for a system with a finite-impedance ground surface at $z = 0$ is (see Sec. D.4)

$$G(\kappa, z', z) = \frac{2\pi i}{k_v} \left\{\exp(ik_v|z - z'|) + R(k_v) \exp(ik_v[z + z'])\right\}, \tag{H.26}$$

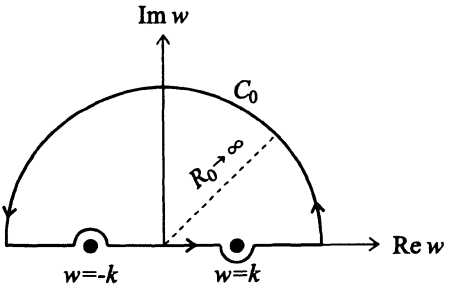

Figure H.4. Integration path in the complex w plane for $x > 0$. The poles are at $w = -k$ and $w = k$.

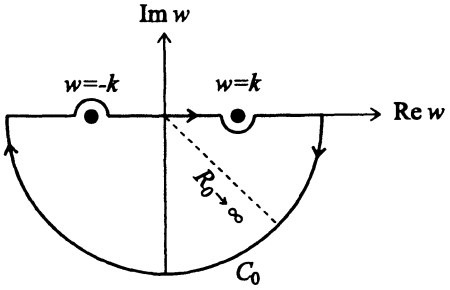

Figure H.5. Integration path in the complex w plane for $x < 0$. The poles are at $w = -k$ and $w = k$.

where the vertical wave number k_v is defined by

$$k_v^2 = k^2(z) - \kappa^2 \tag{H.27}$$

and

$$R(k_v) = \frac{k_v Z - k_0}{k_v Z + k_0} \tag{H.28}$$

is the plane-wave reflection coefficient; Z is the normalized impedance of the locally reacting ground surface. Substitution of Eq. (H.26) into Eq. (H.24) gives

$$q(r + \Delta r, z) = \frac{1}{\pi i} \int_{-\infty}^{\infty} \exp(i\kappa \Delta r)\, \kappa\, d\kappa \int_0^{\infty} \frac{i}{2k_v} \{\exp(ik_v|z - z'|) + R(k_v) \exp(ik_v[z + z'])\}\, q(r, z')\, dz'. \tag{H.29}$$

We introduce two identities:

$$\frac{i}{2k_v} \exp(ik_v|z - z'|) = \frac{1}{2\pi} \int_{-\infty}^{\infty} \frac{\exp[ik_z(z - z')]}{k_z^2 - k_v^2}\, dk_z \tag{H.30}$$

and

$$\frac{i}{2k_v} R(k_v) \exp[ik_v(z + z')] = \frac{1}{2\pi} \int_{-\infty}^{\infty} R(k_z) \frac{\exp[ik_z(z + z')]}{k_z^2 - k_v^2}\, dk_z + 2i\beta \frac{\exp[-i\beta(z + z')]}{\beta^2 - k_v^2}, \tag{H.31}$$

with $\beta = k_0/Z$. The integration paths along the real axis are deformed near the poles, as indicated in the following proof of Eqs. (H.30) and (H.31).

We consider the integral

$$I(x) = \frac{1}{2\pi i} \int_{-\infty}^{\infty} \frac{\exp(iwx)}{w^2 - k^2} dw, \tag{H.32}$$

which is of the form of the integral on the right-hand side of Eq. (H.30). The integrand has two poles, at $w = k$ and $w = -k$. The integration path along the real w axis is deformed by inserting two small semicircles around the poles, and the path is closed by a semicircle C_0 with radius $R_0 \to \infty$ (see Figs. H.4 and H.5).

For $x > 0$ we choose the path shown in Fig. H.4, with the semicircle C_0 in the upper half plane. The integrand vanishes at C_0 as the radius approaches infinity, so the contribution from C_0 to the integral vanishes. The integration

path encloses only the pole at $w = k$. The integral can be evaluated with the residue theorem. The residue theorem is

$$\oint_C f(z)\,dz = 2\pi i \sum_k c_k, \tag{H.33}$$

where the function $f(z)$ has poles at $z = a_k$, which are enclosed by the counterclockwise integration path along the contour C, and c_k are the residues at the poles:

$$c_k = \lim_{z \to a_k} [(z - a_k) f(z)]. \tag{H.34}$$

This gives

$$I(x) = \frac{1}{2k} \exp(ikx), \quad \text{for } x > 0. \tag{H.35}$$

For $x < 0$ we choose the path shown in Fig. H.5, with the semicircle C_0 in the lower half plane. Again, the integrand vanishes at C_0 as the radius approaches infinity, so the contribution from C_0 to the integral vanishes. The integration path encloses only the pole at $w = -k$. The residue theorem gives

$$I(x) = \frac{1}{2k} \exp(-ikx), \quad \text{for } x < 0 \tag{H.36}$$

(the contour is traversed clockwise, which yields a minus sign). Equations (H.35) and (H.36) can be written as

$$I(x) = \frac{1}{2k} \exp(ik|x|), \tag{H.37}$$

which is valid for both $x > 0$ and $x < 0$. This completes the proof of Eq. (H.30). It should be noted that the value of the integral $I(x)$ depends on the choice of the integration path.

The proof of Eq. (H.31) is an analogous application of the residue theorem. The only difference is that the reflection coefficient introduces an additional pole at $w = -k_0/Z$.

We substitute Eqs. (H.30) and (H.31) into Eq. (H.29) and rearrange the integration order:

$$\begin{aligned} q(r + \Delta r, z) = {} & \\ & \frac{1}{2\pi} \int_{-\infty}^{\infty} \exp(ik_z z) dk_z \int_0^{\infty} \exp(-ik_z z') q(r, z') dz' \frac{1}{\pi i} \int_{-\infty}^{\infty} \frac{\exp(i\kappa \Delta r)}{k_z^2 - k_v^2} \kappa \, d\kappa \\ & + \frac{1}{2\pi} \int_{-\infty}^{\infty} R(k_z) \exp(ik_z z) dk_z \int_0^{\infty} \exp(ik_z z') q(r, z') dz' \frac{1}{\pi i} \int_{-\infty}^{\infty} \frac{\exp(i\kappa \Delta r)}{k_z^2 - k_v^2} \kappa \, d\kappa \\ & + 2i\beta \exp(-i\beta z) \int_0^{\infty} \exp(-i\beta z') q(r, z') dz' \frac{1}{\pi i} \int_{-\infty}^{\infty} \frac{\exp(i\kappa \Delta r)}{\beta^2 - k_v^2} \kappa \, d\kappa. \end{aligned} \tag{H.38}$$

The integrals over κ in the first two terms on the right-hand side can be evaluated with the residue theorem:

$$\frac{1}{\pi i}\int_{-\infty}^{\infty}\frac{\exp(i\kappa\Delta r)}{k_z^2-k_v^2}\kappa\,d\kappa=\frac{1}{\pi i}\int_{-\infty}^{\infty}\frac{\exp(i\kappa\Delta r)}{\kappa^2-(k_0^2-k_z^2)}\kappa\,d\kappa=\exp(i\Delta r\sqrt{k_0^2-k_z^2}), \tag{H.39}$$

where the integration path is closed in the upper complex half plane as in Fig H.4; the path encloses only the positive pole at $\kappa=\sqrt{k_0^2-k_z^2}$. The choice of the integration path is justified by the fact that the result, Eq. (H.40) below, agrees with the result (H.6) for the situation without a ground surface. The integral over κ in the third term on the right-hand side of Eq. (H.38) follows from Eq. (H.39) with k_z replaced by β. Equation (H.38) becomes

$$\begin{aligned}q(r+\Delta r,z)=&\\ &\frac{1}{2\pi}\int_{-\infty}^{\infty}\exp(i\Delta r\sqrt{k_0^2-k_z^2})\exp(ik_z z)dk_z\int_0^{\infty}\exp(-ik_z z')q(r,z')dz'\\ &+\frac{1}{2\pi}\int_{-\infty}^{\infty}R(k_z)\exp(i\Delta r\sqrt{k_0^2-k_z^2})\exp(ik_z z)dk_z\int_0^{\infty}\exp(ik_z z')q(r,z')dz'\\ &+2i\beta\exp(-i\beta z)\exp(i\Delta r\sqrt{k_0^2-\beta^2})\int_0^{\infty}\exp(-i\beta z')q(r,z')dz'.\end{aligned} \tag{H.40}$$

The three terms on the right-hand side represent three different sound waves. The first term represents the direct wave, the second term represents the wave reflected by the ground surface, and the third term represents a wave that is called the surface wave. For the situation without a ground surface, the second and third term vanish, and Eq. (H.40) is identical to Eq. (H.6) if the lower integration limit $z'=0$ is replaced by $z'=-\infty$.

H.6 Refracting atmosphere

We return to Eq. (H.1) for a refracting atmosphere, so the wave number k varies with the height z. As in Sec. G.4, we write this equation as

$$\partial_r^2 q(r,z)=-H_2(z)q(r,z), \tag{H.41}$$

where the operator $H_2(z)$ is defined as

$$H_2(z)=k^2(z)+\partial_z^2. \tag{H.42}$$

The corresponding one-way wave equation is

$$\partial_r q(r,z)=iH_1(z)q(r,z), \tag{H.43}$$

for waves traveling in the positive r direction. The square-root operator $H_1(z)$ satisfies $H_1^2 = H_2$. As in Sec. G.4, we write

$$k^2(z) = k_a^2 + \delta k^2(z), \tag{H.44}$$

where k_a is a constant wave number and δk^2 is a function of the height z. For the constant wave number k_a one may use the value of the wave number $k(z)$ at some average height or the value $k_0 \equiv k(0)$ at the ground surface; for the numerical examples in this book we used $k_a = k_0$. Equation (H.42) becomes

$$H_2(z) = H_{2a} + \delta k^2(z) \tag{H.45}$$

with $H_{2a} = k_a^2 + \partial_z^2$. The square-root operator can be approximated as

$$H_1(z) = \sqrt{H_{2a} + \delta k^2(z)} \approx H_{1a} + \frac{\delta k^2(z)}{2k_a} \tag{H.46}$$

with $H_{1a}^2 = H_{2a}$, where we have used $H_{2a} \approx k_a^2$. Substitution into the one-way wave equation (H.43) gives

$$\partial_r q(r,z) = iH_{1a} q(r,z) + i\frac{\delta k^2(z)}{2k_a} q(r,z). \tag{H.47}$$

The two terms on the right-hand side of the one-way wave equation (H.47) can be interpreted as follows:

i) the first term represents propagation in a non-refracting atmosphere with constant wave number $k(z) = k_a$,

ii) the second term represents the effect of atmospheric refraction.

Integration of Eq. (H.47) from range r to range $r + \Delta r$ gives

$$q(r + \Delta r, z) = \exp\left(i\Delta r \frac{\delta k^2(z)}{2k_a}\right) \exp(iH_{1a}\Delta r) q(r,z). \tag{H.48}$$

The factor $\exp(iH_{1a}\Delta r)q(r,z)$ is a formal expression for the solution of Eq. (H.47) for a non-refracting atmosphere. We have seen in the previous section that the solution for a non-refracting atmosphere is given by Eq. (H.40). From Eq. (H.48) we see that atmospheric refraction can be taken into account by multiplication of the solution by a phase factor, after each extrapolation step.

We replace $q(r,z)$ by $\psi(r,z) = \exp(-ik_a r)q(r,z)$, for improved accuracy in numerical computations (see Sec. G.3). Equation (H.40) becomes, with the refraction factor given in Eq. (H.48) included,

$$\begin{aligned}\psi(r + \Delta r, z) = \exp\left(i\Delta r \frac{\delta k^2(z)}{2k_a}\right) \Bigg\{ \frac{1}{2\pi} \int_{-\infty}^{\infty} [\Psi(r,k_z) + R(k_z)\Psi(r,-k_z)] \\ \times \exp\left(i\Delta r \left[\sqrt{k_a^2 - k_z^2} - k_a\right]\right) \exp(ik_z z) dk_z \\ + 2i\beta\Psi(r,\beta) \exp\left(i\Delta r \left[\sqrt{k_a^2 - \beta^2} - k_a\right]\right) \exp(-i\beta z) \Bigg\},\end{aligned} \tag{H.49}$$

where

$$\Psi(r, k_z) = \int_0^\infty \exp(-ik_z z')\psi(r, z')dz' \tag{H.50}$$

is the spatial Fourier transform of $\psi(r, z)$. Equations (H.49) and (H.50) are the basic equations of the GFPE method.

H.7 Alternate derivation

We have derived the basic equations (H.49) and (H.50) of the GFPE method from Eq. (H.24), which we derived from the Kirchhoff-Helmholtz integral equation. Equation (H.24) can also be derived from the spectral theorem of functional analysis [58], which gives the following expression for a general function F of an operator Q:

$$F(Q) = \frac{1}{2\pi i}\int_C \frac{F(\tau)}{\tau - Q}d\tau. \tag{H.51}$$

The operator $(\tau - Q)^{-1}$ is the inverse of $(\tau - Q)$. The integral over τ is along a contour C that encloses the poles of the integrand, *i.e.* the eigenvalues τ in the equation $Qu_\tau = \tau u_\tau$, where u_τ are the associated eigenfunctions which satisfy the boundary conditions [58]. Equation (H.51) is analogous to the residue theorem for ordinary functions.

To derive Eq. (H.24) we note that

$$q(r + \Delta r, z) = \exp(i\Delta r\, H_2^{1/2})\, q(r, z) \tag{H.52}$$

is a formal solution of the one-way wave equation $\partial_r q = iH_2^{1/2}q$, with $H_2 = \partial_z^2 + k^2$. Application of Eq. (H.51) with $Q = H_2$ and $F(x) = \exp(i\Delta r\, x^{1/2})$ gives

$$q(r + \Delta r, z) = \frac{1}{2\pi i}\int_C \frac{\exp(i\Delta r\, \tau^{1/2})}{\tau - H_2} q(r, z)\, d\tau. \tag{H.53}$$

With $\tau = \kappa^2$ and $G(\kappa, z', z)$ defined by Eq. (H.25) we find Eq. (H.24), where the integral over κ is along the real axis, with small deviations near the poles (see Sec. H.5).

H.8 Relation to the Fourier split-step method

For a system without a ground surface, Eq. (H.49) reduces to

$$\psi(r + \Delta r, z) = \exp\left(i\Delta r \frac{\delta k^2(z)}{2k_a}\right) \frac{1}{2\pi} \int_{-\infty}^{\infty} \Psi(r, k_z) \exp\left(-i\Delta r \frac{k_z^2}{2k_a}\right) \exp(ik_z z) dk_z, \tag{H.54}$$

where we have used the small-angle approximation

$$\sqrt{k_a^2 - k_z^2} - k_a \approx -\frac{k_z^2}{2k_a}. \tag{H.55}$$

Equation (H.54) is known as the Fourier split-step algorithm for the parabolic equation. This algorithm is used in underwater acoustics [45].

Equation (H.54) can be derived directly from the narrow-angle parabolic equation [see Eq. (G.6)]

$$\partial_r \psi = \frac{i}{2k_a}(\partial_z^2 + \delta k^2)\psi, \tag{H.56}$$

by treating the two terms on the right-hand side separately in an extrapolation step; this explains the name "split-step algorithm". The first term leads to the integral in Eq. (H.54) (see Sec. H.2). The second term leads to the refraction factor in Eq. (H.54).

H.9 Alternate refraction factor

Equation (H.49) contains the refraction factor

$$\exp\left(i\Delta r \frac{\delta k^2(z)}{2k_a}\right) \tag{H.57}$$

with $\delta k^2(z) = k^2(z) - k_a^2$. An alternate refraction factor is

$$\exp[i\Delta r\ \delta k(z)] \tag{H.58}$$

with $\delta k(z) = k(z) - k_a$. This factor follows from the following expansion of the square-root operator

$$\begin{aligned} H_1(z) &= \sqrt{k^2(z) + \partial_z^2} \\ &= \sqrt{(k_a + \delta k)^2 + \partial_z^2} \\ &\approx \sqrt{k_a^2 + \partial_z^2 + 2k_a\delta k} \\ &\approx \sqrt{k_a^2 + \partial_z^2} + \delta k. \end{aligned} \tag{H.59}$$

If this expansion is used in the derivation of the basic GFPE equations (H.49) and (H.50) in Sec. H.6, we find the refraction factor (H.58). Alternately, the refraction factor (H.58) follows directly from the refraction factor (H.57) if we neglect the term $(\delta k)^2$ in the relation $\delta k^2 = 2k_a\delta k + (\delta k)^2$. Numerical computations show that the refraction factor (H.58) gives slightly more accurate results than the factor (H.57) does [152, 134].

H.10 Starting field

In this section we derive a starting field for the GFPE method. The derivation is similar to the derivation of the starting field for the CNPE method in Sec. G.12. In Sec. G.12.3 we showed that the expression

$$q(0,z) = q_0(z - z_s) + Cq_0(z + z_s) \tag{H.60}$$

can be used for a source at position $(r,z) = (0,z_s)$ above a finite-impedance ground surface at $z = 0$. Here C is a reflection coefficient (see Sec. G.12.3) and $q_0(z)$ is the starting field for a source at position $(r,z) = (0,0)$ in an unbounded atmosphere. The function $q_0(z)$ for the GFPE method will be derived in this section.

As in Sec. G.12, we assume a constant wave number $k = k_a$ in Eq. (H.1) and write the solution as a plane-wave expansion

$$q = \int_{-\infty}^{\infty} S(k_z) \exp(ik_z z + ik_r r) dk_z. \tag{H.61}$$

Substitution into Eq. (H.1) gives

$$k_r = \sqrt{k_a^2 - k_z^2}, \tag{H.62}$$

where we have chosen the positive square-root, corresponding to waves traveling in the positive r direction.

We write Eq. (H.61) as

$$q = \int_{-\infty}^{\infty} S(k_z) \exp\left[iF(k_z)\right] dk_z \tag{H.63}$$

with

$$F(k_z) = k_z z + r\sqrt{k_a^2 - k_z^2}, \tag{H.64}$$

where we have used Eq. (H.62). To evaluate the integral in Eq. (H.63) we use the method of stationary phase (see Appendix P). At the stationary phase point we have $F'(k_{z,0}) = 0$, which gives

$$k_{z,0} = k_a z/R \tag{H.65}$$

with $R = \sqrt{r^2 + z^2}$. The stationary phase approximation of Eq. (H.61) is

$$q \approx \sqrt{\frac{2\pi}{|F''(k_{z,0})|}} S(k_{z,0}) \exp\left[iF(k_{z,0}) - i\frac{1}{4}\pi\right], \tag{H.66}$$

and we find

$$q = \frac{1}{\sqrt{r}}\sqrt{\frac{2\pi k_a}{i}}\left(1 - \frac{z^2}{R^2}\right)^{3/4} S(k_{z,0})\exp(ik_a R). \tag{H.67}$$

If we compare this with the exact expression $q = \sqrt{r}\exp(ik_a R)/R$ for a monopole source we find

$$S(k_{z,0}) = \sqrt{\frac{i}{2\pi k_a}}\left(1 - \frac{z^2}{R^2}\right)^{-1/4}. \tag{H.68}$$

Using Eq. (H.65) we find

$$S(k_z) = \sqrt{\frac{i}{2\pi k_a}}\left(1 - \frac{k_z^2}{k_a^2}\right)^{-1/4}. \tag{H.69}$$

This expression diverges for $k_z \to k_a$, corresponding to waves traveling vertically upward. For the PE method, however, we are interested in waves traveling with limited elevation angles. Therefore we approximate Eq. (H.69) by the following expression

$$S(k_z) = \sqrt{\frac{i}{2\pi k_a}}\left(1 + a_2\frac{k_z^2}{k_a^2} + a_4\frac{k_z^4}{k_a^4} + a_6\frac{k_z^6}{k_a^6} + a_8\frac{k_z^8}{k_a^8}\right)\exp\left(-b_2\frac{k_z^2}{k_a^2}\right) \tag{H.70}$$

with adjustable parameters a_2, a_4, a_6, a_8, and b_2.

For $a_2 = a_4 = a_6 = a_8 = 0$ and $b_2 = \frac{1}{2}$ this leads to the Gaussian starter (G.64). In this case the agreement between Eqs. (H.69) and (H.70) is limited to elevation angles γ between zero and about $\gamma_{\max} = 10°$. Here the elevation angle is defined as $\gamma = \arcsin(z/R)$; from Eq. (H.65) we find $\gamma \approx \arcsin(k_z/k_a)$.

By using nonzero parameters a_j with $j = 2, 4, 6, 8$ in Eq. (H.70), the maximum elevation angle $\gamma_{\max}$ can be enhanced. Optimized values of the parameters a_j are given in Table H.1, for $b_2 = 0.75$. For the orders 2, 4, and 8, the maximum elevation angle $\gamma_{\max}$ is approximately equal to 30°, 40°, and 60°, respectively.

From Eqs. (H.70) and (H.61) we find the following expressions for the GFPE starting field:

$$q(0,z) = \sqrt{ik_a}\left(A_0 + A_2 k_a^2 z^2 + A_4 k_a^4 z^4 + A_6 k_a^6 z^6 + A_8 k_a^8 z^8\right)\exp\left(-\frac{k_a^2 z^2}{B}\right). \tag{H.71}$$

The coefficients A_j and B are given in Table H.2. Here we have used the expressions

$$\begin{aligned}
I_0 &= \sqrt{\frac{\pi}{b_2}}\exp(-\frac{z^2}{4b_2}) \\
I_2 &= [\nu + \chi^2]I_0 \\
I_4 &= [3\nu^2 + 6\nu\chi^2 + \chi^4]I_0 \\
I_6 &= [15\nu^3 + 45\nu^2\chi^2 + 15\nu\chi^4 + \chi^6]I_0 \\
I_8 &= [105\nu^4 + 420\nu^3\chi^2 + 210\nu^2\chi^4 + 28\nu\chi^6 + \chi^8]I_0
\end{aligned} \tag{H.72}$$

for the integral

$$I_n = \int_{-\infty}^{\infty} k^n \exp(ikz - b_2 k^2)\, dk, \tag{H.73}$$

with $\nu = (2b_2)^{-1}$ and $\chi = iz\nu$. The expressions (H.72) follow by repeated integration by parts of the integral (H.73).

Numerical computations indicate that the starting field of order 4 gives accurate results up to an elevation angle of about 40°, not only for a non-refracting atmosphere but also for refracting atmospheres with a linear or a logarithmic sound speed profile. Apparently, the small-angle approximation used for the derivation of the refraction factor of the GFPE method (see Sec. H.6) works well for relatively large elevation angles. The starting field of order 8 gives accurate results for elevation angles higher than 40°, but also generates small numerical errors if the source is close to the ground surface. The starting field of order 2 is identical to the starting field (G.75) for the CNPE method. For the GFPE method, the starting field of order 4 is a good choice.

Table H.1. Optimized values of the parameters a_j in Eq. (H.70).

order	a_2	a_4	a_6	a_8	b_2
0	0	0	0	0	0.5
2	1.02	0	0	0	0.75
4	1.02	0.55	0	0	0.75
8	1.01	0.52	0.60	0.33	0.75

Table H.2. Values of the parameters A_j and B in Eq. (H.71).

order	A_0	A_2	A_4	A_6	A_8	B
0	1	0	0	0	0	2
2	1.3717	-0.3701	0	0	0	3
4	1.9705	-1.1685	0.0887	0	0	3
8	9.6982	-20.3785	6.0191	-0.4846	0.0105	3

H.11 Discretization of the Fourier integrals

The computation of the sound field with the GFPE method is basically a stepwise extrapolation of the field $\psi(r, z)$ in the positive r direction; the extrapolation is based on Eqs. (H.49) and (H.50). As in the CNPE method, we use a rectangular grid in the rz plane, with grid spacings Δr and Δz (see Fig. G.1). The vertical grid spacing Δz should not exceed about $\lambda/10$, where λ is an average wavelength. The horizontal grid spacing Δr, however, can be chosen considerably larger, with a maximum value of typically 10λ [58, 134]. As in the

CNPE method, we use an absorbing layer at the top of the grid (see Fig. G.1 and Sec. G.9).

The Fourier integrals in Eqs. (H.49) and (H.50) are approximated by discrete Fourier sums, which are efficiently evaluated with the Fast Fourier Transform (FFT) algorithm (see Sec. B.4). We will consider two approaches for this approximation (the second approach is more accurate).

In the first approach we discretize the height z' and the wave number k_z [the two integration variables in Eqs. (H.49) and (H.50)] as follows:

$$\begin{aligned} &z' \to z_j = j\Delta z, \quad \text{with } j = 0, 1, \ldots, N-1, \\ &k_z \to k_n = n\Delta k, \quad \text{with } n = 0, 1, \ldots, \tfrac{1}{2}N, -\tfrac{1}{2}N+1, -\tfrac{1}{2}N+2, \ldots, -1, \end{aligned} \tag{H.74}$$

where we have $N = 2M$, and $\Delta k = 2\pi/(N\Delta z)$ is the wave number spacing; the reason for using $N = 2M$ is indicated below. The Fourier integral (H.50) can be approximated as follows:

$$\Psi(r, k_n) \approx \left[\sum_{j=0}^{N-1} \exp(-ik_n z_j)\, \psi(r, z_j) \right] \Delta z. \tag{H.75}$$

The factor in rectangular brackets is the Discrete Fourier Transform (DFT) of $\psi(r, z)$. This is the usual method of approximating a Fourier integral by a Discrete Fourier Transform. For $\Psi(r, -k_n)$, Eq. (H.75) holds with k_n replaced by $-k_n$. The 'vector' with elements $\Psi(r, k_n)$ and the 'vector' with elements $\Psi(r, -k_n)$ are related to each other by a simple permutation of elements. Therefore, $\Psi(r, k_n)$ and $\Psi(r, -k_n)$ can be obtained from a single FFT of size $N = 2M$. For the function $\Psi(r, \beta)$ in Eq. (H.49), Eq. (H.75) is used with k_n replaced by β. The evaluation of $\Psi(r, \beta)$ requires a single summation of N terms. After the quantities $\Psi(r, k_n)$, $\Psi(r, -k_n)$, and $\Psi(r, \beta)$ have been calculated, $\psi(r, z_j)$ can be calculated by the evaluation of the integral in Eq. (H.49). This requires an inverse FFT of size N. For the inverse Fourier integral in Eq. (H.49), an approximation analogous to Eq. (H.75) can be used.

An alternate approach for computing the Fourier integrals is based on the midpoint rule for numerical integration [112]. This rule yields the following approximation for the Fourier integral (H.50):

$$\begin{aligned} \Psi(r, k_n) &\approx \left[\sum_{j=0}^{N-1} \exp(-ik_n[z_j + \tfrac{1}{2}\Delta z])\, \psi(r, z_j + \tfrac{1}{2}\Delta z) \right] \Delta z \\ &= \left[\sum_{j=0}^{N-1} \exp(-ik_n z_j)\, \psi(r, z_j + \tfrac{1}{2}\Delta z) \right] \exp(-ik_n \tfrac{1}{2}\Delta z)\, \Delta z. \end{aligned} \tag{H.76}$$

The last factor in rectangular brackets is the Discrete Fourier Transform of $\psi(r, z_j + \frac{1}{2}\Delta z)$. Numerical computations show that Eq. (H.76) yields more

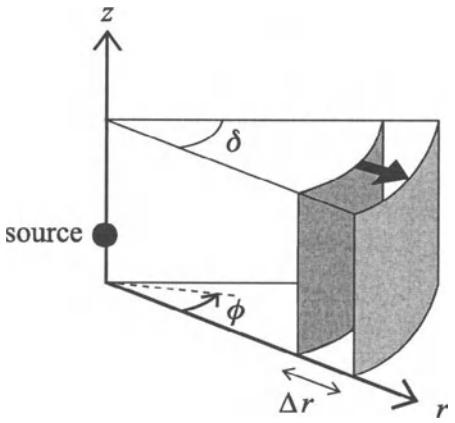

Figure H.6. Pie slice region used in the three-dimensional GFPE method. An extrapolation step from range r to range $r + \Delta r$ is indicated.

accurate results than Eq. (H.75) does. In some cases the difference in accuracy between Eqs. (H.75) and (H.76) is very large [134]. The accuracy of Eq. (H.76) originates from the choice of the z coordinates at the centers of the integration intervals $[z_j, z_{j+1}]$; in Eq. (H.76) we use the heights $z = \frac{1}{2}\Delta z, \frac{3}{2}\Delta z, \frac{5}{2}\Delta z, \ldots$, while in Eq. (H.75) we use the heights $z = 0, \Delta z, 2\Delta z, \ldots$. Therefore the lower limit $z = 0$ of the Fourier integral (H.50) is represented more accurately by Eq. (H.76) than by Eq. (H.75). For the inverse Fourier integral in Eq. (H.49), an approximation analogous to Eq. (H.76) can be used.

After each extrapolation step we set $\psi(r, z_j) = 0$ at the grid points with $j = M, M+1, \ldots, N-1$, to eliminate the coupling between the top surface and the ground surface introduced by the periodicity inherent to the Discrete Fourier Transform. This can also be understood from the fact that the heights z_j with $j = M, M+1, \ldots, N-1$ correspond to negative heights, by the periodicity; we need only positive heights since the lower limit of the integral in Eq. (H.50) is $z = 0$.

H.12 Three-dimensional GFPE method

In this section we describe a three-dimensional GFPE method [44]. For axisymmetric systems this method is identical to the two-dimensional GFPE method described in the previous sections.

In the three-dimensional GFPE method, the sound field of a point source is computed in a pie slice region (see Fig. H.6). Periodic boundary conditions are imposed on the straight sides of the slice at $\phi = 0$ and $\phi = \delta$. By choosing a low value for δ we keep the computation efficient. As in the two-dimensional

GFPE method, we use an impedance condition at the ground surface at $z = 0$, and an absorbing layer at the top of the slice.

The computation is basically a repetition of extrapolation steps in the positive r direction. In an extrapolation step, the field on the curved surface at range $r + \Delta r$ is computed from the field on the curved surface at range r (see Fig. H.6). It will be shown that an extrapolation step in the three-dimensional GFPE method requires the evaluation of a forward two-dimensional FFT and an inverse two-dimensional FFT, whereas an extrapolation step in the two-dimensional GFPE method requires the evaluation of a forward one-dimensional FFT and an inverse one-dimensional FFT.

We start from the following far-field Helmholtz equation in cylindrical $r\phi z$ coordinates:

$$\frac{\partial^2 q}{\partial r^2} + \frac{1}{r^2}\frac{\partial^2 q}{\partial \phi^2} + \frac{\partial^2 q}{\partial z^2} + k^2 q = 0. \tag{H.77}$$

This equation differs from Eq. (H.1), *i.e.* the starting equation of the two-dimensional GFPE method, by the presence of the term $r^{-2}\partial_\phi^2 q$. Equation (H.77) follows from the general Helmholtz equation (E.50), with the approximation $\partial_z^2 q$ for $k^2 \partial_z (k^{-2} \partial_z q)$ as before.

In agreement with the far-field approximation (see Sec. E.4), we neglect the curvature of the curved surface of the pie slice (see Fig. H.6). Consequently, we can use the two-dimensional analogue of the one-dimensional Rayleigh integral (H.19) in rectangular xyz coordinates:

$$p(\mathbf{R}_1) = \frac{1}{2\pi} \iint_{-\infty}^{\infty} \left(p(\mathbf{R}) \frac{\partial g(\mathbf{R}, \mathbf{R}_1)}{\partial x} \right)_{x=x_0} dy\, dz, \tag{H.78}$$

where we have $\mathbf{R} = (x, y, z)$ and $\mathbf{R}_1 = (x_1, y_1, z_1)$, and the Green's function g satisfies the Helmholtz equation

$$(\partial_x^2 + \partial_y^2 + \partial_z^2 + k^2) g(\mathbf{R}, \mathbf{R}_1) = -4\pi \delta(x - x_1)\delta(y - y_1)\delta(z - z_1). \tag{H.79}$$

The derivation presented in Sec. H.4 for the two-dimensional GFPE method can be generalized for the three-dimensional geometry shown in Fig. H.6. This gives

$$q(r + \Delta r, \phi, z) = \frac{1}{4\pi^2 i} \int_{-\infty}^{\infty} \exp(i\kappa \Delta r)\, \kappa\, d\kappa \int_0^{\delta} r\, d\phi' \int_0^{\infty} dz'\, G(\kappa, \phi', \phi, z', z) q(r, \phi', z'), \tag{H.80}$$

where the Green's function G satisfies the equation

$$\left[r^{-2}\partial_\phi^2 + \partial_z^2 + k^2(z) - \kappa^2 \right] G(\kappa, \phi', \phi, z', z) = -4\pi \delta(r\phi - r\phi')\delta(z - z'). \tag{H.81}$$

Equations (H.80) and (H.81) correspond to Eqs. (H.24) and (H.25) for the two-dimensional GFPE method. Equations (H.80) and (H.81) can also be derived from the spectral theorem of functional analysis (see Sec. H.7).

We first assume a non-refracting atmosphere, as in Sec. H.5. The wave number k in Eq. (H.81) is a constant in this case, so the Green's function $G(\kappa, \phi', \phi, z', z)$ depends on ϕ and ϕ' only through the difference $\phi - \phi'$. We apply a Fourier transformation $r\phi - r\phi' \to k_{r\phi}$, so that we have

$$G(\kappa, \phi', \phi, z', z) = \frac{1}{2\pi} \int_{-\infty}^{\infty} \exp(ik_{r\phi}[r\phi - r\phi'])G_\phi(\kappa, k_{r\phi}, z', z)\, dk_{r\phi}, \tag{H.82}$$

where G_ϕ is the Fourier transform of G. Substitution of the relation

$$\delta(r\phi - r\phi') = \frac{1}{2\pi} \int_{-\infty}^{\infty} \exp(ik_{r\phi}[r\phi - r\phi'])\, dk_{r\phi} \tag{H.83}$$

and Eq. (H.82) into Eq. (H.81) gives

$$\partial_z^2 G_\phi + (k^2 - \kappa^2 - k_{r\phi}^2)G_\phi = -4\pi\delta(z - z'). \tag{H.84}$$

The solution G_ϕ of this equation is given by Eq. (H.26) with vertical wave number k_v given by

$$k_v^2 = k^2 - \kappa^2 - k_{r\phi}^2. \tag{H.85}$$

Proceeding as in Sec. H.5, we find

$$\begin{aligned} q(r + \Delta r, \phi, z) = {} & \frac{1}{2\pi} \int_{-\infty}^{\infty} e^{ik_\phi \phi}\, dk_\phi \\ & \times \left\{ \frac{1}{2\pi} \int_{-\infty}^{\infty} e^{ik_z z} dk_z e^{i\Delta r\sqrt{k_0^2 - k_z^2 - k_\phi^2/r^2}} \int_0^\delta e^{-ik_\phi \phi'} d\phi' \int_0^\infty e^{-ik_z z'} q(r, \phi', z') dz' \right. \\ & + \frac{1}{2\pi} \int_{-\infty}^{\infty} R(k_z) e^{ik_z z} dk_z e^{i\Delta r\sqrt{k_0^2 - k_z^2 - k_\phi^2/r^2}} \int_0^\delta e^{-ik_\phi \phi'} d\phi' \int_0^\infty e^{ik_z z'} q(r, \phi', z') dz' \\ & \left. + 2i\beta e^{-i\beta z} e^{i\Delta r\sqrt{k_0^2 - \beta^2 - k_\phi^2/r^2}} \int_0^\delta e^{-ik_\phi \phi'} d\phi' \int_0^\infty e^{-i\beta z'} q(r, \phi', z') dz' \right\} \end{aligned} \tag{H.86}$$

with $k_\phi \equiv k_{r\phi} r$. Equation (H.86) corresponds to Eq. (H.40) for the two-dimensional GFPE method.

For a refracting atmosphere we follow the derivation presented in Secs. H.6 and H.9. This yields

$$\psi(r+\Delta r,\phi,z)=\exp(i\Delta r\,\delta k)\frac{1}{2\pi}\int_{-\infty}^{\infty}\exp(ik_\phi\phi)\,dk_\phi\left\{\frac{1}{2\pi}\int_{-\infty}^{\infty}\exp(ik_z z)dk_z\right.$$
$$\times\left[\Psi(r,k_\phi,k_z)+R(k_z)\Psi(r,k_\phi,-k_z)\right]\exp\left(i\Delta r\left[\sqrt{k_{\rm a}^2-k_z^2-k_\phi^2/r^2}-k_{\rm a}\right]\right)$$
$$\left.+2i\beta\exp(-i\beta z)\Psi(r,k_\phi,\beta)\exp\left(i\Delta r\left[\sqrt{k_{\rm a}^2-\beta^2-k_\phi^2/r^2}-k_{\rm a}\right]\right)\right\}, \quad \text{(H.87)}$$

where

$$\Psi(r,k_\phi,k_z)=\int_0^\delta\exp(-ik_\phi\phi')d\phi'\int_0^\infty\exp(-ik_z z')\psi(r,\phi',z')dz' \quad \text{(H.88)}$$

is the two-dimensional Fourier transform of $\psi(r,\phi,z)$. Equations (H.87) and (H.88) are the basic equations of the three-dimensional GFPE method. In the case of axial symmetry, k and ψ are independent of ϕ and Eqs. (H.87) and (H.88) are equivalent to Eqs. (H.49) and (H.50) for the two-dimensional GFPE method, with the refraction factor replaced by the factor (H.58). The equivalence follows by using the relation $2\pi\delta(k_\phi)=\int_0^\delta\exp(-ik_\phi\phi')d\phi'$ in Eq. (H.88).

The integration variables z' and k_z in Eqs. (H.87) and (H.88) are discretized as described in Sec. H.11. The integration variables ϕ' and k_ϕ are discretized as follows:

$$\begin{aligned}&\phi'\to\phi_j=j\Delta\phi,\quad\text{with } j=0,1,\ldots,K-1,\\&k_\phi\to k_n=n\Delta k_\phi,\quad\text{with } n=0,1,\ldots,K-1,\end{aligned} \quad \text{(H.89)}$$

with $\Delta\phi=\delta/K$ and $\Delta k_\phi=2\pi/\delta$. In this way, the integrals over ϕ' and k_ϕ can be evaluated efficiently by forward and inverse FFT's of size K. To avoid the divergence of k_ϕ^2/r^2 in Eq. (H.87) in the first step from $r=0$ to $r=\Delta r$, one can use $k_\phi^2/(r+\Delta r/2)^2$ instead of k_ϕ^2/r^2.

The choice of the angular spacing $\Delta\phi$ depends on the variation of the field ψ with the angle ϕ. In the limiting case of axial symmetry, the field ψ is independent of the angle ϕ, and the result of Eqs. (H.87) and (H.88) is independent of the angular spacing $\Delta\phi$. In the opposite case in which there is a large variation of the field ψ with the angle ϕ, the angular spacing should satisfy the condition $r\Delta\phi\lesssim\lambda/10$.

Appendix I

Atmospheric turbulence

I.1 Introduction

In the computational models described in Appendices F, G, and H, the atmosphere was represented by the vertical profiles of the temperature and the wind velocity. We assumed that the profiles are independent of time. In reality, however, the profiles change continuously. There are slow variations, on a time scale of hours or longer. There are also faster variations, or fluctuations, on time scales of seconds or minutes. The latter fluctuations are usually referred to as atmospheric turbulence [145].

The term turbulence is also used to indicate that the flow in a fluid is 'irregular' (see Fig. I.1). In a laminar flow, fluid 'particles' move parallel to each other in the flow direction. This occurs, for example, in a flow through a pipe at low speed. If the speed of the flow is increased, fluid particles deviate from the straight paths and the flow becomes turbulent. The atmospheric boundary layer is nearly always in a turbulent state.

The paths of fluid particles in a turbulent flow often contain 'loops', as shown in Fig. I.1. The loops correspond to swirls in the fluid, which are called *eddies*. Not only the paths deviate from a straight line, also the speeds of the particles deviate from the mean speed. If a fluid particle moves faster than neighboring particles, it soon encounters other particles which force the particle to deviate

Figure I.1. Illustration of laminar flow (left) and turbulent flow (right). The curves represent the paths of fluid 'particles'.

from its straight path. This deviation corresponds to the development of eddies in a turbulent flow.

The term eddy is also used in general for a velocity fluctuation in a limited region in a turbulent flow. The size of the region is called the eddy size. An eddy moves through a fluid as a more or less 'frozen' fluctuation [145]. Consequently, the eddy size is related to a characteristic period of the fluctuation (at a fixed point in the fluid) by the relation $l = v\tau_t$, where l is the eddy size, v is the mean flow velocity in the fluid, and τ_t is the characteristic period. The temperature of an eddy may differ from the temperature of the surrounding fluid, so the eddy corresponds not only to a velocity fluctuation but also to a temperature fluctuation.

The eddy sizes that occur in a turbulent flow depend on a characteristic dimension of the flow. In a pipe, for example, eddies larger than the pipe diameter do not occur. In the atmospheric boundary layer, a characteristic dimension is the height above the ground surface. With increasing height, larger eddies occur. We will see in Sec. I.3 that the largest eddies break down into smaller eddies, which break down into even smaller eddies, and so on. Consequently, there is a broad distribution of eddy sizes in the atmosphere. This distribution corresponds to a broad distribution of characteristic periods of turbulent fluctuations. Small eddies correspond to rapid fluctuations and large eddies correspond to slow variations of the wind velocity and the temperature.

I.2 Turbulence in sound propagation models

In models of atmospheric sound propagation, the turbulent atmosphere is usually described as a medium with a randomly fluctuating effective sound speed. The effective sound speed was defined in Sec. E.3 as $c_{\text{eff}} = c + u$, where c is the adiabatic sound speed and u is the horizontal wind velocity component in the direction of sound propagation. The adiabatic sound speed is related to the temperature T by the relation $c = c_0\sqrt{T/T_0}$, where c_0 is the sound speed at temperature T_0. In Appendix A we used the values $c_0 = 331$ m/s and $T_0 = 273$ K. In this appendix and Appendix J, however, T_0 is some average temperature and c_0 is the corresponding sound speed. Turbulent fluctuations of the temperature T and the wind velocity component u correspond to turbulent fluctuations of the effective sound speed c_{eff}.

A quantity that is equivalent to the effective sound speed is the (acoustic) refractive index $n = c_0/c_{\text{eff}}$. In a turbulent atmosphere, the refractive index fluctuates at each point around an average value, which is of the order of unity. The average value is denoted as $\overline{n}$ and the fluctuation is denoted as μ. Thus, we have

$$n = \overline{n} + \mu, \tag{I.1}$$

with $\mu \ll \overline{n}$ and $\overline{\mu} = 0$. In a non-refracting turbulent atmosphere we have $\overline{n} = 1$. In a refracting turbulent atmosphere $\overline{n}$ is a function of position. The fluctuation

μ is related to the turbulent temperature fluctuation T_t and the turbulent wind velocity fluctuation u_t by the expression

$$\mu = -\frac{T_t}{2T_0} - \frac{u_t}{c_0}, \tag{I.2}$$

which follows from $n = c_0/c_{\text{eff}}$ and $c_{\text{eff}} = c_0\sqrt{T/T_0} + u$. A more rigorous derivation of this expression can be found in Ref. [98].

We are interested in sound pressure fields averaged (logarithmically) over turbulent fluctuations in a short period, for example a period of ten minutes. We assume that such an average sound pressure field can be approximated by a (logarithmic) average of a set of sound pressure fields computed for a set of random realizations of the turbulent atmosphere. Each realization represents a 'snapshot' of the atmosphere. This approach is known as the frozen medium approach, and is based on the fact that sound waves travel so fast that the medium can be considered as a 'frozen' medium.

The random realizations of the turbulent atmosphere are represented by random fields of the refractive-index fluctuations μ. The sound pressure fields for different random fields can be computed with the PE method, as described in Appendix J. The random fields are calculated with the aid of a random number generator; this is also described in Appendix J. The calculation takes into account the condition that the correlation function of the refractive-index fluctuations should have the correct value. The correlation function, and the related spectral density, are introduced in the remainder of this appendix.

I.3 Reynolds number and onset of turbulence

An important parameter of a fluid is the viscosity. To define the viscosity, we consider an infinitesimal rectangular volume element in a fluid in which the horizontal velocity u increases with the height z (see Fig. I.2). The velocity gradient results in a deformation, or shear, of the element: the upper face moves faster than the lower face. Friction in the fluid tends to reduce the velocity gradient over the element. The gradient can only be sustained by a shear stress τ as indicated in Fig. I.2. The shear stress corresponds to two equal but opposite forces on the upper and lower faces. The force on either face is equal to $\tau\,dx\,dy$, where $dx\,dy$ is the area of the face. In most fluids, the shear stress is proportional to the velocity gradient: $\tau = \eta\,du/dz$. The constant η is called the viscosity.

The work done by the shear stress in the deformation is irreversible, *i.e.* converted into heat. The displacement of the upper face with respect to the lower face, per unit time, is equal to $(du/dz)\,dz$, where dz is the height of the volume element. The irreversible work per unit time per unit mass is therefore equal to $\nu(du/dz)^2$, where $\nu = \eta/\rho$ is called the kinematic viscosity; ρ is the mass density of the fluid.

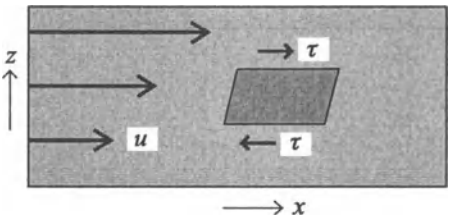

Figure I.2. Deformation of a small volume element in a fluid in which the horizontal velocity u increases with the height z.

A fluid flow can be characterized by three parameters:

- the kinematic viscosity ν,
- a characteristic velocity v,
- a characteristic length L.

For the characteristic velocity v we can use some average velocity of the flow. For the characteristic length L we can use the pipe diameter in the case of flow through a pipe, or the height above the ground in the case of the atmospheric boundary layer. In general, L is determined by the boundary conditions of the flow.

The Reynolds number N_{R} is defined as $N_{\mathrm{R}} = vL/\nu$. If N_{R} is smaller than a critical value $N_{\mathrm{R,crit}}$, the flow is laminar. If N_{R} is increased to values larger than the critical value, the flow becomes turbulent. This is explained in the remainder of this section, where we follow Tatarski [149].

We consider a velocity fluctuation v_l' in a region of size l (*i.e.* an eddy of size l) in an initially laminar flow in a viscous fluid (the prime indicates that v_l' is a fluctuation of the velocity, which is smaller than the mean velocity v, in general). The time required for the development of the fluctuation is $\tau_l = l/v_l'$. Here one may think of a row of particles moving parallel to each other with equal velocities; if the velocity of one of the particles is suddenly enhanced by an amount v_l', it takes the particle a time l/v_l' to move a distance l away from the other particles. The energy per unit mass of the fluctuation is of the order of $v_l'^2$. It follows that the amount of energy, per unit mass and per unit time, which goes over from the laminar flow to the fluctuation is of the order of $v_l'^2/\tau_l = v_l'^3/l$.

Local velocity gradients are of the order of v_l'/l. From the above discussion of viscosity it follows that the fluctuation dissipates an amount of energy, per unit time and per unit mass, of the order of $\epsilon = \nu v_l'^2/l^2$.

We find that velocity fluctuations v_l' of size l are easily created if we have $v_l'^3/l > \nu v_l'^2/l^2$. This condition can also be expressed as $N_{\mathrm{R},l} > 1$, where $N_{\mathrm{R},l} = v_l' l/\nu$ is the 'inner' Reynolds number of fluctuations of size l, which

differs from the Reynolds number $N_R = vL/\nu$. Since we ignored numerical factors, the condition is in fact $N_{R,l} > N_{R,crit}$, where $N_{R,crit}$ is some critical value.

In general we have $v_l' < v$. Hence, if N_R is only a little larger than $N_{R,crit}$, only large fluctuations are created. If N_R is increased further, smaller fluctuations are also created. In fact, a cascade process occurs: large eddies create smaller eddies, which create even smaller eddies, and so on. The creation of an eddy by a larger eddy can be attributed to the velocity gradient in the larger eddy. The cascade process begins with the creation of the largest eddies, by velocity gradients in the atmosphere; these gradients are commonly referred to as wind shear. Wind shear is large near the ground surface and near obstacles.

Eddies of size l receive an amount of energy $v_l'^3/l$ per unit mass and per unit time from larger eddies, and pass this energy on to smaller eddies. The dissipation of all eddies, except for the smallest eddies, is small compared with the energy they receive from larger eddies. It follows that the energy $v_l'^3/l$ is constant for all eddies. In the smallest eddies of size l_0, with velocity fluctuation v_0, this energy is converted into heat, at a rate $\epsilon \sim \nu v_0^2/l_0^2$. Hence we have $\epsilon \sim v_l'^3/l$ for all $l \geq l_0$, or

$$v_l' \sim (\epsilon l)^{1/3}. \tag{I.3}$$

From $v_0 \sim (\epsilon l_0)^{1/3}$ and $\epsilon \sim \nu v_0^2/l_0^2$ it follows that the size l_0 of the smallest eddies is given by $l_0 \sim (\nu^3/\epsilon)^{1/4}$. The size l_0 can also be related to the size L of the largest eddies. From $\epsilon \sim v_L^3/L$ we find $l_0 \sim L/N_R^{3/4}$. From the value $\nu \sim 0.15\ \mathrm{cm}^2/\mathrm{s}$ for air we find $N_R \sim 10^5$ for $L \sim 1$ m and $v_L \sim 1$ m/s. Hence, the smallest eddies are at least three orders of magnitude smaller than the largest eddies; the size l_0 of the smallest eddies is typically 1 mm.

I.4 Random fields

The wind velocity components and the temperature in the turbulent atmosphere are rapidly fluctuating functions of position and time. These functions are called random functions. The fields of the wind velocity components and the temperature are called random fields. Random fields can be characterized by a correlation function or a structure function [149, 150, 125, 68]. These functions are introduced in this section.

The time average of a random function $f(\mathbf{r})$ is denoted as $\overline{f(\mathbf{r})}$. We will consider only random functions with $\overline{f(\mathbf{r})} = 0$. An example of a random function with $\overline{f(\mathbf{r})} = 0$ is the deviation of the temperature from the average temperature.

The correlation function of a random function $f(\mathbf{r})$ is defined as

$$B(\mathbf{r}_1, \mathbf{r}_2) = \overline{f(\mathbf{r}_1) f(\mathbf{r}_2)}. \tag{I.4}$$

A random function $f(\mathbf{r})$ is called homogeneous if the correlation function B depends on $\mathbf{r}_1$ and $\mathbf{r}_2$ only through the difference $\mathbf{r} = \mathbf{r}_1 - \mathbf{r}_2$, so that we have

$B(\mathbf{r}_1, \mathbf{r}_2) = B(\mathbf{r})$. A homogeneous function $f(\mathbf{r})$ is called isotropic if B depends only on the length r of the vector $\mathbf{r}$, so that we have $B(\mathbf{r}) = B(r)$.

If the correlation function depends not only on the vector $\mathbf{r} = \mathbf{r}_1 - \mathbf{r}_2$ but also on the position in the atmosphere, the random function is not homogeneous. In this case one can use the structure function, which is defined as

$$D(\mathbf{r}_1, \mathbf{r}_2) = \overline{[f(\mathbf{r}_1) - f(\mathbf{r}_2)]^2}. \tag{I.5}$$

Since the structure function contains the difference between the values of the random function at two points, gradual changes in the random field have a smaller effect on the structure function than on the correlation function. A random function $f(\mathbf{r})$ is called locally homogeneous if we have $D(\mathbf{r}_1, \mathbf{r}_2) = D(\mathbf{r})$, with $\mathbf{r} = \mathbf{r}_1 - \mathbf{r}_2$. If we have $D(\mathbf{r}) = D(r)$, the random function is called locally isotropic.

The correlation function $B(r)$ and the structure function $D(r)$ of an isotropic random function $f(\mathbf{r})$ are related to each other:

$$D(r) = 2B(0) - 2B(r), \tag{I.6}$$

as follows from Eqs. (I.4) and (I.5). In practice we always have $B(\infty) = 0$, so we find $D(\infty) = 2B(0)$. This gives

$$B(r) = \frac{1}{2}D(\infty) - \frac{1}{2}D(r). \tag{I.7}$$

The foregoing applies to scalar functions, such as the temperature fluctuation in the atmosphere. The wind velocity fluctuation in the atmosphere, however, is a vector function. A homogeneous vector function $\mathbf{v}(\mathbf{r})$ can be characterized by a set of nine correlation functions

$$B_{ij}(\mathbf{r}) = \overline{v_i(\mathbf{r}_1)v_j(\mathbf{r}_2)} \tag{I.8}$$

and a set of nine structure functions

$$D_{ij}(\mathbf{r}) = \overline{[v_i(\mathbf{r}_1) - v_i(\mathbf{r}_2)][v_j(\mathbf{r}_1) - v_j(\mathbf{r}_2)]}, \tag{I.9}$$

with $\mathbf{r} = \mathbf{r}_1 - \mathbf{r}_2$ and $i, j = 1, 2, 3$, where v_1, v_2, and v_3 are the x, y, and z components of the vector $\mathbf{v}$, respectively. If the vector field is isotropic, the nine correlation functions B_{ij} can all be expressed in two functions, the longitudinal structure function $B_{rr}(r)$ and the transverse correlation function $B_{tt}(r)$:

$$B_{ij}(\mathbf{r}) = \left(\delta_{ij} - \frac{r_i r_j}{r^2}\right) B_{tt}(r) + \frac{r_i r_j}{r^2} B_{rr}(r), \tag{I.10}$$

with $\mathbf{r} = (r_1, r_2, r_3)$, and $\delta_{ij} = 1$ for $i = j$ and $\delta_{ij} = 0$ for $i \neq j$ [150, 98]. Analogously, the nine structure functions D_{ij} for locally isotropic turbulence can all be expressed in the longitudinal structure function $D_{rr}(r)$ and the transverse structure function $D_{tt}(r)$:

$$D_{ij}(\mathbf{r}) = \left(\delta_{ij} - \frac{r_i r_j}{r^2}\right) D_{tt}(r) + \frac{r_i r_j}{r^2} D_{rr}(r). \tag{I.11}$$

Examples of the longitudinal structure function are $D_{11}(\mathbf{e}_x)$, $D_{22}(\mathbf{e}_y)$, and $D_{33}(\mathbf{e}_z)$, where $\mathbf{e}_x$, $\mathbf{e}_y$, and $\mathbf{e}_z$ are the unit vectors in the x, y, and z directions, respectively. Equation (I.11) gives $D_{11}(\mathbf{e}_x) = D_{22}(\mathbf{e}_y) = D_{33}(\mathbf{e}_z)$. An example of the transverse structure function is $D_{11}(\mathbf{e}_y)$.

If one assumes that the flow is incompressible ($\nabla \cdot \mathbf{v} = 0$), one can derive a relation between $B_{rr}(r)$ and $B_{tt}(r)$, and a relation between $D_{rr}(r)$ and $D_{tt}(r)$ [149]:

$$B_{tt}(r) = \frac{1}{2r}\frac{d}{dr}\left[r^2 B_{rr}(r)\right], \tag{I.12}$$

$$D_{tt}(r) = \frac{1}{2r}\frac{d}{dr}\left[r^2 D_{rr}(r)\right]. \tag{I.13}$$

In this case, the nine correlation functions can all be expressed in a single function, either $B_{rr}(r)$ or $B_{tt}(r)$, and the nine structure functions can all be expressed in a single function, either $D_{rr}(r)$ or $D_{tt}(r)$.

I.5 The 'two-thirds law'

We consider the longitudinal structure function $D_{rr}(r) = \overline{[v_r(\mathbf{r}_1 + \mathbf{r}) - v_r(\mathbf{r}_1)]^2}$. If we have $l_0 \ll r \ll L$, where l_0 and L are the sizes of the smallest and largest eddies, respectively, the velocity difference $v_r(\mathbf{r}_1 + \mathbf{r}) - v_r(\mathbf{r}_1)$ between the points $\mathbf{r}_1 + \mathbf{r}$ and $\mathbf{r}_1$ is mainly determined by eddies of size r. Therefore we have $D_{rr} \sim v_r^2$, where v_r is the velocity fluctuation corresponding to an eddy of size r. From Eq. (I.3) we have $v_r \sim (\epsilon r)^{1/3}$, so we find $D_{rr}(r) = C(\epsilon r)^{2/3}$, where C is a dimensionless constant of the order of unity. This result, the 'two-thirds law' of Kolmogorov and Obukhov [149], is valid for $l_0 \ll r \ll L$. For $r \ll l_0$ the flow can be considered as laminar, and one can derive $D_{rr} = \frac{1}{15}\epsilon r^2/\nu$ [149]. Hence we have

$$D_{rr}(r) = \begin{cases} C(\epsilon r)^{2/3} & \text{for } l_0 \ll r \ll L, \\ \frac{1}{15}\epsilon r^2/\nu & \text{for } r \ll l_0. \end{cases} \tag{I.14}$$

In the context of this equation, the length scales l_0 and L are called the inner and outer scales of turbulence, respectively. The inner scale of turbulence l_0 can be defined as the value of r where the two branches in Eq. (I.14) intersect:

$$l_0 = \left[(15C\nu)^3/\epsilon\right]^{1/4}. \tag{I.15}$$

This expression can be used to replace ϵ in Eq. (I.14) by l_0:

$$D_{rr}(r) = \begin{cases} C^2 r^{2/3} & \text{for } l_0 \ll r \ll L, \\ C^2 l_0^{2/3}(r/l_0)^2 & \text{for } r \ll l_0, \end{cases} \tag{I.16}$$

where the factor $C^3(15\nu)^2 l_0^{-8/3}$ has been redefined as C^2. As l_0 is typically of the order of 1 mm, the region $r \ll l_0$ is usually unimportant in acoustics (*cf.* Sec. I.7.1).

I.6 Spectral density

The spectral density of a homogeneous random function $f(\mathbf{r})$ is the spatial Fourier transform of the correlation function $B(\mathbf{r})$ [149, 150, 68]. One distinguishes one-, two-, and three-dimensional spectral densities, to describe correlation along a line, in a plane, and in a volume, respectively.

In the one-dimensional case, the Fourier transform pair is

$$B(r) = \int_{-\infty}^{\infty} \exp(ikr) V(k)\, dk \tag{I.17}$$

$$V(k) = \frac{1}{2\pi} \int_{-\infty}^{\infty} \exp(-ikr) B(r)\, dr, \tag{I.18}$$

where $V(k)$ is the one-dimensional spectral density of the random function. In the three-dimensional case, the Fourier transform pair is

$$B(\mathbf{r}) = \iiint_{-\infty}^{\infty} \exp(i\mathbf{k}\cdot\mathbf{r}) \Phi(\mathbf{k})\, d\mathbf{k} \tag{I.19}$$

$$\Phi(\mathbf{k}) = \frac{1}{(2\pi)^3} \iiint_{-\infty}^{\infty} \exp(-i\mathbf{k}\cdot\mathbf{r}) B(\mathbf{r})\, d\mathbf{r}, \tag{I.20}$$

where $\Phi(\mathbf{k})$ is the three-dimensional spectral density of the random function and $\mathbf{r}$ and $\mathbf{k}$ are three-dimensional vectors. If the field is isotropic, we have $B(\mathbf{r}) = B(r)$, and Eq. (I.20) reduces to

$$\Phi(\mathbf{k}) = \frac{1}{2\pi^2 k} \int_{0}^{\infty} \sin(kr) B(r)\, r\, dr, \tag{I.21}$$

so we have $\Phi(\mathbf{k}) = \Phi(k)$. To prove Eq. (I.21) one uses spherical $r\theta\phi$ coordinates for the vector $\mathbf{r}$ in Eq. (I.20), with $\mathbf{k}\cdot\mathbf{r} = kr\cos\theta$ and $d\mathbf{r} = r^2\, dr\, \sin\theta\, d\theta\, d\phi$.

Comparison of Eqs. (I.18) and (I.21) yields the relation

$$\Phi(k) = -\frac{1}{2\pi k} \frac{dV(k)}{dk}. \tag{I.22}$$

With this relation we can derive the three-dimensional spectral density of an isotropic random function from the one-dimensional spectral density.

In the two-dimensional case, the Fourier transform pair is

$$B(\mathbf{r}) = \iint_{-\infty}^{\infty} \exp(i\mathbf{k}\cdot\mathbf{r}) F(\mathbf{k})\, d\mathbf{k} \tag{I.23}$$

$$F(\mathbf{k}) = \frac{1}{(2\pi)^2} \iint_{-\infty}^{\infty} \exp(-i\mathbf{k}\cdot\mathbf{r}) B(\mathbf{r})\, d\mathbf{r}, \tag{I.24}$$

where $F(\mathbf{k})$ is the two-dimensional spectral density of the random function and $\mathbf{r}$ and $\mathbf{k}$ are two-dimensional vectors, *e.g.* $\mathbf{r} = (x, z)$ and $\mathbf{k} = (k_x, k_z)$. Comparison of Eqs. (I.19) and (I.23) for $\mathbf{r} = 0$ yields the relation

$$F(k_x, k_z) = \int_{-\infty}^{\infty} \Phi(k_x, k_y, k_z)\, dk_y, \tag{I.25}$$

and analogous relations for $F(k_x, k_y)$ and $F(k_y, k_z)$. If the field is isotropic, Eq. (I.24) reduces to

$$F(\mathbf{k}) = \frac{1}{2\pi} \int_0^{\infty} J_0(kr) B(r) r\, dr, \tag{I.26}$$

so we have $F(\mathbf{k}) = F(k)$. Here we have used Eq. (E.59).

The structure function $D(\mathbf{r})$ is also related to the spectral density. In the one-dimensional case we have

$$D(r) = 2 \int_{-\infty}^{\infty} [1 - \exp(ikr)] V(k)\, dk, \tag{I.27}$$

as follows from Eqs. (I.6) and (I.17). Analogous relations hold in the two- and three-dimensional cases.

For vector functions we defined a set of nine correlation functions $B_{ij}(\mathbf{r})$ in Eq. (I.8). Each correlation function $B_{ij}(\mathbf{r})$ corresponds to a three-dimensional spectral density $\Phi_{ij}(\mathbf{k})$ defined by Eq. (I.20) (with $\Phi_{ij} = \Phi$ and $B_{ij} = B$), and a two-dimensional spectral density $F_{ij}(\mathbf{k})$ defined by Eq. (I.24) (with $F_{ij} = F$ and $B_{ij} = B$).

I.7 Gaussian, Kolmogorov, and von Kármán spectra

In the previous sections we introduced the following statistical functions to describe a random field:

- correlation function $B(\mathbf{r})$,
- structure function $D(\mathbf{r})$,
- one-dimensional spectral density $V(k)$,
- two-dimensional spectral density $F(\mathbf{k})$,
- three-dimensional spectral density $\Phi(\mathbf{k})$.

In atmospheric acoustics, turbulence is represented by the random field of refractive-index fluctuations (see Sec. I.2). The refractive-index fluctuation μ is related to the temperature fluctuation T_t and the wind velocity fluctuation u_t by the expression $\mu = -\frac{1}{2}T_t/T_0 - u_t/c_0$, in the effective sound speed approximation [see Eq. (I.2)].

In the acoustic literature [98], various mathematical functions have been used to approximate the statistical functions $B(\mathbf{r})$, $D(\mathbf{r})$, $V(k)$, $F(\mathbf{k})$, and $\Phi(\mathbf{k})$ of the refractive-index fluctuation μ. A Gaussian function has been widely used. A Gaussian correlation function corresponds to Gaussian spectral densities, as will be shown in Sec. I.7.1. In this case the atmosphere is referred to as an atmosphere with a Gaussian spectrum of refractive-index fluctuations. A more realistic representation is the von Kármán spectrum, which is related to the Kolmogorov spectrum.

In Secs. I.7.1 and I.7.2 we give expressions for the statistical functions $B(\mathbf{r})$, $D(\mathbf{r})$, $V(k)$, $F(\mathbf{k})$, and $\Phi(\mathbf{k})$ of the refractive-index fluctuation μ, for the Gaussian spectrum, the Kolmogorov spectrum, and the von Kármán spectrum. In Sec. I.7.1 we give expressions for an isotropic turbulent atmosphere with only temperature fluctuations, so we have $u_t = 0$ [149, 150]. In Sec. I.7.2 we give expressions for an isotropic turbulent atmosphere with temperature and wind fluctuations [98].

I.7.1 Atmosphere with temperature fluctuations

For an atmosphere with only temperature fluctuations we have $u_t = 0$, and we find from Eq. (I.2) the relation $\mu = -\frac{1}{2}T_t/T_0$. This implies $B(\mathbf{r}) = \frac{1}{4}B_T(\mathbf{r})/T_0^2$, where $B_T(\mathbf{r})$ is the correlation function of the temperature fluctuations. For isotropic turbulence we have $B_T(\mathbf{r}) = B_T(r)$, which implies $B(\mathbf{r}) = B(r)$. In the same way we find $D(\mathbf{r}) = D(r)$, $F(\mathbf{k}) = F(k)$, and $\Phi(\mathbf{k}) = \Phi(k)$.

For the Gaussian spectrum, the statistical functions of the refractive-index fluctuations are given by the following expressions:

$$B(r) = \mu_0^2 \exp(-r^2/a^2) \tag{I.28}$$

$$D(r) = 2\mu_0^2 \left[1 - \exp(-r^2/a^2)\right] \tag{I.29}$$

$$V(k) = \mu_0^2 \frac{a}{2\sqrt{\pi}} \exp(-k^2a^2/4) \tag{I.30}$$

$$F(k) = \mu_0^2 \frac{a^2}{4\pi} \exp(-k^2a^2/4) \tag{I.31}$$

$$\Phi(k) = \mu_0^2 \frac{a^3}{8\pi^{3/2}} \exp(-k^2a^2/4), \tag{I.32}$$

where a is the correlation length and μ_0 is the standard deviation of μ. The standard deviation μ_0 is related to the standard deviation σ_T of the temperature fluctuations by the expression $\mu_0 = \frac{1}{2}\sigma_T/T_0$, which follows from the expression $\mu = -\frac{1}{2}T_t/T_0$. If we assume that the correlation function $B(r)$ is given by Eq. (I.28), the expressions in Eqs. (I.29) to (I.32) for the other functions follow by

using the relations given in the previous sections. Equation (I.29) follows from Eq. (I.6). Equation (I.30) follows by substitution of Eq. (I.28) into Eq. (I.18):

$$V(k) = \frac{\mu_0^2}{2\pi} \int_{-\infty}^{\infty} \exp\left(-ikr - \frac{r^2}{a^2}\right) dr = \frac{\mu_0^2}{2\pi} \int_{-\infty}^{\infty} \exp\left(-\left[\frac{r}{a} + \frac{ika}{2}\right]^2 - \frac{k^2a^2}{4}\right) dr, \tag{I.33}$$

and deformation of the integration path along the real axis to the line $\mathrm{Im}(r/a) = -ika/2$. Using the relation $\int_{-\infty}^{\infty} \exp(-x^2)\,dx = \sqrt{\pi}$ we obtain the well-known result that the Fourier transform of a Gaussian is a Gaussian. Equations (I.31) and (I.32) follow from Eqs. (I.22) and (I.25). The Gaussian spectrum has been widely used in atmospheric acoustics, with a value of about 1 m for the correlation length a and values ranging from about 10^{-6} to 10^{-5} for the variance μ_0^2 [33, 35, 159] (*cf.* Sec. I.7.2).

For the Kolmogorov spectrum the expressions are [see Eq. (I.16)]

$$D(r) = C^2 r^p \tag{I.34}$$

$$V(k) = C^2 \frac{\Gamma(p+1)}{2\pi} \sin(\tfrac{1}{2}\pi p)|k|^{-p-1} \tag{I.35}$$

$$F(k) = C^2 \frac{\Gamma^2(\frac{1}{2}p+1)2^p}{2\pi^2} \sin(\tfrac{1}{2}\pi p)|k|^{-p-2} \tag{I.36}$$

$$\Phi(k) = C^2 \frac{\Gamma(p+2)}{4\pi^2} \sin(\tfrac{1}{2}\pi p)|k|^{-p-3} \tag{I.37}$$

with $p = 2/3$; here Γ is the gamma function [1]. The correlation function $B(r)$ is undefined in this case, as follows from Eq. (I.7). To prove that Eq. (I.35) corresponds to Eq. (I.34), one substitutes Eq. (I.35) into Eq. (I.27); by integration by parts one finds Eq. (I.34), using the relation (see Eq. 3.764 of Ref. [61])

$$\int_0^{\infty} x^p \sin(ax+b)\,dx = a^{-p-1}\Gamma(1+p)\cos(b+p\pi/2), \quad (a>0,\ -1<p<0) \tag{I.38}$$

and the relation $\Gamma(x)\Gamma(1-x) = \pi/\sin x\pi$, or $\Gamma(1+x)\Gamma(1-x) = x\pi/\sin x\pi$ from $\Gamma(x+1) = x\Gamma(x)$. Equations (I.36) and (I.37) follow from Eqs. (I.22) and (I.25).

For the von Kármán spectrum the expressions are

$$B(r) = \mu_0^2 \frac{2^{2/3}}{\Gamma(1/3)} \left(\frac{r}{a}\right)^{1/3} K_{1/3}\left(\frac{r}{a}\right) \tag{I.39}$$

$$D(r) = 2\mu_0^2 \left[1 - \frac{2^{2/3}}{\Gamma(1/3)} \left(\frac{r}{a}\right)^{1/3} K_{1/3}\left(\frac{r}{a}\right)\right] \tag{I.40}$$

$$V(k) = \mu_0^2 \frac{\Gamma(5/6)}{\Gamma(1/3)\sqrt{\pi}} \frac{a}{(1+k^2a^2)^{5/6}} \tag{I.41}$$

$$F(k) = \mu_0^2 \frac{\Gamma(8/6)}{\Gamma(1/3)\pi} \frac{a^2}{(1+k^2a^2)^{8/6}} \tag{I.42}$$

$$\Phi(k) = \mu_0^2 \frac{\Gamma(11/6)}{\Gamma(1/3)\pi^{3/2}} \frac{a^3}{(1+k^2a^2)^{11/6}}, \tag{I.43}$$

where a is the correlation length, μ_0 is the standard deviation of μ, and $K_{1/3}$ is a modified Bessel function of order 1/3 [1]. For $r \ll a$ the structure function (I.40) reduces to

$$D(r) \approx \mu_0^2 \frac{\sqrt{\pi}}{\Gamma(7/6)} \left(\frac{r}{a}\right)^{2/3}. \tag{I.44}$$

Hence, for $r \ll a$ the von Kármán spectrum is of the same form as the Kolmogorov spectrum. Equation (I.40) follows from Eqs. (I.39) and (I.6). To prove that Eq. (I.41) corresponds to Eq. (I.39), one substitutes Eq. (I.41) into Eq. (I.17), which yields Eq. (I.39) if one uses the relation (see Eq. 3.771 of Ref. [61])

$$\int_0^\infty (\beta^2 + x^2)^{\nu-1/2} \cos(ax)\, dx = \frac{1}{\sqrt{\pi}} \left(\frac{2\beta}{a}\right)^\nu \cos(\pi\nu)\Gamma(\nu + \frac{1}{2}) K_{-\nu}(a\beta) \tag{I.45}$$

and the relation $\Gamma(x)\Gamma(1-x) = \pi/\sin x\pi$. Equation (I.43) follows then from Eq. (I.22), if one uses $\Gamma(x+1) = x\Gamma(x)$. Next, Eq. (I.42) follows from Eq. (I.25), by using the relation

$$\int_0^\infty (a + x^2)^{-11/6}\, dx = a^{-8/6} \frac{\Gamma(\frac{1}{2})\Gamma(\frac{8}{6})}{2\Gamma(\frac{11}{6})}, \tag{I.46}$$

which follows from Eq. 3.251 of Ref. [61].

It should be noted that for electromagnetic wave propagation one usually includes an exponential cut-off factor $\exp(-k^2/k_{\max}^2)$ in the expression (I.43) for $\Phi(k)$, with $k_{\max} = 5.48/l_0$, where l_0 is the inner scale of turbulence [149]. This factor represents a rapid decay of the spectral density $\Phi(k)$ for $k > k_{\max}$, and corresponds to the branch $r \ll l_0$ in Eq. (I.16). The corresponding cut-off factor for $F(k)$ is $\exp(-k^2/k_{\max}^2)$, with $k_{\max} = 4.60/l_0$. The cut-off factor can be omitted in acoustics, since l_0 is typically of the order of 1 mm and the effect of sound scattering by inhomogeneities with sizes of the order of 1 mm is negligible [98].

I.7.2 Atmosphere with wind and temperature fluctuations

In this section we give expressions for the statistical functions of refractive-index fluctuations in an isotropic turbulent atmosphere with wind and temperature fluctuations ($u_t \neq 0$). These expressions were developed by Ostashev [98].

From Eq. (I.2) we have the relation $\mu = -\frac{1}{2}T_t/T_0 - u_t/c_0$. Consequently, the correlation function $B(\mathbf{r})$ of the refractive-index fluctuation μ is related to the correlation function $B_T(\mathbf{r})$ of the temperature fluctuation T_t and the correlation function $B_{11}(\mathbf{r})$ of the wind velocity fluctuation u_t [see Eq. (I.8)], by the equation

$$B(\mathbf{r}) = \frac{B_T(\mathbf{r})}{4T_0^2} + \frac{B_{11}(\mathbf{r})}{c_0^2}. \tag{I.47}$$

The analogous equations for the spectral densities are $F(\mathbf{k}) = F_T(\mathbf{k})/(4T_0^2) + F_{11}(\mathbf{k})/c_0^2$ and $\Phi(\mathbf{k}) = \Phi_T(\mathbf{k})/(4T_0^2) + \Phi_{11}(\mathbf{k})/c_0^2$. The indices 11 of B_{11}, F_{11}, and Φ_{11} corresponds to the x coordinate of a rectangular xyz coordinate system, where the x direction is the direction of sound propagation. The functions $B(\mathbf{r})$, $F(\mathbf{k})$, and $\Phi(\mathbf{k})$ are anisotropic in this case (in Sec. I.7.1 the functions were isotropic), due to the anisotropy of the functions $B_{11}(\mathbf{r})$, $F_{11}(\mathbf{k})$, and $\Phi_{11}(\mathbf{k})$. Although the wind and temperature fluctuations are still assumed to be isotropic, the effective sound speed for propagation in the x direction and the corresponding refractive-index fluctuations are anisotropic. Below we give the functions $B(x,y,z)$, $F(k_x,k_z) = F(k_x,k_y)$, $F(k_y,k_z)$, and $\Phi(k_x,k_y,k_z)$ for the Gaussian spectrum and the von Kármán spectrum. Because of the anisotropy we indicate the components of the vectors $\mathbf{r}$ and $\mathbf{k}$ explicitly in the arguments of the functions. The functions $B(x,y,z)$, $F(k_x,k_z)$, and $\Phi(k_x,k_y,k_z)$ will be used in Appendix J for the calculation of sound propagation in a turbulent atmosphere. For the derivation of the expressions given below, the reader is referred to Ref. [98]. It should be noted that in Ref. [98] the expression for $\Phi(k_x,k_y,k_z)$ is given for the case $k_x = 0$; this case corresponds to the so-called Markov approximation [*cf.* Eq. (K.9)].

For the Gaussian spectrum, with a Gaussian temperature correlation function $B_T(r) = \sigma_T^2 \exp(-r^2/a^2)$ and a Gaussian longitudinal wind velocity correlation function $B_{rr}(r) = \sigma_v^2 \exp(-r^2/a^2)$, the correlation function of refractive-index fluctuations follows from Eqs. (I.10), (I.12), and (I.47):

$$B(x,y,z) = \left[\frac{\sigma_T^2}{4T_0^2} + \frac{\sigma_v^2}{c_0^2}\left(1 - \frac{\rho^2}{a^2}\right)\right] \exp(-r^2/a^2), \tag{I.48}$$

where a is the correlation length, σ_T and σ_v are the standard deviations of the temperature and wind velocity fluctuations, respectively, and the distances r and ρ are given by $r^2 = x^2 + y^2 + z^2$ and $\rho^2 = y^2 + z^2$. The two-dimensional spectral densities $F(k_x,k_z)$ and $F(k_y,k_z)$ for the Gaussian spectrum are given by

$$F(k_x,k_z) = \frac{a^2}{4\pi}\left(\frac{\sigma_T^2}{4T_0^2} + \frac{\sigma_v^2[k_z^2a^2+2]}{4c_0^2}\right) \exp(-k^2a^2/4) \tag{I.49}$$

with $k^2 = k_x^2 + k_z^2$, and

$$F(k_y, k_z) = \frac{a^2}{4\pi}\left(\frac{\sigma_T^2}{4T_0^2} + \frac{\sigma_v^2 k^2 a^2}{4c_0^2}\right)\exp(-k^2a^2/4) \tag{I.50}$$

with $k^2 = k_y^2 + k_z^2$. The three-dimensional spectral density for the Gaussian spectrum is given by

$$\Phi(k_x, k_y, k_z) = \frac{a^3}{8\pi^{3/2}}\left(\frac{\sigma_T^2}{4T_0^2} + \frac{\sigma_v^2 k^2 a^2}{4c_0^2}\left[1 - \frac{k_x^2}{k^2}\right]\right)\exp(-k^2a^2/4) \tag{I.51}$$

with $k^2 = k_x^2 + k_y^2 + k_z^2$.

For the von Kármán spectrum, the correlation function of refractive-index fluctuations is given by the expression

$$B(x, y, z) = \frac{\Gamma(1/3)(K_0 r)^{1/3}}{\pi 2^{2/3} K_0^{2/3}\sqrt{3}}\left(K_{1/3}(K_0 r)\frac{C_T^2}{4T_0^2} + \left[K_{1/3}(K_0 r) - \frac{K_0\rho^2}{2r}K_{2/3}(K_0 r)\right]\frac{C_v^2}{c_0^2}\right), \tag{I.52}$$

where $K_0 = 2\pi/L$ is related to the size L of the largest eddies, C_T^2 and C_v^2 are the structure parameters of the temperature and wind velocity fluctuations, respectively, and the distances r and ρ are given by $r^2 = x^2 + y^2 + z^2$ and $\rho^2 = y^2 + z^2$. The two-dimensional spectral densities $F(k_x, k_z)$ and $F(k_y, k_z)$ for the von Kármán spectrum are given by

$$F(k_x, k_z) = \frac{A}{(k^2 + K_0^2)^{8/6}}\left(\frac{\Gamma(\frac{1}{2})\Gamma(\frac{8}{6})}{\Gamma(\frac{11}{6})}\frac{C_T^2}{4T_0^2} + \left[\frac{\Gamma(\frac{3}{2})\Gamma(\frac{8}{6})}{\Gamma(\frac{17}{6})} + \frac{k_z^2}{k^2 + K_0^2}\frac{\Gamma(\frac{1}{2})\Gamma(\frac{14}{6})}{\Gamma(\frac{17}{6})}\right]\frac{22C_v^2}{12c_0^2}\right) \tag{I.53}$$

with $k^2 = k_x^2 + k_z^2$, and

$$F(k_y, k_z) = \frac{A}{(k^2 + K_0^2)^{8/6}}\left(\frac{\Gamma(\frac{1}{2})\Gamma(\frac{8}{6})}{\Gamma(\frac{11}{6})}\frac{C_T^2}{4T_0^2} + \left[\frac{\Gamma(\frac{3}{2})\Gamma(\frac{8}{6})}{\Gamma(\frac{17}{6})} + \frac{k^2}{k^2 + K_0^2}\frac{\Gamma(\frac{1}{2})\Gamma(\frac{14}{6})}{\Gamma(\frac{17}{6})}\right]\frac{22C_v^2}{12c_0^2}\right) \tag{I.54}$$

with $k^2 = k_y^2 + k_z^2$. Here we have introduced the constant $A = 5/[18\pi\Gamma(1/3)] \approx 0.0330$. The three-dimensional spectral density for the von Kármán spectrum is given by

$$\Phi(k_x, k_y, k_z) = \frac{A}{(k^2 + K_0^2)^{11/6}}\left(\frac{C_T^2}{4T_0^2} + \frac{k^2}{k^2 + K_0^2}\left[1 - \frac{k_x^2}{k^2}\right]\frac{22C_v^2}{12c_0^2}\right) \tag{I.55}$$

with $k^2 = k_x^2 + k_y^2 + k_z^2$. These expressions agree with the expressions given in Sec. I.7.1 for an atmosphere with only temperature fluctuations if we set $\mu_0^2 = \Gamma^2(1/3)\,(\pi 2^{4/3} K_0^{2/3}\sqrt{3})^{-1}\, C_T^2/(4T_0^2)$, $C_v = 0$, and $K_0 = 1/a$.

For the parameters a and $\mu_0^2 \equiv \sigma_T^2/(4T_0^2)$ of the Gaussian spectrum the following empirical values are used in the acoustic literature: a value of about 1 m for a and values ranging from about 10^{-6} to 10^{-5} for μ_0^2. Wilson [159] indicated that these values are not well justified from a meteorological point of view. The values give a reasonable 'fit', however, of the Gaussian spectrum to the 'actual' spectrum in a limited wave number range, which may be just the range that is most relevant for an acoustic experiment. Actual turbulent length scales are often larger than 1 m and values of μ_0^2 are often larger than 10^{-5}.

The von Kármán spectrum gives a better fit to the actual spectrum, over a broader wave number range. In Ref. [98] the following ranges of values are given for the normalized structure parameters C_T^2/T_0^2 and C_v^2/c_0^2 near the ground on a summer day:

$$\begin{aligned} 2\times 10^{-10}\ \mathrm{m}^{-2/3} &\le C_T^2/T_0^2 \le 6\times 10^{-7}\ \mathrm{m}^{-2/3} \\ 1\times 10^{-9}\ \mathrm{m}^{-2/3} &\le C_v^2/c_0^2 \le 2\times 10^{-6}\ \mathrm{m}^{-2/3}. \end{aligned} \tag{I.56}$$

If we use the von Kármán correlation function (I.52) with $C_T^2/T_0^2 = 6\times10^{-7}\ \mathrm{m}^{-2/3}$ and $C_v^2/c_0^2 = 2\times10^{-6}\ \mathrm{m}^{-2/3}$, we find $B(0) = 1.1\times10^{-6}$, 5.2×10^{-6}, and 24×10^{-6} for $K_0^{-1} = 1$, 10, and 100 m, respectively. Figure I.3 shows the von Kármán spectral density $\Phi(0, k_y, k_z)$ for $C_T^2/T_0^2 = 6\times10^{-7}\ \mathrm{m}^{-2/3}$, $C_v^2/c_0^2 = 2\times10^{-6}\ \mathrm{m}^{-2/3}$, and $K_0^{-1} = 10$ m. Also shown is the Gaussian spectral density for $a = 1$ m, $\mu_0^2 = 10^{-5}$, and $\sigma_v^2 = 0$. The Gaussian spectrum agrees with the von Kármán spectrum only in a narrow wave number region.

I.8 Limitations of the statistical description of turbulence

The turbulent atmosphere was described in Secs. I.1 and I.3 as a 'mixture' of eddies, with a wide range of length scales (*cf.* Ref. [95]). The size of the largest eddies is of the order of the height above the ground. The size of the smallest eddies is of the order of 1 mm. The sizes of the largest and smallest eddies are called the outer and inner scale of turbulence, respectively.

Based on the picture of the cascade process, Kolmogorov derived the 'two-thirds law' for the velocity structure function (see Sec. I.5). This law is valid for eddy sizes between the inner and outer scale of turbulence, which will be denoted here as L_{in} and L_{out}, respectively. The corresponding Kolmogorov spectral density is valid only in the wave number range $L_{\mathrm{out}}^{-1} < k < L_{\mathrm{in}}^{-1}$. This range is called the inertial subrange. The range $k < L_{\mathrm{out}}^{-1}$ is called the energy-containing subrange, and the range $k > L_{\mathrm{in}}^{-1}$ is called the dissipation subrange. The three subranges are indicated in Fig. I.3.

The von Kármán spectrum is related to the Kolmogorov spectrum. In the inertial subrange, the von Kármán spectral density satisfies $\Phi \sim k^{-11/3}$ and

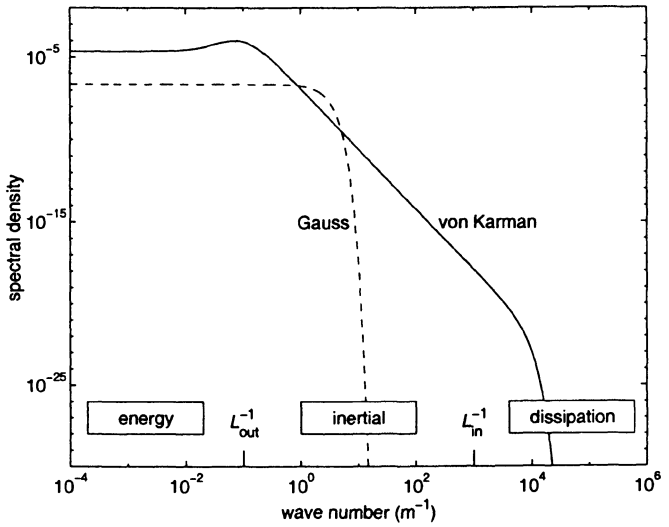

Figure I.3. Example of a Gaussian spectrum and a von Kármán spectrum. The graph shows the spectral density $\Phi(k_x, k_y, k_z)$ for $k_x = 0$. The wave number along the horizontal axis is $k = \sqrt{k_y^2 + k_z^2}$. The Gaussian spectrum is given by Eq. (I.51) or (I.32), with parameters $a = 1$ m, $\sigma_T^2/(4T_0^2) \equiv \mu_0^2 = 10^{-5}$, and $\sigma_v^2 = 0$. The von Kármán spectrum is given by Eq. (I.55), including an exponential cut-off factor $\exp(-k^2/k_{\text{max}}^2)$, with parameters $K_0^{-1} = 10$ m, $C_T^2/T_0^2 = 6\times10^{-7}$ m$^{-2/3}$, $C_v^2/c_0^2 = 2\times10^{-6}$ m$^{-2/3}$, and $k_{\text{max}} = 5.48/l_0$ with $l_0 = 0.001$ m. Also shown are the three spectral subranges: the energy-containing subrange ($k < L_{\text{out}}^{-1}$), the inertial subrange ($L_{\text{out}}^{-1} < k < L_{\text{in}}^{-1}$), and the dissipation subrange ($k > L_{\text{in}}^{-1}$), where $L_{\text{out}} \sim K_0^{-1}$ is the outer scale of turbulence and $L_{\text{in}} \sim l_0$ is the inner scale of turbulence.

agrees with the Kolmogorov spectral density. In the energy-containing subrange, the von Kármán spectral density levels off (see Fig. I.3). This represents the fact that the occurrence of eddies larger than the outer scale L_{out} is limited by the boundary conditions of the flow. While the form of the von Kármán functions for $F(\mathbf{k})$ and $\Phi(\mathbf{k})$ in the inertial subrange is justified by the Kolmogorov model of turbulence, the form of the von Kármán functions for $F(\mathbf{k})$ and $\Phi(\mathbf{k})$ in the energy-containing subrange is more uncertain. This is related to the variation of the value of the outer scale L_{out} with atmospheric conditions, height above the ground, terrain topology, and other factors [159].

The influence of atmospheric turbulence on sound propagation is dominated by eddies with sizes of the order of the wavelength of the sound waves. Depending on the geometry and the atmospheric conditions, this size is in the energy-containing subrange or in the inertial subrange. Eddies in the dissipa-

tion subrange are very small compared with acoustic wavelengths.

As noted before, with proper values of the parameters, the Gaussian spectrum may agree with the actual spectrum in the relevant wave number range. With the von Kármán spectrum, however, agreement can be expected over a broader range, although the choice of the numerical parameters of the spectrum is difficult.

Moreover, the Gaussian and von Kármán spectra are valid only if the turbulence is homogeneous and isotropic. This condition is usually not met. Turbulence is inhomogeneous for example because the outer scale of turbulence increases with height above the ground. Turbulence is anisotropic for example because the correlation length parallel to the wind vector is larger than the correlation length perpendicular to the wind vector.

Appendix J

Atmospheric turbulence in the PE method

J.1 Introduction

In Appendix I, atmospheric turbulence was represented by a random field of refractive-index fluctuations. Refractive-index fluctuations correspond to fluctuations of the (effective) sound speed. Sound propagation in a turbulent atmosphere can be computed by using a sound speed profile $c(z)$ that includes these fluctuations. The fluctuations induce a range-dependence of the sound speed profile. The CNPE and GFPE methods can be used for an atmosphere with a range-dependent sound speed profile (see Appendices G and H).

In this appendix we describe the incorporation of atmospheric turbulence in the CNPE and GFPE methods [57, 43, 25]. We also describe the calculation of the random fields of refractive-index fluctuations, which are used in the CNPE and GFPE methods. Two-dimensional fields of refractive-index fluctuations are used in the two-dimensional CNPE and GFPE methods; three-dimensional fields are used in the three-dimensional GFPE method (see Sec. H.12). The fields can be considered as 'frozen' realizations of the turbulent atmosphere. The realizations are calculated with the aid of a random number generator.

PE computations for different random realizations yield different sound pressure fields. We are interested in a sound pressure field averaged (logarithmically) over turbulent fluctuations in a short period, for example a period of ten minutes. We assume that this average field can be approximated by a (logarithmic) average of a set of sound pressure fields computed for a set of random realizations. In other words, averaging over time is replaced by ensemble averaging over random realizations of the turbulent atmosphere.

In principle, the refractive-index fluctuations can be included directly in the sound speed profile used in the PE method. This is not very efficient, however, as the modification of the profile between successive range steps is time-consuming.

A more efficient method is described in Sec. J.2. The calculation of the random fields of refractive-index fluctuations is described in Sec. J.3

Sections J.2 and J.3 apply to the two-dimensional PE methods. Section J.4 describes the incorporation of atmospheric turbulence in the three-dimensional GFPE method.

The axisymmetric approximation used in the two-dimensional PE methods has a spurious effect on computed sound pressure fields. This effect will be described in Appendix K (Section K.4).

J.2 Turbulent phase factor in the PE method

In the two-dimensional PE methods, the sound field is represented by the complex pressure amplitude $p(r,z)$ in the rz plane through the source and the receiver (see Appendices G and H). The computation of the field is based on the following one-way wave equation for the quantity $q(r,z) = p(r,z)\sqrt{r}$:

$$\partial_r q(r,z) - iH_1(z)q(r,z) = 0, \tag{J.1}$$

where

$$H_1(z) = \sqrt{k^2(z) + \partial_z^2} \tag{J.2}$$

is the square-root operator. The formal solution of Eq. (J.1) is

$$q(r + \Delta r, z) = \exp(iH_1 \Delta r) q(r,z). \tag{J.3}$$

The corresponding expression for the quantity $\psi(r,z) = q(r,z)\exp(-ik_a r)$ is

$$\psi(r + \Delta r, z) = \exp(iH_1 \Delta r - ik_a \Delta r)\psi(r,z), \tag{J.4}$$

where k_a is some average wave number (see Sec. G.3).

The acoustic refractive index n is defined as $n = c_0/c$, where c is the effective sound speed ($c \equiv c_{\text{eff}}$) and c_0 is some average sound speed (see Sec. I.2). In a turbulent atmosphere, the refractive index fluctuates at each point around an average value, which is of the order of unity. The average value is denoted as $\overline{n}$ and the fluctuation is denoted as μ. Thus, we have

$$n = \overline{n} + \mu, \tag{J.5}$$

with $\mu \ll \overline{n}$ and $\overline{\mu} = 0$. From the relation $n \approx k/k_a$ we find

$$k = \overline{k} + k_a \mu \tag{J.6}$$

with $\overline{k} = k_a \overline{n}$. In the PE method we assume that $\overline{n}$ and $\overline{k}$ are functions of the height z only (within a range step). Substitution of Eq. (J.6) into Eq. (J.2) gives

$$H_1 \approx \sqrt{\overline{k}^2 + 2\overline{k}k_a\mu + \partial_z^2}, \tag{J.7}$$

where we have neglected a term of the order of μ^2. A first-order expansion of the square-root function gives

$$H_1 \approx \overline{H_1} + k_a \mu \tag{J.8}$$

with

$$\overline{H_1} = \sqrt{\overline{k}^2 + \partial_z^2}. \tag{J.9}$$

In Eq. (J.8) we have used $\overline{H_1} \approx k_a$. Substitution of Eq. (J.8) into Eq. (J.4) gives

$$\psi(r + \Delta r, z) = \exp(i\overline{H_1}\Delta r - ik_a\Delta r)\exp(ik_a\mu\Delta r)\psi(r, z). \tag{J.10}$$

The first exponential factor on the right-hand side represents the solution for a non-turbulent atmosphere. The second exponential factor represents the effect of atmospheric turbulence. As μ is real, the second factor is a phase factor.

Hence, turbulence is taken into account by multiplication of the field by a z-dependent phase factor after each PE range step. This is computationally more efficient than changing the sound speed profile after each PE step.

A slightly more accurate approach is to split the turbulent phase factor into two factors [45, 57]:

$$\psi(r + \Delta r, z) = \exp(\tfrac{1}{2}ik_a\mu\Delta r)\exp(i\overline{H_1}\Delta r - ik_a\Delta r)\exp(\tfrac{1}{2}ik_a\mu\Delta r)\psi(r, z). \tag{J.11}$$

Thus, half of the turbulent phase shift is applied before the 'non-turbulent PE step' and the other half is applied after the step. In a sequence of PE steps, a step from range r to range $r + \Delta r$ ends with multiplication by the turbulent phase factor $\exp[\frac{1}{2}ik_a\mu(r, z)\Delta r]$, and the next step from range $r + \Delta r$ to range $r + 2\Delta r$ begins with multiplication by the factor $\exp[\frac{1}{2}ik_a\mu(r + \Delta r, z)\Delta r]$. This is equivalent to multiplication by a single factor

$$\exp(ik_a\mu_2\Delta r) \tag{J.12}$$

between the two successive PE steps, where μ_2 is given by

$$\mu_2 = \frac{1}{2}\left[\mu(r, z) + \mu(r + \Delta r, z)\right]. \tag{J.13}$$

In the CNPE method, the range step Δr is usually small compared with the turbulent correlation length, so turbulent fluctuations are accurately sampled. In the GFPE method, however, the range step Δr can be chosen considerably larger than the correlation length. In this case the following phase factor gives more accurate results than the phase factor (J.12) does:

$$\exp(i\Theta), \tag{J.14}$$

where

$$\Theta = k_a \int_r^{r+\Delta r} \mu(r,z)\, dr \tag{J.15}$$

is the turbulent phase fluctuation integrated over a range step. The use of Eq. (J.14) is called the 'phase screen' method [88]. We note that the phase factor (J.14) reduces to the phase factor (J.12) if the integral in Eq. (J.15) is approximated by $\mu_2\, \Delta r$.

J.3 Random realizations of the field of refractive-index fluctuations

The expressions derived in the previous section for the turbulent phase factor contain the field of refractive-index fluctuations $\mu(r,z)$ in the rz plane. In this section we show that realizations of the random field $\mu(r,z)$ can be calculated with a random number generator, in such a way that the field has the correct value of the correlation function $B(\mathbf{s}) \equiv \overline{\mu(\mathbf{r}+\mathbf{s})\mu(\mathbf{r})}$ [25, 72]. We assume that the random field $\mu(r,z)$ is homogeneous (see Sec. I.4).

We have from Eq. (I.23)

$$B(\mathbf{s}) = \int_{-\infty}^{\infty}\int \cos(\mathbf{k}\cdot\mathbf{s}) F(\mathbf{k})\, d\mathbf{k}, \tag{J.16}$$

where $F(\mathbf{k})$ is the two-dimensional spectral density of the refractive-index fluctuations in the rz plane; with the notation used in Sec. I.7.2 we have $F(\mathbf{k}) = F(k_x, k_z)$ (the horizontal r coordinate used here corresponds to the horizontal x coordinate used in Sec. I.7.2). We have replaced the exponential function in Eq. (I.23) by a cosine function, as $F(\mathbf{k})$ is an even function of the components of the vector $\mathbf{k}$ (see Sec. I.7). We introduce polar $k\theta$ coordinates for the vector $\mathbf{k}$, so Eq. (J.16) can be written as

$$B(\mathbf{s}) = \int_0^{2\pi}\int_0^{\infty} \cos(\mathbf{k}\cdot\mathbf{s}) F(\mathbf{k})\, k\, dk\, d\theta \tag{J.17}$$

with $\mathbf{k} = (k\cos\theta, k\sin\theta)$. The integration over the angle θ can be replaced by 2π times the average over θ:

$$B(\mathbf{s}) = 2\pi < \int_0^{\infty} \cos(\mathbf{k}\cdot\mathbf{s}) F(\mathbf{k})\, k\, dk\ >_\theta, \tag{J.18}$$

where the brackets $< . >_\theta$ denote the average over the angle θ. The integral is approximated by a finite sum:

$$B(\mathbf{s}) = 2\pi < \Delta k \sum_n \cos(\mathbf{k}_n \cdot \mathbf{s}) F(\mathbf{k}_n)\, k_n >_\theta, \tag{J.19}$$

with discrete wave number vectors $\mathbf{k}_n$. We will show below that random realizations of the corresponding random field $\mu(\mathbf{r})$ can be calculated with the following expression:

$$\mu(\mathbf{r}) = \sqrt{4\pi\Delta k} \sum_n \cos(\mathbf{k}_n \cdot \mathbf{r} + \alpha_n) \sqrt{F(\mathbf{k}_n) k_n}, \tag{J.20}$$

with $\mathbf{k}_n = (k_n \cos\theta_n, k_n \sin\theta_n)$ and $k_n = n\,\Delta k$ for $n = 1, 2, \ldots, N$; here θ_n and α_n are random angles between 0 and 2π. Thus, the field $\mu(\mathbf{r})$ is calculated by superposition of N harmonic functions, or 'modes', with regularly spaced wave numbers k_n, random polar angles θ_n, and random phase angles α_n.

We will now prove that the field given by Eq. (J.20) corresponds to the correlation function (J.19). From the definition of the correlation function we have

$$B(\mathbf{s}) = < \mu(\mathbf{r} + \mathbf{s}) \mu(\mathbf{r}) >_{\theta,\alpha}, \tag{J.21}$$

where the brackets $< . >_{\theta,\alpha}$ denote an average over the random angles θ and α, *i.e.* an average over random realizations of the field $\mu(\mathbf{r})$. Substitution of Eq. (J.20) into Eq. (J.21) gives

$$B(\mathbf{s}) = 4\pi\Delta k < \sum_n \cos(\mathbf{k}_n \cdot \mathbf{r} + \alpha_n + \mathbf{k}_n \cdot \mathbf{s}) \sqrt{F(\mathbf{k}_n) k_n} \times \sum_m \cos(\mathbf{k}_m \cdot \mathbf{r} + \alpha_m) \sqrt{F(\mathbf{k}_m) k_m} >_{\theta,\alpha} . \tag{J.22}$$

The average of a term

$$\cos(\mathbf{k}_n \cdot \mathbf{r} + \alpha_n + \mathbf{k}_n \cdot \mathbf{s}) \sqrt{F(\mathbf{k}_n) k_n} \cos(\mathbf{k}_m \cdot \mathbf{r} + \alpha_m) \sqrt{F(\mathbf{k}_m) k_m}$$

vanishes unless we have $n = m$. The average of a term with $n = m$ can be written as follows:

$$\begin{aligned} < \cos(\mathbf{k}_n \cdot \mathbf{r} + \alpha_n + \mathbf{k}_n \cdot \mathbf{s}) \cos(\mathbf{k}_n \cdot \mathbf{r} + \alpha_n) F(\mathbf{k}_n) k_n >_{\theta,\alpha} = \\ < \cos^2(\mathbf{k}_n \cdot \mathbf{r} + \alpha_n) \cos(\mathbf{k}_n \cdot \mathbf{s}) F(\mathbf{k}_n) k_n \\ - \sin(\mathbf{k}_n \cdot \mathbf{r} + \alpha_n) \cos(\mathbf{k}_n \cdot \mathbf{r} + \alpha_n) \sin(\mathbf{k}_n \cdot \mathbf{s}) F(\mathbf{k}_n) k_n >_{\theta,\alpha} \\ = \frac{1}{2} < \cos(\mathbf{k}_n \cdot \mathbf{s}) F(\mathbf{k}_n) k_n >_\theta, \end{aligned} \tag{J.23}$$

where we have used the goniometrical relations $\cos^2 x = \frac{1}{2} + \frac{1}{2}\cos 2x$ and $\sin x \cos x = \frac{1}{2}\sin 2x$. Substitution of Eq. (J.23) into Eq. (J.22) gives Eq. (J.19), which completes the proof.

J.3.1 Refractive-index fluctuations in the CNPE method

In the CNPE method we use a rectangular grid in the rz plane through the source and the receiver. Turbulence is incorporated by multiplication of the field $\psi(r, z_j)$ at the grid points (r, z_j) by the phase factor given by Eq. (J.12), after each range step. This requires the evaluation of the refractive-index fluctuations $\mu(r, z_j)$ at the grid points. From Eq. (J.20) we have

$$\mu(r, z_j) = \sum_n G(\mathbf{k}_n) \cos(r\, k_{nr} + z_j\, k_{nz} + \alpha_n) \tag{J.24}$$

with $G(\mathbf{k}_n) = \sqrt{4\pi\Delta k\, F(\mathbf{k}_n) k_n}$, $k_{nr} = k_n \cos\theta_n$, and $k_{nz} = k_n \sin\theta_n$. As the calculation of the cosine function for all grid points is time-consuming, we write

$$\cos(r\, k_{nr} + z_j\, k_{nz} + \alpha_n) = \mathrm{Re}\left\{\exp(ik_{nr}r + i\alpha_n)[\exp(ik_{nz}\Delta z)]^j\right\}, \tag{J.25}$$

where we have used $z_j = j\Delta z$. The two exponential factors on the right-hand side are independent of z_j, so the cosine factors for fixed r and n can be calculated efficiently for all z_j by repeated multiplication by the constant factor $\exp(ik_{nz}\Delta z)$.

J.3.2 Refractive-index fluctuations in the GFPE method

In the two-dimensional GFPE method we also use a rectangular grid in the rz plane, but the horizontal grid spacing can be considerably larger than in the CNPE method. Therefore we use the turbulent phase factor (J.14) in the GFPE method, instead of the phase factor (J.12) used in the CNPE method.

The refractive-index fluctuations $\mu(r, z_j)$ at the grid points are given by Eq. (J.24). Substitution into Eq. (J.15) gives

$$\Theta = \Upsilon(r + \Delta r, z_j) - \Upsilon(r, z_j), \tag{J.26}$$

with

$$\Upsilon(r, z_j) = k_a \sum_n \frac{G(\mathbf{k}_n)}{k_{nr}} \sin(r\, k_{nr} + z_j\, k_{nz} + \alpha_n). \tag{J.27}$$

For an efficient calculation of the sine factors in this expression, an approach analogous to the approach described in Sec. J.3.1 can be used.

J.3.3 Numerical parameters

Figure J.1 shows an example of the variation of the refractive-index fluctuation $\mu(r, z)$ along a horizontal line in the r direction, calculated with Eq. (J.24) for a Gaussian spectrum and for a von Kármán spectrum. The corresponding function $G(\mathbf{k})$ in Eq. (J.24) is also shown in the figure (for $k_x = 0$); this function can be considered as a 'mode amplitude'. For the Gaussian spectrum, the

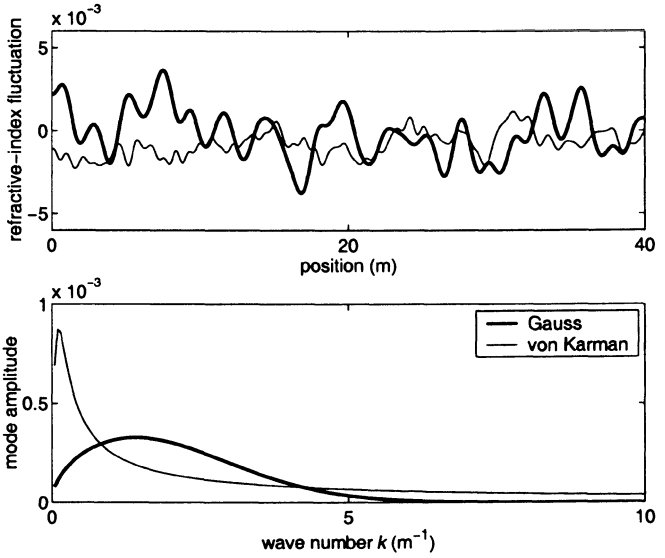

Figure J.1. Example of the variation of the refractive-index fluctuation $\mu(r, z)$ along a horizontal line in the r direction (top) and the corresponding 'mode amplitude' $G(\mathbf{k})$ in Eq. (J.24) for $k_x = 0$ (bottom), for a Gaussian spectrum and for a von Kármán spectrum. The Gaussian spectral density $F(\mathbf{k})$ is given by Eq. (I.49), with parameters $a = 1$ m, $\sigma_T^2/T_0^2 = 10^{-5}$, and $\sigma_v^2 = 0$. The von Kármán spectral density $F(\mathbf{k})$ is given by Eq. (I.53), with parameters $K_0^{-1} = 10$ m, $C_T^2/T_0^2 = 1\times10^{-7}$ m$^{-2/3}$, and $C_v^2/c_0^2 = 1\times10^{-6}$ m$^{-2/3}$. For both spectra we used $N = 200$ and $k_{n,\max} = 10$ m^{-1}.

function $G(\mathbf{k})$ is negligible for wave numbers $k > 7$ m^{-1}, in this example. For the von Kármán spectrum, however, the function $G(\mathbf{k})$ still has a finite value at $k = 10$ m^{-1}. The representation of the von Kármán spectrum up to wave numbers where the function $G(\mathbf{k})$ is negligible requires a large number (N) of 'modes', as the wave number spacing Δk should be chosen sufficiently small to properly sample the range of small wave numbers. This problem can be solved by using a variable wave number spacing Δk_n, instead of the constant wave number spacing Δk used in Eq. (J.19). For the examples in this book, however, we used a constant wave number spacing Δk, with a value of 10 m^{-1} for the maximum wave number $k_{n,\max}$ and a value of 100 for the number of modes N (except for Fig. J.1, where we used $N = 200$). Modes with wave numbers larger than 10 m^{-1} represent relatively small fluctuations of the refractive index, so the cut-off of the spectrum at $k_{n,\max} = 10$ m^{-1} is a reasonable approximation.

J.4 Turbulence in the three-dimensional GFPE method

In this section we describe the incorporation of atmospheric turbulence in the three-dimensional GFPE method, which was described in Sec. H.12.

In Sec. J.2 we derived the turbulent phase factor for the two-dimensional PE methods. It is straightforward to generalize the derivation for the three-dimensional GFPE method. The square-root operator given by Eq. (J.2) becomes $H_1 = \sqrt{k^2(z) + r^{-2}\partial_\phi^2 + \partial_z^2}$. The resulting turbulent phase factor for the three-dimensional GFPE method is given by Eq. (J.14) with

$$\Theta = k_a \int_r^{r+\Delta r} \mu(r, \phi, z)\, dr. \tag{J.28}$$

The only difference from Eq. (J.15) is that μ is a function of the azimuthal angle ϕ in this case.

In Sec. J.3 we described the calculation of random realizations of two-dimensional fields of refractive-index fluctuations. The calculation is modified as follows for three-dimensional fields. We have from Eq. (I.19)

$$B(\mathbf{s}) = \iiint_{-\infty}^{\infty} \cos(\mathbf{k} \cdot \mathbf{s}) \Phi(\mathbf{k})\, d\mathbf{k}, \tag{J.29}$$

where $\Phi(\mathbf{k})$ is the three-dimensional spectral density of refractive-index fluctuations. We introduce spherical $k\theta\varphi$ coordinates for the vector $\mathbf{k}$, so Eq. (J.29) can be written as

$$B(\mathbf{s}) = \int_0^{2\pi} \int_0^{\pi} \int_0^{\infty} \cos(\mathbf{k} \cdot \mathbf{s}) \Phi(\mathbf{k})\, k^2\, dk\, \sin\theta d\theta\, d\varphi. \tag{J.30}$$

The integration over the angles θ and φ can be replaced by 4π times the angular average:

$$B(\mathbf{s}) = 4\pi < \int_0^{\infty} \cos(\mathbf{k} \cdot \mathbf{s}) \Phi(\mathbf{k})\, k^2\, dk\ >_{\theta,\varphi} . \tag{J.31}$$

The integral is approximated by a finite sum:

$$B(\mathbf{s}) = 4\pi < \Delta k \sum_n \cos(\mathbf{k}_n \cdot \mathbf{s}) \Phi(\mathbf{k}_n)\, k_n^2 >_{\theta,\varphi}, \tag{J.32}$$

with discrete wave number vectors $\mathbf{k}_n$. Random realizations of the corresponding random field $\mu(\mathbf{r})$ can be calculated with the following expression:

$$\mu(\mathbf{r}) = \sqrt{8\pi\Delta k} \sum_n \cos(\mathbf{k}_n \cdot \mathbf{r} + \alpha_n) \sqrt{\Phi(\mathbf{k}_n) k_n^2}, \tag{J.33}$$

with $\mathbf{k}_n = (k_n \cos\varphi_n \sin\theta_n, k_n \sin\varphi_n \sin\theta_n, k_n \cos\theta_n)$ and $k_n = n\,\Delta k$ for $n = 1, 2, \ldots, N$; here φ_n and α_n are random angles between 0 and 2π, and θ_n is a random angle chosen in such a way that values of $\cos\theta_n$ are distributed uniformly over the interval between 1 and -1 [as we have $\sin\theta\, d\theta = d\cos\theta$ in Eq. (J.30)]. The proof that $\mu(\mathbf{r})$ given by Eq. (J.33) corresponds to the correlation function $B(\mathbf{s})$ given by Eq. (J.32) is analogous to the proof given in Sec. J.3 for two-dimensional fields $\mu(\mathbf{r})$.

In the three-dimensional GFPE method we use a cylindrical grid in the pie slice region shown in Fig. H.6. The refractive-index fluctuations $\mu(r, \phi_k, z_j)$ at the grid points follow from Eq. (J.33):

$$\mu(r, \phi_k, z_j) = \sum_n G(\mathbf{k}_n) \cos(r \cos\phi_k\, k_{nx} + r \sin\phi_k\, k_{ny} + z_j\, k_{nz} + \alpha_n), \quad \text{(J.34)}$$

with $G(\mathbf{k}_n) = \sqrt{8\pi\Delta k\, \Phi(\mathbf{k}_n) k_n^2}$, $k_{nx} = k_n \cos\varphi_n \sin\theta_n$, $k_{ny} = k_n \sin\varphi_n \sin\theta_n$, and $k_{nz} = k_n \cos\theta_n$. Substitution of Eq. (J.34) into Eq. (J.28) gives

$$\Theta = \Upsilon(r + \Delta r, \phi_k, z_j) - \Upsilon(r, \phi_k, z_j), \quad \text{(J.35)}$$

with

$$\Upsilon(r, \phi_k, z_j) = k_a \sum_n \frac{G(\mathbf{k}_n) \sin(r \cos\phi_k\, k_{nx} + r \sin\phi_k\, k_{ny} + z_j\, k_{nz} + \alpha_n)}{\cos\phi_k\, k_{nx} + \sin\phi_k\, k_{ny}}. \quad \text{(J.36)}$$

Appendix K

Analytical model for a non-refracting turbulent atmosphere

K.1 Introduction

Sound propagation in a turbulent atmosphere can be computed numerically with the PE method, as described in Appendix J. If the (average) atmosphere is non-refracting, *i.e.* if we have $\overline{n} = 1$ in Eq. (I.1), sound propagation can also be computed analytically. In this appendix we present an analytical model for sound propagation in a non-refracting turbulent atmosphere above a ground surface. The model is based on work of Daigle *et al.* [33, 35], Clifford and Lataitis [27], Ostashev *et al.* [100], and Salomons *et al.* [139].

Daigle *et al.* [33, 35] developed a model that can be considered as a heuristic extension of analytical solutions for an unbounded non-refracting turbulent atmosphere [150, 68, 98]. Clifford and Lataitis [27] developed a more rigorous analytical model, which was improved by Ostashev *et al.* [100] and Salomons *et al.* [139].

The model presented in this appendix can be used to study the effects of turbulence on sound propagation over relatively short distances (for large distances the effects of refraction can usually not be neglected). The model can also be used to study the accuracy of numerical computations performed with the PE method, by comparison of analytical results with PE results for a non-refracting turbulent atmosphere. An example of such a comparison is presented in Chap. 5.

In Sec. K.2 we describe the model. In Sec. K.3 we describe the application of the model for Gaussian and von Kármán spectra of turbulence. In Sec K.4 we describe the spurious effect of the axisymmetric approximation, which is used in the two-dimensional PE methods. This effect should be taken into account

in comparisons of analytical results with PE results.

K.2 Model

We consider a harmonic monopole source and a receiver in a non-refracting turbulent atmosphere above a ground surface. For a non-refracting turbulent atmosphere, the fluctuating refractive index n can be written as $n = 1 + \mu$, with $\overline{\mu} = 0$ (see Sec. I.2). We use an rz coordinate system in the vertical plane through the source and the receiver; r is the horizontal range measured from the source and z is the height above the ground surface. The source is at position $(0,z_s)$ and the receiver is at position (L,z). We assume $L \gg z_s$ and $L \gg z$.

The (fluctuating) complex pressure amplitude p_c at the receiver is written as the sum of the contribution p_1 of the direct field and the contribution Qp_2 of the field reflected by the ground surface:

$$p_c = p_1 + Qp_2, \tag{K.1}$$

where Q is the spherical-wave reflection coefficient (see Sec. D.4) and p_1 and p_2 are given by

$$p_j = S\frac{\exp(ikR_j + \psi_j)}{R_j}) \quad \text{for } j = 1,2, \tag{K.2}$$

where $R_1 = \sqrt{L^2 + (z_s - z)^2}$ and $R_2 = \sqrt{L^2 + (z_s + z)^2}$ are the direct and reflected path lengths, respectively, S is a constant, $k = \omega/c$ is the wave number, and the quantity ψ_j is called the complex phase fluctuation. The effect of turbulence is represented by the factor $\exp(\psi_j)$. For a non-turbulent atmosphere we have $\psi_j = 0$, so Eq. (K.1) reduces to Eq. (3.2). From Eq. (K.2) we have

$$\psi_j = \ln(p_j/p_{j,0}), \tag{K.3}$$

where $p_{j,0}$ is the value of p_j in a non-turbulent atmosphere. We write

$$\psi_j = \chi_j + iS_j, \tag{K.4}$$

where χ_j is called the log-amplitude fluctuation and S_j is called the phase fluctuation.

The sound pressure as a function of time is given by $p(t) = \mathrm{Re}(p_c e^{-i\omega t})$. The variation of the sound pressure with time consists of two contributions: harmonic oscillations with period $\tau_\omega = 2\pi/\omega$ and turbulent fluctuations with a characteristic period τ_t. We assume that the (relevant) turbulent fluctuations are slow compared with the harmonic variations of the sound pressure, so we have $\tau_\omega \ll \tau_t$ [27].

The (fluctuating) short-time average of the squared sound pressure, denoted as $(p^2)_{av}$, is defined as an average over a time τ_1, with $\tau_\omega \ll \tau_1 \ll \tau_t$. From Sec. B.3 we have the relation $(p^2)_{av} = \frac{1}{2}p_c p_c^*$. The corresponding (fluctuating)

relative sound pressure level is $\Delta L = 10\lg[(p^2)_{\rm av}/(p^2_{1,0})_{\rm av}]$, where $(p^2_{1,0})_{\rm av}$ is given by $\frac{1}{2}S^2/R_1^2$. The long-time average of the squared sound pressure, denoted as $\overline{(p^2)_{\rm av}} = \frac{1}{2}\overline{p_{\rm c}p_{\rm c}^*}$, is defined as an average over a time τ_2, with $\tau_2 \gg \tau_{\rm t}$. The corresponding long-time average of the relative sound pressure level is $\overline{\Delta L} = 10\lg[\overline{(p^2)_{\rm av}}/(p^2_{1,0})_{\rm av}]$.

With the notation $Q = |Q|e^{i\vartheta}$ we find

$$\overline{\Delta L} = 10\lg\left\{\overline{\exp(2\chi_1)} + |Q|^2\frac{R_1^2}{R_2^2}\overline{\exp(2\chi_2)} + |Q|\frac{R_1}{R_2}\exp(i[kR_1 - kR_2 - \vartheta])\overline{\exp(\psi_1 + \psi_2^*)} + |Q|\frac{R_1}{R_2}\exp(-i[kR_1 - kR_2 - \vartheta])\overline{\exp(\psi_1^* + \psi_2)}\right\}. \quad \text{(K.5)}$$

Conservation of energy implies $\overline{(p_j^2)_{\rm av}} = (p^2_{j,0})_{\rm av}$, which gives $\overline{\exp(2\chi_j)} = 1$ for $j = 1, 2$ [27]. To evaluate the factors $\overline{\exp(\psi_1 + \psi_2^*)}$ and $\overline{\exp(\psi_1^* + \psi_2)}$ in Eq. (K.5) we use the fact that Gaussian distributions can be assumed for χ_j and S_j [68, 126]. For a fluctuating variable y with a Gaussian distribution we have the relation $\overline{\exp(y)} = \exp(\frac{1}{2}\sigma_y^2 + \overline{y})$, where $\sigma_y^2 = \overline{(y - \overline{y})^2}$ is the variance of y [150, 27]. Using $\overline{\exp(2\chi_j)} = 1$ we find $\overline{\chi_j} = -\sigma^2_{\chi_j}$. A more complex derivation yields $\overline{S_j} = -\overline{\chi_j S_j}$, where terms of the order of $\overline{\mu^4}$ and higher-order terms have been neglected [150, 100] (a term like $\overline{\chi_j}\,\overline{S_j} = \sigma^2_{\chi_j}\overline{\chi_j S_j}$ is of the order of $\overline{\mu^4}$, as the fluctuations χ_j and S_j are of the order of μ). Using the relation $\overline{\exp(y)} = \exp(\frac{1}{2}\sigma_y^2 + \overline{y})$ for $y = \psi_1 + \psi_2^*$ and $y = \psi_1^* + \psi_2$, and neglecting terms of the order of $\overline{\mu^4}$ and higher-order terms, we find

$$\overline{\Delta L} = 10\lg\left(1 + |Q|^2\frac{R_1^2}{R_2^2} + 2|Q|\frac{R_1}{R_2}\cos(kR_1 - kR_2 - \vartheta + \overline{\chi_2 S_1} - \overline{\chi_1 S_2})\,\Gamma\right), \quad \text{(K.6)}$$

where

$$\Gamma = \exp\left(\overline{\chi_1\chi_2} - \frac{1}{2}\overline{\chi_1^2} - \frac{1}{2}\overline{\chi_2^2} + \overline{S_1 S_2} - \frac{1}{2}\overline{S_1^2} - \frac{1}{2}\overline{S_2^2}\right) \quad \text{(K.7)}$$

is called the coherence factor. The terms $\overline{\chi_2 S_1}$ and $\overline{\chi_1 S_2}$ in Eq. (K.6) are small for weak fluctuations [27, 139], and will be neglected. The calculation of $\overline{\Delta L}$ has been reduced to the calculation of the correlation functions $\overline{\chi_j\chi_m}$ and $\overline{S_j S_m}$ $(j, m = 1, 2)$. In the remainder of this section we describe a model for the calculation of the correlation functions [33, 35, 81, 139].

The physical system with a single receiver above a ground surface is replaced by an unbounded system with two receivers (see Fig. K.1). The direct and reflected rays in the physical system are replaced by two direct rays to the receivers in the unbounded system. Consequently, we can apply the theory

of wave propagation in unbounded turbulent media [150, 68, 126, 98]. In this theory, the correlation functions $\overline{\chi_j \chi_m}$ and $\overline{S_j S_m}$ are usually denoted as $B_\chi(\rho)$ and $B_S(\rho)$, respectively, where ρ is the vertical separation between the two receivers in the unbounded system (see Fig. K.1). We have $\overline{\chi_1^2} \approx \overline{\chi_2^2} \approx B_\chi(0)$ and $\overline{S_1^2} \approx \overline{S_2^2} \approx B_S(0)$, using the assumption $L \gg z_s$ and $L \gg z$. Equation (K.7) becomes

$$\Gamma(\rho) = \exp[B_\chi(\rho) - B_\chi(0) + B_S(\rho) - B_S(0)]. \tag{K.8}$$

For the argument ρ we use the maximum vertical separation $2z_s z/(z_s + z)$ between the two sound rays in the physical system (see Fig. K.1). The *mean* vertical separation between the two rays is then equal to $z_s z/(z_s + z)$, both in the physical system and in the unbounded system. A more rigorous approach is presented in Refs. [100, 139], based on the work described in Ref. [27]. With this more rigorous approach it can be verified that the heuristic approach described here gives accurate results.

It should be noted that we replace the physical system by the unbounded system only for the approximation of the coherence factor Γ in Eq. (K.6) by the expression given in Eq. (K.8). For the other quantities in Eq. (K.6) we use the physical system.

The calculation of $\overline{\Delta L}$ has been reduced to the calculation of the correlation functions $B_\chi(\rho)$ and $B_S(\rho)$ for an unbounded turbulent atmosphere. General expressions for the correlation functions for homogeneous turbulence can be derived with Rytov's perturbation method, which is valid for weak fluctuations (see, for example, Chaps. 17 and 18 of Ref. [68]). With the notation $B_1(\mathbf{r}) \equiv B_\chi(\mathbf{r}) = \overline{\chi(\mathbf{R})\chi(\mathbf{R}+\mathbf{r})}$ and $B_2(\mathbf{r}) \equiv B_S(\mathbf{r}) = \overline{S(\mathbf{R})S(\mathbf{R}+\mathbf{r})}$, with $\mathbf{R} = (L, 0, 0)$ and $\mathbf{r} = (0, y, z)$, these expressions can be represented as follows ($m = 1, 2$):

$$B_m(\mathbf{r}) = 2\pi L \int_0^1 d\tau \int_{-\infty}^{\infty} \int_{-\infty}^{\infty} \exp(i\tau \mathbf{k} \cdot \mathbf{r})\, H_m^2(L\tau - L\tau^2, |\mathbf{k}|)\, \Phi(\mathbf{k})\, dk_y\, dk_z, \tag{K.9}$$

where we have $\mathbf{k} = (0, k_y, k_z)$, $|\mathbf{k}| = \sqrt{k_y^2 + k_z^2}$, $H_1(x, \kappa) = k \sin(\frac{1}{2} x \kappa^2/k)$, and $H_2(x, \kappa) = k \cos(\frac{1}{2} x \kappa^2/k)$ (with $k = \omega/c$), and $\Phi(\mathbf{k})$ is the three-dimensional spectral density of refractive-index fluctuations (see Sec. I.6). Equation (K.9) is valid for $L \gg |\mathbf{r}| = \sqrt{y^2 + z^2}$. The Gaussian and von Kármán spectral densities $\Phi(\mathbf{k})$ given in Sec. I.7 satisfy $\Phi(\mathbf{k}) = \Phi(|\mathbf{k}|)$ for $\mathbf{k} = (0, k_y, k_z)$, so Eq. (K.9) implies $B_m(\mathbf{r}) = B_m(|\mathbf{r}|)$. Therefore the correlation functions $B_\chi(\rho)$ and $B_S(\rho)$ in Eq. (K.8) follow from Eq. (K.9) with $\rho = |\mathbf{r}|$. In the next section we evaluate the coherence factor given by Eq. (K.8) for Gaussian and von Kármán spectra.

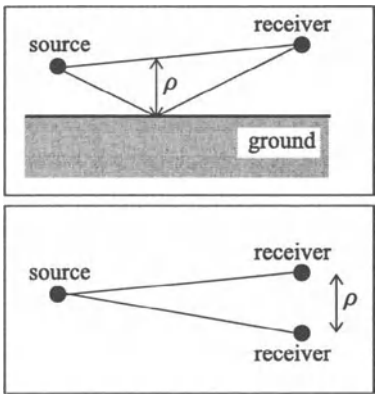

Figure K.1. For the calculation of the coherence factor Γ in Eq. (K.6) we replace the physical system (top) by an unbounded system with two receivers (bottom). The vertical separation ρ between the two receivers in the unbounded system is equal to the maximum vertical separation between the two sound rays in the physical system.

K.3 Coherence factor for Gaussian and von Kármán spectra

We first consider a turbulent atmosphere with the Gaussian spectral density given by Eq. (I.32): $\Phi(|\mathbf{k}|) = \mu_0^2 a^3 \exp(-|\mathbf{k}|^2 a^2/4)/(8\pi^{3/2})$, which is valid for an atmosphere with only temperature fluctuations. Substitution of this expression into Eq. (K.9) gives integral expressions for $B_1(\rho) \equiv B_\chi(\rho)$ and $B_2(\rho) \equiv B_S(\rho)$. After substitution of these integral expressions into Eq. (K.8), the integrals can be performed analytically. In this way we find the following expression for the coherence factor [98, 97, 139]:

$$\Gamma(\rho) = \exp\left(-\sqrt{\pi} L k^2 \mu_0^2 a \left[1 - \frac{1}{2}\sqrt{\pi}\frac{\mathrm{erf}(\rho/a)}{\rho/a}\right]\right), \qquad \text{(K.10)}$$

where $\mathrm{erf}(x) = (2/\sqrt{\pi}) \int_0^x \exp(-\tau^2)\, d\tau$ is the error function [1].

Next we consider a turbulent atmosphere with the von Kármán spectral density given by Eq. (I.55), which is valid for an atmosphere with wind and temperature fluctuations. In this case we find the following expression for the

coherence factor [100]:

$$\Gamma(\rho) = \exp\left\{ -\frac{2L}{K_0\rho} \int_0^{K_0\rho} \left[\gamma_T \left(1 - \frac{2^{1/6} t^{5/6}}{\Gamma(5/6)} K_{5/6}(t) \right) \right.\right.$$
$$\left.\left. + \gamma_v \left(1 - \frac{2^{1/6} t^{5/6}}{\Gamma(5/6)} [K_{5/6}(t) - \frac{t}{2} K_{1/6}(t)] \right) \right] dt \right\}, \quad \text{(K.11)}$$

with $\gamma_T = 3\pi^2 A k^2 K_0^{-5/3} C_T^2/(10 T_0^2)$ and $\gamma_v = 6\pi^2 A k^2 K_0^{-5/3} C_v^2/(5 c_0^2)$.

It should be noted that Eq. (K.9) is valid only for small turbulent fluctuations. With increasing distance L, the turbulent fluctuations increase. Equation (K.9) predicts that the correlation functions increase linearly with L, for large L [the integral in Eq. (K.9) is approximately constant for large L]. In reality this occurs only for the correlation function B_S of phase fluctuations. The correlation function B_χ of log-amplitude fluctuations increases up to a value of the order of unity and then remains constant for larger distances. In other words, the log-amplitude fluctuations saturate for large distances [150, 35, 139].

The saturation of log-amplitude fluctuations can be taken into account approximately by neglecting the contributions from the log-amplitude fluctuations to the coherence factor, *i.e.* by using $B_\chi = 0$ in Eq. (K.8), for large distances [35] (this has not been done for the examples presented in Chap. 5). The correlation functions given by Eq. (K.9) satisfy the relation $B_S(\rho) \approx B_\chi(\rho)$ for large distances [68, 98], so using $B_\chi = 0$ in Eq. (K.8) is equivalent to replacing Γ by the square root $\sqrt{\Gamma}$.

K.4 Axisymmetric turbulence

The two-dimensional PE methods for sound propagation in a turbulent atmosphere (see Appendix J) are based on the axisymmetric approximation (see Sec. E.4). The axisymmetric approximation corresponds to the assumption that the system has axial symmetry around the vertical axis through the source (or rather that the variation of the sound field with the azimuthal angle can be neglected; see Sec. E.4). Consequently, sound propagation can be computed in two dimensions, in the vertical plane through the source and the receiver. The assumption of axial symmetry, however, also affects the turbulence: fluctuations are constant along horizontal circles around the source, such as the circle shown in Fig. E.1. This has a spurious effect on sound fields computed with the two-dimensional PE methods for a turbulent atmosphere.

The analytical model for a non-refracting turbulent atmosphere, which was described in the previous sections of this appendix, can be used to study the spurious effect of the axisymmetric approximation on PE results [138]. Application of the analytical model requires an expression for the spectral density $\Phi(\mathbf{k})$ [the spectral density determines the coherence factor Γ in Eq. (K.6), through Eqs. (K.8) and (K.9)]. The spectral density for axisymmetric turbulence is different

from the spectral density for isotropic turbulence. This difference should also be taken into account in comparisons of PE results with analytical results. Below we derive an expression for the spectral density for axisymmetric turbulence [138].

We use a rectangular xyz coordinate system, with the source and the receiver in the xz plane. We represent the axisymmetric turbulent atmosphere by a field $\mu(\mathbf{r})$ that is independent of y and isotropic in the xz plane. In the far field, the independence of y is equivalent to the axisymmetric approximation. Hence, the correlation function $B(\mathbf{r}) \equiv \overline{\mu(\mathbf{R})\mu(\mathbf{R}+\mathbf{r})}$ can be written as $B(\mathbf{r}) = B(\sqrt{x^2+z^2})$, with $\mathbf{r} = (x, y, z)$. From Eq. (I.20) we find the following expression for the spectral density for axisymmetric turbulence:

$$\Phi(\mathbf{k}) = F(\sqrt{k_x^2 + k_z^2})\delta(k_y) \tag{K.12}$$

with $\mathbf{k} = (k_x, k_y, k_z)$; here $\delta(k_y)$ is the Dirac delta function and

$$F(\sqrt{k_x^2 + k_z^2}) = \frac{1}{(2\pi)^2} \iint_{-\infty}^{\infty} \exp(-ik_x x - ik_z z) B(\sqrt{x^2+z^2})\, dx\, dz \tag{K.13}$$

is the two-dimensional spectral density of refractive-index fluctuations [see Eq. (I.24)].

To calculate the coherence factor Γ for axisymmetric turbulence, one substitutes Eq. (K.12) into Eq. (K.9) (with $k_x = 0$) and substitutes the resulting expressions for the correlation functions B_χ and B_S into Eq. (K.8). For the Gaussian correlation function $B(\rho) = \mu_0^2 \exp(-\rho^2/a^2)$, the two-dimensional spectral density is given by $F(k) = \mu_0^2 a^2 \exp(-k^2 a^2/4)/(4\pi)$ (see Sec. I.7.1); in this case one finds that the coherence factor for axisymmetric turbulence is identical to the coherence factor (K.10) for isotropic turbulence [139]. In general, however, the coherence factor for axisymmetric turbulence is different from the coherence factor for isotropic turbulence.

Appendix L

Ray model including caustic diffraction fields

L.1 Introduction

The ray model for sound propagation in a refracting medium has been widely used, both in ocean acoustics and in atmospheric acoustics. The modeling of sound propagation by means of sound rays is called geometrical acoustics. The principles of geometrical acoustics are described in Refs. [2, 17, 106].

Sound rays in a downward refracting atmosphere are curved toward the ground, so rays with multiple ground reflections occur (see Figs. 4.6 and 4.7). The number of rays between a source near the ground and a distant receiver near the ground is typically a few tens, in a downward refracting atmosphere. The sound pressure at the receiver is equal to the sum of the contributions of all rays.

Curved sound rays focus at certain points in the atmosphere, analogously to focusing of light rays at focal points. A set of such points is called a caustic. In two dimensions, *i.e.* in the vertical plane through the source and the receiver, a caustic is a curve. Sound rays focus on one side of a caustic curve; this side is called the illuminated side. The focusing rays are absent on the other side of the caustic curve; this side is called the shadow side. In other words, a caustic curve is a boundary between an illuminated region and a shadow region.

Geometrical acoustics predicts that the sound pressure is infinite at a caustic. In reality the sound pressure is always finite of course. This implies that geometrical acoustics fails at a caustic. Ludwig [85] and Kravtsov [73] developed a theory for the field in the vicinity of a caustic. This theory yields finite amplitudes at caustics. The effects of caustics are represented by caustic diffraction fields in this theory.

In this appendix we describe a ray model that employs the theory of Ludwig and Kravtsov for the effects of caustics [135]. We assume a downward refracting

layered atmosphere with a smooth vertical profile of the effective sound speed, *e.g.* the logarithmic profile given by Eq. (4.5).

It should be emphasized that caustic diffraction fields are very important in a ray model. To illustrate this we note that if caustic diffraction fields in caustic shadow regions are ignored, discontinuities of about 10 dB may occur in the sound pressure field [135].

In Sec. L.2 we describe the setup of the model, with a distinction between the geometrical acoustics solution and the effects of caustics on the solution. In Sec. L.3 we describe the geometrical acoustics solution and in Sec. L.4 we describe the effects of caustics. In Sec. L.5 we include the effects of atmospheric turbulence in the geometrical acoustics solution, by generalizing the analytical model for a non-refracting atmosphere that was described in Appendix K.

L.2 Setup of the model

L.2.1 System

We consider a system with a monopole source and a receiver in a downward refracting atmosphere above a homogeneous finite-impedance ground surface. We assume a layered non-moving atmosphere; the effect of wind is taken into account by the effective sound speed (see Sec. E.3). The system is axisymmetric with respect to the vertical axis through the source, so we can describe the sound field in two dimensions, in the vertical plane through the source and the receiver. We use a rectangular rz coordinate system in this plane, where r is the horizontal range measured from the source and z is the height above the ground surface. The source position is $(0, z_s)$ and the receiver position is (r, z_r). The ground surface is at height $z_g = 0$.

The model described in this appendix is valid for smooth sound speed profiles $c(z)$ with $c'(z) > 0$. The condition $c'(z) > 0$ implies that the sound speed increases monotonically with height. The set of profiles for which the model is valid is defined indirectly by the fact that all profiles have the same caustic structure. Examples of this caustic structure are shown in Fig. L.7 in Sec. L.3. From various other examples we concluded that the profiles for which the model is valid have no change of sign of the second derivative $c''(z)$. Examples are the logarithmic profile $c(z) = c_0 + b\ln(1 + z/z_0)$ and the linear profile $c(z) = c_0 + az$.

L.2.2 Sound pressure field

The sound pressure field is represented by the complex pressure amplitude $p_c(\mathbf{r})$ as a function of the receiver position $\mathbf{r} = (r, z_r)$. We use the symbol p for the normalized amplitude $p_c/|p_{\text{free}}|$, where $|p_{\text{free}}|$ is the amplitude of the free-field sound pressure; with the notation used in Chap. 3 we have $|p_{\text{free}}| = S/R_1$. We write

$$p = p_{\text{illum}} + p_{\text{shadow}}. \tag{L.1}$$

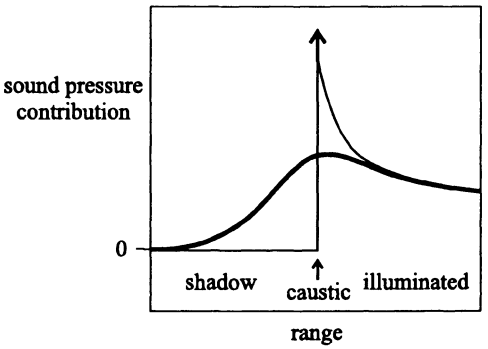

Figure L.1. Schematic illustration of the sound pressure contribution of two sound rays focusing at a caustic point. The thin line represents the geometrical acoustics solution, which has an infinite discontinuity at the caustic. The thick line represents the real continuous solution, including the caustic diffraction field.

The term p_{illum} is the sum of the geometrical acoustics field and caustic diffraction fields in caustic illuminated regions. The term p_{shadow} is the sum of caustic diffraction fields in caustics shadow regions. In the geometrical acoustics approximation, p_{shadow} vanishes and p_{illum} reduces to the geometrical acoustics solution.

In the geometrical acoustics approximation, the field $p = p_{\text{illum}}$ has an infinite discontinuity at the caustic, due to the appearance of two sound rays in the illuminated region, which are absent in the shadow region (see Fig. L.1). The two rays have infinite amplitudes at the caustic, in the geometrical acoustics approximation. By including the caustic diffraction field in the solution, we obtain the correct finite amplitudes and correct phases.

A caustic diffraction field is largest near the caustic and goes to zero with increasing distance from the caustic, both on the illuminated side and on the shadow side. The caustic diffraction field on the illuminated side is included in the term p_{illum} and the caustic diffraction field on the shadow side is included in the term p_{shadow}. The contribution of a caustic diffraction field to p_{shadow} is discontinuous at the caustic, with a finite value on the shadow side and zero on the illuminated side. The total field p is continuous (see Fig. L.1), as the field p_{illum} has an opposite discontinuity at the caustic.

In Sec. L.3 we describe the geometrical acoustics solution and caustic parameters that are used in Sec. L.4. In Sec. L.4 we include caustic diffraction fields in the solution.

L.3 Geometrical acoustics solution

In the geometrical acoustics approximation, the term p_{shadow} in Eq. (L.1) vanishes and the term p_{illum} is written as (see Sec. 4.4)

$$p_{\text{illum}} = \sum_m A_m \exp(i\phi_m), \tag{L.2}$$

where the sum is over all rays m, and A_m and ϕ_m are the amplitude and phase, respectively, of ray m. The amplitude is given by

$$A_m = f_m C_m^{N_m}, \tag{L.3}$$

where f_m is a focusing factor, C_m is a ground reflection coefficient, and N_m is the number of ground reflections. The phase is given by

$$\phi_m = \omega t_m, \tag{L.4}$$

where ω is the angular frequency and t_m is the travel time along the ray. Equation (L.3) differs from Eq. (4.8) in Sec. 4.4 by a factor S/R_1, because we consider the *normalized* sound pressure here; for simplicity, we use the same symbol A_m for the amplitude as in Sec. 4.4.

For a system with a rigid ground surface, Brekhovskikh [17] presented a rigorous derivation of Eqs. (L.2) to (L.4). In the derivation, ray theory is developed as a high-frequency limit of wave theory, for the case of a monopole source in a surface waveguide, *i.e.* a downward refracting atmosphere above a rigid ground surface.

For a system with a finite-impedance ground surface, Eq. (L.2) was proposed by L'Espérance *et al.* [81]. These authors also presented a method to include the effects of atmospheric turbulence (see Sec. L.5).

In Secs. L.3.1 to L.3.3 we describe the calculation of ray paths and caustic curves. In Secs. L.3.4 to L.3.6 we describe the calculation of the quantities f_m, C_m, N_m, and t_m in Eqs. (L.3) and (L.4).

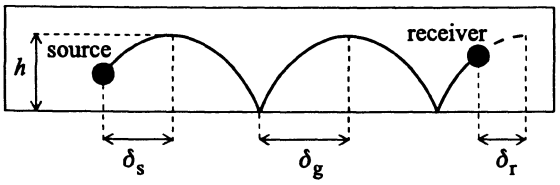

Figure L.2. Sound ray with two ground reflections between the source and the receiver. The maximum height h and the horizontal dimensions δ_g, δ_s, and δ_r of ray segments are indicated.

L.3.1 Ray paths

For a given source position and sound speed profile, the path of a sound ray is completely determined by the maximum height of the ray, *i.e.* the height of the turning point [17]; we use the symbol h for this maximum height (see Fig. L.2). The horizontal distance covered by a ray can be written as

$$r_{nj}(h) = 2(n + m_{gj})\delta_g(h) + m_{sj}\delta_s(h) + m_{rj}\delta_r(h), \tag{L.5}$$

where index n is the number of turning points of the ray ($n = 0, 1, \ldots$), index j distinguishes four rays with equal n ($j = 1, 2, 3, 4$; see Fig. L.3), the quantities m_{xj} with $x = g, s, r$ are given in Table L.1, and the function $\delta_x(h)$ is defined as (see Fig. L.2)

$$\delta_x(h) = \int_{z_x}^{h} \frac{dz}{\tan\gamma(z)}, \tag{L.6}$$

where $\gamma(z)$ is the elevation angle of the ray at height z, so we have $\tan\gamma(z) = dz/dx$. In Eq. (L.5) we use two indices n and j to identify a ray, while in Eq. (L.2) we used for simplicity only one index m.

Table L.1. The quantities m_{xj} for $x = g, s, r$ and $j = 1, 2, 3, 4$.

	$j=1$	$j=2$	$j=3$	$j=4$
m_{gj}	-1	0	0	1
m_{sj}	1	-1	1	-1
m_{rj}	1	1	-1	-1

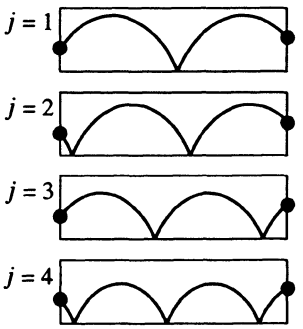

Figure L.3. The four sound rays with $n = 2$ and $j = 1, 2, 3, 4$.

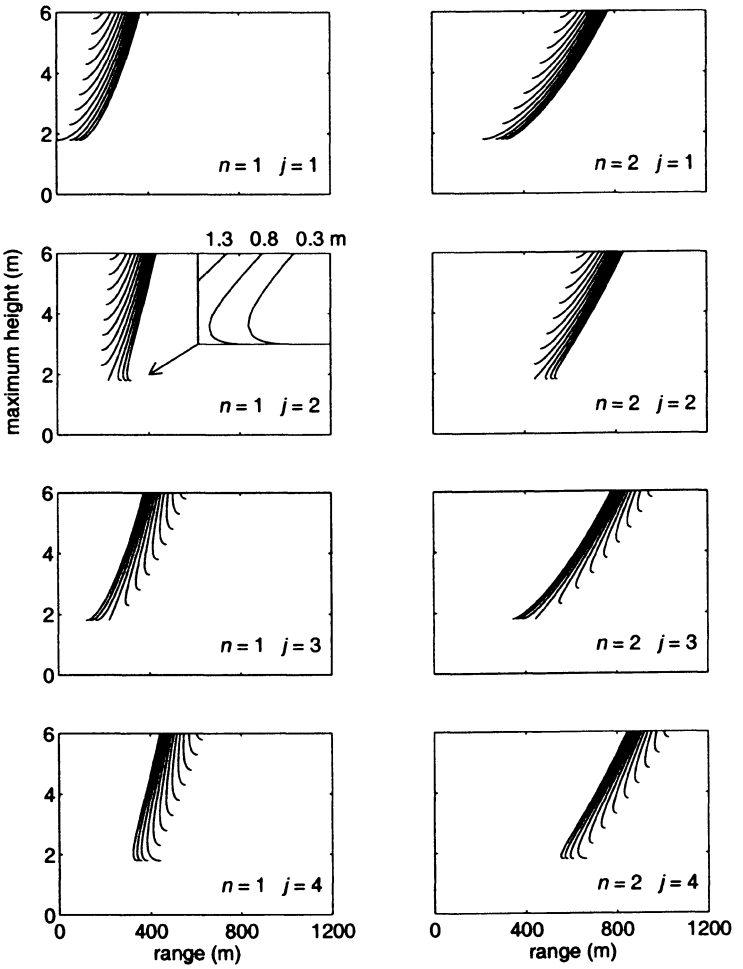

Figure L.4. The functions $r_{nj}(h)$ for $n = 1$, 2 and $j = 1,2,3,4$, with r_{nj} along the horizontal axes and h along the vertical axes. The graphs are for a linear sound speed profile $c(z) = c_0 + az$, with $c_0 = 340$ m/s and $a = 0.1$ s^{-1}, a source height of 1.8 m, and a range of receiver heights: 0.3, 0.8, 1.3, ..., 5.8 m. The curves for receiver heights of 0.3, 0.8, and 1.3 m are labeled in the enlarged section in the graph for $n = 1$, $j = 2$.

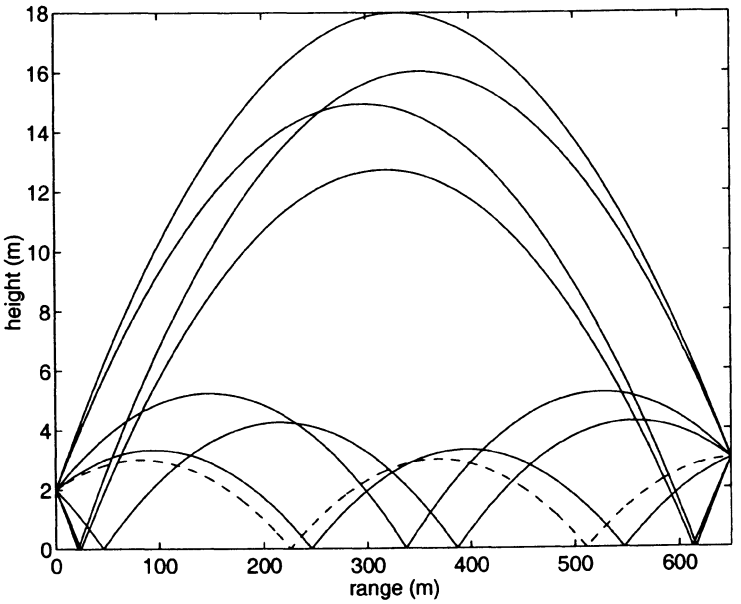

Figure L.5. Sound rays to a receiver at a distance of 650 m from the source, for a linear sound speed profile $c(z) = c_0 + az$, with $c_0 = 340$ m/s and $a = 0.1$ s^{-1}. The dashed line represents a ray with $j = 7$ and the full lines represent rays with $j \leq 4$.

Ray tracing is now reduced to solving the height h from the equation

$$r_{nj}(h) = r, \tag{L.7}$$

where r is the horizontal distance between the source and the receiver. Figure L.4 shows a typical example of the functions $r_{nj}(h)$, for a source height of 1.8 m and a range of receiver heights. The figure illustrates that, for each $n > 0$, the number of solutions of Eq. (L.7) is zero or one for $j = 1$, and zero, one, or two for $j = 2, 3, 4$. For $n = 0$ the number of solutions is zero or one for all j. The solutions are denoted as h_{nj}. To distinguish the two solutions for $j = 2, 3, 4$ we extend the range of j to $j = 1, \ldots, 8$. For a possible second solution we use $j+4$ instead of j, so we use $j = 6$ for $j = 2$, $j = 7$ for $j = 3$, and $j = 8$ for $j = 4$. We choose $h_{nj} > h_{n(j+4)}$. The points where we have $dr_{nj}/dh = 0$ correspond to caustic points; here the number of solutions changes from zero to two, with increasing range (see Fig. L.4). Figure L.5 shows an example of all rays to a receiver, for a linear sound speed profile.

The ray tracing approach is as follows. For $n = 1, 2, \ldots$ we successively determine all solutions of Eq. (L.7) for $j = 1, \ldots, 8$. At a certain value of n we find for all j that Eq. (L.7) has no solution, so all rays have been found. For

computational efficiency we prepare a matrix of values of the function $\delta_x(h)$ for a set of maximum heights h (*e.g.* $h = 0, 0.1, 0.2, \ldots, 100$ m) and a set of heights z_x (*e.g.* $z_x = 0, 0.1, 0.2, \ldots, 9.9, 10, 11, 12, \ldots, 100$ m). This matrix is denoted as $\delta_x^*(h)$, and is used here for ray tracing but will also be used in the next section for the calculation of caustic curves. With the matrix $\delta_x^*(h)$ we obtain a first estimate of the solution of Eq. (L.7). Next we obtain an accurate solution by iteratively approaching the zero point of the function $r_{nj}(h) - r$.

The case $n = 0$ is treated separately. This case corresponds to two rays without turning points: the direct ray and the ray with a ground reflection. For the direct ray we have $j = 2$ for $z_s > z_r$ and $j = 3$ for $z_s < z_r$. Beyond a certain value of r, the direct ray has a turning point, so the ray with $n = 0$ does not exist, but is replaced by a ray with $n = 1$. For the ray with a ground reflection we have $j = 4$. Again, this ray exists only up to a limiting value of r.

A computational aspect of interest is the numerical evaluation of the integral in Eq. (L.6). From Snell's law (4.3) we have $\cos\gamma(z)/c(z) = 1/c(h)$, so we find

$$\delta_x(h) = \int_{z_x}^{h} \frac{c(z)/c(h)}{\sqrt{1 - c^2(z)/c^2(h)}} dz. \tag{L.8}$$

The divergence of the integrand at $z = h$ is eliminated by a change of the integration variable to $y = [1 - c^2(z)/c^2(h)]^{1/2}$. This gives

$$\delta_x(h) = c(h) \int_0^{y(z_x)} \frac{1}{c'(z)} dy, \tag{L.9}$$

where the derivative $c'(z)$ is a function of y. The integrand is bounded as we assume that the sound speed increases monotonically with height, so we have $c'(z) > 0$. The trapezoidal rule can be used for the evaluation of the integral, with a typical value of 0.0001 for the integration step dy. We note that Eq. (4.9) in Chap. 4 follows from Eq. (L.9) and $r \approx 2n\delta_g(h)$.

L.3.2 Caustic curves

In the previous section we identified caustic points as points where we have $dr_{nj}/dh = 0$. In three dimensions, the complete set of caustic points forms a set of surfaces, which are called caustic surfaces. The intersection of the caustic surfaces and the vertical plane through the source and the receiver is a set of curves, which are called caustic curves. Caustic curves play an important role in the ray model.

The caustic curve for indices n and j is calculated as follows. The caustic curve is represented by a discrete set of caustic points (r, z). To determine this set, we choose a set of heights z (ranging from, for example, $z = 0$ to $z = 100$ m); for each height z we determine the corresponding caustic range r by solving the equation $dr_{nj}/dh = 0$ (see Fig. L.4). A first estimate is obtained from the

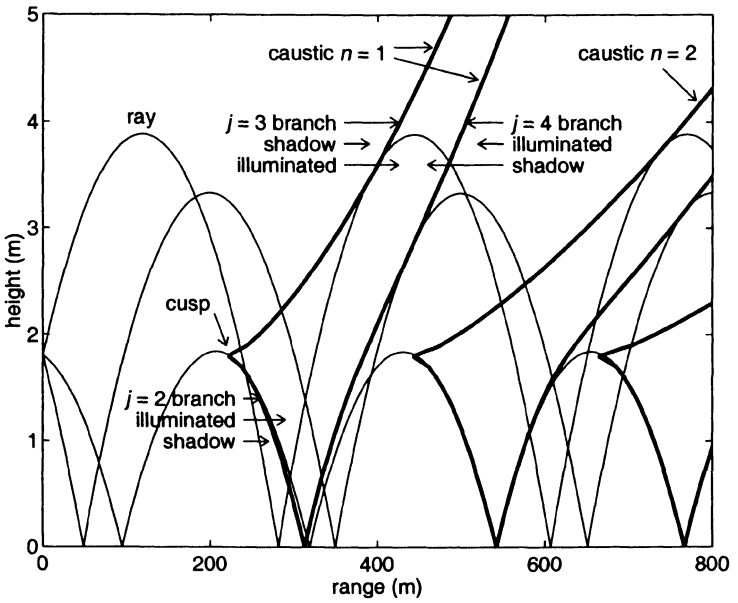

Figure L.6. Caustics (thick curves) and sound rays (thin curves), for a source height of 1.8 m and a linear sound speed profile $c(z) = c_0 + az$, with $c_0 = 340$ m/s and $a = 0.1$ s^{-1}. The $j = 2$, $j = 3$, and $j = 4$ branches are labeled for $n = 1$; the illuminated sides and shadow sides are indicated for each branch.

limited set $r_{nj}(h)$ calculated with the matrix $\delta_x^*(h)$ described in the previous section. Next, the caustic point is approached iteratively until the variation is negligible. For each value of n we determine caustic curves for $j = 2$, 3, and 4. The caustic curves for $j = 2$, 3, and 4 will be referred to as caustic branches, so a caustic curve for index n consists of three caustic branches. Figure L.6 shows caustic curves for $n = 1$, 2, and 3; the branches for $j = 2$, 3, and 4 are labeled for $n = 1$. The $j = 2$ branch and the $j = 3$ branch touch each other at one point, and the $j = 2$ branch and the $j = 4$ branch touch each other at one point. The two points of contact are cusps of the corresponding caustic curve. The cusp at the point of contact of the $j = 2$ branch and the $j = 3$ branch is always at the source height. The cusp at the point of contact of the $j = 2$ branch and the $j = 4$ branch is always at the ground surface. The latter cusp is not a real cusp, but is a consequence of the ground reflection; the cusp disappears if the $j = 4$ branch is replaced by its image below the ground surface.

Figure L.6 shows also three sound rays, with different elevation angles at the source. One ray touches the caustic $j = 3$ branches, one ray touches the $j = 2$ branches, and one ray touches the $j = 4$ branches. The $j = 3$ and $j = 4$ branches are touched by rays from below; the $j = 2$ branch is touched by rays

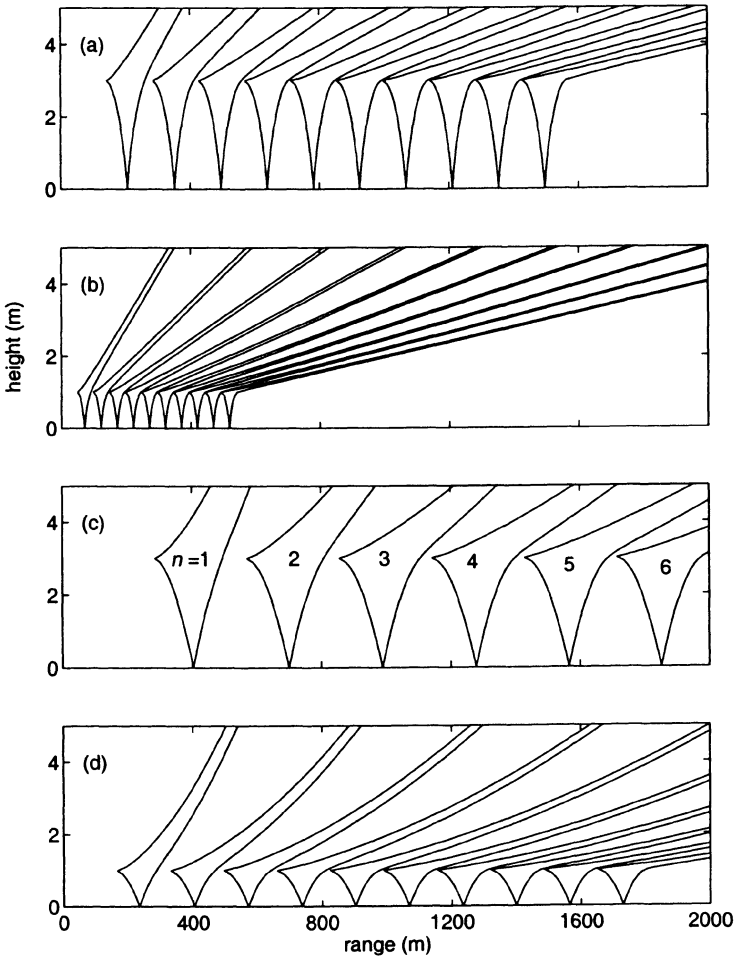

Figure L.7. Caustic curves for a logarithmic sound speed profile $c(z) = c_0 + b\ln(z/z_0 + 1)$, with $c_0 = 340$ m/s, $b = 1$ m/s, and $z_0 = 0.1$ m, for source heights of 3 m (a) and 1 m (b), and for a linear sound speed profile $c(z) = c_0 + az$, with $a = 0.1$ s^{-1}, for source heights of 3 m (c) and 1 m (d).

from above. This means that there are shadow regions above the $j = 3$ and $j = 4$ branches and below the $j = 2$ branch.

Figure L.7 shows caustic curves for a linear sound speed profile and for a logarithmic sound speed profile, for source heights of 1 m and 3 m. The four sets of caustic curves shown in the figure have a similar structure. The caustic structure was used in Sec. L.2 to define the set of sound speed profiles for which the ray model described in this appendix is valid.

In this section we have represented a caustic curve by a set of points. The (r, z) coordinates of these points will be used in Sec. L.4 for the calculation of caustic diffraction fields.

L.3.3 Indices of caustic rays

A ray touches each caustic curve ($n = 1, 2, \ldots$) at one point. These points will be referred to as caustic contact points. Let γ_s denote the elevation angle of the ray at the source. For $\gamma_s = 0$ the caustic contact point is exactly at the caustic cusp at the source height, for all n. With increasing $\gamma_s > 0$, the caustic contact point moves up along the $j = 3$ branch. With decreasing $\gamma_s < 0$, the caustic contact point moves first down along the $j = 2$ branch and next up along the $j = 4$ branch.

We consider a receiver with a variable range and a constant height. With increasing range, the receiver crosses caustic branches from the shadow side to the illuminated side. If we have $z_r > z_s$, the $j = 3$ and $j = 4$ branches are crossed alternately. If we have $z_r < z_s$, the $j = 2$ and $j = 4$ branches are crossed alternately. Each time a branch is crossed, two new rays appear. These rays will be referred to as the *caustic rays* of the caustic branch. Table L.2 gives the indices (n, j) of the caustic rays of the branches $j = 2, 3, 4$. The indices of caustic rays will be used in Sec. L.4 for the calculation of caustic diffraction fields.

Table L.2. Indices of the two caustic rays of the branches $j = 2, 3, 4$.

caustic branch	(n, j) of ray 1	(n, j) of ray 2
$j = 2$	$(n, 2)$	$(n, 6)$ or $(n + 1, 1)$
$j = 3$	$(n, 3)$	$(n, 7)$ or $(n + 1, 1)$
$j = 4$	$(n, 4)$	$(n, 8)$ or $(n + 1, 2)$ if $z_r > z_s$
		$(n, 8)$ or $(n + 1, 3)$ if $z_r < z_s$

Figure L.8 shows an example of the caustic rays of $j = 3$ branches. The caustic rays of the first branch near $r = 350$ m have indices $(n, j) = (1,3)$ and $(1,7)$ at the point of intersection near the branch. At the second branch near $r = 700$ m the indices are $(2,3)$ and $(3,1)$. This illustrates the fact that, with increasing distance from the caustic, the second caustic ray develops a turning point in front of the receiver, so that its indices change from $(n, 7)$ to $(n + 1, 1)$ (see Table L.2).

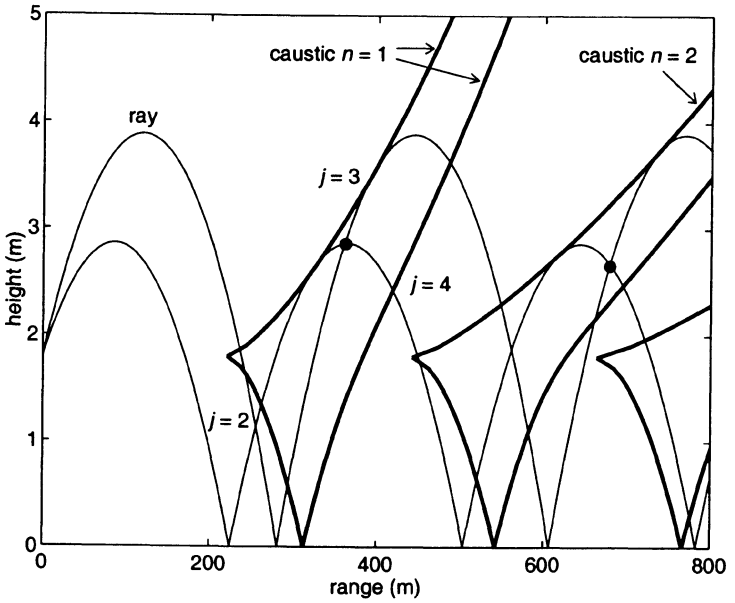

Figure L.8. Two caustic rays crossing each other at receiver positions (dots) in the illuminated regions of the $j = 3$ caustic branches. The source height is 1.8 m and the sound speed profile is $c(z) = c_0 + az$, with $c_0 = 340$ m/s and $a = 0.1$ s^{-1}.

For the $j = 2$ branch the indices of the second caustic ray change from $(n, 6)$ to $(n + 1, 1)$ with increasing range (see Table L.2). This change corresponds to the fact that the caustic contact point moves from the $j = 2$ branch through the cusp to the $j = 3$ branch.

For the $j = 4$ branch the indices of the second caustic ray are different for $z_r > z_s$ and $z_r < z_s$. For $z_r > z_s$ the indices change from $(n, 8)$ to $(n + 1, 2)$ with increasing range, corresponding to the development of a turning point in front of the receiver. For $z_r < z_s$ the indices change from $(n, 8)$ to $(n + 1, 3)$ with increasing range, corresponding to the fact that the caustic contact point moves from the $j = 2$ branch through the cusp to the $j = 3$ branch.

The description of the ordered set of rays is now complete. The number of rays increases with increasing range. Figure L.9 shows the set of rays as a function of range for receiver heights of 1 m and 3 m, a source height of 1.8 m, and a linear sound speed profile. Single rays with index $j = 1$, 2, 3, or 4 are represented by open circles. Ray pairs $j = (2,6)$, $(3,7)$, or $(4,8)$ are represented by filled circles.

The graph in Fig. L.9 for a receiver height of 3 m illustrates the case $z_r > z_s$. In this case new rays appear each time a $j = 3$ or $j = 4$ caustic branch is crossed.

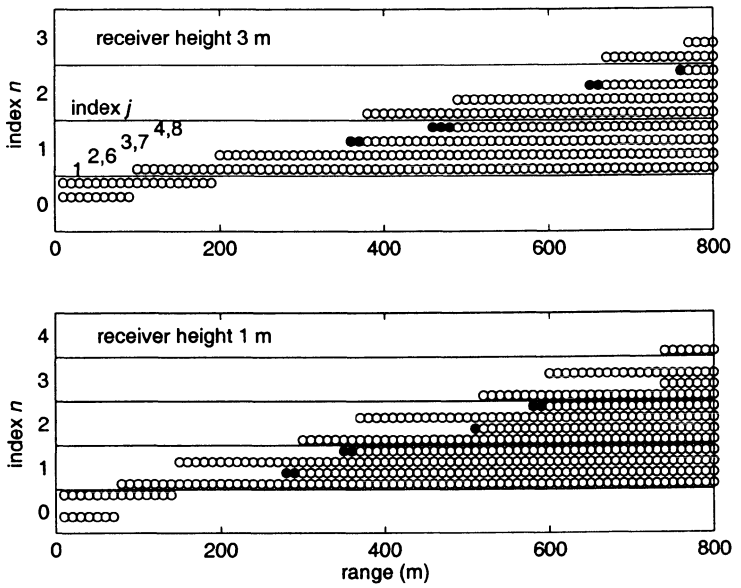

Figure L.9. Sets of sound rays as a function of range, for receiver heights of 3 m (top) and 1 m (bottom), a source height of 1.8 m, and a linear sound speed profile $c(z) = c_0 + az$, with $c_0 = 340$ m/s and $a = 0.1$ s^{-1}. Single rays with index $j = 1$, 2, 3, or 4 are represented by open circles. Ray pairs with $j = (2,6)$, (3,7), or (4,8) are represented by filled circles.

Up to range $r = 350$ m there are only two rays. At range $r = 360$ m the first $j = 3$ branch has been crossed (*cf.* Fig. L.8) and two new rays have appeared, with indices $(n, j) = (1,3)$ and $(1,7)$. At range $r = 380$ m the indices of the latter ray have changed to $(2,1)$. At range $r = 460$ m the first $j = 4$ branch has been crossed and again two new rays have appeared, with indices $(n, j) = (1,4)$ and $(1,8)$. At range $r = 490$ m the indices of the latter ray have changed to $(2,2)$. The cycle starts again at range $r = 650$ m for $n = 2$.

The graph in Fig. L.9 for a receiver height of 1 m illustrates the case $z_r < z_s$. In this case $j = 2$ and $j = 4$ caustic branches are crossed. New rays appear in a different order than in the case $z_r > z_s$.

L.3.4 Ground reflections

In a downward refracting atmosphere, sound rays with multiple ground reflections occur. The contribution of a sound ray with indices n and j to the geometrical acoustics field p_{illum} depends on the number of ground reflections N_{nj} and the reflection coefficient C_{nj}. This dependence is represented by Eqs. (L.2)

and (L.3) with index m replaced by indices n and j. The number of ground reflections N_{nj} is given by

$$N_{nj} = n + m_{gj}, \tag{L.10}$$

where the quantity m_{gj} has been defined in Sec. L.3.1. An exact expression for the reflection coefficient C_{nj} for a refracting atmosphere is not available. As an approximation we use the spherical-wave reflection coefficient (see Sec. D.4), which represents an analytical solution for a non-refracting atmosphere. The spherical-wave reflection coefficient is a function of the ground impedance, the reflection angle, and the distance $[r^2 + (z_s + z_r)^2]^{1/2}$, *i.e.* the path length of the reflected ray in a non-refracting atmosphere. The use of the spherical-wave reflection coefficient in Eq. (L.3) was also proposed by L'Espérance *et al.* [81]. The theoretical justification of this approach was studied by Li [82].

L.3.5 Phases of the rays

The phase of a sound ray with indices n and j depends on the travel time t_{nj} along the ray, as represented by Eq. (L.4) with index m replaced by indices n and j. The travel time is given by

$$t_{nj}(h) = 2(n + m_{gj})\tau_g(h) + m_{sj}\tau_s(h) + m_{rj}\tau_r(h), \tag{L.11}$$

where τ_x is the travel time along the ray segment between height z_x and the turning point (see Fig. L.2; x = g, s, r):

$$\tau_x(h) = \int_{z_x}^{h} \frac{dz}{c \sin\gamma}. \tag{L.12}$$

By a change of the integration variable to $y = [1 - c^2(z)/c^2(h)]^{1/2}$ [see Eq. (L.9)] we find

$$\tau_x(h) = \int_0^{y(z_x)} \frac{1}{c'(z)(1-y^2)} dy. \tag{L.13}$$

In Sec. L.4 we will see that the phase of a ray changes discontinuously by $-\pi/2$ each time the ray touches a caustic (see also end of Sec. L.3.6). Therefore, the number of touched caustics between the source and the receiver will be required. This number depends on the indices n and j of the sound ray, and is denoted as K_{nj}. We have

$$\begin{aligned} K_{nj} &= n - 1 \quad \text{for } j = 1, 2, 3, 4 \\ K_{nj} &= n \qquad \text{for } j = 6, 7, 8. \end{aligned} \tag{L.14}$$

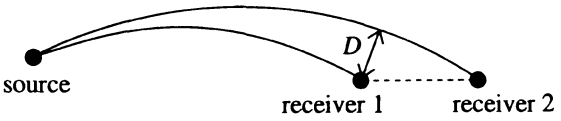

Figure L.10. The ray tube diameter D is the normal distance between two rays with slightly different elevation angles at the source.

L.3.6 Focusing factors

The focusing factor f_m in Eq. (L.3) accounts for the fact that, in a refracting atmosphere with curved sound rays, there are regions where the 'concentration' of sound rays is high and regions where the 'concentration' of sound rays is low (see Sec. 4.4). The focusing factor is calculated from the spatial divergence of two rays with slightly different elevation angles at the source. A measure of the spatial divergence is the ray tube diameter D, which is defined as the normal distance between the two rays (see Fig. L.10). The system is axisymmetric with respect to the vertical axis through the source, so the sound pressure is inversely proportional to the square root of the ray tube diameter. As the focusing factor should be unity in the free field, *i.e.* the field in an unbounded non-refracting atmosphere, we find $f_m = \sqrt{D_{\text{free}}/D}$, where D_{free} is the ray tube diameter in the free field.

The ray tube diameter for ray m is calculated as follows. After ray m to the receiver at position (r, z_{r}) has been traced, a second ray is traced to a receiver at position $(r + r\rho_r, z_{\text{r}})$, with $\rho_r \ll 1$ (we use typically $\rho_r = 10^{-5}$). The elevation angle at the source is denoted as γ_{s} for the original ray and as γ'_{s} for the second ray; the corresponding elevation angles at the receiver are denoted as γ_{r} and γ'_{r}, respectively. We have $\gamma_{\text{s}} \approx \gamma'_{\text{s}}$ and $\gamma_{\text{r}} \approx \gamma'_{\text{r}}$. The ray tube diameter is given by $D = r\rho_r |\sin\gamma_{\text{r}}|$ (see Fig. L.10). For small γ_{s} (near-horizontal propagation), the ray tube diameter in the free field is given by $D_{\text{free}} \approx r|\delta\gamma_{\text{s}}|$ with $\delta\gamma_{\text{s}} = \gamma_{\text{s}} - \gamma'_{\text{s}}$. This gives the following expression for the focusing factor

$$f_m \approx \left(\frac{|\delta\gamma_{\text{s}}|}{\rho_r |\sin\gamma_{\text{r}}|} \right)^{1/2} . \tag{L.15}$$

For small γ_{s} and $|z_{\text{s}} - z_{\text{r}}| \ll r$, this expression agrees with the general expression [17]

$$f_m = \left(\frac{r^2 + (z_{\text{s}} - z_{\text{r}})^2}{r^2} \right)^{1/2} \left(\frac{\cos\gamma_{\text{s}} |\delta\gamma_{\text{s}}|}{\rho_r |\sin\gamma_{\text{r}}|} \right)^{1/2} , \tag{L.16}$$

which follows from $D_{\text{free}} = [r^2 + (z_{\text{s}} - z_{\text{r}})^2] r^{-1} \cos\gamma_{\text{s}} |\delta\gamma_{\text{s}}|$. Equation (L.16) gives the correct result $f_m = 1$ in the free field.

Geometrical acoustics fails near caustic points. At a caustic point the focusing factor given by Eq. (L.16) diverges (we must use $\rho_r \to 0$ here), corresponding to an infinite amplitude of the field in the geometrical acoustics approximation. The theory of caustics yields an improved approximation for the field near caustic points; this will be described in Sec. L.4.

The diverging focusing factor at a caustic point corresponds to a vanishing ray tube diameter. The two rays used for the calculation of the ray tube diameter cross each other at a caustic point. The phase change of $-\pi/2$ at a caustic point (see end of Sec. L.3.5) can be interpreted as a change of sign of the ray tube diameter D, as the focusing factor is proportional to $1/\sqrt{D}$ and we have $1/\sqrt{-1} = \exp(-i\pi/2)$. We ignore the sign of D, however, and take the phase change of $-\pi/2$ into account through the phase of a ray.

L.4 Caustic diffraction fields

L.4.1 Theory of caustics

In this section we describe the theory of caustics developed by Ludwig [85] and Kravtsov [73].

Ludwig [85] presents asymptotic expansions in k^{-1} of the solution of the Helmholtz equation $\nabla^2 p + k^2 p = 0$. In general the solution can be written as a superposition of plane waves [17]:

$$p(x) = \int e^{ik\phi(x,\beta)} Z(x,\beta) d\beta, \tag{L.17}$$

where $k\phi$ is a phase function, Z is an amplitude function, x represents the position coordinates (r and z for example), and β is an integration variable; β can be considered as a horizontal wave number (see Appendix E).

At most points x, the method of stationary phase can be applied (see Appendix P). This gives the solution, for high frequency, as a sum of terms of the following form (we will see later in this section that each term corresponds to a sound ray):

$$p_m(x) = e^{ik\phi_m} Z_m \tag{L.18}$$

with $\phi_m(x) = \phi(x, \beta_m(x))$, where β_m is the value of β at a point of stationary phase, *i.e.* β_m is a solution of the equation

$$\frac{\partial \phi(x, \beta_m(x))}{\partial \beta} \equiv \phi_\beta(x, \beta_m(x)) = 0, \tag{L.19}$$

and Z_m is given by

$$Z_m(x) = e^{i\mu\pi/4} \sqrt{\frac{2\pi}{k}} \frac{Z(x, \beta_m(x))}{\sqrt{|\phi_{\beta\beta}(x, \beta_m)|}} \tag{L.20}$$

with $\mu = \text{sign}(\phi_{\beta\beta}(x, \beta_m))$. This solution breaks down near points where we have $\phi_{\beta\beta}(x, \beta_m) = 0$, *i.e.* points where two stationary phase points coincide. These points are the caustic points introduced in Sec. L.3. To derive a solution that is valid near caustics, Ludwig follows Chester *et al.* [24] and introduces functions $\xi(x, \beta)$, $\theta(x)$, and $\rho(x)$ such that $\phi(x, \beta)$ is given by

$$\phi(x, \beta) = \theta + \rho\xi - \frac{1}{3}\xi^3. \tag{L.21}$$

This expression is substituted into Eq. (L.17) and the integration variable is changed to ξ. From the resulting expression only the terms most significant for large k are retained. This gives [85, 24]

$$p(x) = e^{ik\theta}\left(g_0 \int e^{ik(\rho\xi - \xi^3/3)} d\xi + g_1 \int \xi e^{ik(\rho\xi - \xi^3/3)} d\xi\right) \tag{L.22}$$

where $g_0 = g_0(x)$ and $g_1 = g_1(x)$ are functions that will be determined later in this section. Equation (L.22) can be written as

$$p(x) = 2\pi e^{ik\theta(x)}\left[g_0(x) k^{-1/3} \text{Ai}(-k^{2/3}\rho(x)) + g_1(x) i k^{-2/3} \text{Ai}'(-k^{2/3}\rho(x))\right], \tag{L.23}$$

where $\text{Ai}(t)$ is the Airy function of t and $\text{Ai}'(t)$ is the derivative. The Airy function is defined as [1]

$$\text{Ai}(t) = \frac{1}{2\pi} \int_{-\infty}^{\infty} e^{i(t\tau + \tau^3/3)} d\tau. \tag{L.24}$$

The integration path in this expression must be deformed near infinity into the complex plane to obtain a convergent integral [1].

Ludwig substitutes the solution (L.23) into the Helmholtz equation $\nabla^2 p + k^2 p = 0$ and derives differential equations that can be used to determine the functions $\theta(x)$, $\rho(x)$, $g_0(x)$, and $g_1(x)$. Ludwig shows that, to first order, θ is a measure of arc length along the caustic curve and ρ is equal to $(2/R_c)^{1/3} y$, where R_c is the local radius of curvature of the caustic curve and y is the normal distance to the caustic curve.

A caustic is identified as a set of points where we have simultaneously $\phi_\xi = 0$ and $\phi_{\xi\xi} = 0$. From Eq. (L.21) we find, after elimination of ξ, that we have $\rho = 0$ at the caustic. We have $\rho > 0$ in the illuminated region and $\rho < 0$ in the shadow region. In the illuminated region, Eq. (L.23) reduces to the geometrical acoustics approximation if the method of stationary phase is applied. The field in the shadow region can formally be described with complex rays [140, 141], *i.e.* rays with a complex phase. The complex rays represent a field that decreases exponentially with increasing distance from the caustic.

The solution (L.23) is valid only for smooth caustics. Ludwig presents a higher-order solution for the field near a cusp of a caustic curve (see Fig. L.6).

The solution (L.23) for smooth caustics, however, is sufficiently accurate for the representation of the effects of caustics in the ray model (see Sec. L.4.3) [135]. Local effects of the cusps are neglected.

Kravtsov [73] presents a practical method to determine the functions θ, ρ, g_0, and g_1. This method is described in the remainder of this section.

From Eqs. (L.21) and (L.22) we have

$$p(x) = \int e^{ik\phi(x,\xi)}(g_0 + g_1\xi)d\xi. \tag{L.25}$$

We consider a point x far from the caustic, on the illuminated side. We will evaluate the solution (L.25) at this point with the stationary phase method and equate the resulting expression to the geometrical acoustics solution.

The value of ξ at the stationary phase point, denoted as $\xi_m(x)$, is determined by the equation

$$\frac{\partial\phi(x,\xi_m)}{\partial\xi} = 0. \tag{L.26}$$

Substitution of Eq. (L.21) into Eq. (L.26) gives a quadratic equation for ξ_m, which has two solutions: $\xi_m = \pm\rho^{1/2}$. We use $m = 1$ for the solution $-\rho^{1/2}$ and $m = 2$ for the solution $\rho^{1/2}$. The stationary phase approximation of Eq. (L.25) is

$$p(x) = \sum_{m=1}^{2} p_m(x) \tag{L.27}$$

with

$$p_m(x) = |\phi_{\xi\xi}(x,\xi_m)|^{-1/2} e^{i\mu\pi/4}\sqrt{\frac{2\pi}{k}}(g_0 + g_1\xi_m)e^{ik\phi(x,\xi_m)}. \tag{L.28}$$

From Eq. (L.2) we have the following expression for the geometrical acoustics field of a caustic ray pair:

$$p(x) = \sum_{m=1}^{2} A_m(x)e^{ik\phi_m(x)}. \tag{L.29}$$

Comparison of Eqs. (L.27) and (L.29) gives

$$\phi(x,\xi_m) = \phi_m(x) \tag{L.30}$$

$$g_0 + g_1\xi_m = |\phi_{\xi\xi}(x,\xi_m)|^{1/2} e^{-i\mu\pi/4}\sqrt{\frac{k}{2\pi}}A_m(x). \tag{L.31}$$

Substitution of $\xi_m = \pm\rho^{1/2}$ into Eq. (L.30) gives $\phi_m = \theta \pm \frac{2}{3}\rho^{3/2}$, where we have used Eq. (L.21). This gives

$$\theta(x) = \frac{1}{2}(\phi_1 + \phi_2) \tag{L.32}$$

$$\frac{2}{3}\rho^{3/2}(x) = \frac{1}{2}(\phi_2 - \phi_1). \tag{L.33}$$

From Eq. (L.31) we find

$$g_0(x) = \sqrt{\frac{ik}{\pi}}\frac{\rho^{1/4}}{2}(A_2 - iA_1) \tag{L.34}$$

$$g_1(x) = \sqrt{\frac{ik}{\pi}}\frac{\rho^{-1/4}}{2}(A_2 + iA_1). \tag{L.35}$$

The functions θ, ρ, g_0, and g_1 at point x are calculated with Eqs. (L.32) to (L.35) from the parameters ϕ_1, ϕ_2, A_1, and A_2 of the geometrical acoustics solution at point x. The field at point x is then given by Eq. (L.23), which replaces the geometrical acoustics solution. Kravtsov shows that the solution (L.23) is also valid at points x close to a caustic, both on the illuminated side and on the shadow side.

The two stationary phase points corresponding to $m = 1$ and $m = 2$ represent two rays touching the caustic in the vicinity of the receiver (see Fig. L.8). The ray with $m = 1$ has yet to touch the caustic and the ray with $m = 2$ has already touched it. Close to the caustic, the sound pressure contributions of the two rays differ only by a phase shift of $\pi/2$, as can be seen from Eqs. (L.18) and (L.20). Thus, the phase of a ray drops by $\pi/2$ upon touching a caustic. Consequently, we have $A_2 \approx \exp(-i\pi/2)A_1 = -iA_1$ near the caustic. Therefore the second term on the right-hand side of Eq. (L.23), with g_1 given by Eq. (L.35), is small near the caustic.

L.4.2 Extrapolation into the shadow region

With the approach of Kravtsov we can calculate the field on the illuminated side of a caustic. First the geometrical acoustics solution is determined, including the phases ϕ_m and amplitudes A_m of the rays touching the caustic. Next the quantities θ, ρ, g_0, and g_1 are determined, and Eq. (L.23) is used for the modified sound pressure contribution of the rays touching the caustic. This approach works only for receivers in the illuminated region. To calculate the caustic diffraction field at a receiver in the shadow region we have to extrapolate the quantities θ, ρ, g_0, and g_1 from the illuminated region into the shadow region. The field in the shadow region is still given by Eq. (L.23), with the extrapolated values of the quantities θ, ρ, g_0, and g_1.

Since the quantities θ, ρ, g_0, and g_1 are regular functions of the position x, linear extrapolation can be used for receivers close to the caustic [135]. With

increasing distance from the caustic, linear extrapolation becomes inaccurate, but this is not a problem, since the diffraction field goes to zero with increasing distance from the caustic.

L.4.3 Application of caustic theory in the ray model

In this section we use the caustic theory described in the previous sections to incorporate the effects of caustics in the ray model [135].

We distinguish two types of rays contributing to the sum in Eq. (L.2), caustic rays and non-caustic rays (see Sec. L.3.3). There are at most four non-caustic rays, two with index $n = 0$ and two with index $n = 1$. Caustic rays are the new rays that appear when a receiver crosses a caustic branch from the shadow side to the illuminated side. These rays appear in pairs. Each caustic branch is touched by a single ray pair.

Caustics affect the contribution of a caustic ray pair to the field in two ways:

- the phase along a ray shifts by $-\pi/2$ each time a caustic is touched,
- the field of the ray pair is modified in the vicinity of a caustic.

The calculation of these two effects is described in the remainder of this section.

It follows from the last paragraph of Sec. L.4.1 that the phase shifts of $-\pi/2$ should be included in the amplitudes A_m. Therefore Eq. (L.3) is replaced by

$$A_m = f_m C_m^{N_m} e^{-iK_m\pi/2}, \tag{L.36}$$

where K_m is the number of touched caustics. This number is given directly by Eq. (L.14), which is an advantage of the ray tracing algorithm described in Sec. L.3. Rays and caustics are ordered in this algorithm, and for each ray the number of touched caustics between the source and the receiver follows directly from the order indices of the ray. It is not necessary to count the number of touched caustics numerically.

With the phases ϕ_m given by Eq. (L.4) and the modified amplitudes A_m given by Eq. (L.36), the quantities θ, ρ, g_0, and g_1 follow from Eqs. (L.32) to (L.35), and the modified field contributions of the caustic ray pairs follow from Eq. (L.23). Each contribution replaces two terms in the sum in Eq. (L.2).

Next we consider the calculation of the field p_{shadow} in Eq. (L.1). This field is the sum of all caustic diffraction fields in caustic shadow regions. The calculation of a caustic diffraction field in the caustic shadow region requires the extrapolation of the quantities θ, ρ, g_0, and g_1 into the caustic shadow region. We assume $z_r > z_s$; for systems with $z_r < z_s$ we apply the principle of reciprocity. Figure L.11 illustrates two different extrapolation methods: horizontal extrapolation at constant receiver height and vertical extrapolation at constant receiver range. As shown in Ref. [135], horizontal extrapolation gives more accurate results than vertical extrapolation. Therefore, we choose two points at the receiver height on the illuminated side of the caustic branch, at distances of typically 10 and 20 m from the caustic; to locate these points we use the

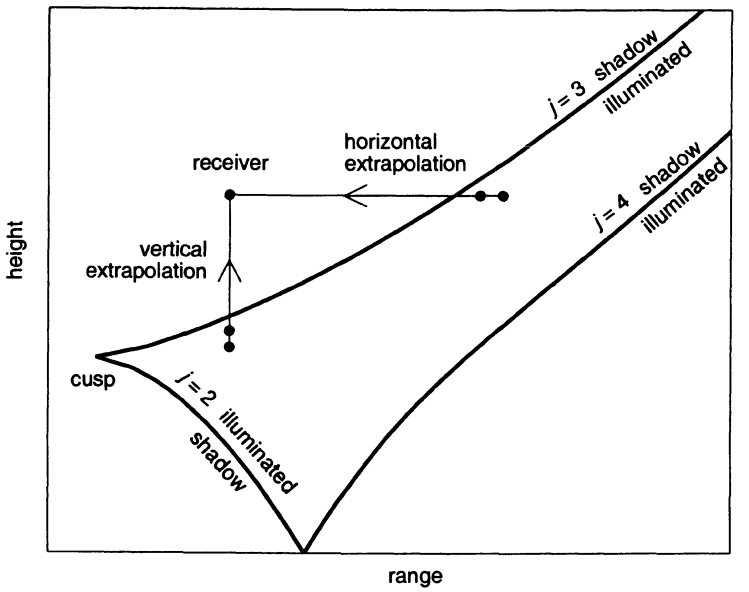

Figure L.11. Illustration of horizontal and vertical extrapolation into the shadow region of a caustic $j = 3$ branch.

representation of a caustic curve by a discrete set of caustic points, which was described in Sec. L.3.2. First we calculate the quantities θ, ρ, g_0, and g_1 at the two points on the illuminated side of the caustic branch, and next we determine the quantities θ, ρ, g_0, and g_1 at the receiver position by linear horizontal extrapolation.

Finally we mention four practical points about the implementation of the ray model, as described in Ref. [135]. First, the horizontal extrapolation range into caustic shadow regions was limited to 400 m; to avoid small discontinuities at 400 m from the caustic, the field was linearly tapered to zero in a range interval of 50 m. Second, only the diffraction fields of the two nearest $j = 3$ branches and the two nearest $j = 4$ branches were taken into account. These two limitations were included in the model for computational efficiency, and have an effect on the field only at low frequency. At high frequency, a caustic diffraction field goes rapidly to zero with increasing distance from the caustic, and the two limitations have no effect. Third, the ground reflections of the caustic diffraction fields of the $j = 2$ branches were neglected. The corresponding error is minimized by the choice $z_r > z_s$ mentioned before. The fourth point concerns the caustic cusps (see Fig. L.6). Although the effects of caustic cusps are neglected, it was found that the accuracy in the region close to a cusp can be improved by the following (empirical) approach: the diffraction field above a cusp is linearly tapered to

zero in a range interval between $r_{\text{cusp}} - \delta r$ and $r_{\text{cusp}} + \delta r$, where r_{cusp} is the range of the cusp and $\delta r = 50$ m. The same approach is applied to the end points at the ground surface of the $j = 4$ branches.

L.5 Effects of atmospheric turbulence

In the previous sections of this appendix we ignored the effects of atmospheric turbulence. In general, atmospheric turbulence causes a reduction of the depth of interference minima in spectra of the sound pressure level (see Chap. 5). In this section we describe how the effects of atmospheric turbulence can be taken into account in the ray model for a downward refracting atmosphere, which was described in the previous sections [81]. The model presented in this section is a generalization of the ray model for a non-refracting turbulent atmosphere, which was described in Appendix K. The effects of caustics are ignored, except for the phase shift of $-\pi/2$ at a caustic (see end of this section).

As before, we use the symbol p for the normalized complex pressure amplitude, *i.e.* the complex pressure amplitude divided by the amplitude $|p_{\text{free}}|$ of the free-field sound pressure. Atmospheric turbulence causes fluctuations of the sound pressure. The fluctuating normalized complex pressure amplitude at the receiver is the sum of the contributions of all sound rays:

$$p = \sum_{m=1}^{N} p_m, \tag{L.37}$$

where N is the number of rays and p_m is given by

$$p_m = A_m \exp(i\phi_m + \psi_m) \tag{L.38}$$

with $\phi_m = \omega t_m$, $A_m = f_m C_m^{N_m}$ (see Sec. L.3), and

$$\psi_m = \chi_m + iS_m, \tag{L.39}$$

where χ_m is the log-amplitude fluctuation and S_m is the phase fluctuation (see Appendix K). We write

$$C_m = |C_m| \exp(i\alpha_m) \tag{L.40}$$

and

$$C_m^{N_m} = U_m \exp(i\beta_m) \tag{L.41}$$

with $U_m = |C_m|^{N_m}$ and $\beta_m = N_m \alpha_m$.

The time-averaged relative sound pressure level is given by $\overline{\Delta L} = 10 \lg(\overline{|p|^2})$. For weak turbulence we find (see Appendix K)

$$\overline{\Delta L} = 10 \lg \left(\sum_{m=1}^{N} U_m^2 f_m^2 + 2 \sum_{m=2}^{N} \sum_{n=1}^{m-1} U_m f_m U_n f_n \cos(\phi_m - \phi_n + \beta_m - \beta_n) \Gamma_{mn} \right), \tag{L.42}$$

where the coherence factor Γ_{mn} of ray pair (m, n) is given by

$$\Gamma_{mn} = \exp\left(\overline{\chi_m \chi_n} - \frac{1}{2}\overline{\chi_m^2} - \frac{1}{2}\overline{\chi_n^2} + \overline{S_m S_n} - \frac{1}{2}\overline{S_m^2} - \frac{1}{2}\overline{S_n^2}\right). \tag{L.43}$$

Following the arguments given in Appendix K, we approximate the coherence factor by

$$\Gamma_{mn}(\rho_{mn}) = \exp[B_\chi(\rho_{mn}) - B_\chi(0) + B_S(\rho_{mn}) - B_S(0)], \tag{L.44}$$

where B_χ and B_S are the correlation functions of the log-amplitude fluctuations and phase fluctuations, respectively. For the argument ρ_{mn}, twice the mean vertical separation between rays m and n should be used. This can be approximated by $\rho_{mn} \approx |h_m - h_n|$, where h_m and h_n are the maximum heights of rays m and n, respectively.

The phase shift of $-\pi/2$ at a caustic (see Secs. L.3 and L.4) can be taken into account in Eq. (L.42) by replacing the phases ϕ_m and ϕ_n by $\phi_m - K_m\pi/2$ and $\phi_n - K_n\pi/2$, respectively. It is less obvious how the effects of caustic diffraction fields can be taken into account in Eq. (L.42).

Appendix M

Computational methods for irregular terrain

M.1 Introduction

In the computational models described in Appendices F, G, H, and L we assumed a flat ground surface. In practice there are always local variations of the ground level. These variations have a considerable effect on sound propagation.

In this appendix we describe two methods for the computation of sound propagation over more or less smooth terrain profiles: the conformal mapping method [43] and the Generalized Terrain PE (GTPE) method [129]. The conformal mapping method is described in Sec. M.2 and the GTPE method is described in Sec. M.3. Both methods are two-dimensional methods, based on the axisymmetric approximation (see Sec. E.4).

In the conformal mapping method we approximate the terrain profile by a chain of circle segments. The system with the terrain profile is transformed to a system with a flat ground surface and a modified sound speed profile, by a coordinate transformation that is called a conformal mapping. The CNPE method or the GFPE method can be used for the computation of sound propagation in the transformed system.

The conformal mapping method is illustrated in Fig. M.1. The figure shows the effect of the conformal mapping on the straight sound ray from the source to the receiver in a non-refracting atmosphere above a curved ground surface. If the curvature is convex, the straight ray is transformed to an upward refracted ray; if the curvature is concave, the straight ray is transformed to a downward refracted ray. In other words, a convex curvature of the ground surface is transformed to an upward refracting contribution to the sound speed profile and a concave curvature of the ground surface is transformed to a downward refracting contribution to the sound speed profile.

The GTPE method is a generalization of the CNPE method for a system

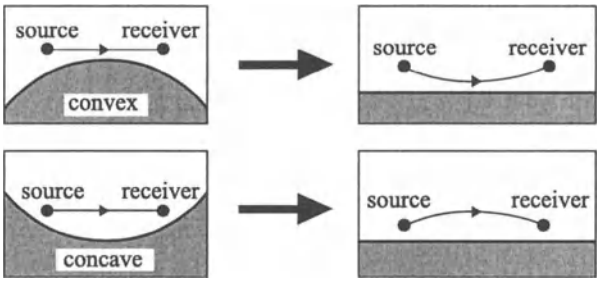

Figure M.1. Ray illustration of the conformal mapping method. A convex curvature of the ground surface is transformed to an upward refracting contribution to the sound speed profile; a concave curvature of the ground surface is transformed to a downward refracting contribution to the sound speed profile.

with a smooth terrain profile. The terrain profile introduces several terms in the PE matrices, which vanish for a flat ground surface. The boundary condition at the ground surface is formulated with the local slope of the ground surface as a parameter.

Both the conformal mapping method and the GTPE method are limited to smooth terrain profiles. In the conformal mapping method, the local radii of curvature of the terrain profile should be larger than the height of the numerical grid, which is typically 100 m. Therefore, terrain profiles with local radii of curvature smaller than typically 100 m cannot be modeled with the conformal mapping method. In the GTPE method, the local slope of the terrain profiles that can be handled is limited. Numerical computations show that the GTPE method gives accurate results if the local slope does not exceed about 30°.

M.2 The conformal mapping method

In this section we describe the conformal mapping method [43]. The terrain profile in the vertical plane through the source and the receiver is approximated by a chain of circle segments (see Fig. M.2). The radius of curvature of a circle segment is denoted as R_c. To make a distinction between convex and concave circle segments, we add a sign to the radius of curvature: we use $R_c > 0$ for convex segments and $R_c < 0$ for concave segments. For each segment we apply a different coordinate transformation (see Fig. M.3). The transformation replaces a subsystem with a curved ground segment by a subsystem with a flat ground segment and a modified sound speed profile. Sound propagation is computed in the transformed subsystems, with the CNPE method or the GFPE method. The starting field for a subsystem is obtained from the final field of the previous subsystem. For the first subsystem we use a PE starting field for a monopole source.

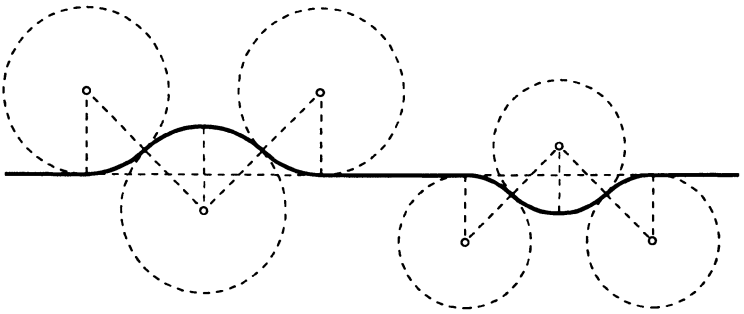

Figure M.2. Approximation of a terrain profile by a chain of circle segments.

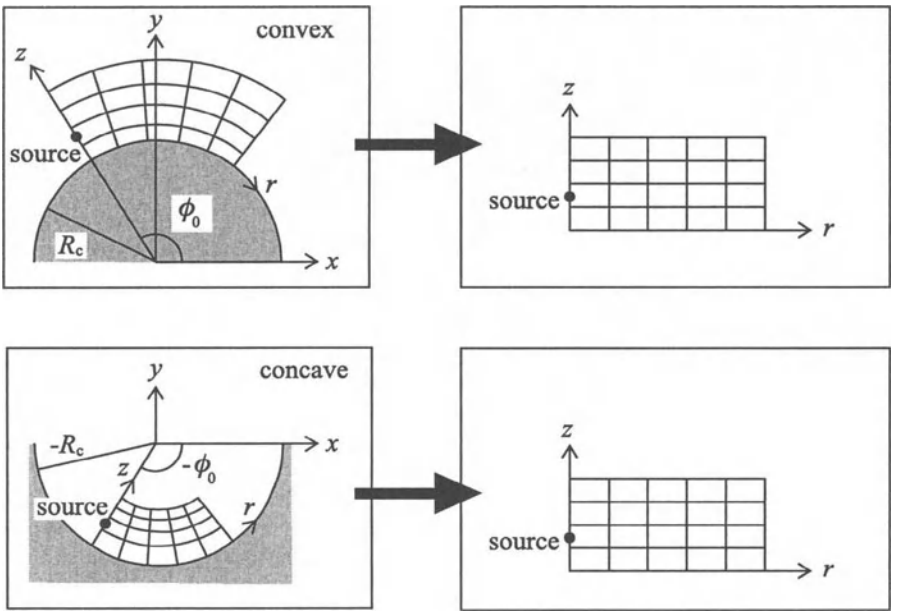

Figure M.3. Illustration of the coordinate transformation $(x, y) \rightarrow (r, z)$ in the conformal mapping method. In the rz domain we use a rectangular grid for the PE method. The corresponding grid in the xy domain is not rectangular. For a convex ground surface (top) the radius of curvature R_c and the starting angle ϕ_0 are positive. For a concave ground surface (bottom) R_c and ϕ_0 are negative. For the field at $r = 0$ we use a PE starting field for a point source (shown here) or the field from a previous subsystem.

The vertical grid spacing in a transformed subsystem is a constant. In the original subsystem, however, the vertical grid spacing increases exponentially with height for a convex ground surface and decreases exponentially with height for a concave ground surface. Neighbouring subsystems have different vertical grid spacings, so interpolation is required to calculate the starting field for a subsystem from the final field of the previous subsystem.

For each subsystem we use a local rectangular xy coordinate system (see Fig. M.3). The origin of the coordinate system is at the center of the circle segment that represents the ground surface. We assume that the system is axisymmetric with respect to the vertical axis through the source (within a limited sector of azimuthal angle; see Sec. E.4). Consequently, the three-dimensional Helmholtz equation reduces to the two-dimensional Helmholtz equation

$$\frac{\partial^2 q}{\partial x^2} + \frac{\partial^2 q}{\partial y^2} + k^2 q = 0 \tag{M.1}$$

with $q = p\sqrt{x}$, where p is the complex pressure amplitude (we omit the subscripts of q_c, p_c, and k_{eff}, as in Appendices G and H).

We apply a coordinate transformation $(x, y) \to (r, z)$ given by

$$\begin{aligned} x &= |R_c| \exp\left(\frac{z}{R_c}\right) \cos\left(-\frac{r}{R_c} + \phi_0\right) \\ y &= |R_c| \exp\left(\frac{z}{R_c}\right) \sin\left(-\frac{r}{R_c} + \phi_0\right), \end{aligned} \tag{M.2}$$

where ϕ_0 is the angle between the positive x axis and the starting radial line (see Fig. M.3). The coordinate transformation (M.2) is a conformal mapping, *i.e.* a transformation that preserves angles. The Helmholtz equation (M.1) becomes

$$\frac{\partial^2 q}{\partial r^2} + \frac{\partial^2 q}{\partial z^2} + J k^2 q = 0, \tag{M.3}$$

where

$$J \equiv \left| \frac{\partial x}{\partial r}\frac{\partial y}{\partial z} - \frac{\partial y}{\partial r}\frac{\partial x}{\partial z} \right| = \exp\left(\frac{2z}{R_c}\right) \tag{M.4}$$

is the Jacobian of the transformation. The transformed Helmholtz equation (M.3) still has the form of a two-dimensional Helmholtz equation, with a wave number equal to $J^{1/2}k$, corresponding to a sound speed $J^{-1/2}c$, where c is the original sound speed.

The inverse transformation $(r, z) \to (x, y)$ is given by

$$\begin{aligned} r &= R_c \left[\phi_0 - \arctan\left(\frac{y}{x}\right)\right] \\ z &= R_c \ln\left(\frac{\sqrt{x^2 + y^2}}{|R_c|}\right). \end{aligned} \tag{M.5}$$

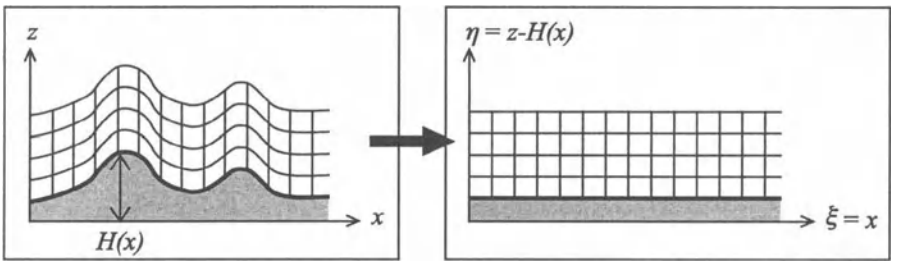

Figure M.4. Coordinate transformation $(x, z) \rightarrow (\xi, \eta)$ in the GTPE method.

The first expression in Eq. (M.5) shows that r is the distance from the starting radial line measured along the surface. The second expression in Eq. (M.5) implies that z is related to the normal distance h from the curved surface by

$$z = R_c \ln\left(\frac{R_c + h}{R_c}\right). \tag{M.6}$$

For $h \ll R_c$ we have $z \approx h$.

If a source term is included on the right-hand side of the Helmholtz equation (M.1) (see Sec. A.4), this term appears in Eq. (M.3) multiplied by the Jacobian J. For a source close to the ground, however, the Jacobian is approximately equal to unity, so the modification of the source term can be neglected. Consequently, we can use the PE starting field in the rz domain without modification, for a source close to the ground.

The ground impedance $Z\,\rho c$ is an invariant of the transformation. This follows from the definition $Z\,\rho c = p/v_n$, where v_n the normal component of the complex fluid velocity amplitude, and the relations $v_n = -(\partial p/\partial h)\,/\,(i\omega\rho)$ and $(dz/dh)_{h=0} = 1$. Consequently, we can use the ground impedance without modification in the PE computation in the rz domain.

M.3 Generalized Terrain PE (GTPE) method

In this section we describe the Generalized Terrain PE (GTPE) method [129]. This method is not limited to circular ground segments, but works for arbitrary terrain profiles, provided the local slope does not exceed about 30°.

M.3.1 Terrain following coordinates

We use a rectangular xz coordinate system in the vertical plane through the source and the receiver; x is the horizontal range and z is the height with respect to an arbitrary, constant level (see Fig. M.4). The terrain profile in the xz plane is represented by the function $z = H(x)$, which gives the local height of the

ground surface at each point x. In the next section we will apply a coordinate transformation $(x, z) \rightarrow (\xi, \eta)$ to the Helmholtz equation; the transformation is given by

$$\begin{aligned} \xi &= x \\ \eta &= z - H(x). \end{aligned} \tag{M.7}$$

This coordinate transformation is *not* applied to transform the Helmholtz equation to an equivalent Helmholtz equation for a system with a flat ground surface, as in the conformal mapping method (see Sec. M.2). The coordinates ξ and η are used only to denote the position of a point in the atmosphere with respect to the local ground level.

The boundary condition at the ground surface yields a relation between the pressure and the fluid velocity component normal to the ground surface. We will use the local slope of the ground surface to determine the normal fluid velocity component at each point. The local slope is given by the derivative $dH/dx = dH/d\xi$, which will be denoted as H'. The second derivative $d^2H/dx^2 = d^2H/d\xi^2$, denoted as H'', also plays a role in the GTPE method.

M.3.2 Transformation of the Helmholtz equation

We assume that the system is axisymmetric with respect to the vertical axis through the source (within a limited sector of azimuthal angle; see Sec. E.4). Consequently, the three-dimensional Helmholtz equation reduces to the two-dimensional Helmholtz equation

$$\frac{\partial^2 q}{\partial x^2} + \frac{\partial^2 q}{\partial z^2} + k^2 q = 0 \tag{M.8}$$

with $q = p\sqrt{x}$, where p is the complex pressure amplitude. The Helmholtz equation (M.8) will be transformed to the $\xi\eta$ coordinate system. We will use the notation $\partial_x = \partial/\partial x$ and $\partial_x^2 = \partial^2/\partial x^2$, and similarly for the variables z, ξ, and η.

From Eqs. (M.7) we find

$$\begin{aligned} \partial_z &= \partial_\eta \\ \partial_z^2 &= \partial_\eta^2 \\ \partial_x &= \partial_\xi - H'\partial_\eta \\ \partial_x^2 &= \partial_\xi^2 - 2H'\partial_{\xi\eta}^2 - H''\partial_\eta + H'^2\partial_\eta^2. \end{aligned} \tag{M.9}$$

From Eqs. (M.8) and (M.9) we find the Helmholtz equation in the $\xi\eta$ coordinate system:

$$\partial_\xi^2 q - 2H'\partial_{\xi\eta}^2 q - H''\partial_\eta q + (H'^2 + 1)\partial_\eta^2 q + k^2 q = 0. \tag{M.10}$$

For improved numerical accuracy we write the solution as (see Sec. G.3)

$$q(\xi,\eta) = \psi(\xi,\eta)\exp(ik_a\xi), \tag{M.11}$$

where k_a is the wave number at some average height or at the ground surface. The quantity ψ usually varies slowly with ξ. Substitution of Eq. (M.11) into Eq. (M.10) gives

$$\partial_\xi^2\psi + 2ik_a\partial_\xi\psi - 2H'(\partial_{\xi\eta}^2\psi + ik_a\partial_\eta\psi) - H''\partial_\eta\psi + (H'^2+1)\partial_\eta^2\psi + (k^2 - k_a^2)\psi = 0. \tag{M.12}$$

M.3.3 First-order GTPE

A first-order GTPE is obtained by neglecting the terms $\partial_\xi^2\psi$ and $\partial_{\xi\eta}^2\psi$ in Eq. (M.12):

$$\partial_\xi\psi = \frac{i}{2k_a}L_1(\psi), \tag{M.13}$$

where the operator L_1 is given by

$$L_1 = \alpha\partial_\eta^2 - \beta\partial_\eta + \gamma \tag{M.14}$$

with

$$\begin{aligned}\alpha(\xi) &= H'^2 + 1\\ \beta(\xi) &= 2ik_aH' + H''\\ \gamma(\eta) &= k^2(\eta) - k_a^2.\end{aligned} \tag{M.15}$$

For a flat ground surface we have $\alpha = 1$ and $\beta = 0$, and Eq. (M.13) reduces to the narrow-angle PE (G.6).

M.3.4 Second-order GTPE

In this section we derive a second-order GTPE from Eq. (M.12). In the derivation we use the first-order solution (M.13) to estimate the term $\partial_\xi^2\psi$ in Eq. (M.12). For a flat ground surface, the second-order GTPE solution reduces to the wide-angle CNPE solution (see Sec. M.3.5). Therefore the derivation of the GTPE solution is an alternate derivation of the CNPE solution [128].

Equation (M.12) is integrated over one range step from $\xi = a$ to $\xi = b$, with $b = a + \Delta\xi$. For the integral of the term $\partial_\xi^2\psi$ we use the first-order solution (M.13). The term $\partial_{\xi\eta}^2\psi$ is integrated by parts. This gives the second-order GTPE:

$$\left[\frac{i}{2k_a}L_1(\psi) + 2ik_a\psi - 2H'\partial_\eta\psi\right]_a^b + I_\alpha + I_\chi + I_\gamma = 0 \tag{M.16}$$

with

$$I_\alpha = \int_a^b \alpha(\xi)\, \partial_\eta^2 \psi \, d\xi$$

$$I_\chi = \int_a^b \chi(\xi)\, \partial_\eta \psi \, d\xi \tag{M.17}$$

$$I_\gamma = \int_a^b \gamma(\eta)\, \psi \, d\xi,$$

where α and γ are given by Eqs. (M.15) and χ is given by

$$\chi(\xi) = H'' - 2ik_a H'. \tag{M.18}$$

The three integrals in Eqs. (M.17) can be written as

$$I_R = \int_a^b R(\xi)\, \partial_\eta^n \psi \, d\xi \tag{M.19}$$

with $n = 2$ for $R = \alpha$, $n = 1$ for $R = \chi$, and $n = 0$ for $R = \gamma$. The three integrals I_R are approximated by assuming a linear variation of $\partial_\eta^n \psi$ with ξ over the range step from $\xi = a$ to $\xi = b$:

$$\partial_\eta^n \psi(\xi) = \frac{b - \xi}{\Delta\xi} \partial_\eta^n \psi(a) + \frac{\xi - a}{\Delta\xi} \partial_\eta^n \psi(b). \tag{M.20}$$

Substitution of Eq. (M.20) into Eq. (M.19) gives

$$I_R = A_R \partial_\eta^n \psi(a) + B_R \partial_\eta^n \psi(b) \tag{M.21}$$

with

$$A_R = \frac{1}{\Delta\xi} \int_a^b (b - \xi) R(\xi)\, d\xi$$

$$B_R = \frac{1}{\Delta\xi} \int_a^b (\xi - a) R(\xi)\, d\xi. \tag{M.22}$$

These integrals are approximated by assuming a linear variation of R with ξ over the range step from $\xi = a$ to $\xi = b$:

$$R(\xi) = \frac{b - \xi}{\Delta\xi} R(a) + \frac{\xi - a}{\Delta\xi} R(b). \tag{M.23}$$

This gives

$$A_R = \Delta\xi \left[\frac{1}{3}R(a) + \frac{1}{6}R(b)\right]$$
$$B_R = \Delta\xi \left[\frac{1}{6}R(a) + \frac{1}{3}R(b)\right]. \tag{M.24}$$

M.3.5 Finite-difference solution

The second-order GTPE (M.16) can be solved numerically by approximating the vertical derivatives $\partial_\eta^2\psi$ and $\partial_\eta\psi$ with finite differences. We use the grid shown in Fig. M.4, with grid points a heights

$$\eta_j = j\,\Delta\eta \quad \text{with } j = 1, 2, \ldots, M, \tag{M.25}$$

where $\Delta\eta$ is the vertical grid spacing. We denote the field ψ at range ξ as a vector $\vec{\psi}(\xi)$ with elements $\psi_j = \psi(\xi, \eta_j)$. Using the central difference formulas

$$(\partial_\eta\psi)_{\eta_j} = \frac{\psi_{j+1} - \psi_{j-1}}{2\Delta\eta}$$
$$(\partial_\eta^2\psi)_{\eta_j} = \frac{\psi_{j+1} - 2\psi_j + \psi_{j-1}}{(\Delta\eta)^2}, \tag{M.26}$$

we write Eq. (M.16) as

$$M_2\,\vec{\psi}(b) = M_1\,\vec{\psi}(a), \tag{M.27}$$

where M_2 and M_1 are tridiagonal matrices given by

$$M_2 = c_3\delta^2 + c_2\delta + c_1$$
$$M_1 = d_3\delta^2 + d_2\delta + d_1. \tag{M.28}$$

The quantities c_1, c_2, and c_3 are given by

$$c_3 = \frac{1}{2ik_a\,(\Delta\eta)^2}\left(\frac{i\alpha}{2k_a} + B_\alpha\right)$$
$$c_2 = -\frac{1}{2ik_a\,\Delta\eta}\left(\frac{i\beta}{2k_a} + 2H' - B_\chi\right) \tag{M.29}$$
$$c_1 = 1 + \frac{\gamma}{4k_a^2} + \frac{B_\gamma}{2ik_a},$$

where α, β, and H' are evaluated at $\xi = b$. The quantities d_1, d_2, and d_3 are given by

$$d_3 = \frac{1}{2ik_a\,(\Delta\eta)^2}\left(\frac{i\alpha}{2k_a} - A_\alpha\right)$$
$$d_2 = -\frac{1}{2ik_a\,\Delta\eta}\left(\frac{i\beta}{2k_a} + 2H' + A_\chi\right) \tag{M.30}$$
$$d_1 = 1 + \frac{\gamma}{4k_a^2} - \frac{A_\gamma}{2ik_a},$$

where α, β, and H' are evaluated at $\xi = a$. The quantities γ, A_γ, B_γ, c_1, and d_1 are diagonal matrices. The quantities δ^2 and δ are tridiagonal matrices given by

$$\delta^2 = \begin{pmatrix} -2 & 1 & & & & & \\ 1 & -2 & 1 & & & & \\ & 1 & -2 & 1 & & & \\ & & \ddots & \ddots & \ddots & & \\ & & & 1 & -2 & 1 & \\ & & & & 1 & -2 & \end{pmatrix} \tag{M.31}$$

$$\delta = \frac{1}{2}\begin{pmatrix} 0 & 1 & & & & & \\ -1 & 0 & 1 & & & & \\ & -1 & 0 & 1 & & & \\ & & \ddots & \ddots & \ddots & & \\ & & & -1 & 0 & 1 & \\ & & & & -1 & 0 & \end{pmatrix} \tag{M.32}$$

Here we have ignored the boundary conditions at the ground surface and at the top of the grid. These conditions will be taken into account in the next section.

For a flat ground surface we have $\alpha = 1$, $\beta = 0$, and $\chi = 0$, and the tridiagonal matrices (M.28) reduce to the tridiagonal CNPE matrices (G.33).

M.3.6 Boundary conditions at the ground and the top

At the ground surface we use the local reaction boundary condition (see Appendices C and D)

$$\left(\frac{p}{v_\mathrm{n}}\right)_{\eta=0} = Z\rho c, \tag{M.33}$$

where Z is the normalized ground impedance, ρc is the impedance of air (evaluated just above the ground surface), p is the complex pressure amplitude ($p \equiv p_\mathrm{c}$), and v_n is the component of the complex velocity amplitude normal to the ground surface, in downward direction ($v_\mathrm{n} \equiv v_{\mathrm{c,n}}$). From Eq. (A.19) we have

$$v_\mathrm{n} = \frac{1}{i\omega\rho}\frac{\partial p}{\partial \mathbf{n}} \tag{M.34}$$

with

$$\frac{\partial p}{\partial \mathbf{n}} = n_x\frac{\partial p}{\partial x} + n_z\frac{\partial p}{\partial z}, \tag{M.35}$$

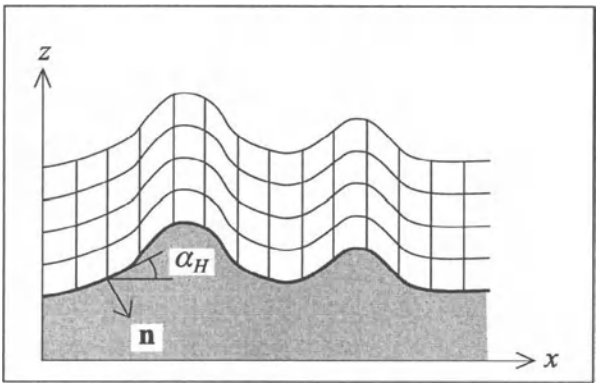

Figure M.5. Unit normal vector **n** and local elevation angle α_H of the ground surface, used for the boundary condition at the ground surface.

where $\mathbf{n} = (n_x, n_z)$ is the unit normal vector at the ground surface, in downward direction (see Fig. M.5). We write

$$\mathbf{n} = (\sin\alpha_H, -\cos\alpha_H), \tag{M.36}$$

where α_H is the local elevation angle of the ground surface, which satisfies

$$\tan\alpha_H = H'(x). \tag{M.37}$$

Using Eqs. (M.9) we find

$$\frac{\partial p}{\partial \mathbf{n}} = \sin\alpha_H \frac{\partial p}{\partial \xi} - \frac{1}{\cos\alpha_H}\frac{\partial p}{\partial \eta}. \tag{M.38}$$

The boundary condition (M.33) becomes

$$\frac{ik_0}{Z}p_0 = \sin\alpha_H \left(\frac{\partial p}{\partial \xi}\right)_{\eta=0} - \frac{1}{\cos\alpha_H}\left(\frac{\partial p}{\partial \eta}\right)_{\eta=0}, \tag{M.39}$$

with $p_0 = p_{\eta=0}$. Using $q = p\sqrt{x}$ and $q = \psi\exp(ik_a\xi)$ we find

$$\frac{ik_0}{Z}\psi_0 = \sin\alpha_H \left[\left(\frac{\partial \psi}{\partial \xi}\right)_{\eta=0} + ik_a\psi_0\right] - \frac{1}{\cos\alpha_H}\left(\frac{\partial \psi}{\partial \eta}\right)_{\eta=0}, \tag{M.40}$$

where we have neglected a term $-\frac{1}{2}\psi_0/\xi$ in the factor in square brackets.

From Eq. (M.40) we will derive expressions for $\psi_0(a)$ and $\psi_0(b)$. Using these expressions we will modify the tridiagonal matrices M_1 and M_2 given by Eqs. (M.28), to take the boundary condition at the ground surface into account. For matrix M_2 we will use the expression for $\psi_0(b)$; for matrix M_1 we will use the

expression for $\psi_0(a)$. Analogously, we will use expressions for $\psi_{M+1}(a)$ and $\psi_{M+1}(b)$ to take the boundary condition at the top of the grid into account.

We first consider $\psi_0(b)$ for matrix M_2. The first-order finite-difference approximations of the derivatives in Eq. (M.40) are

$$\begin{aligned}\left(\frac{\partial\psi}{\partial\xi}\right)_{\eta=0} &= \frac{1}{\Delta\xi}[\psi_0(b) - \psi_0(a)] \\ \left(\frac{\partial\psi}{\partial\eta}\right)_{\eta=0} &= \frac{1}{\Delta\eta}[\psi_1(b) - \psi_0(b)].\end{aligned} \tag{M.41}$$

These approximations are centered at $\xi = b - \frac{1}{2}\Delta\xi$ and $\eta = \frac{1}{2}\Delta\eta$, respectively. For second-order approximations, we estimate the change of the derivatives over the intervals $\xi = [b - \frac{1}{2}\Delta\xi, b]$ and $\eta = [0, \frac{1}{2}\Delta\eta]$, respectively, using central-difference approximations of the second derivatives $\partial_\xi^2\psi$ and $\partial_\eta^2\psi$, respectively (*cf.* Sec. G.8). This gives

$$\begin{aligned}\left(\frac{\partial\psi}{\partial\xi}\right)_{\eta=0} &= \frac{1}{2\Delta\xi}[-4\psi_0(a) + 3\psi_0(b) + \psi_0(\bar{a})] \\ \left(\frac{\partial\psi}{\partial\eta}\right)_{\eta=0} &= \frac{1}{2\Delta\eta}[4\psi_1(b) - 3\psi_0(b) - \psi_2(b)]\end{aligned} \tag{M.42}$$

with $\bar{a} = a - \Delta\xi$. From Eqs. (M.40) and (M.42) we find the expression for $\psi_0(b)$:

$$\psi_0(b) = u\psi_1(b) + v\psi_2(b) + w\psi_0(a) + y\psi_0(\bar{a}), \tag{M.43}$$

where u, v, w, and y are given by

$$u = \frac{4}{d\epsilon},\ v = -\frac{u}{4},\ w = \frac{2\sin\alpha_H}{d\,\Delta\xi},\ y = -\frac{w}{4}, \tag{M.44}$$

with

$$\epsilon = 2\Delta\eta\cos\alpha_H \tag{M.45}$$

and

$$d = -\frac{ik_0}{Z} + \frac{3}{\epsilon} + \left(\frac{3/2}{\Delta\xi} + ik_a\right)\sin\alpha_H. \tag{M.46}$$

It should be noted that the term $\frac{3}{2}/\Delta\xi$ in Eq. (M.46) is erroneously represented as $1/\Delta\xi$ in Ref. [129]. The normalized ground impedance Z and the elevation angle α_H are evaluated at $\xi = b$ in these expressions.

Next we consider $\psi_0(a)$ for matrix M_1. From Eq. (M.43) we find directly

$$\psi_0(a) = u\psi_1(a) + v\psi_2(a) + w\psi_0(\bar{a}) + y\psi_0(\bar{\bar{a}}), \tag{M.47}$$

with $\bar{\bar{a}} = a - 2\Delta\xi$; the quantities u, v, w, and y are given by Eqs. (M.44) to (M.46), where Z and α_H are now evaluated at $\xi = a$.

At the top of the grid we apply an analogous boundary condition, with normalized impedance $Z = 1$. From Eq. (M.43) we find, by the substitutions $\sin\alpha_H \rightarrow -\sin\alpha_H$ and $\cos\alpha_H \rightarrow -\cos\alpha_H$ (from $\mathbf{n} \rightarrow -\mathbf{n}$), $\Delta\eta \rightarrow -\Delta\eta$, $k_0 \rightarrow k_{M+1}$, and $Z \rightarrow 1$:

$$\psi_{M+1}(b) = u_t\psi_M(b) + v_t\psi_{M-1}(b) + w_t\psi_{M+1}(a) + y_t\psi_{M+1}(\bar{a}), \tag{M.48}$$

where u_t, v_t, w_t, and y_t are given by

$$u_t = \frac{4}{d_t\epsilon_t},\ v_t = -\frac{u_t}{4},\ w_t = -\frac{2\sin\alpha_H}{d_t\,\Delta\xi},\ y_t = -\frac{w_t}{4}, \tag{M.49}$$

with

$$\epsilon_t = 2\Delta\eta\cos\alpha_H \tag{M.50}$$

and

$$d_t = -ik_{M+1} + \frac{3}{\epsilon_t} - \left(\frac{3/2}{\Delta\xi} + ik_a\right)\sin\alpha_H. \tag{M.51}$$

The elevation angle α_H of the ground surface is evaluated at $\xi = b$ in these expressions. The expression for $\psi_{M+1}(a)$ follows directly from Eq. (M.48):

$$\psi_{M+1}(a) = u_t\psi_M(a) + v_t\psi_{M-1}(a) + w_t\psi_{M+1}(\bar{a}) + y_t\psi_{M+1}(\bar{\bar{a}}). \tag{M.52}$$

Here the quantities u_t, v_t, w_t, and y_t are given by Eqs. (M.49) to (M.51), where α_H is now evaluated at $\xi = a$. As in the CNPE method for a flat ground surface, we use an absorbing layer just below the top of the grid to eliminate reflections from the top surface (see Sec. G.9).

The implementation of the boundary conditions in the GTPE matrices (M.28) will be described in the remainder of this section.

We first consider the left-hand side $M_2\,\vec{\psi}(b)$ of Eq. (M.27). In the column vector $\delta^2\vec{\psi}(b)$, the term $\psi_0(b)$ is 'missing' in the first element and the term $\psi_{M+1}(b)$ is 'missing' in the last element. In the column vector $\delta\vec{\psi}(b)$, the term $-\frac{1}{2}\psi_0(b)$ is 'missing' in the first element and the term $\frac{1}{2}\psi_{M+1}(b)$ is 'missing' in the last element. To correct for the 'missing' terms we make use of the boundary conditions (M.43) and (M.48). The result is that the boundary conditions at the ground and the top can be taken into account in the left-hand side $M_2\,\vec{\psi}(b)$ of Eq. (M.27) by

- replacing $\delta^2\vec{\psi}(b)$ by $T_3\vec{\psi}(b) + k_3$,
- replacing $\delta\vec{\psi}(b)$ by $T_2\vec{\psi}(b) + k_2$,

where T_3, k_3, T_2, and k_2 are given by

$$T_3 = \begin{pmatrix} -2+u & 1+v & & & & & \\ 1 & -2 & 1 & & & & \\ & 1 & -2 & 1 & & & \\ & & \ddots & \ddots & \ddots & & \\ & & & 1 & -2 & 1 & \\ & & & & 1+v_t & -2+u_t \end{pmatrix} \tag{M.53}$$

$$k_3 = \begin{pmatrix} w\psi_0(a) + y\psi_0(\bar{a}) \\ 0 \\ 0 \\ \vdots \\ 0 \\ w_t\psi_{M+1}(a) + y_t\psi_{M+1}(\bar{a}) \end{pmatrix} \tag{M.54}$$

$$T_2 = \frac{1}{2}\begin{pmatrix} -u & 1-v & & & & & \\ -1 & 0 & 1 & & & & \\ & -1 & 0 & 1 & & & \\ & & \ddots & \ddots & \ddots & & \\ & & & -1 & 0 & 1 & \\ & & & & -1+v_t & u_t \end{pmatrix} \tag{M.55}$$

$$k_2 = \frac{1}{2}\begin{pmatrix} -w\psi_0(a) - y\psi_0(\bar{a}) \\ 0 \\ 0 \\ \vdots \\ 0 \\ w_t\psi_{M+1}(a) + y_t\psi_{M+1}(\bar{a}) \end{pmatrix} \tag{M.56}$$

The quantities u, v, w, y, u_t, v_t, w_t, and y_t in these expressions are evaluated at $\xi = b$. The left-hand side $M_2\,\vec{\psi}\,(b)$ of Eq. (M.27) becomes

$$(c_3T_3 + c_2T_2 + c_1)\,\vec{\psi}\,(b) + c_3k_3 + c_2k_2. \tag{M.57}$$

The approach for the right-hand side $M_1\,\vec{\psi}\,(a)$ of Eq. (M.27) is analogous. In the column vector $\delta^2\,\vec{\psi}\,(a)$, the term $\psi_0(a)$ is 'missing' in the first element and the term $\psi_{M+1}(a)$ is 'missing' in the last element. In the column vector $\delta\,\vec{\psi}\,(a)$, the term $-\frac{1}{2}\psi_0(a)$ is 'missing' in the first element and the term $\frac{1}{2}\psi_{M+1}(a)$ is 'missing' in the last element. To correct for the 'missing' terms we make use of the boundary conditions (M.47) and (M.52). The result is that the boundary conditions at the ground and the top can be taken into account in the right-hand side $M_1\,\vec{\psi}\,(a)$ of Eq. (M.27) by

- replacing $\delta^2 \overrightarrow{\psi}(a)$ by $S_3 \overrightarrow{\psi}(a) + m_3$,
- replacing $\delta \overrightarrow{\psi}(a)$ by $S_2 \overrightarrow{\psi}(a) + m_2$.

The expressions for the matrices S_3 and S_2 are identical to the expressions (M.53) and (M.55) for T_3 and T_2, respectively; the quantities u, v, u_t, and v_t in Eqs. (M.53) and (M.55) are now evaluated at $\xi = a$ instead of $\xi = b$. The expressions for the vectors m_3 and m_2 are

$$m_3 = \begin{pmatrix} w\psi_0(\overline{a}) + y\psi_0(\overline{\overline{a}}) \\ 0 \\ 0 \\ \vdots \\ 0 \\ w_t\psi_{M+1}(\overline{a}) + y_t\psi_{M+1}(\overline{\overline{a}}) \end{pmatrix} \tag{M.58}$$

$$m_2 = \frac{1}{2} \begin{pmatrix} -w\psi_0(\overline{a}) - y\psi_0(\overline{\overline{a}}) \\ 0 \\ 0 \\ \vdots \\ 0 \\ w_t\psi_{M+1}(\overline{a}) + y_t\psi_{M+1}(\overline{\overline{a}}) \end{pmatrix}, \tag{M.59}$$

where w, y, w_t, and y_t are evaluated at $\xi = a$. The right-hand side $M_1 \overrightarrow{\psi}(a)$ of Eq. (M.27) becomes

$$(d_3 S_3 + d_2 S_2 + d_1) \overrightarrow{\psi}(a) + d_3 m_3 + d_2 m_2. \tag{M.60}$$

Appendix N

Wind and temperature profiles in the atmosphere

N.1 Introduction

In computational models for atmospheric sound propagation, the atmosphere is represented by vertical profiles of the temperature and the wind velocity. The profiles are usually combined into a profile of the effective sound speed (see Sec. E.3). In this appendix we present a meteorological description of the temperature and wind velocity profiles.

The profiles represent time averages of the temperature and the wind velocity, over a period of typically ten minutes. The profiles do not represent turbulent fluctuations of the temperature and the wind velocity. The effect of atmospheric turbulence on sound propagation is taken into account separately, as described in Appendices I, J, and K.

The profiles are often rather irregular above a height of typically 100 m. Below 100 m the profiles are more predictable and repeatable. Consequently, meteorologists have been able to develop empirical expressions for the temperature and wind velocity profiles in the atmospheric surface layer, which has a height of typically 100 m. The expressions are based on so-called similarity relations, and are presented in Sec. N.6. Meteorological quantities and concepts used in the description of similarity relations are introduced in Secs. N.2 to N.5.

The similarity relations give a realistic representation of the atmospheric surface layer in many situations, but not in all situations. The similarity relations are not valid above heterogeneous grounds or above areas consisting of land and water [145]. The similarity relations are also not valid above hills or in valleys [151, 63]. In other words, the similarity relations are not valid if the ground surface is not flat and homogeneous. Moreover, deviations from the similarity relations occur also for flat and homogeneous ground surfaces. Nevertheless, the similarity relations give a realistic illustration of the variation of wind and

temperature profiles in the atmospheric surface layer.

N.2 Boundary layer and surface layer of the atmosphere

The atmospheric boundary layer is the part of the atmosphere that is directly influenced by the earth's surface, and responds to surface effects on a time scale of about an hour or less [145]. The surface effects include friction forces on moving air in the atmosphere and heat transfer from the ground to the atmosphere.

The height of the boundary layer varies considerably with time and also with horizontal position. The height varies between a few hundred meters and a few kilometers. The lower 10% of the boundary layer is called the surface layer.

The wind velocity in the atmosphere is represented by a vector with three components, in general. The mean wind velocity is usually represented by a horizontal vector, with only two components, as the vertical component of the mean wind velocity is usually small. Fluctuations of the vertical wind velocity, however, are not small, and play an important role in the vertical transport of heat and momentum in the boundary layer.

The wind velocity profile in the boundary layer depends on the roughness of the ground surface. Friction forces at the surface 'slow down' moving air near the surface. Consequently, the wind speed is zero (or negligibly small) at the surface, and increases with increasing height above the surface.

The direction of the mean wind velocity vector is called the wind direction. The wind direction usually varies with height above the ground. This is a consequence of the rotation of the earth; the corresponding pseudo-force is called the Coriolis force. The variation of the wind direction with increasing height is clockwise in the northern hemisphere and counter-clockwise in the southern hemisphere (on a 'clock' with East = 3 o'clock, South = 6 o'clock, West = 9 o'clock, and North = 12 o'clock). The variation of the wind direction with height may be as large as 45° in the boundary layer. In the surface layer, the variation is smaller.

The temperature profile in the boundary layer is determined predominantly by heating of the ground due to solar radiation in the daytime, and cooling of the ground at night. Clouds play an important role in this periodic cycle, which is called the diurnal cycle. Heat exchange between the ground and the air is due to various transport processes. One of the transport processes is mixing of air by wind velocity fluctuations, *i.e.* by atmospheric turbulence.

We distinguish two types of turbulence in the boundary layer: turbulence driven by temperature gradients and turbulence driven by wind velocity gradients.

Buoyancy and gravity play a role in turbulence driven by temperature gradients. A volume of air that is warmer, and therefore less dense, than the surrounding air, rises as a consequence of buoyancy. Such a rising volume of

warm air is called a thermal. The upward movement of warm air is accompanied by a downward movement of cool air. Hence, thermals can be considered as large turbulent eddies (eddies are described in Sec. I.1).

Turbulence driven by wind velocity gradients is called mechanical turbulence. The term wind shear is often used for wind velocity gradients in this context. The generation of turbulent eddies by wind shear is described in Sec. I.3. Wind shear in the boundary layer is usually large near the ground surface and near obstacles, *e.g.* buildings. Consequently, mechanical turbulence is created near the ground and near obstacles.

As a consequence of the cascade process described in Sec. I.3, the boundary layer contains a mixture of eddies with various sizes. The size of the smallest eddies is of the order of 1 mm. The size of the largest eddies in the boundary layer is of the order of the height of the boundary layer.

N.3 Potential temperature

The pressure in the boundary layer decreases with increasing height above the ground, due to gravity (see Sec. E.2). From Eqs. (A.6) and (A.10) we have

$$\frac{T}{p^{(\gamma-1)/\gamma}} = \text{constant} \tag{N.1}$$

for an adiabatic ideal gas, where p is the pressure, T is the temperature, and γ is the specific-heat ratio ($\gamma = 1.4$ for air). Consequently, the temperature in the boundary layer also decreases with increasing height, in the adiabatic approximation. From Eqs. (E.6) and (N.1) we find

$$\alpha_0 \equiv \frac{dT}{dz} = -\frac{\gamma - 1}{\gamma}\frac{\rho T}{p}g, \tag{N.2}$$

where ρ is the density and $g \approx 9.8$ m·s^{-2} is the gravitational acceleration. Substitution of $\rho = 1.2$ kg·m^{-3}, $p = 10^5$ Pa, and $T = 300$ K gives $\alpha_0 \approx -0.01$ K·m^{-1}. Hence, the temperature decreases with increasing height at a rate of 1 degree per 100 m. Humidity causes deviations from Eq. (N.2). The quantity α_0 is called the dry adiabatic lapse rate.

The potential temperature θ is defined as

$$\theta = T\left(\frac{p_0}{p}\right)^{(\gamma-1)/\gamma} \tag{N.3}$$

with $p_0 = 10^5$ Pa. From Eqs. (N.1) to (N.3) we find, using $p \approx p_0 + (dp/dz)z$,

$$\theta \approx T - \alpha_0 z. \tag{N.4}$$

Consequently, the potential temperature θ is constant as a function of height in a dry adiabatic atmosphere, while the absolute temperature T decreases with height by 1 degree per 100 m.

One also uses the virtual potential temperature, which depends on the humidity of the atmosphere. The virtual potential temperature θ_v of moist air is defined as the potential temperature θ of *dry* air with the same density and pressure. For unsaturated air we have the relation $\theta_v = \theta(1 + 0.61r)$, where r is the mixing ratio, *i.e.* the mass ratio of water vapour to dry air in the atmosphere [145]. The difference between θ_v and θ is small and is neglected here.

N.4 Mean and turbulent parts

The wind velocity in the atmosphere is represented by a vector with components u, v, and w in a rectangular coordinate system; u and v are horizontal components and w is the vertical component. The wind velocity components are split into mean parts $\overline{u}$, $\overline{v}$, $\overline{w}$ and turbulent parts u', v', w':

$$\begin{aligned} u &= \overline{u} + u' \\ v &= \overline{v} + v' \\ w &= \overline{w} + w'. \end{aligned} \tag{N.5}$$

The mean vertical component $\overline{w}$ is small compared with the mean horizontal components $\overline{u}$ and $\overline{v}$, in general. The potential temperature θ is also split into a mean part $\overline{\theta}$ and a turbulent part θ':

$$\theta = \overline{\theta} + \theta'. \tag{N.6}$$

By definition, the time averages of the turbulent parts u', v', w', and θ' are zero.

N.5 Heat flux and momentum flux

The flux of a quantity (*e.g.* mass, heat, momentum, moisture) is the amount of the quantity that passes through a unit area per unit time. In meteorology, the fluxes of heat and momentum play an important role.

We distinguish advective fluxes and eddy fluxes. Advective fluxes are fluxes associated with the mean wind velocity components; eddy fluxes are fluxes associated with the turbulent wind velocity components.

The quantity $\overline{w}\overline{\theta}$ is an example of an advective heat flux, corresponding to the mean vertical transport of heat. It is not a true heat flux, which has the dimensions of energy per unit area per unit time, but is called a kinematic heat flux [145]. The three mean wind velocity components $\overline{u}$, $\overline{v}$, and $\overline{w}$ correspond to the advective kinematic heat fluxes $\overline{u}\overline{\theta}$, $\overline{v}\overline{\theta}$, and $\overline{w}\overline{\theta}$.

The quantity $\overline{w}\,\overline{u}$ is an example of an advective momentum flux, corresponding to the mean vertical transport of horizontal momentum (but also to the horizontal transport of vertical momentum, as we have $\overline{w}\,\overline{u} = \overline{u}\,\overline{w}$). The quantity $\overline{w}\,\overline{u}$ is not a true momentum flux, which has the dimensions of mass times velocity per unit area per unit time, but is called a kinematic momentum flux. The

three mean wind velocity components $\overline{u}$, $\overline{v}$, and $\overline{w}$ correspond to nine advective kinematic momentum fluxes.

The quantity $\overline{w'\theta'}$ is an example of a kinematic eddy heat flux. It represents the vertical transport of the turbulent part of the potential temperature by the turbulent wind velocity component w'. The quantity $\overline{w'u'}$ is an example of a kinematic eddy momentum flux. It represents the vertical transport of u' momentum by the turbulent wind velocity component w'. The three turbulent wind velocity components u', v', and w' correspond to three kinematic eddy heat fluxes and nine kinematic eddy momentum fluxes.

The vertical kinematic eddy heat flux $\overline{w'\theta'}$ is of particular importance in meteorology. This flux is a measure of atmospheric stability [145]. To explain this we distinguish the atmosphere in the daytime and the atmosphere at night.

In the daytime, the temperature θ usually decreases with increasing height (above land). An air volume moving upward ($w' > 0$) ends up being warmer than its surroundings ($\theta' > 0$), so we have $w'\theta' > 0$. An air volume moving downward ($w' < 0$) ends up being cooler than its surroundings ($\theta' < 0$), so we have again $w'\theta' > 0$. The positive sign of $\overline{w'\theta'}$ in the daytime corresponds to a net upward heat flux. Thermals occur frequently in this case, and the atmosphere is called unstable.

At night, the temperature θ usually increases with increasing height. Similar arguments as above show that this corresponds to $\overline{w'\theta'} < 0$, and a net downward heat flux. The atmosphere is called stable in this case.

N.6 Similarity relations

In this section we present expressions for the vertical profiles of the mean potential temperature $\overline{\theta}$ and the mean wind speed $\overline{u}$ in the atmospheric surface layer; we represent the mean wind speed by the single velocity component $\overline{u}$, by assuming $\overline{w} = 0$ and choosing the coordinate system in such a way that we have $\overline{v} = 0$. The profiles will be derived from empirical relations between dimensionless groups of meteorological quantities, which are called similarity relations [145].

For atmospheric sound propagation we need the vertical profiles of the absolute temperature, the wind speed, and the wind direction. The absolute temperature can be calculated from the potential temperature with the approximate relation (N.4). For the wind direction in the surface layer one may assume a constant value, as an approximation.

We define the dimensionless wind speed derivative

$$\phi_{\mathrm{w}} = \frac{\kappa z}{u_*} \frac{d\overline{u}}{dz} \tag{N.7}$$

and the dimensionless temperature derivative

$$\phi_{\mathrm{t}} = \frac{\kappa z}{\theta_*} \frac{d\overline{\theta}}{dz}, \tag{N.8}$$

where $\kappa = 0.41$ is the von Kármán constant, u_* is the friction velocity defined by

$$u_*^2 = \left[\overline{(u'w')_s}^2 + \overline{(v'w')_s}^2\right]^{1/2}, \tag{N.9}$$

and the temperature θ_* is defined by

$$\theta_* = \frac{-\overline{(w'\theta')_s}}{u_*}. \tag{N.10}$$

The subscript 's' in Eqs. (N.9) and (N.10) indicates that the eddy fluxes are evaluated near the ground surface. We define the Obukhov length L by

$$L = -\frac{\overline{\theta} u_*^3}{\kappa g \overline{(w'\theta')_s}}. \tag{N.11}$$

From Eqs. (N.10) and (N.11) we find the relation $L = \overline{\theta} u_*^2/(\kappa g \theta_*)$. In Sec. N.5 we indicated that the eddy flux $\overline{w'\theta'}$ is a measure of atmospheric stability. Consequently, the reciprocal Obukhov length L^{-1} is also a measure of atmospheric stability. We have $L^{-1} < 0$ for an unstable atmosphere and $L^{-1} > 0$ for a stable atmosphere. If we have $L^{-1} \approx 0$ the atmosphere is called neutral.

Similarity relations between the dimensionless quantities ϕ_w, ϕ_t, and z/L have been developed by several meteorologists [145, 103, 19, 47]. For an unstable atmosphere, with $L^{-1} < 0$, we have the similarity relations

$$\begin{aligned} \phi_w &= (1 - 16\, z/L)^{-1/4} \\ \phi_t &= (1 - 16\, z/L)^{-1/2}. \end{aligned} \tag{N.12}$$

For a stable atmosphere, with $L^{-1} > 0$, we have the similarity relations

$$\phi_w = \phi_t = 1 + 5\, z/L. \tag{N.13}$$

The relations (N.12) and (N.13) are called Businger-Dyer relations. It should be noted that slightly varying versions of the Businger-Dyer relations are used in the meteorological literature. From the Businger-Dyer relations we will derive expressions for the wind speed profile $\overline{u}(z)$ and the potential temperature profile $\overline{\theta}(z)$; the profiles are called Businger-Dyer profiles.

We integrate Eqs. (N.7) and (N.8) from a height z_0 close to the ground surface to an arbitrary height z:

$$\overline{u}(z) - \overline{u}(z_0) = \frac{u_*}{\kappa}\left[\int_{z_0}^{z} \frac{1}{z'} dz' - \int_{z_0}^{z} \frac{1 - \phi_w(z'/L)}{z'} dz'\right] \tag{N.14}$$

$$\overline{\theta}(z) - \overline{\theta}(z_0) = \frac{\theta_*}{\kappa}\left[\int_{z_0}^{z} \frac{1}{z'} dz' - \int_{z_0}^{z} \frac{1 - \phi_t(z'/L)}{z'} dz'\right], \tag{N.15}$$

where the functions $\phi_w(z/L)$ and $\phi_t(z/L)$ are given by Eqs. (N.12) and (N.13). Close to the ground surface the wind speed is approximately zero. Therefore we set $\overline{u}(z_0) = 0$ in Eq. (N.14). With the notation $\theta_0 = \overline{\theta}(z_0)$ we find

$$\overline{u}(z) = \frac{u_*}{\kappa}\left[\ln\frac{z}{z_0} - \psi_w\right] \tag{N.16}$$

$$\overline{\theta}(z) = \theta_0 + \frac{\theta_*}{\kappa}\left[\ln\frac{z}{z_0} - \psi_t\right] \tag{N.17}$$

with

$$\psi_w = \int_0^{z/L} \frac{1-\phi_w(\zeta)}{\zeta} d\zeta \tag{N.18}$$

$$\psi_t = \int_0^{z/L} \frac{1-\phi_t(\zeta)}{\zeta} d\zeta, \tag{N.19}$$

where we have approximated the lower integration limit $z = z_0$ by $z = 0$. Substitution of the similarity relations (N.12) and (N.13) into Eqs. (N.18) and (N.19) gives

$$\psi_w = 2\ln\frac{1+x}{2} + \ln\frac{1+x^2}{2} - 2\arctan x + \frac{\pi}{2} \qquad \text{for } L^{-1} < 0 \tag{N.20}$$

$$\psi_w = -5\,z/L \qquad \text{for } L^{-1} > 0 \tag{N.21}$$

and

$$\psi_t = 2\ln\frac{1+x^2}{2} \qquad \text{for } L^{-1} < 0 \tag{N.22}$$

$$\psi_t = -5\,z/L \qquad \text{for } L^{-1} > 0 \tag{N.23}$$

with $x = (1 - 16\,z/L)^{1/4}$.

Holtslag [64] found that the following relations for $L^{-1} > 0$ are more accurate than relations (N.13):

$$\phi_w = \phi_t = 1 + 5\,z/L \qquad \text{for } z/L \leq 0.5 \tag{N.24}$$

$$\phi_w = \phi_t = 8 - \frac{4.25}{z/L} + \frac{1}{(z/L)^2} \qquad \text{for } z/L > 0.5. \tag{N.25}$$

If we use Eqs. (N.24) and (N.25) for the functions ϕ_w and ϕ_t, we find the following expressions for ψ_w and ψ_t for $L^{-1} > 0$:

$$\psi_w = \psi_t = -5\,z/L \qquad \text{for } z/L \leq 0.5 \tag{N.26}$$

$$\psi_w = \psi_t = -7\ln(z/L) - \frac{4.25}{z/L} + \frac{0.5}{(z/L)^2} - 0.852 \qquad \text{for } z/L > 0.5. \tag{N.27}$$

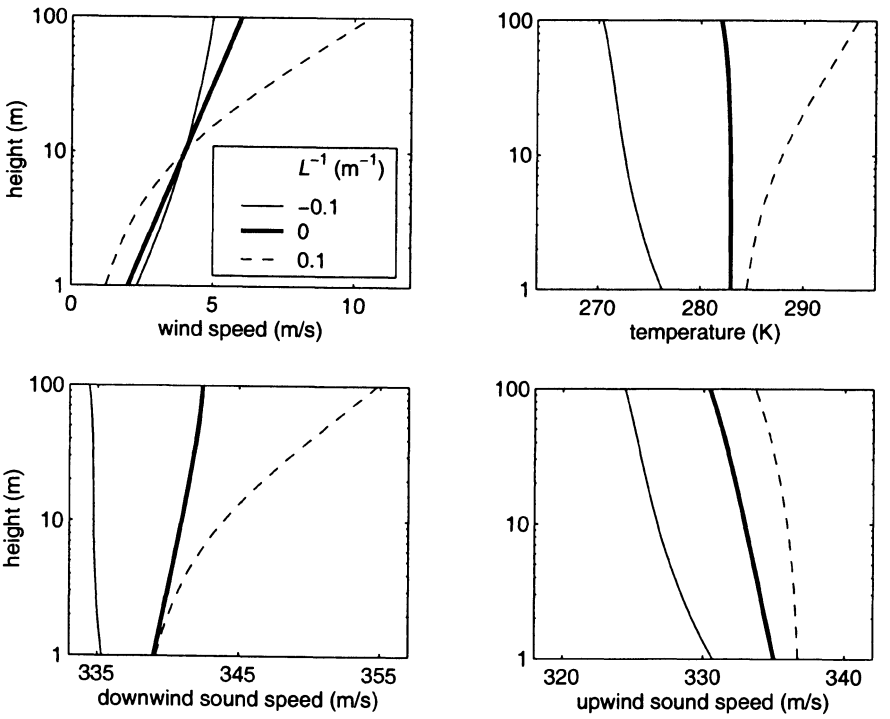

Figure N.1. Businger-Dyer profiles of the wind speed $\overline{u}$ and the temperature $\overline{T}$, for $z_0 = 0.1$ m, $\overline{u}_{10} = 4$ m/s (the wind speed for $z = 10$ m), and three values of the reciprocal Obukhov length L^{-1} (see legend). The profiles have been calculated with Eqs. (N.16), (N.17), (N.20), (N.22), (N.26), and (N.27). Also shown are the corresponding profiles of the downwind sound speed $\overline{c}+\overline{u}$ and the upwind sound speed $\overline{c}-\overline{u}$. Here $\overline{c}$ is the (mean) adiabatic sound speed, which is a function of $\overline{T}$.

For a neutral atmosphere, with $L^{-1} = 0$, we have $\psi_w = \psi_t = 0$. In this case the profiles $\overline{u}(z)$ and $\overline{\theta}(z)$ given by Eqs. (N.16) and (N.17) are logarithmic functions.

The height z_0 is called the (aerodynamic) roughness length of the ground surface [145]. The roughness length is an average quantity for a relatively large area of the ground surface. Typical values for an open field of grassland are between 0.01 m and 0.1 m. Obstacles like trees or buildings enhance the roughness length. The roughness length of a water surface is typically between 10^{-4} m and 10^{-3} m.

The profiles given by Eqs. (N.16) and (N.17) are not valid for $z < z_0$ (substitution of $z = 0$ gives $\overline{u} = \overline{\theta} = -\infty$). In sound propagation models, however, we usually choose the ground surface at $z = 0$, so we need the profiles down to $z = 0$. As z_0 is relatively small, we can approximate z by $z + z_0$ in the argument of the logarithmic functions in Eqs. (N.16) and (N.17). With this approximation we can use the profiles down to $z = 0$, and we have $\overline{u}(z) = 0$ and $\overline{\theta}(z) = \theta_0$ for $z = 0$.

The parameters u_*, θ_*, θ_0, z_0, and L of the Businger-Dyer profiles can be considered as adjustable parameters. The parameters may be determined by fitting the profiles to measured values of the temperature and the wind speed at a few heights.

Figure N.1 shows examples of Businger-Dyer profiles of the wind speed and the temperature, for an unstable atmosphere ($L^{-1} = -0.1$ m^{-1}), a neutral atmosphere ($L^{-1} = 0$), and a stable atmosphere ($L^{-1} = 0.1$ m^{-1}). Also shown are corresponding profiles of the effective sound speed $\overline{c} + \overline{u}$ for downwind sound propagation and the effective sound speed $\overline{c} - \overline{u}$ for upwind sound propagation. Here $\overline{c}$ is the (mean) adiabatic sound speed, which is a function of $\overline{T}$ (see Sec. A.2).

The graphs in Fig. N.1 have logarithmic vertical axes. Consequently, the logarithmic wind speed profile for a neutral atmosphere is represented by a straight line. The temperature profile for a neutral atmosphere is given by $\overline{T}(z) = T_0 + \alpha_0 z$, where $\alpha_0 \approx -0.01$ K·m^{-1} is the dry adiabatic lapse rate and T_0 is the surface temperature (we assumed $T_0 = 283$ K). The figure shows that the temperature in the unstable atmosphere decreases with height more rapidly than in the neutral atmosphere. The temperature in the stable atmosphere increases with height. The wind speed always increases with height. The wind speed derivative $d\overline{u}/dz$ is smaller in the unstable atmosphere than in the neutral atmosphere, and larger in the stable atmosphere than in the neutral atmosphere. The large positive wind speed gradients in the stable atmosphere dominate the downwind sound speed profile in the stable atmosphere.

Appendix O

Sound propagation over a screen

O.1 Introduction

Noise barriers are used for the reduction of noise from sources near the ground. The simplest noise barrier is a vertical screen, *e.g.* a thin wall. In this appendix we describe computational models for sound propagation over a vertical screen on a ground surface.

In Sec. O.2 we describe an analytical model for sound propagation over a rigid screen in a non-refracting atmosphere [70, 106, 52]. The sound pressure at a receiver is calculated as a sum of contributions of sound rays diffracted at the top of the screen. Similar models have been developed for more complex situations with wedge-shaped barriers, absorbing barriers, and impedance discontinuities [80, 76, 90, 93, 109, 71, 16, 21, 65, 36, 116, 133]. The term 'geometrical theory of diffraction' is sometimes used for this analytical approach for a non-refracting atmosphere [52]. The model presented here is based on an analytical diffraction solution developed by Pierce [104, 106], but other solutions can also be used (see Ref. [133]).

In Sec. O.3 we describe the application of the PE method to sound propagation over a screen in a refracting atmosphere. In general, atmospheric refraction has large effects on sound propagation over a screen. Therefore, the computation of sound propagation over a screen requires an accurate representation of the wind and temperature profiles near the screen. The wind field near a screen is a complex field, with large wind speed gradients in the region near the screen top. These screen-induced wind speed gradients may have a large effect on sound propagation over the screen [118, 136, 137].

In Sec. O.4 we present an approximate analytical representation of the wind speed field near a screen. This analytical representation can be used for computations of sound propagation over a screen with the PE method. A theoretical

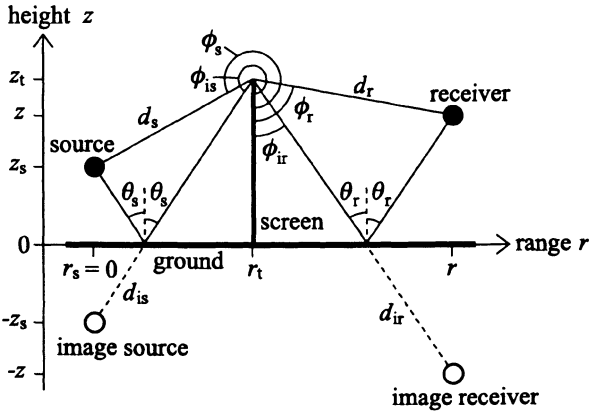

Figure O.1. Geometry with a screen on a ground surface. The screen is infinitely long in the direction normal to the paper. The distances from the screen top to the source, image source, receiver, and image receiver are indicated as d_s, d_{is}, d_r, and d_{ir}, respectively. The diffraction angles ϕ_s, ϕ_{is}, ϕ_r, and ϕ_{ir} and the reflection angles θ_s and θ_r are also indicated.

model for the calculation of the wind speed field near an obstacle is described in Ref. [29].

An alternate method for the computation of sound propagation over a barrier in a refracting atmosphere is described in Refs. [111, 147]. This method is based on the Kirchhoff-Helmholtz integral equation [Equation (H.7)] in combination with a Green's function for a refracting atmosphere, which is calculated with a numerical method such as the FFP or PE method.

O.2 Analytical model for a non-refracting atmosphere

We consider the geometry shown in Fig. O.1, with a rigid screen on a finite-impedance ground surface. The source and the receiver are located in a vertical plane perpendicular to the screen (for the case of oblique propagation over a screen, see Refs. [104, 106]). We assume a non-refracting atmosphere in this section.

The source is represented by the complex pressure amplitude of the free field, which is given by (see Chap. 2)

$$p_{\text{free}} = S \frac{\exp(ikR)}{R}, \tag{O.1}$$

where R is the distance from the source. The complex pressure amplitude at

the receiver in the geometry shown in Fig. O.1 is given by [70, 106, 52, 133]

$$p_c = SD_1 \frac{\exp(ikR_1)}{R_1} + SQ_sD_2 \frac{\exp(ikR_2)}{R_2} + SQ_rD_3 \frac{\exp(ikR_3)}{R_3} + SQ_sQ_rD_4 \frac{\exp(ikR_4)}{R_4}. \quad \text{(O.2)}$$

The four terms on the right-hand side represent the contributions from four sound paths, or sound rays,
ray 1: source → screen top → receiver
ray 2: source → ground → screen top → receiver
ray 3: source → screen top → ground → receiver
ray 4: source → ground → screen top → ground → receiver.
The four rays are illustrated in Fig. 7.1. The path lengths of the four rays, denoted as R_1, R_2, R_3, and R_4, respectively, are given by (see Fig. O.1)
ray 1: $R_1 = d_s + d_r$
ray 2: $R_2 = d_{is} + d_r$
ray 3: $R_3 = d_s + d_{ir}$
ray 4: $R_4 = d_{is} + d_{ir}$.
The factors D_1, D_2, D_3, and D_4 in Eq. (O.2) are spherical-wave diffraction coefficients for the four rays, and are specified below. The factors Q_s and Q_r in Eq. (O.2) are spherical-wave reflection coefficients (see Chap. 3 and Sec. D.4), corresponding to the ground reflections near the source and near the receiver, respectively (see Fig. O.1). For the calculation of Q_s we use the geometrical arguments d_{is} and θ_s, and for the calculation of Q_r we use d_{ir} and θ_r (in Chap. 3 and Sec. D.4 these arguments are denoted as R_2 and θ, respectively).

We have assumed here that the receiver is below the shadow boundary of the source, *i.e.* the line through the source and the screen top. If the receiver is above the shadow boundary of the source, the direct ray (source → receiver) also contributes to the complex pressure amplitude at the receiver. If the receiver is above the shadow boundary of the image source (see Fig. O.1), the reflected ray (source → ground → receiver) also contributes.

The spherical-wave diffraction coefficients are given by

$$\begin{aligned} D_1 &= D(\phi_s, \phi_r, d_s, d_r) \\ D_2 &= D(\phi_{is}, \phi_r, d_{is}, d_r) \\ D_3 &= D(\phi_s, \phi_{ir}, d_s, d_{ir}) \\ D_4 &= D(\phi_{is}, \phi_{ir}, d_{is}, d_{ir}), \end{aligned} \quad \text{(O.3)}$$

where the function D is defined by the expression [104, 106]

$$D(\phi_s, \phi_r, d_s, d_r) = \frac{e^{i\pi/4}}{\sqrt{2}} \{A_D[X(\phi_r + \phi_r)] + A_D[X(\phi_r - \phi_r)]\}. \quad \text{(O.4)}$$

The function X in this expression is given by

$$X(\phi) = -2\cos(\phi/2)\sqrt{\frac{kd_sd_r}{\pi(d_s + d_r)}}, \quad \text{(O.5)}$$

where k is the wave number. The function $A_D(X)$ is given by

$$A_D(X) = \text{sign}(X)\,[f(|X|) - ig(|X|)]\,, \tag{O.6}$$

where sign(X) is 1 for $X \geq 0$ and -1 for $X < 0$, and $f(X)$ and $g(X)$ are the auxiliary Fresnel functions, which can be calculated with the following expressions [1]:
$f(X) = (1 + 0.926X)/(2 + 1.792X + 3.104X^2)$ and
$g(X) = 1/(2 + 4.142X + 3.492X^2 + 6.67X^3)$.
For $X \geq 2$ these expressions reduce to $f(X) = 1/(\pi X)$ and $g(X) = 1/(\pi^2 X^3)$, in good approximation.

The sound pressure level at the receiver can be represented by a relative sound pressure level, analogous to the case of sound propagation over a ground surface described in Chaps. 3 and 4. The relative sound pressure level is given by the expression $\Delta L = 10\lg(|p_c|^2/|p_{\text{free}}|^2)$, where p_c is given by Eq. (O.2) and p_{free} is given by Eq. (O.1).

O.3 PE method for a refracting atmosphere

In Appendices G and H we described the CNPE and GFPE methods for sound propagation in a refracting atmosphere over a flat ground surface. In this section we describe the application of the two PE methods to sound propagation over a ground surface with a vertical screen [132].

The basic approach of the two PE methods is as follows (see Appendices G and H for details). Based on the axisymmetric approximation (see Sec. E.4), the sound field of a harmonic monopole source is computed in the rz plane, where r is the horizontal range and z is the height (see Fig. E.1). The field is represented by the variable $\psi(r, z)$, which is related to the complex pressure amplitude by Eqs. (G.2) and (G.4). The source is represented by a starting function $\psi(0, z)$ at range $r = 0$. The field $\psi(r, z)$ is computed on a rectangular grid in the rz plane, by a step-wise extrapolation in the positive r direction.

A vertical screen on the ground surface, at range $r = r_t$, is taken into account as follows. For $r < r_t$ the field ψ is computed as usual. At $r = r_t$ we set $\psi = 0$ at all grid points located on the screen; in other words, we set $\psi(r_t, z) = 0$ for $z < H$, where H is the screen height. For $r > r_t$ the computation of the field continues as usual. Thus, the part of the sound field that falls on the screen is eliminated.

This simple approach gives accurate results in the region behind the screen ($r > r_t$), as follows from comparisons of PE results with analytical results for a non-refracting atmosphere (see Chap. 7). It should be noted that the computed field shows small spurious oscillations as a function of range. The spatial period of the oscillations is of the order of the acoustic wavelength. The oscillations can be eliminated by averaging the field over a range interval of a few wavelengths.

The reflection of sound waves by the screen is not taken into account in the PE computation. The good agreement of PE results with analytical results

implies that the effect of the reflection on the field behind the screen is small and can be neglected. The effect of the reflection on the field in the region between the source and the screen ($0 < r < r_t$) is not negligible, in general. A PE method that takes the reflection into account is described in Ref. [160].

Not only the reflection, but also the reflective properties of the screen material are ignored in the PE computation. Therefore the screen can be considered neither as a rigid screen nor as an absorbing screen. In general, the reflective properties of a screen are of minor importance for sound propagation over the screen [74].

The approach of setting the field equal to zero at the grid points located on the screen is equivalent to setting the field equal to zero on the back side of the screen, *i.e.* the side not 'seen' by the source. This approach is called the Kirchhoff approximation [142].

The angular limitation of the PE method (see Secs. 4.5 and 4.6.2) implies that the PE method cannot be used if the source or the receiver are close to the screen. The minimum distance is typically a few screen heights. In general, the screen top should be well inside the region of validity of the PE method (see Fig. 4.11). This condition is satisfied in many practical situations.

The assumption of axial symmetry in the PE method implies that we model in fact a circular screen, *i.e.* a screen on a horizontal circle with the source at the center. The effect of the curvature of the circular screen, however, is negligible in practical situations; this follows from the above mentioned comparisons with analytical results for a non-refracting atmosphere, as the analytical results are valid for a straight screen.

In the three-dimensional GFPE method (see Sec. H.12), the effect of a screen can be taken into account in a similar way as in the two-dimensional PE methods. In the three-dimensional GFPE method we use cylindrical $r\phi z$ coordinates and compute the field $\psi(r, \phi, z)$ in a pie slice region (see Fig. H.6), by a step-wise extrapolation in the positive r direction. We assume that the screen is located on a circle segment at range $r = r_t$, in the angular sector $\phi_1 \leq \phi \leq \phi_2$. The angles ϕ_1 and ϕ_2 correspond to the vertical edges of the screen. The length of the screen is $r_t(\phi_2 - \phi_1)$. The effect of the screen is taken into account in the PE computation by setting the field equal to zero at the grid points located on the screen, *i.e.* grid points with $z < H$ and $\phi_1 < \phi < \phi_2$ at range $r = r_t$. This approach corresponds to the Kirchhoff approximation, and is analogous to the approach described before for the two-dimensional PE methods.

O.4 Wind field near a screen

In this section we describe an approximate analytical representation of the wind speed field near a vertical screen (*e.g.* a thin wall) on a ground surface [137]. The analytical representation was developed on the basis of measurements of wind speed profiles in a wind tunnel, and numerical computations of air flow over a screen. Far from the screen we assume a logarithmic wind speed profile.

We assume that the wind direction is normal to the screen.

The screen is located at $x = 0$ on a horizontal x axis. The height of the screen is H. The wind vector is in the positive x direction. The effect of the screen on the wind speed profile is restricted to the region ($-3H \le x \le 20H$, $0 \le z \le 10H$). Outside this region we assume an undisturbed logarithmic profile given by (see Sec. N.6)

$$u_0(z) = \frac{u_*}{\kappa} \ln\left(\frac{z}{z_0} + 1\right), \tag{O.7}$$

where z_0 is the roughness length, u_* is the friction velocity, and $\kappa = 0.41$ is the von Kármán constant. For a given value of z_0, the profile $u_0(z)$ is determined by the value of the friction velocity u_*. Instead of u_* we use the value of the wind speed $u_0(z)$ at height $z = 10$ m, which we denote as u_{10}.

The 'disturbed' profiles in the region ($-3H \le x \le 20H, 0 \le z \le 10H$), which are specified below, are valid for undisturbed wind speeds u_{10} between zero and about 15 m/s. Figure O.2 shows the profiles for $u_{10} = 4$ m/s, $z_0 = 0.1$ m, and $H = 6$ m, at the positions $x = -5H$, $-3H$, $-H$, H, $3H$, ... , $19H$.

The disturbed profiles in the region ($-3H \le x \le 20H, 0 \le z \le 10H$) are calculated from six profiles, at $x = -3H$, $-H$, 0, H, $5H$, and $20H$, respectively. For intermediate values of x we use linear interpolation. The profiles at $x = -3H$ and $20H$ are equal to the undisturbed logarithmic profile $u_0(z)$ given by Eq. (O.7). The profiles at $x = -H$, 0, H, and $5H$ are given by

$$u(z) = \begin{cases} u_2 \sin\left(\frac{1}{2}\pi \dfrac{z}{z_2}\right) & \text{for } z \le z_2 \\ \frac{1}{2}(u_2 + u_3) + \frac{1}{2}(u_2 - u_3)\cos\left(\pi \dfrac{z - z_2}{z_3 - z_2}\right) & \text{for } z_2 < z \le z_3 \\ \frac{1}{2}(u_3 + u_4) + \frac{1}{2}(u_3 - u_4)\cos\left(\pi \dfrac{z - z_3}{z_4 - z_3}\right) & \text{for } z_3 < z \le z_4 \end{cases} \tag{O.8}$$

with $z_4 = 10H$ and $u_4 = u_0(z_4)$; the parameters z_2, u_2, z_3, and u_3 are given in Table O.1, where s_a, s_b, s_c, and s_d are the values of the fractional speed-up factor $s(z) = u(z)/u_0(z)$ at height $z = z_3$ and $x = -H$, 0, H, and $5H$, respectively. These values are calculated from the equation of mass conservation

$$\int u(z)\, dz = \int u_0(z)\, dz. \tag{O.9}$$

The integration intervals in this equation can be restricted to the interval between $z = 0$ and $z_4 = 10H$, since we have $u = u_0$ for $z > 10H$. Substitution of Eqs. (O.7) and (O.8) into Eq. (O.9) gives

$$\begin{aligned} s_a &= [(6 + z_0/H)v_0(10H) - 10]/[5v_0(2H)] \\ s_b &= [(5.65 + z_0/H)v_0(10H) - 10]/[4.5v_0(1.3H)] \\ s_c &= [(6 + 0.1(2\pi^{-1} + 0.5) + z_0/H)v_0(10H) - 10]/[4.5v_0(2H)] \\ s_d &= [(6.5 + 0.3(\pi^{-1} + 1.25) + z_0/H)v_0(10H) - 10]/[4.75v_0(3H)] \end{aligned} \tag{O.10}$$

with $v_0(z) = \ln(1 + z/z_0)$. The values of the speed-up factors given by Eqs. (O.10) are typically between 1.2 and 1.4.

Table O.1. Parameters z_2, u_2, z_3, and u_3 for the wind speed profiles at $x = -H$, 0, H, and $5H$.

	$x = -H$	$x = 0$	$x = H$	$x = 5H$
z_2	0	H	H	$0.5H$
u_2	0	0	$-0.1u_0(z_4)$	$-0.3u_0(z_4)$
z_3	$2H$	$1.3H$	$2H$	$3H$
u_3	$s_a u_0(z_3)$	$s_b u_0(z_3)$	$s_c u_0(z_3)$	$s_d u_0(z_3)$

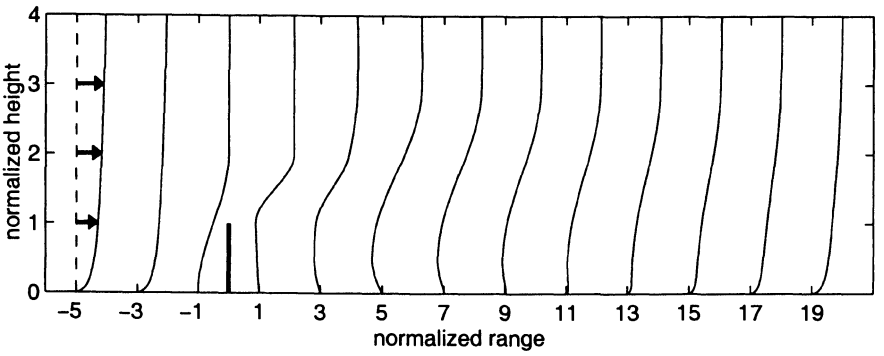

Figure O.2. Wind speed profiles at horizontal positions $x = -5H$, $-3H$, $-H$, H, $3H$, ... , $19H$, calculated for $H = 6$ m, $z_0 = 0.1$ m, and $u_{10} = 4$ m/s. Normalized range is x/H and normalized height is z/H.

Appendix P

The method of stationary phase

The method of stationary phase gives an approximation for large k of the integral

$$I = \int_a^b g(t)e^{ikh(t)}\,dt, \tag{P.1}$$

where a, b, and k are real numbers, $h(t)$ is a real function that is twice continuously differentiable, and $g(t)$ is a continuous function.

For large k the integrand in Eq. (P.1) is a rapidly oscillating function of t. Figure P.1 shows an example for $g(t) = 1$, $k = 2$, and $h(t) = t^2 - 4t$. The upper graph shows the real part of the integrand $F \equiv g(t)e^{ikh(t)}$ as a function of t. The lower graph shows the real part of the function $J(y) = \int_a^y g(t)e^{ikh(t)}\,dt$. We have $I = J(b)$. The figure illustrates that the integral is dominated by a narrow integration interval around the point of stationary phase at $t = t_0$, which is defined by the relation $h'(t_0) = 0$. In this case we have $h'(t) = 2t - 4$, so the point of stationary phase is at $t_0 = 2$.

The stationary phase approximation of Eq. (P.1) for large k is (see, for example, Ref. [52])

$$I = g(t_0)e^{ikh(t_0)}\left(\frac{2\pi}{k|h''(t_0)|}\right)^{1/2} e^{i\mu\pi/4} \tag{P.2}$$

with $\mu = \text{sign}[h''(t_0)]$, where sign$(x)$ is 1 for $x > 0$ and -1 for $x < 0$. In the above example with $g(t) = 1$, $k = 2$, and $h(t) = t^2 - 4t$, Eq. (P.2) gives $I = 0.75 - 1.01i$. The real part 0.75 agrees with the graph of ReJ in Fig. P.1, which gives Re$J \approx 0.75$ at $y = 10$.

Equation (P.2) is valid if there is only one stationary phase point in the integration interval $[a, b]$. If there are several stationary phase points in the

interval $[a, b]$, each point has a contribution given by Eq. (P.2) to the integral in Eq. (P.1).

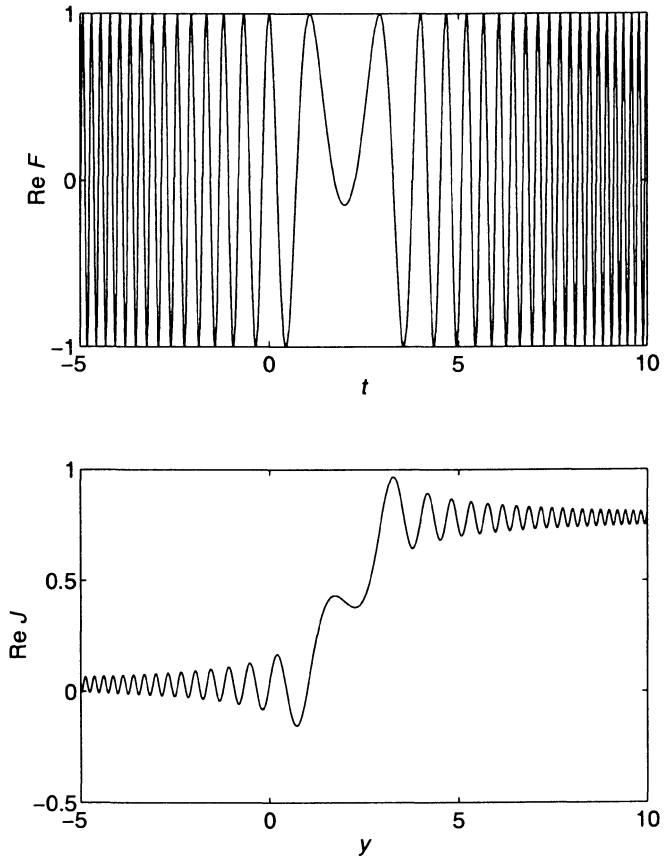

Figure P.1. Illustration of the stationary phase method of approximating the integral $I = \int_a^b g(t)e^{ikh(t)}dt$, for the case $g(t) = 1$, $k = 2$, $h(t) = t^2 - 4t$, $a = -5$, and $b = 10$. The upper graph shows the real part of the integrand $F \equiv g(t)e^{ikh(t)}$ as a function of t. The point of stationary phase, *i.e.* the point where we have $h'(t_0) = 0$, is at $t_0 = 2$ in this example. The lower graph shows the real part of the function $J(y) = \int_a^y g(t)e^{ikh(t)}\,dt$. The integral $I = J(b)$ is dominated by a narrow integration interval around the stationary phase point.

References

[1] M. Abramowitz and I.A. Stegun (editors), *Handbook of Mathematical Functions with Formulas, Graphs, and Mathematical Tables* (Dover, New York, 1972).

[2] D.S. Ahluwalia and J.B. Keller, "Exact and asymptotic representations of the sound field in a stratified ocean," in *Wave Propagation and Underwater Acoustics*, edited by J.B. Keller and J.S. Papadakis (Springer-Verlag, Berlin, 1977) p. 14-85.

[3] K. Attenborough, S.I. Hayek, and J.M. Lawther, "Propagation of sound above a porous half-space," J. Acoust. Soc. Am. **68**, 1493-1501 (1980).

[4] K. Attenborough, "Acoustical characteristics of rigid fibrous absorbents and granular materials," J. Acoust. Soc. Am. **73**, 785-799 (1983).

[5] K. Attenborough, "Acoustical impedance models for outdoor ground surfaces," J. Sound Vib. **99**, 521-544 (1985).

[6] K. Attenborough, "Ground parameter information for propagation modeling," J. Acoust. Soc. Am. **92**, 418-427 (1992).

[7] K. Attenborough, "Models for the acoustical properties of air-saturated granular media," Acta Acustica **1**, 213-226 (1993).

[8] K. Attenborough, "A note on short-range ground characterization," J. Acoust. Soc. Am. **95**, 3103-3108 (1994).

[9] K. Attenborough, S. Taherzadeh, H.E. Bass, X. Di, R. Raspet, G.R. Becker, A. Güdesen, A. Chrestman, G.A. Daigle, A. L'Espérance, Y. Gabillet, K.E. Gilbert, Y.L. Li, M.J. White, P. Naz, J.M. Noble, and H.A.J.M. van Hoof, "Benchmark cases for outdoor sound propagation models," J. Acoust. Soc. Am. **97**, 173-191 (1995).

[10] K. Attenborough and S. Taherzadeh, "Propagation from a point source over a rough finite impedance boundary," J. Acoust. Soc. Am. **98**, 1717-1722 (1995).

[11] K. Attenborough and T. Waters-Fuller, "Effective impedance of rough porous ground surfaces," J. Acoust. Soc. Am. **108**, 949-956 (2000).

[12] N. Barriere and Y. Gabillet, "Sound propagation over a barrier with realistic wind gradients. Comparison of wind tunnel experiments with GFPE computations," ACUSTICA Acta Acustica **85**, 325-334 (1999).

[13] P.G. Bergmann, "The wave equation in a medium with a variable index of refraction," J. Acoust. Soc. Am. **17**, 329-333 (1946).

[14] A.J. Berkhout, *Applied Seismic Wave Theory*, Advances in Exploration Geophysics, Vol. 1 (Elsevier, Amsterdam, 1987).

[15] L.N. Bolen and H.E. Bass, "Effects of ground cover on the propagation of sound through the atmosphere," J. Acoust. Soc. Am. **69**, 950-954 (1981).

[16] P. Boulanger, T. Waters-Fuller, K. Attenborough, and K.M. Li, "Models and measurements of sound propagation from a point source over mixed impedance ground," J. Acoust. Soc. Am. **102**, 1432-1442 (1997).

[17] L.M. Brekhovskikh, *Waves in Layered Media*, second edition (Academic, New York, 1980).

[18] R.N. Buchal and J.B. Keller, "Boundary layer problems in diffraction theory," Commun. Pure Appl. Math. **13**, 85-114 (1960).

[19] J.A. Businger, J.C. Wyngaard, Y. Izumi, and E.F. Bradley, "Flux profile relationships in the atmospheric surface layer," J. Atmos. Sci. **28**, 181-189 (1971).

[20] S. Canard-Caruana, S. Lévwy, J. Vermorel, and G. Parmentier, "Long range sound propagation near the ground," Noise Control Eng. J. **34**, 111-119 (1990).

[21] S.N. Chandler-Wilde and D.C. Hothersall, "Sound propagation above an imhomogeneous impedance plane," J. Sound. Vib. **98**, 475-491 (1985).

[22] C. Chen, Y. Lin, and D. Lee, "A three-dimensional azimuthal wide-angle model for the parabolic wave equation," J. Comp. Acoust. **7**, 269-286 (1999).

[23] C.I. Chessel, "Propagation of noise along a finite impedance boundary," J. Acoust. Soc. Am. **62**, 825-834 (1977).

[24] C. Chester, B. Friedman, and F. Ursell, "An extension of the method of steepest descents," Proc. Cambridge Philos. Soc. **54**, 599-611 (1957).

[25] P. Chevret, Ph. Blanc-Benon, and D. Juvé, "A numerical model for sound propagation through a turbulent atmosphere near the ground," J. Acoust. Soc. Am. **100**, 3587-3599 (1996).

[26] J.F. Claerbout, *Fundamentals of Geophysical Data Processing* (Blackwell, Oxford, 1985).

[27] S.F. Clifford and R.J. Lataitis, "Turbulence effects on acoustic wave propagation over a smooth surface," J. Acoust. Soc. Am. **73**, 1545-1550 (1983).

[28] M.D. Collins and E.K. Westwood, "A higher-order energy-conserving parabolic equation for range-dependent ocean depth, sound speed, and density," J. Acoust. Soc. Am. **89**, 1068-1075 (1991).

[29] J. Counihan, J.C.R. Hunt, and P.S. Jackson, "Wakes behind two-dimensional surface obstacles in turbulent boundary layers," J. Fluid Mech. **64**, 529-563 (1974).

[30] J.N. Craddock and M.J. White, "Sound propagation over a surface with varying impedance: a parabolic equation approach," J. Acoust. Soc. Am. **91**, 3184-3191 (1992).

[31] A.J. Cramond and C.G. Don, "Reflection of impulses as a method of determining acoustic impedance," J. Acoust. Soc. Am. **75**, 382-389 (1984).

[32] A.J. Cramond and C.G. Don, "Effects of moisture content on soil impedance," J. Acoust. Soc. Am. **82**, 293-301 (1987).

[33] G.A. Daigle, J.E. Piercy, and T.F.W. Embleton, "Effects of atmospheric turbulence on the interference of sound waves near a hard boundary," J. Acoust. Soc. Am. **64**, 622-630 (1978).

[34] G.A. Daigle, "Diffraction of sound by a noise barrier in the presence of atmospheric turbulence," J. Acoust. Soc. Am. **71**, 847-854 (1982).

[35] G.A. Daigle, J.E. Piercy, and T.F.W. Embleton, "Line-of-sight propagation through atmospheric turbulence near the ground," J. Acoust. Soc. Am. **74**, 1505-1513 (1983).

[36] G.A. Daigle, J. Nicolas, and J.-L. Berry, "Propagation of noise above ground having an impedance discontinuity," J. Acoust. Soc. Am. **77**, 127-138 (1985).

[37] G.A. Daigle and M.R. Stinson, "Impedance of grass-covered ground at low frequencies measured using a phase difference technique," J. Acoust. Soc. Am. **81**, 62-69 (1987).

[38] R. DeJong and E. Stusnick, "Scale model studies of the effects of wind on acoustic barrier performance," Noise Contr. Eng. **6**, 101-109 (1976).

[39] M.E. Delany and E.N. Bazley, "Acoustical properties of fibrous absorbent materials," Appl. Acoust. **3**, 105-116 (1970).

[40] M. Delany, "Sound propagation in the atmosphere: a historical review," Acustica **38**, 201-223 (1977).

[41] Y. Delrieux and P. Malbéqui, "Atmospheric sound propagation using a three-dimensional parabolic equation," Proc. Fifth Symposium on Long-Range Sound Propagation, Milton Keynes, England, 147-157 (1992).

[42] X. Di and K.E. Gilbert, "An exact Laplace transform formulation for a point source above a ground surface," J. Acoust. Soc. Am. **93**, 714-720 (1993).

[43] X. Di and K.E. Gilbert, "The effect of turbulence and irregular terrain on outdoor sound propagation," Proc. Sixth Symposium on Long-Range Sound Propagation, Ottawa, Canada, 315-333 (1994).

[44] X. Di and K.E. Gilbert, "Wave propagation in a 3-D turbulent atmosphere: horizontal coherence," Proc. Eighth Symposium on Long-Range Sound Propagation, The Pennsylvania State University, Pennsylvania, 169-180 (1998).

[45] F.R. Dinapoli and R.L. Deavenport, "Numerical models of underwater acoustic propagation," in *Ocean Acoustics*, edited by J.A. DeSanto (Springer-Verlag, Berlin, 1979).

[46] A.P. Dowling and J.E. Ffowcs Williams, "Sound and sources of sound," (Ellis Horwood, Chichester, 1983).

[47] A.J. Dyer, "A review of flux-profile relations," Bound. Layer Meteor. **1**, 363-372 (1974).

[48] T.F.W. Embleton, J.E. Piercy, and N. Olson, "Outdoor sound propagation over ground of finite impedance," J. Acoust. Soc. Am. **59**, 267-277 (1976).

[49] T.F.W. Embleton, G.J. Thiessen, and J.E. Piercy, "Propagation in an inversion and reflections at the ground," J. Acoust. Soc. Am. **59**, 278-282 (1976).

[50] T.F.W. Embleton, J.E. Piercy, and G.A. Daigle, "Effective flow resistivity of ground surfaces determined by acoustical measurements," J. Acoust. Soc. Am. **74**, 1239-1244 (1983).

[51] T.F.W. Embleton, "Tutorial on sound propagation outdoors," J. Acoust. Soc. Am. **100**, 31-48 (1996).

[52] P. Filippi, D. Habault, J.P. Lefebvre, and A. Bergassoli, *Acoustics. Basic physics, theory and methods* (Academic, San Diego, 1999).

[53] J. Forssén, "Calculation of sound reduction by a screen in a turbulent atmosphere using the parabolic equation method," ACUSTICA Acta Acustica **84**, 599-606 (1998).

[54] J. Forssén, "Calculation of noise barrier performance in a turbulent atmosphere by using substitute sources above the barrier," ACUSTICA Acta Acustica **86**, 269-275 (2000).

[55] S.J. Franke and G.W. Swenson, jr., "A brief tutorial on the Fast Field Program (FFP) as applied to sound propagation in the air," Appl. Acoust. **27**, 203-215 (1989).

[56] K.E. Gilbert and M.J. White, "Application of the parabolic equation to sound propagation in a refracting atmosphere," J. Acoust. Soc. Am. **85**, 630-637 (1989).

[57] K.E. Gilbert, R. Raspet, and X. Di, "Calculation of turbulence effects in an upward-refracting atmosphere," J. Acoust. Soc. Am. **87**, 2428-2437 (1990).

[58] K.E. Gilbert and X. Di, "A fast Green's function method for one-way sound propagation in the atmosphere," J. Acoust. Soc. Am. **94**, 2343-2352 (1993).

[59] S.A.L. Glegg and J.R. Yoon, "Determination of noise source height, part I: the measurement of equivalent acoustic source height above a reflecting surface," J. Sound Vib. **143**, 19-37 (1990).

[60] S.A.L. Glegg and J.R. Yoon, "Determination of noise source heights, part II: measurement of the equivalent source height of highway vehicles," J. Sound Vib. **143**, 39-50 (1990).

[61] I.S. Gradshteyn and I.M. Ryzhik, *Table of Integrals, Series, and Products*, fifth edition, edited by A. Jeffrey (Academic Press, Boston, 1994).

[62] R.R. Greene, "The rational approximation to the acoustic wave equation with bottom interaction," J. Acoust. Soc. Am. **76**, 1764-1773 (1984).

[63] D. Heimann and G. Gross, "Coupled simulation of meteorological parameters and sound level in a narrow valley," Appl. Acoust. **56**, 73-100 (1999).

[64] A.A.M. Holtslag, "Estimates of diabatic wind speed profiles from near-surface weather observations," Boundary-Layer Meteorol. **29**, 225-250 (1984).

[65] D.C. Hothersall and J.N.B. Harriott, "Approximate models for sound propagation above multi-impedance plane boundaries," J. Acoust. Soc. Am. **97**, 918-926 (1995).

[66] U. Ingard, "A review of the influence of meteorological conditions on sound propagation," J. Acoust. Soc. Am. **25**, 405-411 (1953).

[67] U. Ingard and G.C. Maling, Jr., "On the effect of atmospheric turbulence on sound propagated over ground," J. Acoust. Soc. Am. **35**, 1056-1058 (1963).

[68] A. Ishimaru, *Wave Propagation and Scattering in Random Media. Volume 2: Multiple scattering, turbulence, rough surfaces, and remote sensing* (Academic, New York, 1978).

[69] F.B. Jensen, W.A. Kuperman, M.B. Porter, and H. Schmidt, *Computational Ocean Acoustics* (American Institute of Physics, New York, 1994).

[70] H.G. Jonasson, "Sound reduction by barriers on the ground," J. Sound Vib. **22**, 113-126 (1972).

[71] B.A. de Jong, A. Moerkerken, and J.D. van der Toorn, "Propagation of sound over grassland and over an earth barrier," J. Sound Vib. **86**, 23-46 (1983).

[72] M. Karweit, Ph. Blanc-Benon, D. Juvé, and G. Comte-Bellot, "Simulation of the propagation of an acoustic wave through a turbulent velocity field: a study of phase invariance," J. Acoust. Soc. Am. **89**, 52-62 (1991).

[73] Yu.A. Kravtsov, "Two new asymptotic methods in the theory of wave propagation in inhomogeneous media (review)," Sov. Phys. Acoust. **14**, 1-17 (1968).

[74] U.J. Kurze, "Noise reduction by barriers," J. Acoust. Soc. Am. **55**, 504-518 (1974).

[75] U. Kurze and L.L. Beranek, "Sound propagation outdoors," in *Noise and vibration control*, edited by L.L. Beranek (Institute of Noise Control Engineering, Washington DC, 1988), Chap. 7.

[76] Y.W. Lam and S.C. Roberts, "A simple method for accurate prediction of finite barrier insertion loss," J. Acoust. Soc. Am. **93**, 1445-1452 (1993).

[77] D. Lee and M.H. Schultz, *Numerical ocean acoustic propagation in three dimensions* (World Scientific, Singapore, 1995).

[78] D. Lee, A.D. Pierce, and E. Shang, "Parabolic equation development in the twentieth century," J. Comp. Acoust. **8**, 527-637 (2000).

[79] S.W. Lee, N. Bong, W.F. Richards, and R. Raspet, "Impedance formulation of the fast field program for acoustic wave propagation in the atmosphere," J. Acoust. Soc. Am. **79**, 628-634 (1986).

[80] A. L'Espérance, "The insertion loss of finite length barriers on the ground," J. Acoust. Soc. Am. **86**, 179-183 (1989).

[81] A. L'Espérance, P. Herzog, G.A. Daigle, and J.R. Nicolas, "Heuristic model for outdoor sound propagation based on an extension of the geometrical ray theory in the case of a linear sound speed profile," Appl. Acoust. **37**, 111-139 (1992).

[82] K.M. Li, "A high-frequency approximation of sound propagation in a stratified moving atmosphere above a porous ground surface," J. Acoust. Soc. Am. **95**, 1840-1852 (1994).

[83] I.V. Lindell and E. Alanen, "Exact image theory for the Sommerfeld half-space problem, part I: vertical magnetic dipole," IEEE Trans. Antennas Propagat. **AP-32**, 126-133 (1984).

[84] I.V. Lindell and E. Alanen, "Exact image theory for the Sommerfeld half-space problem, part II: vertical electric dipole," IEEE Trans. Antennas Propagat. **AP-32**, 841-847 (1984).

[85] D. Ludwig, "Uniform asymptotic expansions at a caustic," Commun. Pure Appl. Math. **19**, 215-250 (1966).

[86] Z. Maekawa, "Noise reduction by screens," Appl. Acoust. **1**, 157-173 (1968).

[87] M.J.M. Martens, L.A.M. van der Heijden, H.H.J. Walthaus, and W.J.J.M. van Rens, "Classification of soils based on acoustic impedance, air flow resistivity, and other physical soil properties," J. Acoust. Soc. Am. **78**, 970-980 (1985).

[88] J. Martin, "Simulation of wave propagation in random media: theory and applications," in *Wave propagation in random media (scintillation)*, edited by V.I. Tatarskii, A. Ishimaru, and V.U. Zavorotny (IOP Publishing and SPIE, Washington, 1993) p. 463-486.

[89] W.E. McBride, H.E. Bass, R. Raspet, and K.E. Gilbert, "Scattering of sound by atmospheric turbulence: predictions in a refractive shadow zone," J. Acoust. Soc. Am. **91**, 1336-1340 (1992).

[90] H. Medwin, "Shadowing by finite noise barriers," J. Acoust. Soc. Am. **69**, 1060-1064 (1981).

[91] P.M. Morse and H. Fesbach, *Methods of Theoretical Physics* (McGraw-Hill, New York, 1953).

[92] P.M. Morse and K.U. Ingard, *Theoretical Acoustics* (McGraw-Hill, New York, 1968).

[93] A. Muradali and K.R. Fyfe, "Accurate barrier modeling in the presence of atmospheric effects," Appl. Acoust. **56**, 157-182 (1999).

[94] L. Nijs and C.P.A. Wapenaar, "The influence of wind and temperature gradients on sound propagation, calculated with the two-way wave equation," J. Acoust. Soc. Am. **87**, 1987-1998 (1990). See also: J. Acoust. Soc. Am. **91**, 498-504 (1992).

[95] J.M. Noble, H.E. Bass, and R. Raspet, "The effect of large-scale atmospheric inhomogeneities on acoustic propagation," J. Acoust. Soc. Am. **92**, 1040-1046 (1992).

[96] C. Nocke, V. Mellert, T. Waters-Fuller, K. Attenborough, and K.M. Li, "Impedance deduction from broad-band, point-source measurements at grazing incidence," ACUSTICA Acta Acustica **83**, 1085-1090 (1997).

[97] V.E. Ostashev, F. Gerdes, V. Mellert, and R. Wandelt, "Propagation of sound in a turbulent medium. II. Spherical waves," J. Acoust. Soc. Am. **102**, 2571-2578 (1997).

[98] V.E. Ostashev, *Acoustics in Moving Inhomogeneous Media* (E&FN Spon, London, 1997).

[99] V.E. Ostashev, D. Juvé, and P. Blanc-Benon, "Derivation of a wide-angle parabolic equation for sound waves in inhomogeneous moving media," ACUSTICA Acta Acustica **83**, 455-460 (1997).

[100] V.E. Ostashev, E.M. Salomons, S.F. Clifford, R.J. Lataitis, D.K. Wilson, Ph. Blanc-Benon, and D. Juvé, "Sound propagation in a turbulent atmosphere near the ground: A parabolic equation approach," J. Acoust. Soc. Am. **109**, 1894-1908 (2001).

[101] P.H. Parkin and W.E. Scholes, "The horizontal propagation of sound from a jet engine close to the ground, at Radlett," J. Sound Vib. **1**, 1-13 (1964).

[102] P.H. Parkin and W.E. Scholes, "The horizontal propagation of sound from a jet engine close to the ground, at Hatfield," J. Sound Vib. **2**, 353-374 (1965).

[103] C.A. Paulson, "The mathematical representation of wind speed and temperature profiles in the unstable atmospheric surface layer," J. Appl. Meteor. **9**, 857-861 (1970).

[104] A.D. Pierce, "Diffraction of sound around corners and over wide barriers," J. Acoust. Soc. Am. **55**, 941-955 (1974).

[105] A.D. Pierce, "Wave equation for sound in fluids with unsteady inhomogeneous flow," J. Acoust. Soc. Am. **87**, 2292-2299 (1990).

[106] A.D. Pierce, *Acoustics. An Introduction to its Physical Principles and Applications* (American Institute of Physics, New York, 1991).

[107] A.D. Pierce, "Mathematical theory of wave propagation," in *Encyclopedia of Acoustics*, edited by M.J. Crocker (Wiley, New York, 1997), Chap. 2.

[108] J.E. Piercy, T.F.W. Embleton, and L.C. Sutherland, "Review of noise propagation in the atmosphere," J. Acoust. Soc. Am. **61**, 1403-1418 (1977).

[109] R. Pirinchieva, "Model study of the sound propagation behind barriers of finite length," J. Acoust. Soc. Am. **87**, 2109-2113 (1990).

[110] B. Plovsing, "Aircraft sound propagation over non-flat terrain. Development of prediction algorithms," report AV 1015/93, DELTA Acoustics & Vibration, 1993.

[111] E. Premat and Y. Gabillet, "A new boundary-element method for predicting outdoor sound propagation and application to the case of a sound barrier in the presence of downward refraction," J. Acoust. Soc. Am. **108**, 2775-2783 (2000).

[112] W.H. Press, B.P. Flannery, S.A. Teukolsky, and W.T. Vetterling, *Numerical Recipes. The Art of Scientific Computing* (Cambridge U.P., Cambridge, 1986).

[113] D.C. Pridmore-Brown, "Sound propagation in a temperature- and wind-stratified medium," J. Acoust. Soc. Am. **34**, 438-443 (1962).

[114] K.B. Rasmussen, "On the effect of terrain profile on sound propagation outdoors," J. Sound Vib. **98**, 35-44 (1985).

[115] K.B. Rasmussen, "Outdoor sound propagation under the influence of wind and temperature gradients," J. Sound. Vib. **104**, 321-335 (1986).

[116] K.B. Rasmussen, "Sound propagation from a point source over a two-impedance surface," Acta Acustica **2**, 173-177 (1994).

[117] K.B. Rasmussen, "Model experiments related to outdoor propagation over an earth berm," J. Acoust. Soc. Am. **96**, 3617-3620 (1994).

[118] K.B. Rasmussen and M. Galindo Arranz, "The insertion loss of screens under the influence of wind," J. Acoust. Soc. Am. **104**, 2692-2698 (1998).

[119] R. Raspet, S.W. Lee, E. Kuester, D.C. Chang, W.F. Richards, R. Gilbert, and N. Bong, "A fast-field program for sound propagation in a layered atmosphere above an impedance ground," J. Acoust. Soc. Am. **77**, 345-352 (1985).

[120] R. Raspet, G. Baird, and W. Wu, "Normal mode solution for low-frequency sound propagation in a downward refracting atmosphere above a complex impedance plane," J. Acoust. Soc. Am. **91**, 1341-1352 (1992).

[121] J.W.S. Rayleigh, *The Theory of Sound* (Dover, New York, 1945).

[122] J.S. Robertson, W.L. Siegmann, and M.J. Jacobson, "Low-frequency sound propagation modeling over a locally reacting boundary with the parabolic approximation," J. Acoust. Soc. Am. **98**, 1130-1137 (1995).

[123] J.S. Robertson, P.J. Schlatter, and W.L. Siegmann, "Sound propagation over impedance discontinuities with the parabolic approximation," J. Acoust. Soc. Am. **99**, 761-767 (1996).

[124] I. Rudnick, "Propagation of sound in the open air," in *Handbook of noise control*, edited by C.M. Harris (McGraw-Hill, New York, 1957) Chap. 3.

[125] S.M. Rytov, Yu.A. Kravtsov, and V.I. Tatarskii, *Principles of Statistical Radiophysics. Volume 3: Elements of Random Fields* (Springer-Verlag, Berlin, 1989).

[126] S.M. Rytov, Yu.A. Kravtsov, and V.I. Tatarskii, *Principles of Statistical Radiophysics. Volume 4: Wave Propagation through Random Media* (Springer-Verlag, Berlin, 1989).

[127] J.M. Sabatier, R. Raspet, and C.K. Frederickson, "An improved procedure for the determination of ground parameters using level difference measurements," J. Acoust. Soc. Am. **94**, 396-399 (1993).

[128] R.A. Sack and M. West, "Representation of elliptic by parabolic partial differential equations with an application to axially symmetric sound propagation," Appl. Acoust. **37**, 141-149 (1992).

[129] R.A. Sack and M. West, "A parabolic equation for sound propagation in two dimensions over any smooth terrain profile: the Generalised Terrain Parabolic Equation (GT-PE)," Appl. Acoust. **45**, 113-129 (1995).

[130] R.A. Sack and M. West, "The Lagrange Padé parabolic equation (LP-PE) for the prediction of long range sound propagation in the atmosphere," Appl. Acoust. **49**, 105-125 (1996).

[131] E.M. Salomons, "Downwind propagation of sound in an atmosphere with a realistic sound-speed profile: a semianalytical ray model," J. Acoust. Soc. Am. **95**, 2425-2436 (1994).

[132] E.M. Salomons, "Diffraction by a screen in downwind sound propagation: a parabolic-equation approach," J. Acoust. Soc. Am. **95**, 3109-3117 (1994).

[133] E.M. Salomons, "Sound propagation in complex outdoor situations with a non-refracting atmosphere: model based on analytical solutions for diffraction and reflection," ACUSTICA Acta Acustica **83**, 436-454 (1997).

[134] E.M. Salomons, "Improved Green's function parabolic equation method for atmospheric sound propagation," J. Acoust. Soc. Am. **104**, 100-111 (1998).

[135] E.M. Salomons, "Caustic diffraction fields in a downward refracting atmosphere," J. Acoust. Soc. Am. **104**, 3259-3272 (1998). Erratum: J. Acoust. Soc. Am. **106**, 3036 (1999).

[136] E.M. Salomons, "Reduction of the performance of a noise screen due to screen-induced wind-speed gradients. Numerical computations and wind-tunnel experiments," J. Acoust. Soc. Am. **105**, 2287-2293 (1999).

[137] E.M. Salomons and K.B. Rasmussen, "Numerical computation of sound propagation over a noise screen based on an analytic approximation of the wind speed field," Appl. Acoust. **60**, 327-341 (2000).

[138] E.M. Salomons, "Fluctuations of spherical waves in a turbulent atmosphere: effect of the axisymmetric approximation in computational methods," J. Acoust. Soc. Am. **108**, 1528-1534 (2000).

[139] E.M. Salomons, V.E. Ostashev, S.F. Clifford, and R.J. Lataitis, "Sound propagation in a turbulent atmosphere near the ground: An approach based on the spectral representation of refractive-index fluctuations," J. Acoust. Soc. Am. **109**, 1881-1893 (2001).

[140] B.D. Seckler and J.B. Keller, "Geometrical theory of diffraction in inhomogeneos media," J. Acoust. Soc. Am. **31**, 192-205 (1959).

[141] B.D. Seckler and J.B. Keller, "Asymptotic theory of diffraction in inhomogeneos media," J. Acoust. Soc. Am. **31**, 206-216 (1959).

[142] E. Skudrzyk, *The Foundations of Acoustics. Basic Mathematics and Basic Acoustics* (Springer-Verlag, New York, 1971).

[143] M. Spivack, "A numerical approach to rough-surface scattering by the parabolic equation method," J. Acoust. Soc. Am. **87**, 1999-2004 (1990).

[144] M.R. Stinson and Y. Champoux, "Propagation of sound and the assignment of shape factors in model porous materials having simple pore geometries," J. Acoust. Soc. Am. **91**, 685-695 (1992).

[145] R.B. Stull, *An Introduction to Boundary Layer Meteorology* (Kluwer, Dordrecht, 1991)

[146] L.C. Sutherland and G.A. Daigle, "Atmospheric sound propagation," in *Encyclopedia of Acoustics*, edited by M.J. Crocker (Wiley, New York, 1997), Chap. 32.

[147] S. Taherzadeh, K.M. Li, and K. Attenborough, "Sound propagation in a refracting medium above an uneven terrain," Proc. Eighth Symposium on Long Range Sound Propagation, The Pennsylvania State University, Pennsylvania, 101-111 (1998).

[148] F.D. Tappert, "The parabolic approximation method," in *Wave Propagation and Underwater Acoustics*, edited by J.B. Keller and J.S. Papadakis (Springer-Verlag, Berlin, 1977) p. 224-287.

[149] V.I. Tatarski, *Wave Propagation in a turbulent medium* (McGraw-Hill, New York, 1961).

[150] V.I. Tatarskii, *The Effects of the Turbulent Atmosphere on Wave Propagation* (U.S. Department of Commerce and the National Science Foundation, Washington, D.C., by the Israel Program for Scientific translations, 1971), TT-68-50464.

[151] P.A. Taylor and R.J. Lee, "Simple guidelines for estimating wind speed variations due to small scale topographic features," Climatological Bulletin **18**, 3-32 (1984).

[152] D.J. Thompson and N.R. Chapman, "A wide-angle split-step algorithm for the parabolic equation," J. Acoust. Soc. Am. **74**, 1848-1854 (1983).

[153] J.D. van der Toorn and W.J.A. van Vliet, "Emissiekentallen motorvoertuigen 2000, gebaseerd op metingen uit 1996 en 1999," TNO report HAG-RPT-000048, May 2000 (in Dutch).

[154] B.J. Uscinski, "Sound propagation with a linear sound-speed profile over a rough surface," J. Acoust. Soc. Am. **94**, 491-498 (1993).

[155] M. West, R.A. Sack, and F. Walkden, "The Fast Field Program (FFP). A second tutorial: application to long range sound propagation in the atmosphere," Appl. Acoust. **33** 199-228 (1991).

[156] M. West, K. Gilbert, and R.A. Sack, "A tutorial on the parabolic equation (PE) model used for long range sound propagation in the atmosphere," Appl. Acoust. **37**, 31-49 (1992).

[157] F.M. Wiener and D.N. Keast, "Experimental study of the propagation of sound over ground," J. Acoust. Soc. Am. **31**, 724-733 (1959).

[158] D.K. Wilson, "Sound field computations in a stratified, moving medium," J. Acoust. Soc. Am. **94**, 400-407 (1993).

[159] D.K. Wilson, J.G. Brasseur, and K.E. Gilbert, "Acoustic scattering and the spectrum of atmospheric turbulence," J. Acoust. Soc. Am. **105**, 30-34 (1999).

[160] D. Zhu and L. Bjørnø, "A hybrid 3-D, two-way IFD PE model for 3-D acoustic backscattering," J. Comp. Acoust. **7**, 133-145 (1999).

[161] C. Zwikker and C.W. Kosten, *Sound Absorbing Materials* (Elsevier, New York 1949).

List of symbols

Notation for time averages (see Secs. A.2, B.2, B.3, I.4, K.2, N.4)
A time average over acoustic fluctuations is denoted by a subscript 'av', for example in $(p^2)_{\mathrm{av}}$.
A time average over turbulent fluctuations is denoted by a line above the symbol, for example in $\overline{\chi}$.

Notation for vectors
Boldfaced symbols are used for vectors, for example $\mathbf{r} = (x, y, z)$.

Notation for derivatives
$\partial_x f \equiv \partial f/\partial x$ partial derivative of function f.
$\partial_x^2 f \equiv \partial^2 f/\partial x^2$ second derivative of function f.
$f'(x) \equiv df/dx$ derivative of function $f(x)$.
$D/Dt \equiv \partial/\partial t + \mathbf{v} \cdot \nabla$ (total) time derivative in frame moving with velocity $\mathbf{v}$.
$\nabla \equiv (\partial_x, \partial_y, \partial_z)$ (in rectangular xyz coordinates).
$\nabla f = (\partial_x f, \partial_y f, \partial_z f)$ gradient of scalar function f.
$\nabla \cdot \mathbf{v} = \partial_x v_x + \partial_y v_y + \partial_z v_z$ divergence of vector function $\mathbf{v} = (v_x, v_y, v_z)$.

Roman symbols
a sound speed gradient in linear sound speed profile $c(z) = c_0 + az$,
correlation length of turbulent refractive-index fluctuations,
initial value of ξ coordinate in GTPE range step.
$\overline{a}$ quantity defined below Eq. (M.42).
$\overline{\overline{a}}$ quantity defined below Eq. (M.47).
a_2, a_4, a_6, a_8 constants in PE starting field (Secs. G.12 and H.10).
a_k pole in residue theorem (H.33).
$\arg(z)$ argument of complex number z, $\arg(z) = \arctan[\mathrm{Im}(z)/\mathrm{Re}(z)]$.
A amplitude of sound wave,
quantity defined in Eq. (D.40),
quantity defined below Eq. (I.53).
A_0, A_2, A_4, A_6, A_8 constants in PE starting field (Secs. G.12 and H.10).
A_j constant in Eq. (F.5).
A_m (complex) amplitude of sound ray m.
A_{t} absorption parameter for top layer in PE grid (Sec. G.9).
$A_D(X)$ function defined in Eq. (O.6).
A_R coefficient defined in Eq. (M.24).
$\mathrm{Ai}(t)$ Airy function, defined in Eq. (L.24)
b parameter of logarithmic sound speed profile (4.5),

b final value of ξ coordinate in GTPE range step.
b_1, b_2 quantities defined in Eqs. (B.44) and (B.45).
b_2, B constants in PE starting field (Secs. G.12 and H.10).
b_t, b_u, b_v parameters in profiles (4.12), (4.13), and (4.14).
B correlation function of random function,
correlation function of refractive-index fluctuations.
B_{ij} correlation function of components i and j of random vector function,
correlation function of components i and j of wind velocity fluctuations.
B_j constant in Eq. (F.5).
B_m correlation functions $B_1 \equiv B_\chi$ and $B_2 \equiv B_S$ in Eq. (K.9).
B_{rr} longitudinal correlation function.
B_{tt} transverse correlation function.
B_R coefficient defined in Eq. (M.24).
B_S correlation function of phase fluctuations.
B_T correlation function of temperature fluctuations.
B_χ correlation function of log-amplitude fluctuations.
c (adiabatic) sound speed,
effective sound speed ($c \equiv c_{\text{eff}}$).
c' sound speed in ground (Sec. D.3).
c_0 sound speed at ground surface ($z = 0$),
sound speed at temperature T_0 (*e.g.* $c_0 = 331$ m/s at $T_0 = 273$ K),
average sound speed in turbulence models (see Sec. I.2).
c_1, c_2 sound speeds indicated in Figs. 4.1 and 4.2,
sound speeds above and below ground surface, respectively (Sec. D.4).
c_1, c_2, c_3 quantities defined in Eq. (M.29).
c_{eff} effective sound speed.
c_k residue in residue theorem (H.33).
$c_n^{\pm}$ quantities defined in Eq. (G.48).
c_{p} specific-heat coefficient of air at constant pressure.
c_{s} structure constant of porous medium.
c_{v} specific-heat coefficient of air at constant volume.
C closed integration contour,
constant in Kolmogorov spectrum in Appendix I.
$C, C_{\text{p}}, C_{\text{s}}$ reflection coefficients in PE starting field.
C_1, C_2, C_3, C_4 constants in Eq. (D.36).
C_m reflection coefficient for sound ray m.
C_{sat} quantity defined in Eq. (B.50).
C_v^2 structure parameter of turbulent wind velocity fluctuations.
C_T^2 structure parameter of turbulent temperature fluctuations.
d thickness of porous layer (Fig. C.4),
numerical distance defined in Eq. (D.57),
quantity defined in Eq. (M.46).
d_1, d_2, d_3 quantities defined in Eq. (M.30).
$d_{\text{s}}, d_{\text{r}}, d_{\text{is}}, d_{\text{ir}}$ diffraction distances in Fig. O.1.
d_{t} quantity defined in Eq. (M.51).

d_x, d_y, d_z finite dimensions of source in Fig. 3.13.
D ray tube diameter,
diagonal PE matrix (G.29),
structure function of random function,
structure function of refractive-index fluctuations,
diffraction coefficient (Sec. O.2).
D_1, D_2, D_3, D_4 diffraction coefficients (Sec. O.2).
D_{free} ray tube diameter in free field.
D_{ij} structure function of components i and j of random vector function,
structure function of components i and j of wind velocity fluctuations.
D_{rr} longitudinal structure function.
D_{tt} transverse structure function.
$\mathbf{e}_x, \mathbf{e}_y, \mathbf{e}_z$ unit vectors in positive x, y, and z directions, respectively.
$\text{erf}(x)$ error function.
$\text{erfc}(x)$ complementary error function.
$E_1(z)$ exponential integral function (Sec. G.12.3).
f frequency.
$f(x)$ general notation for function.
$f(X)$ auxiliary Fresnel function.
f_c center frequency of 1/3-octave or octave band.
$f_{c,m}$ center frequency of 1/3-octave or octave band m.
f_m focusing factor for sound ray m.
f_n frequency of interference minimum, Eqs. (3.11) and (3.12),
frequency of harmonic component n in spectral decomposition,
functions defined below Eq. (G.50).
$f_{r,N}, f_{r,O}$ relaxation frequencies of nitrogen and oxygen, respectively.
f_D Doppler factor in Sec. B.6.
F function in spectral theorem (H.51),
two-dimensional spectral density of random function,
two-dimensional spectral density of refractive-index fluctuations.
$F(d)$ boundary loss factor defined in Eq. (D.60).
$F(k_r)$ function defined below Eq. (F.33).
$F(k_z)$ phase function in Eqs. (G.55) and (H.63).
F_{ij} two-dimensional spectral density of components i and j of random vector function,
two-dimensional spectral density of components i and j of wind velocity fluctuations.
F_T two-dimensional spectral density of temperature fluctuations [below Eq. (I.47)].
g grain shape factor of porous medium,
gravitational acceleration,
Green's function,
phase function defined in Eq. (E.44).
$g(x)$ general notation for function.
$g(X)$ auxiliary Fresnel function.

g_0, g_1 functions in Eq. (L.22).
g_2 two-dimensional Green's function (Sec. H.3).
g_3 three-dimensional Green's function (Sec. H.3).
G spatial Fourier transform of Green's function g,
'mode amplitude' in Eqs. (J.24) and (J.34).
$G(k_r)$ function defined below Eq. (F.33).
h maximum height of sound ray (Fig. 4.9),
humidity, molar concentration of water vapour in the atmosphere,
normal distance from curved ground surface (Sec. M.2).
h_n maximum height of sound ray with n turning points [Equation (4.9)].
h_{nj} maximum height of sound ray with indices n and j.
H height of noise screen.
$H(x)$ Heaviside step function in Sec. D.4,
terrain profile in GTPE method.
H_1 square-root operator defined in Eq. (G.13).
H_2 operator defined in Eq. (G.8).
$H_1(x,\kappa), H_2(x,\kappa)$ functions defined below Eq. (K.9).
H_{1a} operator defined below Eq. (H.46).
H_{2a} operator defined below Eq. (H.45).
$H_0^{(1)}(x)$ Hankel function of first kind and order zero.
$H_{j,j+m}^{(n)}$ quantities defined in Eqs. (G.49) and (G.50).
I general symbol for integral.
$\mathbf{I}$ acoustic intensity, $\mathbf{I} = p\mathbf{v}$.
$\mathbf{I}_{av}$ average acoustic intensity.
I_{av} magnitude of $\mathbf{I}_{av}$, $I_{av} = |\mathbf{I}_{av}|$.
I_R integral defined in Eq. (M.21).
$I_\alpha, I_\chi, I_\gamma$ integrals defined in Eq. (M.17).
$\mathrm{Im}(z)$ imaginary part of complex number z.
j integral number.
J Jacobian defined in Eq. (M.4).
$J_n(x)$ Bessel function of order n.
k wave number ($k = \omega/c$ in air; for porous media, see Sec. C.4),
effective wave number $k \equiv k_{\mathrm{eff}}$,
wave number $k \equiv k_{\mathrm{m}}$, see Eq. (F.2).
$\mathbf{k}$ wave number vector, for example in Eq. (I.19).
k' wave number in ground (Sec. D.3).
k_0 wave number in ground in Appendix F,
wave number at ground surface in PE methods.
k_1, k_2 wave numbers above and below ground surface, respectively (Sec. D.4).
k_2, k_3 vectors (M.56) and (M.54).
k_a reference value of wave number $k(z)$ at some average height or at ground surface, in PE methods (Secs. G.3 and H.6).
k_{eff} effective wave number, $k_{\mathrm{eff}} = \omega/c_{\mathrm{eff}}$ (often $k \equiv k_{\mathrm{eff}}$).
k_i small imaginary part of wave number (Sec. 2.5).

k_{jz} wave number defined in Eq. (D.37).
k_{m} generalized wave number for moving atmosphere, defined in Eq. (E.30).
$k_{\max}$ wave number in exponential cut-off factor (Sec. I.7.1).
$k_{\mathrm{m}z}$ wave number defined in Eq. (E.31).
$k_{n,\max}$ maximum wave number defined in Sec. J.3.3.
$k_{nx}, k_{ny}, k_{nz}, k_{nr}$ components of wave number vector $\mathbf{k}_n$ (Secs. J.3 and J.4).
$k_{r\phi}$ wave number corresponding to $r\phi - r\phi'$ by Fourier transformation, in Eq. (H.82).
k_{s} real part of k_r in Eq. (F.23).
$k_{\mathrm{s}x}$ real part of k_x in Eq. (F.25).
$k_{\mathrm{s}y}$ real part of k_y in Eq. (F.25).
k_{t} small positive number in Eqs. (F.23) and (F.25).
k_{v} vertical wave number defined in Eqs. (H.27) and (H.85).
k_x, k_y, k_r wave numbers corresponding to x, y, r by Fourier transformation.
k_x, k_y quantities defined below Eq. (D.1).
k'_x, k'_y quantities defined below Eq. (D.3).
k_x, k_y, k_z components of vector $\mathbf{k}$ in Eq. (I.25).
k_z wave number corresponding to z by Fourier transformation,
wave number related to k_x and k_y or k_r by Eqs. (F.2) and (F.3),
integration variable in Eq. (G.53).
k_ϕ wave number related to $k_{r\phi}$ by $k_\phi = k_{r\phi} r$.
K integral number,
constant in Eq. (A.6).
K_0 parameter of von Karman turbulence spectrum.
K_m number of touched caustics in Eq. (L.36).
K_{nj} number of caustics touched by ray with indices n and j.
$K_\nu(x)$ modified Bessel function of order ν.
l size of turbulent eddy.
l_0 size of smallest eddies, inner scale of turbulence.
$\lg(x)$ logarithm of x to the base 10.
$\ln(x)$ logarithm of x to the base e (natural logarithm).
L characteristic length (Sec. I.3),
size of largest eddies, outer scale of turbulence,
horizontal distance between source and receiver (Appendix K),
Obukhov length.
L_1 operator (M.14).
L_{in} inner scale of turbulence.
L_{out} outer scale of turbulence.
L_p sound pressure level.
$L_{p,\mathrm{free}}$ sound pressure level of free field.
L_{A} A-weighted sound pressure level.
L_W sound power level.
m index of 1/3-octave or octave band,
index of sound ray, *e.g.* in Eq. (4.7).
m_2, m_3 vectors (M.59) and (M.58).

m_x, m_y quantities defined below Eq. (E.30).
m_{xj} quantities given in Table L.1.
M integral number.
M_1, M_2 tridiagonal PE matrices.
M^-, M^+ tridiagonal PE matrices.
$M^{\pm}_{m,j}$ matrix elements (G.47).
n integral number,
acoustic refractive index,
index of harmonic component in spectral decomposition,
number of turning points of sound ray.
$\mathbf{n}$ unit normal vector.
N integral number.
N_m number of ground reflections of sound ray m.
N_{nj} number of ground reflections of sound ray with indices n and j.
N_{pr} Prandtl number.
N_{rays} number of sound rays.
N_{R} Reynolds number.
p acoustic pressure or sound pressure,
in Appendices H and M: complex pressure amplitude $p \equiv p_{\mathrm{c}}$,
in Appendix L: normalized complex pressure amplitude $p_{\mathrm{c}}/|p_{\mathrm{free}}|$,
in Appendix N: total pressure of atmosphere,
exponent $p = 2/3$ in Sec. I.7.
p_1, p_2 complex pressure amplitudes of direct and reflected fields in Eq. (K.1),
complex pressure amplitudes above and below ground surface (Sec. D.4).
p_{a} total pressure of atmosphere, $p_{\mathrm{a}} = p_{\mathrm{av}} + p$.
p_{av} average pressure of atmosphere.
p_{c} complex amplitude of acoustic pressure (complex pressure amplitude).
$p_{\mathrm{c,i}}$ complex pressure amplitude of incident wave.
$p_{\mathrm{c,r}}$ complex pressure amplitude of reflected wave.
p_{free} complex pressure amplitude of free field.
p_{illum} contribution to field p in Appendix L, defined below Eq. (L.1).
p_j complex pressure amplitude at height z_j, $p_j = p_{\mathrm{c}}(z_j)$ (Secs. G.8 and G.9).
p_m contribution of ray m to field p, given by Eqs. (L.28) and (L.38).
p_{r} atmospheric pressure $p_{\mathrm{r}} = 101\,325$ Pa (Sec. B.5).
$p_{\mathrm{r}}, p_{\mathrm{i}}$ real and imaginary parts of $p_{\mathrm{c}} = p_{\mathrm{r}} + ip_{\mathrm{i}}$ (Sec. B.2).
p_{ref} reference sound pressure (20 μPa).
$p_{\mathrm{s}}, p_{\mathrm{is}}$ source and image source contributions to p_1, above Eq. (D.52).
p_{sat} saturation vapour pressure (Sec. B.5).
p_{shadow} contribution to field p in Appendix L, defined below Eq. (L.1).
P Fourier transform of time signal $p(t)$,
(spatial) Fourier transform of $p_{\mathrm{c}}(\mathbf{r})$.
P_1, P_2 Fourier transforms of p_1 and p_2 (Sec. D.4).
$P_{\mathrm{c},n}$ Fourier coefficients related to P_n by Eq. (B.25).
P_j value of P in layer j [Equation (F.5)].
P'_j derivative of P_j.

P_{mu}, P_{ml} values of P at source height in FFP method, defined in Sec. F.3.
P_n Discrete Fourier Transform of time signal $p(t)$, defined in Eq. (B.22).
P_s, P_{is} source and image source contributions to P_1 [Equation (D.44)].
q tortuosity of porous medium,
integration variable (Sec. D.4),
quantity defined in Eq. (G.2) ($q \equiv q_c$).
$q_0(z)$ PE starting function for unbounded atmosphere.
q_c quantity defined in Eq. (C.11),
quantity defined in Eq. (G.2) ($q \equiv q_c$).
Q spherical-wave reflection coefficient,
Fourier transform of quantity q_c (Appendix H),
quantity defined below Eq. (E.23),
operator in spectral theorem (H.51).
Q_j value of Q in layer j (Sec. F.7).
Q'_j derivative of Q_j (Sec. F.7).
Q_{mu}, Q_{ml} values of Q at source height in FFP method, defined in Sec. F.7.
Q_s, Q_r spherical-wave reflection coefficients in Sec. O.2.
r distance,
horizontal range.
$\mathbf{r}$ position vector.
r_1, r_2 distances indicated in Fig. 4.2.
r_h relative humidity (in %).
r_{nj} horizontal distance covered by ray with indices n and j.
r_s source range ($r_s = 0$).
$\mathbf{r}_s$ source position vector.
r_t range of screen in Fig. O.1.
R distance,
radius of circle (segment),
constant in ideal-gas law (A.10),
plane-wave reflection coefficient (Sec. F.7),
quantity $R = \alpha, \chi, \gamma$ (Sec. M.3.4).
$\mathbf{R}$ position vector.
R_1 distance between source and receiver (Fig. D.2).
R_2 distance between image source and receiver (Fig. D.2).
R_1, R_2, R_3, R_4 path lengths of diffracted rays in Eq. (O.2).
R_c radius of curvature.
$R_p, R(k_z)$ plane-wave reflection coefficient.
R_A quantity defined in Eq. (B.37).
$\mathrm{Re}(z)$ real part of complex number z.
s path length along sound ray,
(propagation) distance,
operator defined in Eq. (G.11).
$s(q)$ image source distribution (Sec. D.4).
$s(z)$ fractional speed-up factor (Sec. O.4).
$\mathbf{s}$ separation vector (Secs. J.3 and J.4).

s_a, s_b, s_c, s_d speed-up factors given by Eq. (O.10).
s_f pore shape factor ratio of porous medium.
S constant in expression $p_c = S\exp(ikr)/r$ for spherical wave, turbulent phase fluctuation.
$S(k_z)$ amplitude in Eqs. (G.53) and (H.61).
S_2, S_3 tridiagonal matrices in Eq. (M.60).
S_c closed surface, for example in Gauss' theorem (A.25).
S_m turbulent phase fluctuation of ray m.
S_δ factor in Eq. (F.1).
t time.
t_m acoustic travel time along sound ray m.
t_{nj} acoustic travel time along sound ray with indices n and j.
T period of harmonic sound wave, absolute temperature, tridiagonal PE matrices (G.28) and (G.43).
T_0 constant temperature in Eq. (A.15) ($T_0 = 273$ K), average temperature in turbulence models (see Sec. I.2).
T_{01} triple-point temperature of water (Sec. B.5).
T_{20} temperature $T_{20} = 293.15$ K (Sec. B.5).
T_2, T_3 tridiagonal matrices (M.55) and (M.53).
T_p plane-wave transmission coefficient.
T_t turbulent temperature fluctuation.
u horizontal component of wind velocity (in the direction of sound propagation), horizontal component of acoustic fluid velocity $\mathbf{v}$, quantity defined in Eq. (M.44).
u' turbulent wind velocity component (Appendix N).
u_* friction velocity defined in (N.9).
$u(z)$ horizontal wind speed profile.
$u_0(z)$ horizontal wind speed profile (O.7).
u_{10} wind speed at a height of 10 m (Chap. 7 and Appendix O).
u_2, u_3, u_4 wind speeds defined below Eq. (O.8).
u_{av} horizontal component of average fluid velocity $\mathbf{v}_{av}$.
u_t quantity defined in Eq. (M.49), turbulent wind velocity fluctuation.
U Fourier transform of velocity u, defined in Eq. (E.17).
U_m quantity defined below Eq. (L.41).
v horizontal component of wind velocity, horizontal component of acoustic fluid velocity $\mathbf{v}$, velocity of moving source in Fig. B.2, fluid velocity in x direction (Appendix C), characteristic velocity (Sec. I.3), quantity defined in Eq. (M.44).
$\mathbf{v}$ acoustic fluid velocity, $\mathbf{v} = (u, v, w)$.
v' turbulent wind velocity component (Appendix N).

$v_0(z)$ function defined below Eq. (O.10).
$\mathbf{v}_a$ fluid velocity, $\mathbf{v}_a = \mathbf{v}_{av} + \mathbf{v}$.
$\mathbf{v}_{av}$ average fluid velocity, $\mathbf{v}_{av} = (u_{av}, v_{av}, w_{av})$.
v_{av} horizontal component of average fluid velocity $\mathbf{v}_{av}$.
$\mathbf{v}_c$ complex amplitude of acoustic fluid velocity (complex fluid velocity amplitude, complex velocity amplitude).
v_c magnitude of $\mathbf{v}_c$ (Sec. B.3),
complex fluid velocity amplitude in x direction (Appendix C).
$v_{c,n}$ component of $\mathbf{v}_c$ normal to ground surface, in downward direction.
$v_{c,x}$ x component of $\mathbf{v}_c$ (Appendix D).
v_i velocity components in Eq. (I.9).
v_l' fluctuation of velocity in Sec. I.3.
v_n quantity $v_n \equiv v_{c,n}$ (Sec. M.3.6).
v_r radial component of velocity of moving source in Fig. B.2.
v_r longitudinal component of velocity (Sec. I.5).
$\mathbf{v}_r, \mathbf{v}_i$ real and imaginary parts of $\mathbf{v}_c = \mathbf{v}_r + i\mathbf{v}_i$ (Sec. B.2).
v_t quantity defined in Eq. (M.49).
V Fourier transform of velocity v, defined in Eq. (E.17),
(integration) volume,
one-dimensional spectral density of random function,
one-dimensional spectral density of refractive-index fluctuations.
w vertical component of wind velocity,
vertical component of acoustic fluid velocity $\mathbf{v}$,
acoustic energy density (Sec. B.2),
integration variable in Eq. (H.32),
quantity defined in Eq. (M.44).
w' turbulent wind velocity component (Appendix N).
w_{av} vertical component of average fluid velocity $\mathbf{v}_{av}$.
w_t quantity defined in Eq. (M.49).
W Fourier transform of velocity W, defined in Eq. (E.17).
W_{av} average acoustic power.
W_{ref} reference acoustic power (1 pW).
W_A A-weighting function, defined in Eq. (B.36).
x coordinate of xyz coordinate system,
x coordinate of receiver,
symbol for position in Sec. L.4,
quantity defined below Eq. (N.23).
x_r x coordinate of receiver in Fig. 4.2.
x_s x coordinate of source.
X function defined in Eq. (O.5).
y coordinate of xyz coordinate system,
y coordinate of receiver,
integration variable in Eq. (L.9),
quantity defined in Eq. (M.44).
y_s y coordinate of source.

y_t quantity defined in Eq. (M.49).
z height above ground surface,
coordinate of xyz coordinate system,
z coordinate of receiver, receiver height.
z_0 roughness length of ground surface,
height of ground surface, $z_0 = 0$ (Appendix G).
z_1 height indicated in Figs. 4.1 and 4.2.
z_2, z_3, z_4 heights defined below Eq. (O.8).
z_g z coordinate of ground surface, $z_g = 0$ (Appendix L).
z_r z coordinate of receiver (Fig. 4.2 and Appendix L).
z_s z coordinate of source, source height.
z_{sr} average of source height and receiver height, defined below Eq. (4.9).
z_t height of bottom of absorbing layer in PE grid (Fig. G.1).
screen height in Fig. O.1.
z_M height of PE grid, $z_M = M\Delta z$ (Fig. G.1).
Z normalized (specific) acoustic impedance, $Z = \zeta/\zeta_{air}$.
$Z(x, \beta)$ amplitude function in Eq. (L.17).
Z_2 normalized impedance of backing of porous layer (Fig. C.4).
Z_{layer} normalized impedance of porous layer (Sec. C.6).
Z_m quantity defined in Eq. (L.20).
Z_s normalized acoustic impedance of (ground) surface.

Greek symbols

α atmospheric absorption coefficient (in dB per unit length),
integration variable in Eq. (E.59),
quantity defined below Eq. (G.21),
random angle for calculation of turbulent refractive-index field.
$\alpha(\xi)$ function defined in Eq. (M.15).
α' atmospheric absorption coefficient related to α by $\alpha' = \alpha/(10 \lg e)$.
α_0 dry adiabatic lapse rate, defined in Eq. (N.2).
α_m phase angle in Eq. (L.40).
α_H local slope of curved ground surface, defined in Eq. (M.37).
β imaginary part of wave number (Sec. E.6),
quantity defined below Eq. (G.21),
quantity defined below Eq. (H.31),
integration variable in Eq. (L.17).
$\beta(\xi)$ function defined in Eq. (M.15).
β_m phase angle in Eq. (L.41).
γ elevation angle, $\gamma = \arctan(dz/dx)$,
specific-heat ratio c_p/c_v ($\gamma = 1.4$ for air),
quantity defined below Eq. (D.67),
contribution to wave number from atmospheric absorption (Sec. E.6),
quantity defined below Eq. (G.24).
$\gamma(\eta)$ function defined in Eq. (M.15).
γ_1, γ_2 elevation angles indicated in Figs. 4.1 and 4.2.

$\gamma_{1,j}, \gamma_{0,j}, \gamma_{-1,j}$ matrix elements (G.44).
$\gamma_{\max}$ maximum elevation angle for validity of PE method (Fig. 4.11).
γ_r, γ_r' elevation angles at receiver (Sec. L.3.6).
γ_s, γ_s' elevation angles at source (Sec. L.3.6).
γ_T, γ_v quantities defined below Eq. (K.11).
Γ coherence factor.
$\Gamma(x)$ gamma function.
δ azimuthal angle of pie slice region in Figs. 4.13 and H.6,
matrix (M.32).
δ^2 matrix (M.31).
$\delta(x)$ Dirac delta function.
$\delta(\mathbf{r})$ product of Dirac delta functions, $\delta(\mathbf{r}) = \delta(x)\delta(y)\delta(z)$ for $\mathbf{r} = (x, y, z)$.
δ_{ij} Kronecker delta, $\delta_{ij} = 1$ for $i = j$, $\delta_{ij} = 0$ for $i \neq j$.
$\delta_s, \delta_r, \delta_g$ horizontal dimensions of ray segments, defined in Eq. (L.6).
∂_x partial derivative $\partial_x \equiv \partial/\partial x$.
$\delta_x(h), \delta_x^*(h)$ functions defined in Sec. L.3.1.
$\delta k(z)$ quantity defined below Eq. (H.58).
$\delta k^2(z)$ quantity defined in Eqs. (G.9) and (H.44).
δt time interval.
$\delta\gamma_s$ quantity defined above Eq. (L.15).
Δk wave number spacing.
Δk_ϕ spacing of wave numbers k_ϕ in three-dimensional GFPE method.
Δr horizontal grid spacing (or range step) in PE method.
Δz vertical grid spacing in FFP and PE methods.
ΔL relative sound pressure level.
$\Delta\phi$ spacing of azimuthal angles ϕ in three-dimensional GFPE method.
$\Delta\eta$ grid spacing along η coordinate in GTPE method.
$\Delta\xi$ grid spacing along ξ coordinate in GTPE method.
ϵ quantity defined below Eq. (D.66),
energy dissipation rate of smallest turbulent eddies,
quantity defined in Eq. (M.45),
general symbol for 'small' number.
ϵ_t quantity defined in Eq. (M.50).
ϕ phase angle,
azimuthal angle in cylindrical coordinate system (Figs. 4.10 and E.1),
spherical coordinate below Eq. (I.21),
random angle for calculation of turbulent refractive-index field.
$\phi(x, \beta)$ factor of phase function $k\phi(x, \beta)$ in Eq. (L.17).
ϕ_0 angle indicated in Fig. M.3.
ϕ_1, ϕ_2 azimuthal angles of vertical edges of finite screen (Sec. O.3).
ϕ_m phase angle of sound ray m.
$\phi_s, \phi_r, \phi_{is}, \phi_{ir}$ diffraction angles indicated in Fig. O.1.
ϕ_t dimensionless temperature derivative (N.8).
ϕ_v velocity potential (Sec. E.2.2).
ϕ_w dimensionless wind speed derivative (N.7).

Φ three-dimensional spectral density of random function,
three-dimensional spectral density of refractive-index fluctuations.
Φ_{ij} three-dimensional spectral density of components i and j of random vector function,
three-dimensional spectral density of components i and j of wind velocity components.
Φ_{v} Fourier transform of velocity potential ϕ_{v} (Sec. E.2.2).
Φ_T three-dimensional spectral density of temperature fluctuations [below Eq. (I.47)].
φ random angle for calculation of turbulent refractive-index field.
χ turbulent log-amplitude fluctuation,
quantity defined below Eq. (H.73).
$\chi(\xi)$ function defined in Eq. (M.18).
χ_m turbulent log-amplitude fluctuation of ray m.
η quantity defined below Eq. (E.22),
viscosity,
vertical coordinate in GTPE method.
κ von Karman constant ($\kappa = 0.41$),
wave number corresponding to Δr by Fourier transformation, Eq. (H.22).
λ wavelength.
μ turbulent fluctuation of acoustic refractive index n,
quantity defined below Eqs. (F.34), (L.20), and (P.2).
μ_0 standard deviation of refractive-index fluctuations.
μ_2 average refractive-index fluctuation defined in Eq. (J.13).
ν kinematic viscosity,
quantity defined below Eq. (H.73).
θ reflection angle (Fig. D.2, $\theta_{\mathrm{i}} = \theta_{\mathrm{r}} = \theta$),
spherical coordinate below Eq. (I.21),
random angle for calculation of turbulent refractive-index field,
variable in phase function (L.21),
potential temperature.
θ' turbulent fluctuation of potential temperature,
angle in Figs. C.1 and D.1.
θ_* quantity defined in Eq. (N.10).
θ_0 surface potential temperature, defined above Eq. (N.16).
$\theta_{\mathrm{i}}, \theta_{\mathrm{r}}$ angles of incidence and reflection, respectively, in Figs. C.1 and D.1.
θ_{mn} angle defined below Eq. (F.25).
$\theta_{\mathrm{s}}, \theta_{\mathrm{r}}$ reflection angles in Fig. O.1.
θ_{v} virtual potential temperature.
Θ average turbulent phase fluctuation defined in Eq. (J.15).
ϑ argument of spherical-wave reflection coefficient $Q = |Q| \exp(i\vartheta)$.
ρ (acoustic) density of atmosphere (see ρ_{a} and ρ_{av}),
distance,
distance defined below Eqs. (I.48) and (I.52),
variable in phase function (L.21).

ρ' density of ground (Sec. D.3).
ρ_0 density of air at temperature $T_0 = 273$ K ($\rho_0 = 1.29$ kg·m^{-3}).
ρ_1, ρ_2 densities above and below ground surface, respectively (Sec. D.4).
ρ_a density of atmosphere (mass per unit volume), $\rho_a = \rho_{av} + \rho$.
ρ_{av} average density of atmosphere (subscript 'av' omitted except in Appendices A and E; see Sec. A.2).
ρ_r quantity defined below Eq. (B.43),
quantity defined in Sec. L.3.6.
ρ_{sat} quantity defined below Eq. (B.48).
σ (effective) flow resistivity of ground.
σ_1, σ_2 coefficients in Eq. (G.25).
σ_v standard deviation of wind speed fluctuations.
σ_T standard deviation of temperature fluctuations.
τ sample time,
time interval,
integration variable in spectral theorem (H.51),
shear stress (Fig. I.2),
integration variable in Eq. (K.9).
integration variable in Eq. (L.24).
τ_1, τ_2 coefficients in Eq. (G.26).
τ_l period of turbulent fluctuation.
τ_r quantity defined below Eq. (B.43).
τ_s, τ_r, τ_g travel times along ray segments, defined in Eq. (L.12).
τ_t period of turbulent fluctuation.
τ_ω period of harmonic oscillation.
ω angular frequency.
Ω porosity of porous medium,
Fourier transform of density ρ, defined in Eq. (E.17).
ξ variable in phase function (L.21),
horizontal coordinate in GTPE method.
ψ quantity defined in Eqs. (G.4) and (M.11),
angle defined above Eq. (E.58),
turbulent complex phase fluctuation.
$\vec{\psi}(r)$ vector defined below Eq. (G.22).
$\vec{\psi}(\xi)$ vector defined below Eq. (M.25).
ψ_j value of ψ at height z_j, $\psi_j = \psi(z_j)$, with $\psi_0 = \psi(0)$ (Appendix G),
value of ψ at height z_j, $\psi_j = \psi(\xi, z_j)$, with $\psi_0 = \psi(\xi, 0)$ (Appendix M).
ψ_m turbulent complex phase fluctuation of ray m.
ψ_w, ψ_t functions defined in Eqs. (N.18) and (N.19).
Ψ Fourier transform of ψ defined in Eq. (H.50).
Υ function defined in Eqs. (J.27) and (J.36).
ζ (specific) acoustic impedance of propagation medium.
ζ_{air} (specific) acoustic impedance of air, $\zeta_{air} = \rho c$.
ζ_s (specific) acoustic impedance of (ground) surface.

Index